



**HAL**  
open science

# Nanoscale materials for optoelectronics

Beniamino Sciacca

► **To cite this version:**

Beniamino Sciacca. Nanoscale materials for optoelectronics. Material chemistry. Université Aix Marseille, 2022. tel-04298501

**HAL Id: tel-04298501**

**<https://hal.science/tel-04298501>**

Submitted on 21 Nov 2023

**HAL** is a multi-disciplinary open access archive for the deposit and dissemination of scientific research documents, whether they are published or not. The documents may come from teaching and research institutions in France or abroad, or from public or private research centers.

L'archive ouverte pluridisciplinaire **HAL**, est destinée au dépôt et à la diffusion de documents scientifiques de niveau recherche, publiés ou non, émanant des établissements d'enseignement et de recherche français ou étrangers, des laboratoires publics ou privés.



# **NANOSCALE MATERIALS FOR OPTOELECTRONICS**

HABILITATION À DIRIGER DES RECHERCHES

Dr. Beniamino Sciacca



# TABLE OF CONTENTS

Preface	3
Introduction	4
Chapter 1: Nanowire photovoltaics	6
1.1 Ag-Cu <sub>2</sub> O Metal-semiconductor core-shell nanowires	6
1.2 Quantitative absorption measurements in single NW	9
1.3 Ag-Cu <sub>2</sub> O nanowire solar cell	11
Chapter 2: From single NW towards array: Transparent electrodes	34
Chapter 3: Nanocube epitaxy for monocrystalline nanostructured materials	45
3.1 Ag Nanocube epitaxy	45
3.2 Au Nanocube epitaxy	48
Chapter 4: Perspectives	68
Focus Area 1: Epitaxial Nanowelding - epitaxial welding of nanocube building blocks.	71
Focus Area 2: Nanocube assembly - assembling nanocube patterns on a large scale.	74
Focus Area 3: 3D building - Nanocube printing and stacking of monocrystalline nanopatterns	78
Acknowledgments	82
References	83
Appendix A: selected contributions to the field of Optical Sensing	90
A.1 Porous silicon optical sensors	90
A.2 Surface plasmon resonance biosensors	93
A.3 Infrared gas sensors	94
Appendix B: Curriculum Vitae	96
Appendix C: Publication list	100

# PREFACE

During my Master of Science in biomedical engineering at Politecnico di Torino, I started to develop a deep interest towards Nanoscience. That was sparked by a lecture given by Prof. Nicola Pugno that introduced carbon nanotubes, a material of wonder. That was back in 2005 and the course's topic was solid state mechanics. Although nowadays carbon nanotubes are not yet used as elevators to reach the moon<sup>1</sup>, they sure inspired many to become scientists at a time when nanoscience was still in its infancy.

My scientific career began in 2007, when I started a thesis on Porous silicon photonic nanostructures for biosensing devices, in the team of Prof. F. Geobaldo. During my PhD I had the opportunity to work for six months at University of California San Diego in the group of Prof. M. Sailor, and for three months in the team of Dr. F. Cunin at the University of Montpellier. After obtaining the PhD I moved for nearly two years at the Institute for Photonics and Advanced Sensing (University of Adelaide) to develop surface plasmon resonance based biosensors for gastric cancer in the group of Prof. T. Monro as a postdoctoral researcher. In 2013 I steered my research activity on optoelectronic devices, and in particular solar cells. It was then that I joined the group of Prof. E. Garnett that had just been established at the Institute AMOLF, where I worked until 2016 as a senior postdoc. After a short period at ASML I was hired at TNO as a permanent researcher. In 2018 I was recruited as a *chargée de recherche* at CNRS, in the laboratory CINA M in Marseille, and I started my research group on monocrystalline nanoscale materials for optoelectronics.

Since the start of my career I worked on the study, development and application of nanoscale materials on two big themes (optical (bio)sensors and optoelectronic devices) that have in common light-matter interaction. In this document I will present some selected research activities on nanoscale materials for optoelectronics, and I will briefly summarise in an Appendix the main contributions to the field of optical sensing.

# INTRODUCTION

Optoelectronic devices, are made of a stack of metal and semiconductor layers, that fulfil the basic requirements of **light absorption** and **carrier transport**. The overall performance of the device can thus be related to the efficiency of these two fundamental processes. Among these devices, solar cells play a critical societal role because they are needed to switch away from fossil fuel to a new sustainable era based on the use of renewable energy sources. For this to happen quickly, efficiency must increase and cost must go down. Since the cost for installation is roughly equal to that of the solar cell module, and the margin for producing the module are already quite tight, it is essential to put efforts in increasing the **efficiency**<sup>2</sup>. The average module efficiency of silicon solar cells is 20-24%, and in the single junction configuration could at best reach the thermodynamic limit of 33%<sup>2</sup>. On the other hand, multi-junction solar cells have much higher efficiency (the experimental record for one sun illumination is 38.8%<sup>3</sup>), but are not cost-effective, due to the **expensive** manufacturing process required to epitaxially grow stacks of **lattice-matched** semiconductor materials<sup>4</sup>. Therefore, new technologies or strategies, that can provide efficiencies above that of silicon solar cells at reduced costs, are needed. Working at the **nanoscale** offers the unique opportunity to go beyond conventional processes. The quality of materials/interfaces (carrier management) and

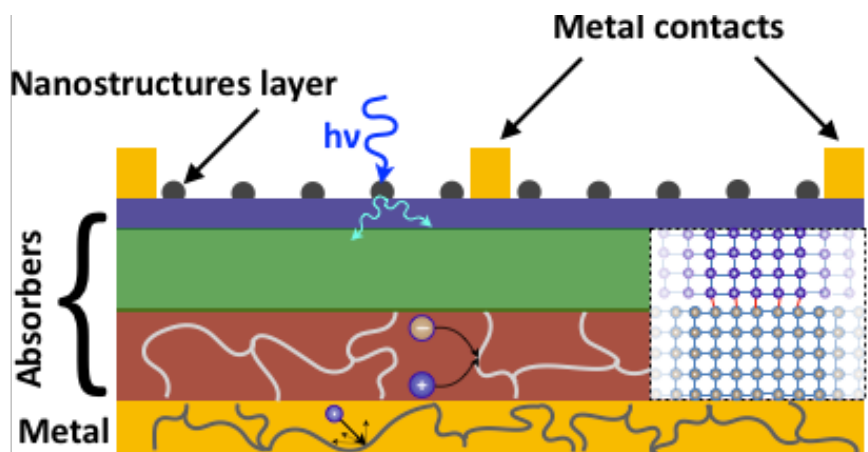


**Figure 1:** Simplified diagram of a multi-junction solar cell device to (i) highlight detrimental effects of grain boundaries, (ii) present constraints of lattice-matching at interfaces, and (iii) show advantages of nanostructuring, such as light-trapping.

light-matter interaction (photon management) are the main ingredients to achieve efficiencies close to the thermodynamical limit, whereas simple fabrication procedures and low material cost (earth abundant, nanostructured) are the main ingredients to reduce price.

Strong efforts and breakthrough at the interface between nanophotonics and physical chemistry, encouraged researchers to explore the opportunities of nanostructuring some of the device layers, to meet those fundamental challenges and achieve ultimate performance.

Nanoscale materials offers several advantages over macroscopic materials, as reduced bulk recombination<sup>5</sup>, the relaxation over lattice matching condition<sup>6</sup>, the possibility to **engineer electronic properties**<sup>7,8</sup>, the potential to **enhance light-matter interaction** to achieve maximum absorption<sup>9-18</sup>, and the opportunity to **make defect-free crystals**<sup>19</sup>. The exquisite combination of nanophotonic engineering, optimised device architecture and use of **high quality monocrystalline materials** has proven effective to achieve record performance<sup>20-23</sup>. The **quality** of materials employed is in fact a crucial pillar upon which the performance of optoelectronic devices stands<sup>24,25</sup>. Grain boundaries dramatically affect performance (see *Figure 1*): in metals increase resistivity with associated energy losses, while in semiconductors cause degradation in mobility and life-time of minority carriers, and are responsible for the non-radiative recombination. Therefore, all grain boundaries must be removed in order to achieve efficient carrier transport and reach the highest possible performance, both for the metal and the semiconductor part of the device<sup>25-31</sup>.

This context has strongly motivated research in various field of nanoscience at the fundamental level, but also for applied purposes. In the next chapter I will present some of my activities in this field.

# CHAPTER 1: NANOWIRE PHOTOVOLTAICS

There is a growing need in technology for devices nanostructuring to have enhanced features, reduced costs and increased efficiency<sup>7,32-34</sup>. Within the toolbox of nanomaterials, nanowires have been recently attracting a lot of attention as building blocks for nanostructured devices as solar cells<sup>35-43</sup>, biosensors<sup>44-51</sup>, logic gates<sup>33,52,53</sup>, transistors<sup>54-56</sup>, nanoprocessors<sup>33,57</sup>, self powered nanosystems<sup>43,58</sup>.

Nanowires have a large surface to volume ratio, and the electronic properties could be tuned by modification of the surface chemistry<sup>36,59</sup>, opening up several opportunities to be employed as a platform for fundamental studies.

Bottom-up synthetic approaches allow to afford several degrees of freedom in the fabrication of nanowires, where aspect ratio (length/diameter), cross-sectional shape, material composition, physical and chemical properties can be tuned in the synthesis stage<sup>40,60</sup>. Metallic<sup>61-64</sup>, semiconducting<sup>37,40,41,65</sup> or insulating<sup>66,67</sup> nanowires can be fabricated by choosing the appropriate synthetic approach and the proper precursors, enabling the realization of heteroepitaxial structures that conventional lattice matching conditions for macroscopic structures would otherwise forbid<sup>58,65</sup>.

Among other interesting features, nanowires offer strong light confinement and can concentrate light into deep-subwavelength volumes<sup>9,65,68,69</sup>, upholding the significant attention they have received as building blocks for opto-electronic devices<sup>32,33,37,70,71</sup>.

## 1.1 Ag-Cu<sub>2</sub>O Metal-semiconductor core-shell nanowires

An absorption cross-section larger than the geometrical cross-section is an interesting advantage of nanowire absorbers, and it has been recently proven effective in solar cell devices<sup>13</sup>. This comes as an effect of the light concentration within the nanowire, which acts as a resonant antenna and effectively absorbs light. Nanophotonics gives the opportunity to squeeze light into sub wavelength structures and to restrict the angular emission profile to

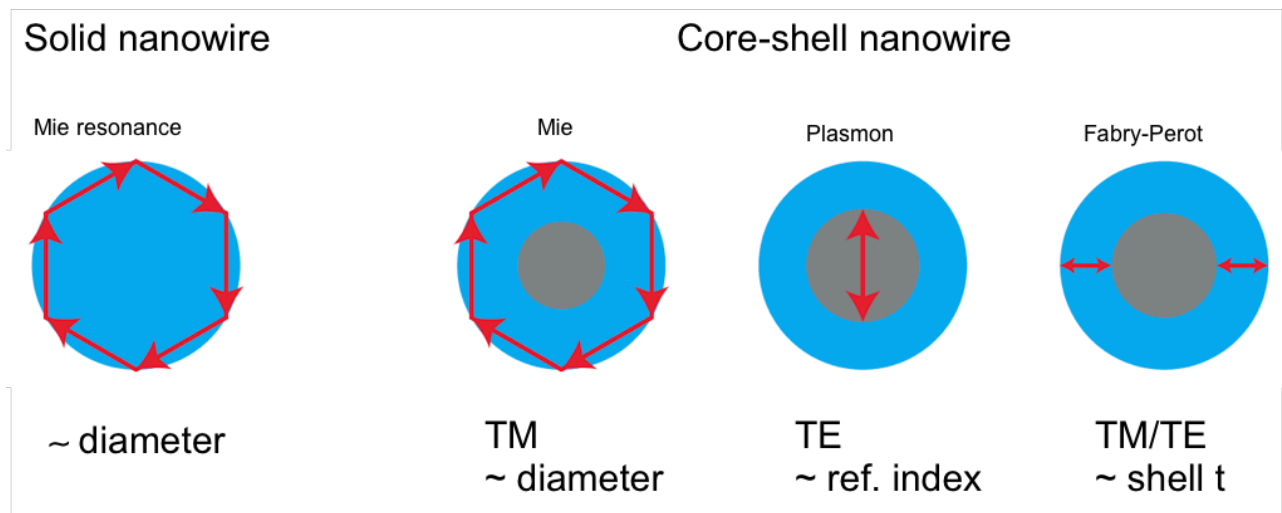


**Figure 2:** Simplified diagram of optical resonances in dielectric nanowires (left) and metal-semiconductor core-shell nanowires (right).

lower solid angles compared to the incoming sunlight radiation<sup>72</sup>. This strategy is beneficial from the perspective of reduced materials cost on one hand, but also allows to exceed the open circuit voltage expected for the same material in a thin film configuration<sup>21</sup>, and therefore to potentially achieve higher efficiency.

Solid semiconducting (horizontal) nanowires support polarisation-dependent Mie resonances, that can be tuned by changing the nanowire diameter<sup>9</sup>, as illustrated in Figure 2. However, this system offers limited possibility to achieve maximum absorption for all photons above the bandgap. This is because the absorption efficiency of a single resonance channel is limited to  $\lambda/2\pi$ , and that only a few Mie resonances can be placed in the desired spectral range. The presence of a metallic core to obtain a hybrid metal-semiconductor core-shell nanowire system would enable to introduce further optical resonances that can independently be tuned to boost light absorption above the limit of a single channel<sup>69</sup>. These include plasmon resonances, that depend on the shell refractive index and Fabry-Perot like resonances that can be tuned via the shell thickness. A substantial improvement of absorption efficiency across a wide spectral range was predicted for a Ag-aSi core-shell nanowire system by using a smaller amount of semiconducting material<sup>69</sup>. In addition to introducing further degrees of freedom to enhance absorption, the metal core can be employed as an electrode for swift charge extraction. Taking into account the minute shell thickness (few tens of nanometer) needed to achieve maximum absorption, materials with a short diffusion length can be employed, in contrast to conventional architectures. This makes the metal-semiconductor core-shell system extremely appealing to employ earth abundant semiconducting materials, such as copper (I) oxide ( $\text{Cu}_2\text{O}$ ).  $\text{Cu}_2\text{O}$  is a semiconductor with a direct bandgap of  $\sim 1.9$  eV, it can yield a maximum power conversion efficiency of  $\sim 20\%$  and it can be grown in solution. Therefore it was chosen as the shell material candidate. Silver was selected as the metal core due to its high conductivity and plasmonic response and to the possibility to synthesise it with colloidal chemistry approaches, that are naturally scalable.

First, Ag nanowires are prepared with the polyol process (see Figure 3), in which a silver salt ( $\text{AgNO}_3$ ) is reduced by ethylene glycol in the presence of a capping agent (PVP). Under the appropriate experimental conditions, pentatwinned seeds are formed in the early stage of the reaction. PVP binds selectively to (100) facets, enabling 1D growth along the [111] crystallographic direction, that result in the formation of nanowires<sup>73</sup>. Length and diameter of

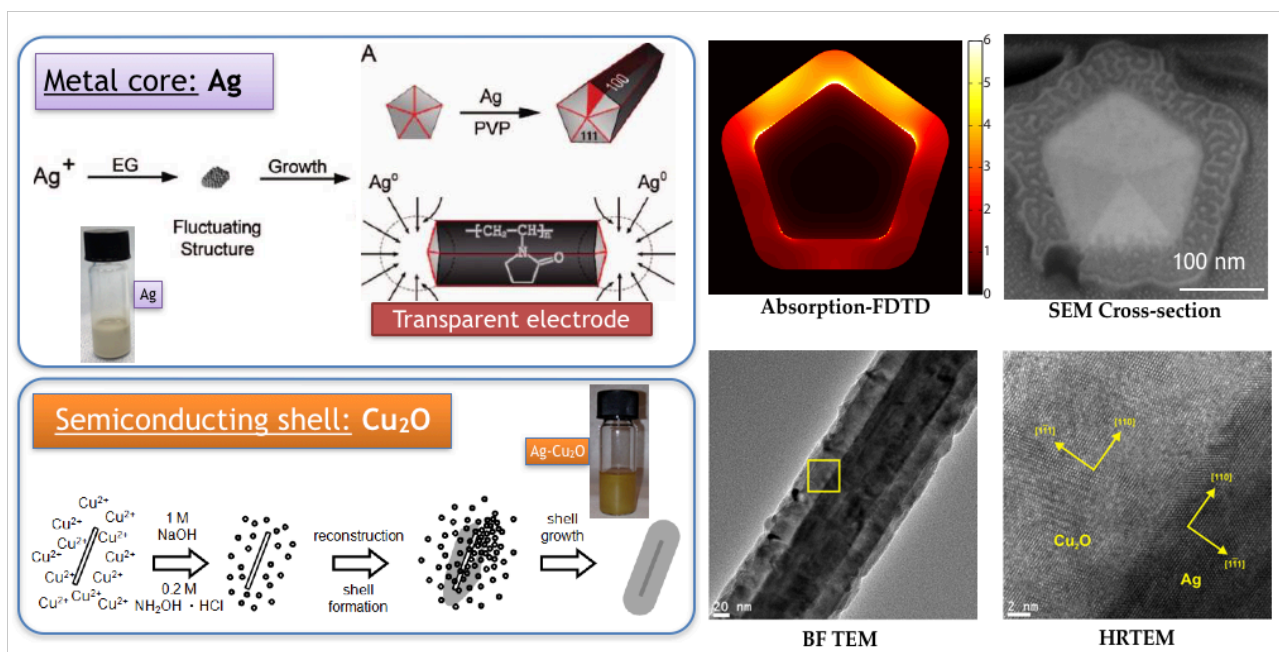


**Figure 3:** Synthesis of Ag-Cu<sub>2</sub>O core-shell nanowires. Top left: synthesis of the Ag nanowire core. Bottom-left: growth of a quasi-monocrystalline Cu<sub>2</sub>O shell. Right: Ag-Cu<sub>2</sub>O nanowire characterisation and simulated absorption.

nanowires can be tuned by varying the experimental conditions. The nanowire cross-section is pentagonal as a result of the seed geometry, and the diameter is uniform along the length.

A Cu<sub>2</sub>O shell is then grown around the Ag nanowires core in liquid phase (see Figure 3). A copper precursor is reduced in the presence of a surfactant by a reducing agent, in basic conditions. Tiny Cu<sub>2</sub>O nanoparticles nucleate on the surface of Ag nanowires and grow to merge. The colour of the nanowire dispersion changes dramatically as the shell grows, due to absorption by Cu<sub>2</sub>O. As a result of the small lattice mismatch, Cu<sub>2</sub>O growth is epitaxial and a quasi-monocrystalline shell is obtained<sup>74</sup>. The opportunity to obtain a quasi-monocrystalline material is such mild conditions (in water, at room temperature) is quite remarkable, in stark contrast with conventional epitaxy approaches. As mentioned earlier, this is very important, because grain boundaries are sources of non-radiative recombinations. Photoluminescence measurements performed on individual Ag-Cu<sub>2</sub>O core-shell nanowires showed room-temperature emission at ~670 nm, corresponding to the direct transition of Cu<sub>2</sub>O. Finite difference time domain (FDTD) simulations showed that most of the photons above the bandgap are indeed absorbed in the Cu<sub>2</sub>O shell.

The next challenge was to **quantify** absorption in individual nanowires to accurately assess the optical properties and compare it to simulations. This is particularly important in the accurate characterisation of single-nanowire solar cell devices, that can be used as a platform for fundamental studies on interfaces, light matter interactions and thermodynamic limits of solar energy conversion. This will be discussed in the following sections.

## 1.2 Quantitative absorption measurements in single NW

To quantify the performance of nanostructured optoelectronic devices, it is essential to measure their quantitative absorptance. Nanophotonics provides with helpful tools to understand, design and characterise nanostructures for visible light harvesting (nanoantennas). Sub-wavelength nanostructures interact strongly with incoming light via absorption and scattering, and can display an absorption/extinction cross-section substantially larger than their geometrical footprint, which is a typical feature of optical antennas. In the ray optics picture, this can be understood as if their size was larger. In Figure 4, it is presented a quintessential example of the need for quantifying absorption in nanoscale optoelectronic devices. In this example<sup>13</sup> a single GaAs nanowire solar cell device is built on a substrate either in the horizontal or vertical configuration. If the external quantum efficiency (EQE: number of electrons extracted per incoming photons) is calculated by taking into account the geometrical cross section as opposed to the absorption cross-section, the results obtained are incoherent, yielding an 'apparent' EQE larger than 1 for both configurations. This indicates that the efficiency of the device cannot be assessed based on geometrical considerations, and requires a quantitative measurement of the absorptance (therefore taking into account the antenna effect of light concentration).

In addition, for single-nanowire solar cell devices, internal quantum efficiency (IQE: number of electrons extracted per absorbed photons) is a more meaningful attribute to assess device performance compared to EQE, that in macroscopic solar cells is calculated on the basis of the device area. This is a logical consequence of the fact that in contrast to macroscopic samples, single-nanowire solar cell devices interact only with a fraction of the incoming beam via their absorption cross-section, the rest being reflected or transmitted. The fraction of incoming photons that interacts with the nanowire sample is either absorbed or scattered. Therefore, quantifying absorption is rather challenging as it requires to measure transmission, reflection and total scattering.

Most experimental approaches available to measure quantitative absorptance are based on the following assumptions: (i) all absorbed power turns into heat; (ii) the nanoparticle does not scatter light; or (iii) it interacts with light as a dipole. Therefore these methods are not

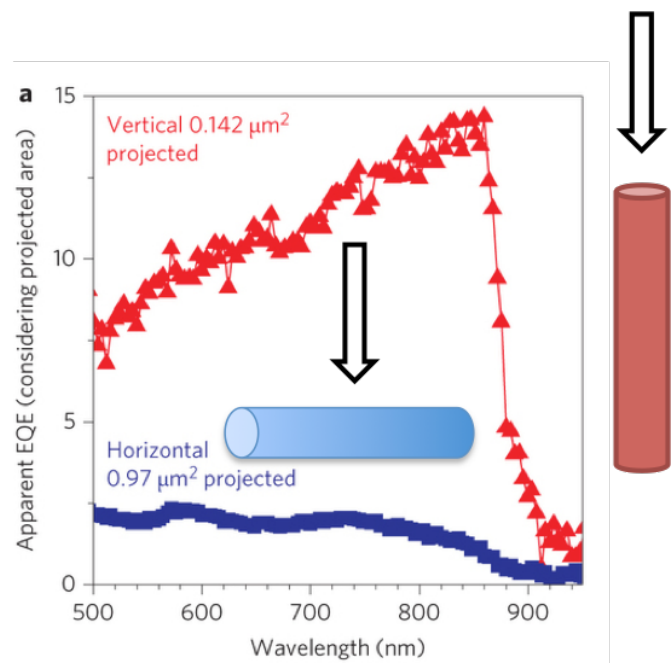


**Figure 4:** Comparison between the performance of individual GaAs nanowire solar cell in the horizontal and vertical configuration.

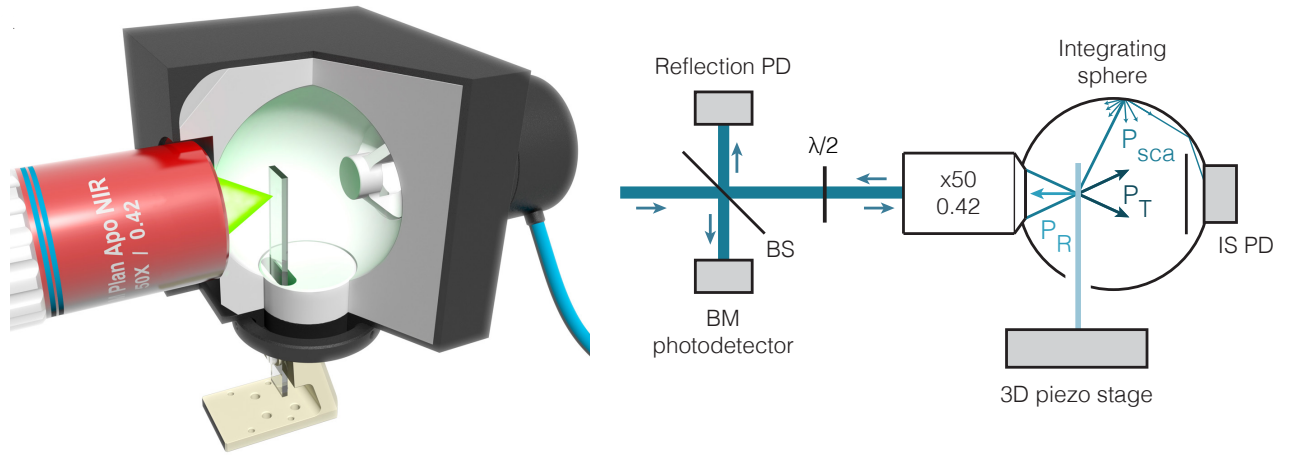


**Figure 5:** Integrating sphere microscopy setup to quantify absorption in individual nanostructures.

general for quantitative absorption measurements of nanostructures since they fail to meet the aforementioned assumptions.

This context led to develop a new approach<sup>75</sup> to quantify the absorption cross-section of diffusing nanostructures with submicron spatial resolution. This was achieved by placing the sample inside an integrating sphere and probing it with an ultralong working distance microscope objective (see Figure 5). Light transmitted and scattered was collected after being randomised by a detector mounted on the integrating sphere. Light reflected within the numerical aperture of the objective was collected via another photodetector. Using a non-absorbing part of the sample as a reference for scattering and a mirror as a reference for reflection, it was possible to determine the absorbed power simply from the power reflected and transmitted/scattered.

$$P_{\text{abs}} = 1 - P_{\text{R}} - P_{\text{T}} - P_{\text{sca}}$$

The sample was mounted on a 3D piezoelectric stage allowing scanning of the sample to obtain quantitative local information on the absorptance. A supercontinuum laser, monochromated by acoustic optical filters, was used as the excitation source. The beam diameter was characterised with knife-edge techniques to convert absorptance to absorption cross-section. To assess the accuracy of this integrating sphere microscopy setup, non-absorbing SiO<sub>2</sub> nanospheres were measured, indicating that ~95% of the total scattered power is collected. Spatially resolved absorptance measurements performed on Si and GaAs nanowires showed quantitative agreement with FDTD simulations across the entire spectrum. This technique was then applied to characterise Ag-Cu<sub>2</sub>O core-shell nanowires. Figure 6 compares the measured absorption cross section to Mie theory calculations for a cylindrical core-shell nanowire with roughly the same dimensions. The ratio between the beam diameter and the core-shell nanowire diameter was taken into account to quantitatively calculate the absorption efficiency. There is good agreement between theory and experiment, and surface roughness is probably responsible for the differences (in particular, the emergence of a second resonance in TE). In the smooth cylindrical geometry TE<sub>31</sub> is strongly overdamped, but the surface roughness increases the radiative loss rate, which alters the absorption cross section and thus leads to the apparent emergence of resonances. The absolute values of absorption

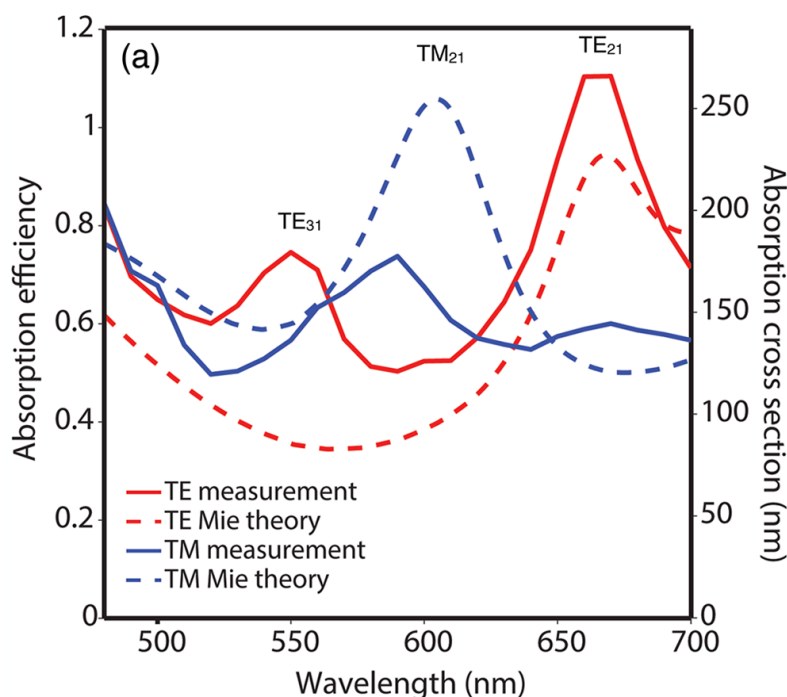


**Figure 6:** Quantitative absorption in individual Ag-Cu<sub>2</sub>O core-shell nanowires for the two polarisation and FDTD simulations.

do not differ substantially from the values calculated for a cylindrical core-shell nanowire, and the measured spectral dependence is similar to calculations for both TE and TM polarizations. This setup allowed to characterise the optoelectronic properties of individual core-shell nanowire solar cells with spatial resolution (see next section).

### 1.3 Ag-Cu<sub>2</sub>O nanowire solar cell

Single-nanowire solar cell devices are a promising platform for correlating performance to material, interface and optical properties. In particular, they allow to quantify the effect of light concentration and directivity on the open circuit voltage, with the opportunity to compare it to thermodynamics. In addition, correlating spatially resolved photocurrent measurements to transmission electron microscopy, the impact of crystallographic defects can be assessed. Finally, the strong dependence of nanostructured solar cells on surface and interface properties presents an opportunity to study these effects in a highly controlled system where changes at the semiconductor surface or metal-semiconductor interface can be directly measured in the photovoltaic response of the device.

The aforementioned metal-semiconductor core-shell nanowire system seemed an interesting architecture to test. The thin semiconductor shell in direct vicinity of the metal core electrode allows for facile extraction of photogenerated carriers, even in materials with short minority carrier diffusion lengths. The radial core-shell geometry has already proven useful in semiconductor nanowire photovoltaics, and even better charge carrier extraction can be obtained in this geometry where photocarriers are injected into a metal immediately. Another previously demonstrated advantage of semiconductor nanowires is their high absorption cross section, which can exceed the geometrical one, despite the minute amount

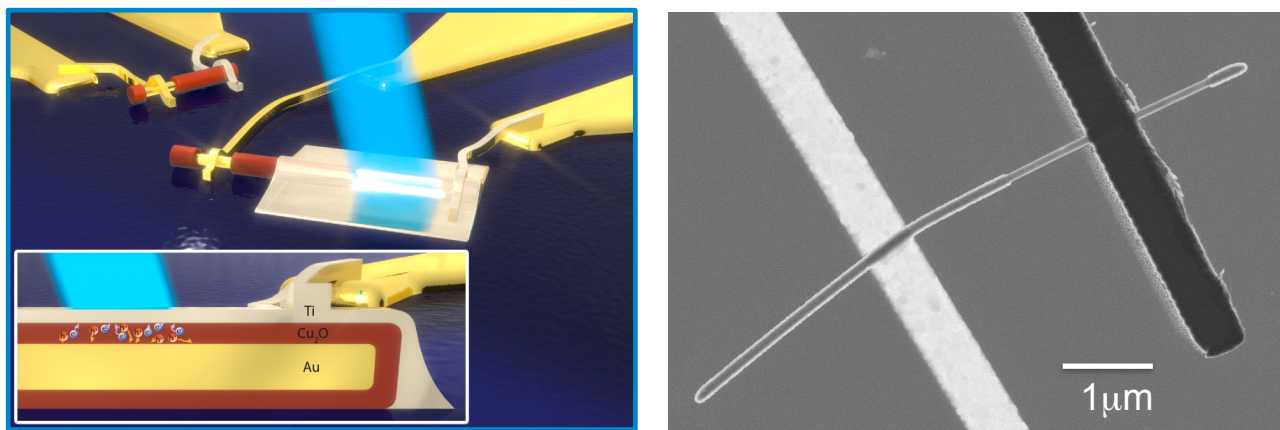


**Figure 7:** Cartoon (left) and SEM image (right) of core-shell metal-semiconductor Au-Cu<sub>2</sub>O individual solar cell devices.

of material employed, due to the presence of optical resonances. In addition, Cu<sub>2</sub>O is an earth abundant non-toxic material that is an excellent candidate for the top absorber when combined with silicon as the bottom absorber in a high efficiency multijunction solar cell because its band gap ( $E_g \sim 2$  eV) is close to ideal (1.7–2.0 eV).

Two electrical contacts are necessary in a solar cell: one that collects photogenerated holes and one that is selective for photogenerated electrons. One simple and effective method for inducing this carrier selectivity is to use metal contacts with different work functions such that one metal makes an Ohmic contact to the Cu<sub>2</sub>O and the other a Schottky junction. Gold was chosen as the metal nanowire core because it has a large work function ( $\sim 5.4$  eV; similar to that of Cu<sub>2</sub>O) and makes an Ohmic contact to Cu<sub>2</sub>O. Furthermore, Au has a high chemical stability, low lattice mismatch with Cu<sub>2</sub>O ( $\sim 4\%$ ), and a simple nanowire synthesis route. Titanium was chosen as the Schottky contact, because of its low work function ( $\sim 4.3$  eV), excellent adhesion to many materials and a stable surface oxide. As reported in previous literature, it is possible that a redox reaction under the Ti contact converts the Cu<sub>2</sub>O to TiO<sub>2</sub> and Cu at the interface. This modified interface still results in charge carrier separation and extraction, but it does lower the maximum achievable Voc value.

Fabrication of the solar cell device was performed with electron beam lithography and metal evaporation (Figure 7). First, Au-Cu<sub>2</sub>O core-shell nanowires were deposited by dropcasting on an insulating substrate containing macroscopic electrodes; next, one step of e-beam lithography was used to evaporate the Ti contact on the Cu<sub>2</sub>O shell; finally, a second step of e-beam lithography was used to deposit a Au contact directly on the Au core (after chemical etch of a Cu<sub>2</sub>O shell section). Figure 8 shows the overlap of the SEM images and the spatially resolved photocurrent of a single nanowire solar cell device under a 410 nm laser illumination with perpendicular polarisation compared to the nanowire axis. This demonstrates photocurrent collection from the nanowire along the entire length covered by the Ti pad, supporting the idea that charge carriers generated by light passing through the thin (10 nm) Ti pad can be separated and collected at the metal core and the Ti top contact. In addition the drop in photocurrent outside the Ti pad indicates that the diffusion length of minority carriers in the shell is small. Interfaces passivation and employing a Schottky contact in the nanowire core would allow to improve performance. Single-nanowire is an ideal platform for fundamental interfacial studies. In fact, insights gained here can be applied to existing thin-film technology where the metal-semiconductor contact is also a crucial source of loss but more difficult to isolate and study.

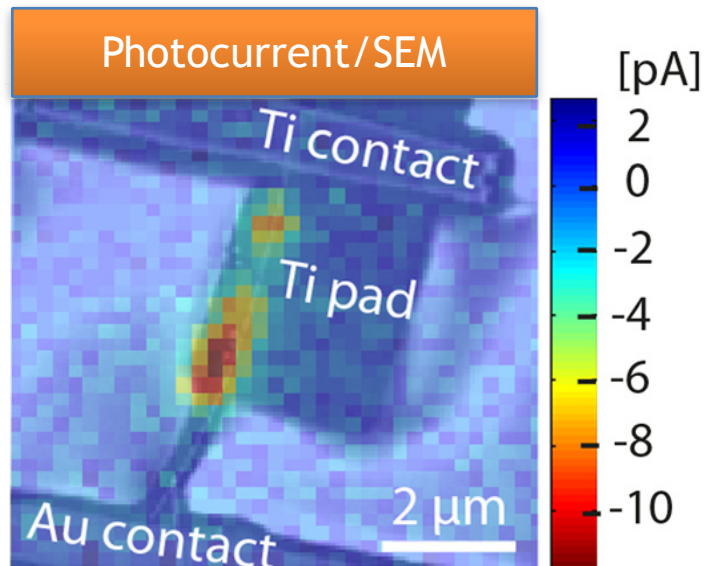


**Figure 8:** Scanning photocurrent measurements on Au-Cu<sub>2</sub>O core-shell nanowires, overlapped with the SEM image.

In addition, considering that metal-semiconductor core-shell nanowire is an interesting geometry for solar cells made from materials with very short minority carrier diffusion lengths, it is important to explore device architecture that can be achieved at the macroscopic scale via inexpensive fabrication methods.

Nanowires can be organised either as vertical or horizontal arrays. Vertical arrays have the advantage of a large absorption cross-section, but fabrication can be challenging, especially because they typically require a transparent top electrode. Horizontal arrays have the advantage that the metal core is truly a transparent electrode and a full device can be obtained simply by evaporating a metal contact on the shell.

If Ag-Cu<sub>2</sub>O core-shell nanowires are placed on a metallic substrate and organised in a dense array (as shown in Figure 9), after optimising core diameter and shell thickness, an integrated absorption (weighted for the AM1.5 spectrum) as large as 72% in the shell can be obtained (core = 100 nm, shell = 40 nm, nanowires touching). In the case of a Cu<sub>2</sub>O thin film on a metal conductor, an absorption as large as 71% of the AM1.5 spectrum could be achieved for the optimized case (50 nm Cu<sub>2</sub>O film thickness). In such a geometry, however, there is only one electrical contacts, while in the core-shell geometry, both contacts are already present, and thus shading is taken into account.

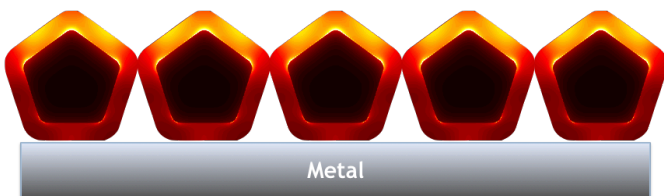


**Figure 9:** Cartoon of a macroscopic solar cell device made of metal-semiconductor core-shell nanowires in a horizontal array configuration.

# Solution-Phase Epitaxial Growth of Quasi-Monocrystalline Cuprous Oxide on Metal Nanowires

Beniamino Sciacca,<sup>†</sup> Sander A. Mann,<sup>†</sup> Frans D. Tichelaar,<sup>‡</sup> Henny W. Zandbergen,<sup>‡</sup> Marijn A. van Huis,<sup>‡,§</sup> and Erik C. Garnett<sup>\*,†</sup>

<sup>†</sup>Center for Nanophotonics, FOM Institute AMOLF, Science Park Amsterdam 104, 1098 XG Amsterdam, The Netherlands

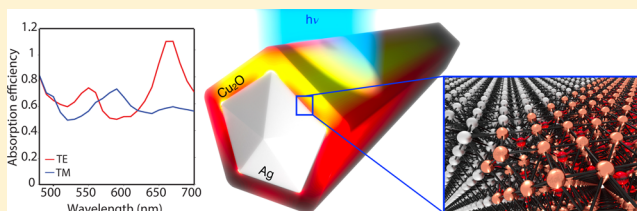
<sup>‡</sup>National Center for HREM, Kavli Institute of Nanoscience, Delft University of Technology, Lorentzweg 1, 2628CJ, Delft, The Netherlands

<sup>§</sup>Debye Institute for Nanomaterials Science and Center for Extreme Matter and Emergent Phenomena, Utrecht University, Princetonplein 5, 3584CC Utrecht, The Netherlands

## S Supporting Information

**ABSTRACT:** The epitaxial growth of monocrystalline semiconductors on metal nanostructures is interesting from both fundamental and applied perspectives. The realization of nanostructures with excellent interfaces and material properties that also have controlled optical resonances can be very challenging. Here we report the synthesis and characterization of metal–semiconductor core–shell nanowires. We demonstrate a solution-phase route to obtain stable core–shell metal–Cu<sub>2</sub>O nanowires with outstanding control over the resulting structure, in which the noble metal nanowire is used as the nucleation site for epitaxial growth of quasi-monocrystalline Cu<sub>2</sub>O shells at room temperature in aqueous solution. We use X-ray and electron diffraction, high-resolution transmission electron microscopy, energy dispersive X-ray spectroscopy, photoluminescence spectroscopy, and absorption spectroscopy, as well as density functional theory calculations, to characterize the core–shell nanowires and verify their structure. Metal–semiconductor core–shell nanowires offer several potential advantages over thin film and traditional nanowire architectures as building blocks for photovoltaics, including efficient carrier collection in radial nanowire junctions and strong optical resonances that can be tuned to maximize absorption.

**KEYWORDS:** Core–shell nanowire, epitaxial growth, solution phase synthesis, metal–semiconductor heterostructures, quasi-monocrystalline cuprous oxide (Cu<sub>2</sub>O), single nanowire quantitative optical absorption measurements



The development of inexpensive and efficient solar cells has been a major research focus over the past 10 years to face the projected increase in global energy consumption.<sup>1</sup> Ideally, the ultimate solar cell would convert light into electricity in the smallest possible volume of material. This desire to minimize volume is not only motivated by the reduced costs associated with using less semiconductor material but also fundamentally linked to a higher solar conversion efficiency. This higher theoretical efficiency has been well documented and arises from two considerations: (1) using less material reduces bulk recombination and thus can boost the open-circuit voltage ( $V_{oc}$ ),<sup>2</sup> and (2) reaching full absorption in less material could lead to higher photogenerated carrier densities and thus higher  $V_{oc}$ .<sup>3,4</sup> The light concentration effect has been historically applied using macroscale concentrating optics, and the efficiency enhancement comes via a <60 mV increase of  $V_{oc}$  per decade of concentration. For example, this  $V_{oc}$  enhancement is largely responsible for the increase in efficiency from 31.3% at 1 sun to 40.7% at 240 sun<sup>5</sup> in triple-junction solar cells. More recently, researchers have shown that single semiconducting nanowires and nanowire arrays can act as antennas, providing a similar concentration effect without

external optics and employing a reduced amount of material.<sup>6,7</sup> Furthermore, the possibility to combine materials with high lattice mismatch in heteroepitaxial junctions,<sup>8–10</sup> and the opportunity to decrease the material volume without compromising light absorption,<sup>11–13</sup> make the development of nanowire-based solar cells intriguing.<sup>14–16</sup>

These results motivated us to investigate a novel core–shell nanowire geometry consisting of a metal nanowire coated by an ultrathin semiconductor shell, which theoretically shows superior absorption compared to solid semiconductor nanowires (Figure 1).<sup>17</sup> In this hybrid core–shell geometry there are several resonances with high field intensity in the shell, leading to efficient light absorption in the semiconductor. Furthermore, this geometry is particularly appealing because the metal core can also function as an electrode embedded within the semiconductor that locally collects photogenerated charge carriers;<sup>18,19</sup> this indeed simplifies the realization of a working device and might reduce fabrication costs. For this scheme to

Received: July 23, 2014

Revised: September 3, 2014

Published: September 18, 2014

work, the quality of the semiconductor and the nature of the interface are extremely important to provide sufficient carrier mobility and to reduce recombination.<sup>9,14,20</sup> Fabrication of related metal–semiconductor heterostructures has recently attracted a lot of attention,<sup>21,22</sup> and the synthesis of core–shell nanoparticles with monocrystalline shells has allowed for the exploration of new avenues in fundamental nanomaterial research<sup>23–25</sup> as well as the demonstration of new technological applications;<sup>26,27</sup> however, solution-phase synthesis of this class of heterostructures has so far been limited mainly to nanoparticles.<sup>24,28–31</sup>

Here we report the synthesis and characterization of metal–Cu<sub>2</sub>O core–shell nanowires. Cu<sub>2</sub>O was chosen as a first model system to demonstrate this concept because it is an earth abundant material with a high absorption coefficient and a band gap close to ideal for the top layer in a tandem solar cell with silicon.<sup>32</sup> Additionally, it provides a relatively low lattice mismatch with both Ag and Au (~4%), which have been used for high-performance nanowire transparent electrodes.<sup>18,19</sup>

We begin by describing the synthetic procedure and resulting morphology and then use numerical simulations and analytical calculations to demonstrate the high electric field intensities in the thin semiconducting shell and the large absorption efficiency that can be reached with these structures. We confirm these theoretical predictions with quantitative single-nanowire absorption measurements. The good agreement with theory gives us confidence to calculate absorption in periodic arrays of these nanowires to predict how they would perform in a macroscopic solar cell. The results show that in our core–shell configuration a 40 nm Cu<sub>2</sub>O shell can absorb approximately the same amount of light as a semi-infinite Cu<sub>2</sub>O slab without an antireflection coating. Photoluminescence measurements on single nanowires also confirm that carriers are not completely quenched by the local metal contact, and the band gap value is similar to what is observed in bulk films. In addition to the optical properties we provide electron microscopy and X-ray spectroscopy to show that the cuprous oxide shell is spatially uniform, quasi-monocrystalline, pure-phase Cu<sub>2</sub>O. Selected area electron diffraction (SAED) and high-resolution transmission electron microscopy (HR-TEM) confirm the epitaxial relationship between the core and the shell. Density functional theory (DFT) calculations provide further insight into the binding configuration at the interface. Finally, the cuprous oxide shell shows no evidence of further oxidation to cupric oxide (CuO) even after extended storage in air. Combined, these results suggest that our core–shell nanowires could be an excellent platform for fundamental studies of metal–semiconductor interfaces, which are critical in many optoelectronic devices. Furthermore, the efficient absorption and local contacting features of such a geometry could have an impact in applications beyond photovoltaics such as sunlight-to-fuel conversion, photodetectors, and light-emitting diodes.

The synthesis of metal–Cu<sub>2</sub>O core–shell nanowires (Figure 2) is performed entirely in solution and involves two steps (see Supporting Information for further details): (i) synthesis of metal nanowires via the polyol process in ethylene glycol; (ii) employing metal nanowires as the nucleation site for the growth of a Cu<sub>2</sub>O shell at room temperature in water.

Core–shell nanowires with a silver core were chosen to illustrate the structural, chemical, and optical properties of such heterostructures (see Supporting Information for core–shell nanowires with a gold core). The advantage of using Ag versus

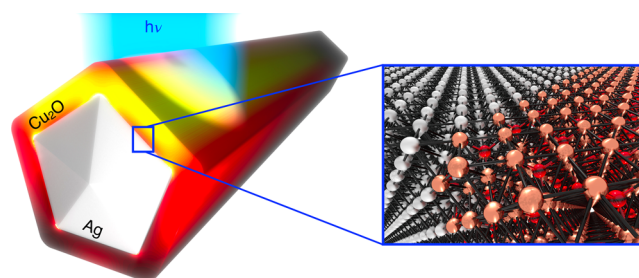


**Figure 1.** Ag–Cu<sub>2</sub>O core–shell nanowires. Artist's impression of a core–shell nanowire illuminated from the top. The light absorption profile is overlaid on the schematic image, and the inset shows the lattice matching at the interface.

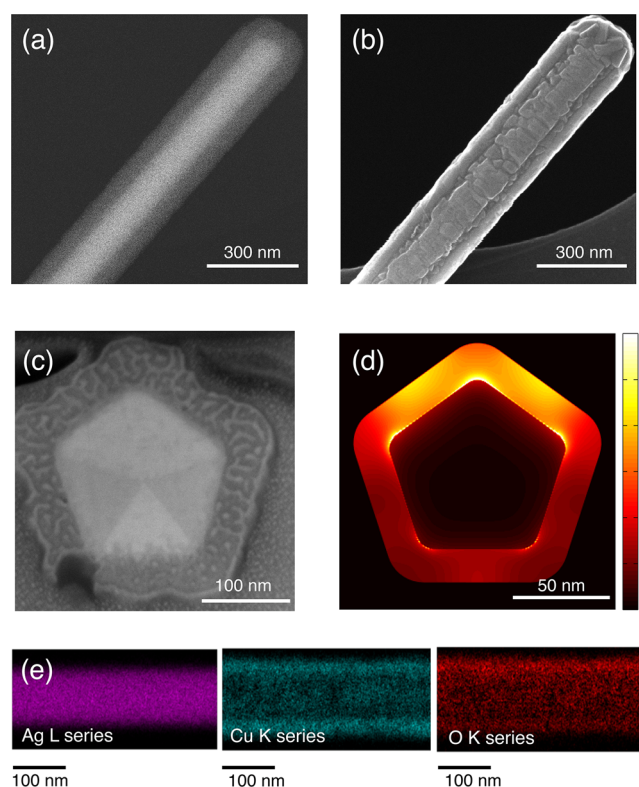


**Figure 2.** Ag–Cu<sub>2</sub>O core–shell nanowire: (a) in-column-detector (ICD) and (b) secondary electrons (SE) image of a Ag–Cu<sub>2</sub>O nanowire lying on a substrate; (c) focused ion beam (FIB) cross-sectional view; (d) distribution profile of the total absorbed power averaged over AM 1.5 (unpolarized), calculated from FDTD simulations for a Ag–Cu<sub>2</sub>O core–shell nanowire in vacuum. The color scale is in  $10^4$  W/m<sup>2</sup> for a 1 V/m plane wave incident from the top. (e) EDS elemental maps of a Ag–Cu<sub>2</sub>O nanowire, for Ag, Cu, and O showing the presence of a core–shell geometry.

Au is the lower cost and the better conductivity. Compared to other metals, such as Cu, Ag is more stable to chemical reactions, but other metals such as Al could be interesting from the optical and economical point of view.

Figure 2c shows a representative cross section of a Ag–Cu<sub>2</sub>O nanowire after focused ion beam milling. In the cross-sectional image there is clear contrast between the Ag core and the Cu<sub>2</sub>O shell. Interestingly, it is also possible to resolve the five twin planes of the Ag nanowire and appreciate a different contrast for different single-crystalline subunits. Note that Ag nanowires grow from 5-fold twinned decahedral seeds along the [110] direction<sup>33</sup> and therefore feature a pentagonal cross section.

The bright features visible on the shell are due to adsorption of sputtered material during preparation of the cross section. Elemental maps recorded using energy dispersive spectroscopy (EDS) in an SEM verify the elemental distribution in our core-shell nanowires (Figure 2e). The emission intensity of characteristic X-rays is plotted as a function of the electron beam position, for three different X-ray energies, characteristic of Ag (L shell), Cu (K shell), and O (K shell). The three plots in Figure 2e confirm the localization of Ag only in the core of the nanowire and show that X-rays from Cu and O are emitted from a larger region in the radial direction. Note that the intensity in the Cu and O chemical maps is higher at the edge, where the projected shell thickness is higher as expected for the proposed Ag-Cu<sub>2</sub>O core-shell nanowire structure. It should be emphasized that different core diameters and shell thicknesses can be achieved by adjusting the synthetic conditions and that other metal nanowires can be employed for the nucleation of the Cu<sub>2</sub>O shell with the same synthetic procedure (see Supporting Information Figure S1 for an example of a Au-Cu<sub>2</sub>O nanowire).

Within the same synthetic batch, some difference in shell thicknesses can be observed for nanowires with very different core sizes. As the shell growth is typically very fast (1–2 min for first nucleation and growth stage), adjacent nanowires in solution compete for Cu precursor. This means that nanowires with larger cores, which require a larger volume of Cu<sub>2</sub>O for the same shell thickness, end up with thinner shells. This often results in higher surface roughness or, in extreme cases, even incomplete shell coverage (see Supporting Information Figure S3).

We used finite-difference time domain (FDTD) to model light absorption in pentagonal Ag-Cu<sub>2</sub>O nanowires. The wavelength-dependent absorbed power density in the nanowire was weighted over the AM1.5 solar spectrum and integrated for photon energies above the band gap (290–650 nm). Figure 2d shows a 2D spatial map of the integrated absorbed power. The power profile is averaged over TE and TM polarizations for the best comparison to unpolarized sunlight. From Figure 2d it is clear that most of the absorption occurs in the Cu<sub>2</sub>O shell, but there is some parasitic absorption in the metal core (<16%). In order to provide a comparison to a thin-film geometry, in Supporting Information Figure S2 we show the absorbed power distribution for three control systems: a 100 nm thick Ag film (Figure S2a), a 40 nm thick Cu<sub>2</sub>O membrane (Figure S2b), and the combination of the previous two (Figure S2c) upon illumination by a plane wave. Note that as for the Ag-Cu<sub>2</sub>O nanowire the absorbed power is weighted over the AM1.5 spectrum and integrated from 290 to 650 nm. The maximum of the absorbed power density in the core-shell geometry is 3 times larger than that absorbed in a Cu<sub>2</sub>O membrane supported on a Ag film. This corroborates the large optical cross section of this new core-shell nanowire architecture. Note that the dimensions of the Ag-Cu<sub>2</sub>O nanowire shown in Figure 2d correspond to the optimum dimensions for the largest absorbed power density (core radius:  $r_c = 50$  nm; shell thickness:  $t_s = 20$  nm).

To verify the absorption properties of such core-shell nanowires experimentally, we measured the quantitative absorption in both polarizations (Figure 3a). In the TE polarization (electric field polarized perpendicular to the nanowire's axis) the core-shell nanowire shows two resonant absorption peaks in the experimental spectrum, while in TM (electric field polarized along nanowire's axis) only one is

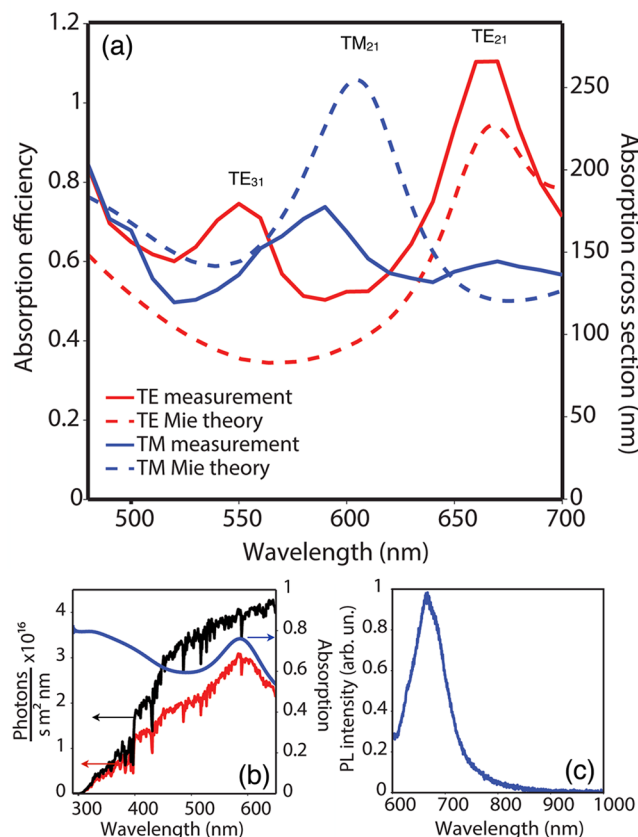


**Figure 3.** Optical characterization of a single Ag-Cu<sub>2</sub>O core-shell nanowire with a core radius of 55 nm and a shell thickness of 65 nm. (a) Experimental (solid lines) and calculated (dashed lines) quantitative absorption spectrum of a single core-shell nanowire in TE (red) and TM (blue) polarizations. (b) FDTD simulation of the photons absorbed in the shell of a Ag-Cu<sub>2</sub>O nanowire array weighted over the AM 1.5 (red line); photon flux in the solar spectrum (black line); absorption in the Cu<sub>2</sub>O shell before weighting for AM 1.5 (blue line). (c) Photoluminescence emission of a single core-shell nanowire.

visible. Figure 3a compares the measured absorption cross section to Mie theory calculations for a cylindrical core-shell nanowire with roughly the same dimensions (see Supporting Information). There is good agreement between theory and experiment. Since we have verified these quantitative absorption measurements in a simpler silicon nanowire system (which will be discussed in a future publication), we attribute the differences between measurement and theory (in particular, the emergence of a second resonance in TE) to significant surface roughness (see Figure S4 for SEM images). In the smooth cylindrical geometry TE<sub>31</sub> is strongly overdamped, but the surface roughness increases the radiative loss rate, which alters the absorption cross section and thus leads to the apparent emergence of resonances.<sup>17</sup> Note that the ratio between the beam diameter, measured by the knife-edge technique, and the core-shell nanowire diameter was taken into account to quantitatively calculate the absorption efficiency reported in Figure 3a.

Interestingly, the absolute values of absorption do not differ substantially from the values calculated for a cylindrical core-shell nanowire, and the measured spectral dependence is similar to calculations for both TE and TM polarizations.

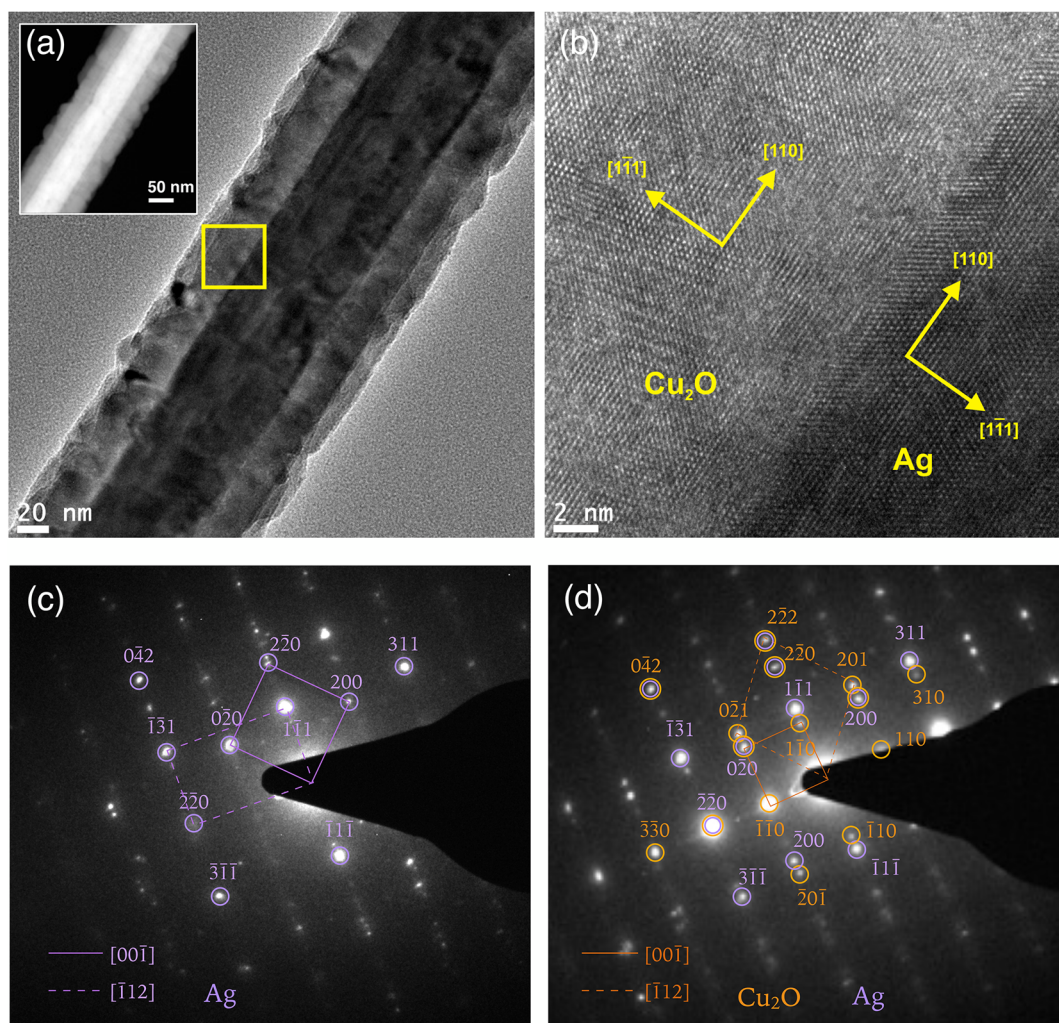


**Figure 4.** Structural characterization of Ag–Cu<sub>2</sub>O core–shell nanowire. (a) Bright field TEM of a representative Ag–Cu<sub>2</sub>O core–shell nanowire, showing a neat contrast between Ag core and Cu<sub>2</sub>O shell; inset: the HAADF image emphasizes Z contrast in the Ag–Cu<sub>2</sub>O nanowire. (b) HRTEM image of the interface between core and shell in the region highlighted in (a). The two lattices match at the interface along the [110] direction and show epitaxial growth. (c, d) SAED pattern for an individual Ag nanowire and Ag–Cu<sub>2</sub>O nanowire, respectively. The indexing of the SAED pattern has been performed along [001] and [112] zone axes and shows a cube-on-cube orientation relationship of the Cu<sub>2</sub>O shell on the Ag core. The spot size included the entire core–shell nanowire shown in (a).

To provide a comparison of the absorption properties of Ag–Cu<sub>2</sub>O nanowires with bulk absorbing materials, we carried out FDTD simulations of Ag–Cu<sub>2</sub>O periodic arrays lying on a perfect electric conductor, with the dimensions used in Mie theory to calculate the absorption spectrum of Figure 3a ( $r_c = 55$  nm,  $t_s = 65$  nm). The spectral dependence of the absorbed photon flux in the shell material (weighted for the AM1.5 spectrum) in a Ag–Cu<sub>2</sub>O nanowire array is presented in Figure 3b (red line), along with the total photon flux in the AM1.5 spectrum (black line) and the absolute absorption (not weighted) fraction in the Cu<sub>2</sub>O shell (blue line). The total absorbed flux integrated in the range of 290–650 nm is 66% (absorbed in the Cu<sub>2</sub>O shell). With further optimization of the core radius and shell thickness it is possible to achieve a total integrated absorption as large as 72% in the shell material for such a Ag–Cu<sub>2</sub>O nanowire array ( $r_c = 100$  nm,  $t_s = 40$  nm, nanowires touching). For comparison, a semi-infinite Cu<sub>2</sub>O film without an antireflection coating absorbs roughly 75% of the AM1.5 spectrum. In the case of a Cu<sub>2</sub>O thin film on a perfect electric conductor, an absorption as large as 71% of the AM1.5 spectrum could be achieved for the optimized case (50

nm Cu<sub>2</sub>O film thickness). In such a geometry, however, there are no electrical contacts, while in the core–shell geometry, both contacts are already present, and thus shading is taken into account.

In addition to optical absorption measurements, photoluminescence (PL) experiments were performed on individual Ag–Cu<sub>2</sub>O nanowires by exciting at a wavelength of 532 nm with a laser (Figure 3c). The band gap luminescence at 670 nm from individual nanowires suggests that the metal–semiconductor interface does not fully quench radiative processes. The emission wavelength is slightly different from what has been observed in bulk Cu<sub>2</sub>O which could be related to the lattice mismatch or optical resonances in the nanostructure.<sup>34–37</sup>

Below we use electron microscopy and X-ray spectroscopy to investigate the quality of the metal–semiconductor interface and to analyze the characteristics of the Cu<sub>2</sub>O shell. Figure 4a shows a representative bright field transmission electron microscopy (BF-TEM) image of a Ag–Cu<sub>2</sub>O nanowire. The Ag core is clearly visible in the center. The apparent double layer contrast in the Cu<sub>2</sub>O shell is the result of a 2D projection

of the 3D pentagonal morphology, whereby  $\text{Cu}_2\text{O}$  shell domains from different pentagonal facets can be overlapping, depending on the orientation of the nanowire on the substrate. The scanning transmission electron microscopy high-angle annular dark-field (STEM-HAADF) image (inset of Figure 4a) displays so-called Z-contrast and highlights the substantial difference in atomic number between the Ag core and the  $\text{Cu}_2\text{O}$  shell. Figure 4b shows a HR-TEM image of the area indicated in Figure 4a. The yellow axes represent the crystallographic directions of core and shell.

Ag and  $\text{Cu}_2\text{O}$  both have a cubic crystal lattice, and Ag has space group  $Fm\bar{3}m$  with a lattice parameter of 4.090 Å,<sup>38</sup> while  $\text{Cu}_2\text{O}$  has space group  $Pn\bar{3}m$  with a lattice parameter of 4.269 Å.<sup>39</sup> Interestingly, in the core-shell nanowire, the primary axes of both crystals are mutually aligned, resulting in a cube-on-cube orientation relationship, with a lattice mismatch of 4.4% (see inset in Figure 5a). The crystals are both oriented with

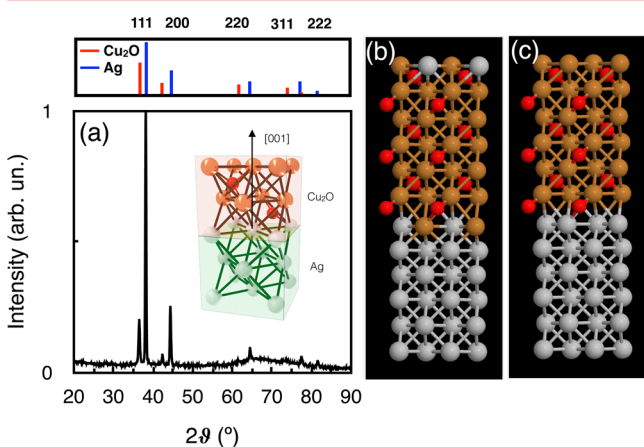


**Figure 5.** Structural characterization of Ag- $\text{Cu}_2\text{O}$  core-shell nanowire. (a) XRD of Ag- $\text{Cu}_2\text{O}$  nanowire ensemble in the range  $20^\circ$ – $90^\circ$ , showing diffraction peaks of Ag and  $\text{Cu}_2\text{O}$ . Top: reference values for Ag (blue) and  $\text{Cu}_2\text{O}$  (red) diffraction peaks.<sup>23</sup> Inset: artistic impression of the cube-on-cube orientation between the core and the shell material. (b, c) Structural atomic models of the Ag- $\text{Cu}_2\text{O}$  interface obtained after structural relaxation using DFT calculations for mixed and unmixed Ag/Cu atomic layers, respectively. Brown spheres represent copper atoms, red spheres oxygen atoms, and gray spheres silver atoms.

their  $[110]$  axes along the length of the nanowire and have the  $[1\bar{1}1]$  and  $[001]$  axes pointing in lateral directions. From this analysis it is evident that the  $\text{Cu}_2\text{O}$  shell grows epitaxially on the Ag nanowire core, and therefore polyvinylpyrrolidone (PVP), which is known to passivate Ag nanowire facets,<sup>33</sup> must be displaced during the nucleation and growth of  $\text{Cu}_2\text{O}$ , as no interlayer is observed. HR-TEM measurements were performed on multiple Ag- $\text{Cu}_2\text{O}$  nanowires along various zone axes to confirm the epitaxial growth and showed similar orientations between the Ag core and the  $\text{Cu}_2\text{O}$  shell. In addition, epitaxial growth was observed for core-shell nanowires with larger core diameters (above 200 nm, Figure S3).

The long-range order of the  $\text{Cu}_2\text{O}$  shell, its crystallographic structure and relationship to the underlying Ag lattice were studied by selected area electron diffraction (SAED), by collecting signal from the entire core-shell nanowire shown in Figure 4a. As a reference, a SAED pattern for an individual Ag nanowire is shown in Figure 4c. The diffraction pattern cannot be assigned to a simple FCC crystal because of the

presence of five twinned subcrystals, leading to two individual diffraction patterns superimposed: one along the  $[00\bar{1}]$  zone axis (solid line) and one along the  $[\bar{1}12]$  zone axis (dashed line).<sup>33</sup>

A series of new spots appear in the diffraction pattern of the Ag- $\text{Cu}_2\text{O}$  core-shell nanowire (Figure 4d), as denoted by the orange circles. Some key features emerge from this pattern: (i) individual spots are observed, as opposed to a continuous ring, demonstrating that the  $\text{Cu}_2\text{O}$  shell on every Ag facet is quasi-monocrystalline; (ii) two sets of superimposed quasi-single-crystal diffraction patterns are observed for  $\text{Cu}_2\text{O}$ , one with square symmetry along the  $[00\bar{1}]$  zone axis and one with rhomboidal symmetry along the  $[\bar{1}12]$  zone axis, confirming the cube-on-cube crystallographic alignment of the  $\text{Cu}_2\text{O}$  shell with the underlying Ag nanowire crystal, as depicted in the inset of Figure 5a; (iii) epitaxial relationship  $(0\bar{2}0)_{\text{Ag}}\parallel(0\bar{2}0)_{\text{Cu}_2\text{O}}$ ,  $(200)_{\text{Ag}}\parallel(200)_{\text{Cu}_2\text{O}}$  and  $[00\bar{1}]_{\text{Ag}}\parallel[00\bar{1}]_{\text{Cu}_2\text{O}}$ ; (iv) epitaxial relationship  $(\bar{2}\bar{2}0)_{\text{Ag}}\parallel(\bar{2}\bar{2}0)_{\text{Cu}_2\text{O}}$ ,  $(1\bar{1}1)_{\text{Ag}}\parallel(2\bar{2}2)_{\text{Cu}_2\text{O}}$ , and  $[\bar{1}12]_{\text{Ag}}\parallel[\bar{1}12]_{\text{Cu}_2\text{O}}$ ; (v) the presence of two zone axes aligned with those of the Ag core (diffraction spots from the  $\text{Cu}_2\text{O}$  in positions contiguous to those of Ag nanowire pattern) suggests that the crystal orientation for  $\text{Cu}_2\text{O}$  is the same everywhere for a specific Ag nanowire subcrystal, therefore confirming the quasi-monocrystallinity of the shell; (vi) it is interesting to note that the  $(110)$  diffraction is forbidden for a Ag nanowire by the FCC structure factor rule (see Figure 4c); however, in the core-shell nanowire a  $(110)$  spot is present because of diffraction in  $\text{Cu}_2\text{O}$ , which belongs to the  $Pn\bar{3}m$  group. Note that the high intensity of spot  $(\bar{2}\bar{2}0)$  is due to the overlap of diffraction along this direction for both core and shell. Also note that diffraction along  $[110]$  for  $\text{Cu}_2\text{O}$  occurs along both zone axes and therefore is more intense.

Figure 4d demonstrates that the matching between Ag and  $\text{Cu}_2\text{O}$  lattices occurs for every twinned subcrystal along the whole interface, and it is consistent with HRTEM measurements. The SAED pattern of Figure 4d included signal from the entire core-shell nanowire shown in Figure 4a and is therefore representative of the crystallinity of the  $\text{Cu}_2\text{O}$  shell on a large scale. On the individual nanowire analyzed in Figure 4, there are no signs of either Cu or  $\text{CuO}$  phases present in the shell material.

The growth process of the  $\text{Cu}_2\text{O}$  shell occurs in three steps:<sup>23,25</sup> (1) epitaxial nucleation of  $\text{Cu}_2\text{O}$  nanoparticles on the metal substrate, (2)  $\text{Cu}_2\text{O}$  nanoparticle growth until the reagents are consumed, and (3) crystal reconstruction to release stress created during the growth. The shell consists of multiple grains that are aligned in rows along each of the five Ag $\{100\}$  facets, as borne out by SAED measurements on the entire core-shell nanowire. These grains might crystallographically be slightly misaligned and not have exactly the same height because of local differences in the growth rate, resulting in surface roughness, which causes the contrast visible in the SEM images (Figure 2b and Figures S3 and S4). However, they all follow the same orientation relationship with the five subcrystals in the pentagonal Ag core, and therefore their mutual crystallographic misalignment is less than what is detectable in SAED. The morphological and structural configuration of the  $\text{Cu}_2\text{O}$  shell is a result of the growth process, whereby  $\text{Cu}_2\text{O}$  nucleates simultaneously at many points along the Ag nanowire. These  $\text{Cu}_2\text{O}$  nuclei grow until their edges touch, leading to rows of almost perfectly aligned  $\text{Cu}_2\text{O}$  grains along each of the pentagonal Ag facets. The five

elongated  $\text{Cu}_2\text{O}$  domains covering the Ag nanowire are therefore nearly single crystalline but may contain planar defects such as low-angle tilt boundaries and low-angle twist boundaries or dislocations. From this point of view, it is more appropriate to call it a *quasi-monocrystal*, using a terminology employed in similar materials for silicon photovoltaics.<sup>40</sup> These low-angle planar defects are indeed not visible in the SAED pattern, showing that the angle misalignment between the grains has to be very low not to be resolved. Although these low-angle planar defects are not visible in the SAED pattern, in bright-field TEM images it is sometimes possible to observe the existence of both low-angle grain boundary regions as well as fully monocrystalline regions (Figure S5).

In order to demonstrate that the growth of pure  $\text{Cu}_2\text{O}$  is achievable in large ensembles, we performed XRD analysis on a thick film of Ag– $\text{Cu}_2\text{O}$  nanowires drop-cast from solution in a  $2\theta$  range of  $20^\circ$ – $90^\circ$  (see Figure 5a). Intense diffraction peaks matching crystalline Ag were observed, along with peaks matching  $\text{Cu}_2\text{O}$ , as labeled in the spectrum of Figure 5a. For comparison, reference values for both Ag (blue) and  $\text{Cu}_2\text{O}$  (red) are reported on the top of the figure. The low intensity of the  $\text{Cu}_2\text{O}$  reflection peak is most likely due to the low  $\text{Cu}_2\text{O}$  ratio in the core–shell nanowire sample employed for the measurements. Importantly, no undesirable phases such as copper(II) oxide ( $\text{CuO}$ ), Cu, mixed metal oxides, or intermetallics were detected even after storage for 6 months in air, revealing the stability of the heterostructure interface and uniformity on a large scale.

While the HR-TEM, SAED, and XRD results confirm epitaxial growth of  $\text{Cu}_2\text{O}$  from the Ag surface, they do not provide information about the atomic binding configurations at the Ag– $\text{Cu}_2\text{O}$  interface. Therefore, plane-wave DFT calculations<sup>41,42</sup> using the generalized gradient approximation (GGA) were performed. A plausible atomic model was constructed in which the FCC metal (sub)lattice of Ag/Cu atoms is continuous across the  $\text{Ag}\{001\}/\text{Cu}_2\text{O}\{001\}$  interface. Two models were considered: one in which the interface contains Ag/Cu mixed atomic layers (Figure 5b) and one model without mixed layers (Figure 5c). The difference in interfacial energy between the two models is very small, indicating that both types of interfaces may be formed. More details are given in the Supporting Information. Free energy calculations and Auger spectroscopy results reported on another noble metal– $\text{Cu}_2\text{O}$  interface, namely Au– $\text{Cu}_2\text{O}$ ,<sup>43</sup> are consistent with the DFT result of Figure 5b, which shows that there is no Ag–O bonding at the interface.

We have shown that under the appropriate experimental conditions silver nanowires can be used as a nucleation site for the epitaxial growth of quasi-monocrystalline, pure phase cuprous oxide shells at room temperature in a water environment. SAED, HRTEM, and XRD analyses prove that the shell consists of pure  $\text{Cu}_2\text{O}$ , which is unusual in bulk  $\text{Cu}_2\text{O}$  samples, whose oxidation to  $\text{CuO}$  has been reported to occur in ambient conditions.<sup>44</sup> By tuning the synthetic parameters, various core diameters and shell thicknesses can be obtained, leading to fine control over optical resonances and ultimately light absorption. We showed that the optical response of Ag– $\text{Cu}_2\text{O}$  is in good agreement with theory/simulations, and most of the power absorption takes place in the semiconductor shell due to the nature of the resonances. FDTD simulations show a 3-fold increase of the maximum absorbed power density within the semiconductor shell, compared to a thin  $\text{Cu}_2\text{O}$  membrane with the same dimensions supported on a Ag film.

Other oxides with similar band gaps and lattice constants, such as  $\text{CoO}$ , can potentially be interesting within this application as well. Metal sulfides such as  $\text{Cu}_2\text{S}$  or  $\text{CdS}$  could also be intriguing absorbing layers, but they require a core material that does not react with sulfur (such as Au). Indeed, heterostructures with a Au core and a  $\text{CdS}$  shell have been synthesized by a nonepitaxial method using an amorphous intermediate,<sup>21</sup> and this approach might be extendable to nanowire core–shell systems with large lattice mismatches.

By combining high quality quasi-monocrystalline materials made at room temperature and efficient light absorption in extraordinarily thin absorbing layers, we expect substantial improvements in the performance of solar devices based on Ag– $\text{Cu}_2\text{O}$  core–shell nanowires. On the other hand, the lower material consumption and the employment of a simple and inexpensive fabrication process—the solution-phase synthesis—could have a large impact on reducing the module cost. Finally, the opportunity to achieve high quality quasi-monocrystalline semiconductor grown on a metal contact with an excellent interface is indeed compelling to pursue fundamental studies on semiconductor properties at the nanoscale.

## ■ ASSOCIATED CONTENT

### 📄 Supporting Information

Details on the synthesis of Ag nanowires and the  $\text{Cu}_2\text{O}$  shell growth, experimental details on the structural and optical characterization, details on the density functional theory (DFT) calculations, and additional SEM and TEM images. This material is available free of charge via the Internet at <http://pubs.acs.org>.

## ■ AUTHOR INFORMATION

### Corresponding Author

\*E-mail [garnett@amolf.nl](mailto:garnett@amolf.nl) (E.C.G.).

### Notes

The authors declare no competing financial interest.

## ■ ACKNOWLEDGMENTS

The authors acknowledge AMOLF technical support, Henk-Jan Boluijt for the realization of the schematic drawing in Figure 1a, and Dr. Toon Coenen, Dr. Sarah Brittan, and Sebastian Oener for helpful discussions. We thank Hans Meeldijk (Utrecht Univ.) for TEM assistance. Furthermore, we acknowledge support from the Light Management in New Photovoltaic Materials (LMPV) center at AMOLF. This work is part of the research program of the Foundation for Fundamental Research on Matter (FOM), which is part of The Netherlands Organization for Scientific Research (NWO). The research leading to these results has received funding from the European Research Council under the European Union's Seventh Framework Programme (FP/2007-2013)/ERC Grant Agreement no. 337328, "NanoEnabledPV".

## ■ REFERENCES

- (1) Lewis, N. S.; Nocera, D. G. Powering the planet: Chemical challenges in solar energy utilization. *Proc. Natl. Acad. Sci. U. S. A.* **2007**, *104* (50), 20142–20142.
- (2) Green, M. A. Limits on the open-circuit voltage and efficiency of silicon solar cells imposed by intrinsic Auger processes. *IEEE Trans.* **1984**, *31* (5), 671–678.

- (3) Cotal, H.; Fetzer, C.; Boisvert, J.; Kinsey, G.; King, R.; Hebert, P.; Yoon, H.; Karam, N. III-V multijunction solar cells for concentrating photovoltaics. *Energy Environ. Sci.* **2009**, *2* (2), 174–192.
- (4) Würfel, P. *Physics of Solar Cells*; Wiley-VCH: Weinheim, 2009.
- (5) King, R. R.; Law, D. C.; Edmondson, K. M.; Fetzer, C. M.; Kinsey, G. S.; Yoon, H.; Sherif, R. A.; Karam, N. H. 40% efficient metamorphic GaInP/GaInAs/Ge multijunction solar cells. *Appl. Phys. Lett.* **2007**, *90*, (18).
- (6) Brongersma, M. L.; Cui, Y.; Fan, S. H. Light management for photovoltaics using high-index nanostructures. *Nat. Mater.* **2014**, *13* (5), 451–460.
- (7) Cao, L. Y.; White, J. S.; Park, J. S.; Schuller, J. A.; Clemens, B. M.; Brongersma, M. L. Engineering light absorption in semiconductor nanowire devices. *Nat. Mater.* **2009**, *8* (8), 643–647.
- (8) Tang, J. Y.; Huo, Z. Y.; Brittan, S.; Gao, H. W.; Yang, P. D. Solution-processed core-shell nanowires for efficient photovoltaic cells. *Nat. Nanotechnol.* **2011**, *6* (9), 568–572.
- (9) Wu, Y.; Xiang, J.; Yang, C.; Lu, W.; Lieber, C. M. Single-crystal metallic nanowires and metal/semiconductor nanowire heterostructures. *Nature* **2004**, *430* (7000), 704–704.
- (10) Lauthon, L. J.; Gudiksen, M. S.; Wang, C. L.; Lieber, C. M. Epitaxial core-shell and core-multishell nanowire heterostructures. *Nature* **2002**, *420* (6911), 57–61.
- (11) Garnett, E.; Yang, P. D. Light trapping in silicon nanowire solar cells. *Nano Lett.* **2010**, *10* (3), 1082–1087.
- (12) Wallentin, J.; Anttu, N.; Asoli, D.; Huffman, M.; Aberg, I.; Magnusson, M. H.; Siefert, G.; Fuss-Kailuweit, P.; Dimroth, F.; Witzigmann, B.; Xu, H. Q.; Samuelson, L.; Deppert, K.; Borgstrom, M. T. InP nanowire array solar cells achieving 13.8% efficiency by exceeding the ray optics limit. *Science* **2013**, *339* (6123), 1057–1060.
- (13) Pala, R. A.; Liu, J. S. Q.; Barnard, E. S.; Askarov, D.; Garnett, E. C.; Fan, S. H.; Brongersma, M. L. Optimization of non-periodic plasmonic light-trapping layers for thin-film solar cells. *Nat. Commun.* **2013**, *4*.
- (14) Tian, B.; Kempa, T. J.; Lieber, C. M. Single nanowire photovoltaics. *Chem. Soc. Rev.* **2009**, *38* (1), 16–24.
- (15) Krogstrup, P.; Jorgensen, H. I.; Heiss, M.; Demichel, O.; Holm, J. V.; Aagesen, M.; Nygard, J.; Morral, A. F. I. Single-nanowire solar cells beyond the Shockley-Queisser limit. *Nat. Photonics* **2013**, *7* (4), 306–310.
- (16) Garnett, E. C.; Brongersma, M. L.; Cui, Y.; McGehee, M. D. Nanowire solar cells. *Annu. Rev. Mater. Res.* **2011**, *41*, 269–295.
- (17) Mann, S. A.; Garnett, E. C. Extreme light absorption in thin semiconductor films wrapped around metal nanowires. *Nano Lett.* **2013**, *13* (7), 3173–3178.
- (18) Garnett, E. C.; Cai, W. S.; Cha, J. J.; Mahmood, F.; Connor, S. T.; Christoforo, M. G.; Cui, Y.; McGehee, M. D.; Brongersma, M. L. Self-limited plasmonic welding of silver nanowire junctions. *Nat. Mater.* **2012**, *11* (3), 241–249.
- (19) Wu, H.; Kong, D. S.; Ruan, Z. C.; Hsu, P. C.; Wang, S.; Yu, Z. F.; Carney, T. J.; Hu, L. B.; Fan, S. H.; Cui, Y. A transparent electrode based on a metal nanotrough network. *Nat. Nanotechnol.* **2013**, *8* (6), 421–425.
- (20) Fan, Z. Y.; Razavi, H.; Do, J. W.; Moriwaki, A.; Ergen, O.; Chueh, Y. L.; Leu, P. W.; Ho, J. C.; Takahashi, T.; Reichertz, L. A.; Neale, S.; Yu, K.; Wu, M.; Ager, J. W.; Javey, A. Three-dimensional nanopillar-array photovoltaics on low-cost and flexible substrates. *Nat. Mater.* **2009**, *8* (8), 648–653.
- (21) Lambright, S.; Butaeva, E.; Razgoniaeva, N.; Hopkins, T.; Smith, B.; Perera, D.; Corbin, J.; Khon, E.; Thomas, R.; Moroz, P.; Mereshchenko, A.; Tarnovsky, A.; Zamkov, M. Enhanced lifetime of excitons in nonepitaxial Au/CdS core/shell nanocrystals. *ACS Nano* **2014**, *8* (1), 352–361.
- (22) Ha, E.; Lee, L. Y.; Wang, J.; Li, F.; Wong, K. Y.; Tsang, S. C. Significant enhancement in photocatalytic reduction of water to hydrogen by Au/Cu<sub>2</sub>ZnSnS<sub>4</sub> nanostructure. *Adv. Mater.* **2014**, *26* (21), 3496–500.
- (23) Kuo, C. H.; Hua, T. E.; Huang, M. H. Au nanocrystal-directed growth of Au-Cu<sub>2</sub>O core-shell heterostructures with precise morphological control. *J. Am. Chem. Soc.* **2009**, *131* (49), 17871–17878.
- (24) Jiang, R.; Li, B.; Fang, C.; Wang, J. Metal/semiconductor hybrid nanostructures for plasmon-enhanced applications. *Adv. Mater.* **2014**, DOI: 10.1002/adma.201400203.
- (25) Meir, N.; Plante, I. J. L.; Flomin, K.; Chockler, E.; Moshofsky, B.; Diab, M.; Volokh, M.; Mokari, T. Studying the chemical, optical and catalytic properties of noble metal (Pt, Pd, Ag, Au)-Cu<sub>2</sub>O core-shell nanostructures grown via a general approach. *J. Mater. Chem. A* **2013**, *1* (5), 1763–1769.
- (26) Li, J. T.; Cushing, S. K.; Bright, J.; Meng, F. K.; Senty, T. R.; Zheng, P.; Bristow, A. D.; Wu, N. Q. Ag@Cu<sub>2</sub>O core-shell nanoparticles as visible-light plasmonic photocatalysts. *ACS Catal.* **2013**, *3* (1), 47–51.
- (27) Cushing, S. K.; Li, J. T.; Meng, F. K.; Senty, T. R.; Suri, S.; Zhi, M. J.; Li, M.; Bristow, A. D.; Wu, N. Q. Photocatalytic activity enhanced by plasmonic resonant energy transfer from metal to semiconductor. *J. Am. Chem. Soc.* **2012**, *134* (36), 15033–15041.
- (28) Sun, H.; He, J. T.; Wang, J. Y.; Zhang, S. Y.; Liu, C. C.; Sritharan, T.; Mhaisalkar, S.; Han, M. Y.; Wang, D.; Chen, H. Y. Investigating the multiple roles of polyvinylpyrrolidone for a general methodology of oxide encapsulation. *J. Am. Chem. Soc.* **2013**, *135* (24), 9099–9110.
- (29) Zhang, J. T.; Tang, Y.; Weng, L.; Ouyang, M. Versatile strategy for precisely tailored core@shell nanostructures with single shell layer accuracy: The case of metallic shell. *Nano Lett.* **2009**, *9* (12), 4061–4065.
- (30) Jin, M. S.; Zhang, H.; Wang, J. G.; Zhong, X. L.; Lu, N.; Li, Z. Y.; Xie, Z. X.; Kim, M. J.; Xia, Y. N. Copper can still be epitaxially deposited on palladium nanocrystals to generate core-shell nanocubes despite their large lattice mismatch. *ACS Nano* **2012**, *6* (3), 2566–2573.
- (31) Zhang, L.; Jing, H.; Boisvert, G.; He, J. Z.; Wang, H. Geometry control and optical tunability of metal-cuprous oxide core-shell nanoparticles. *ACS Nano* **2012**, *6* (4), 3514–3527.
- (32) Beiley, Z. M.; McGehee, M. D. Modeling low cost hybrid tandem photovoltaics with the potential for efficiencies exceeding 20%. *Energy Environ. Sci.* **2012**, *5* (11), 9173–9179.
- (33) Sun, Y. G.; Mayers, B.; Herricks, T.; Xia, Y. N. Polyol synthesis of uniform silver nanowires: A plausible growth mechanism and the supporting evidence. *Nano Lett.* **2003**, *3* (7), 955–960.
- (34) Jang, J. I. A unique system hosting various excitonic matter and exhibiting large third-order nonlinear optical responses. *Optoelectronics - Materials and Techniques*, 2011; DOI 10.5772/18416.
- (35) Li, J. Q.; Mei, Z. X.; Ye, D. Q.; Liang, H. L.; Liu, L. S.; Liu, Y. P.; Galeckas, A.; Kuznetsov, A. Y.; Du, X. L. Engineering of optically defect free Cu<sub>2</sub>O enabling exciton luminescence at room temperature. *Opt. Mater. Express* **2013**, *3* (12), 2072–2077.
- (36) Biccari, F. *Defects and Doping in Cu<sub>2</sub>O*; University of Rome: Rome, 2012.
- (37) Gu, Q.; Wang, B. Correlation between structural defects and optical properties of Cu<sub>2</sub>O nanowires grown by thermal oxidation. arXiv:1012.5338, 2011.
- (38) Srnova-Sloufova, I.; Lednický, F.; Gemperle, A.; Gemperlova, J. Core-shell (Ag)Au bimetallic nanoparticles: Analysis of transmission electron microscopy images. *Langmuir* **2000**, *16* (25), 9928–9935.
- (39) Oba, F.; Ernst, F.; Yu, Y. S.; Liu, R.; Kothari, M.; Switzer, J. A. Epitaxial growth of cuprous oxide electrodeposited onto semiconductor and metal substrates. *J. Am. Ceram. Soc.* **2005**, *88* (2), 253–270.
- (40) Ervik, T.; Stokkan, G.; Buonassisi, T.; Mjos, O.; Lohne, O. Dislocation formation in seeds for quasi-monocrystalline silicon for solar cells. *Acta Mater.* **2014**, *67*, 199–206.
- (41) Kresse, G.; Hafner, J. Ab initio molecular-dynamics for liquid-metals. *Phys. Rev. B* **1993**, *47* (1), 558–561.
- (42) Kresse, G.; Furthmüller, J. Efficiency of ab-initio total energy calculations for metals and semiconductors using a plane-wave basis set. *Comput. Mater. Sci.* **1996**, *6* (1), 15–50.

(43) Olsen, L. C.; Addis, F. W.; Miller, W. Experimental and theoretical studies of  $\text{Cu}_2\text{O}$  solar cells. *Sol. Cells* **1982–1983**, *7*, 247–279.

(44) Ram, S.; Mitra, C. Formation of stable  $\text{Cu}_2\text{O}$  nanocrystals in a new orthorhombic crystal structure. *Mater. Sci. Eng., A* **2001**, *304*, 805–809.

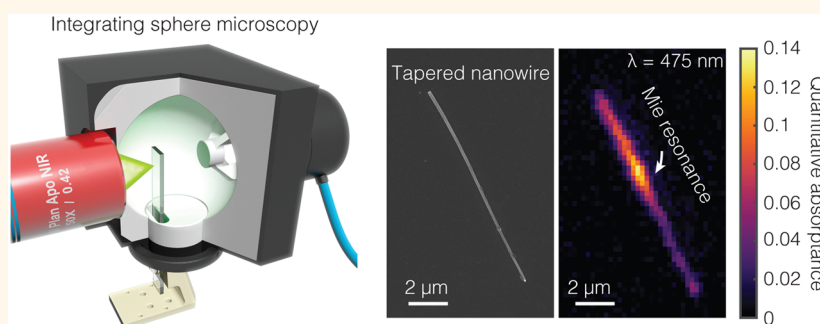
# Integrating Sphere Microscopy for Direct Absorption Measurements of Single Nanostructures

Sander A. Mann,<sup>†</sup> Beniamino Sciacca,<sup>†</sup> Yunyan Zhang,<sup>‡</sup> Jia Wang,<sup>†</sup> Evgenia Kontoleta,<sup>†</sup> Huiyun Liu,<sup>‡</sup> and Erik C. Garnett<sup>\*,†</sup>

<sup>†</sup>Center for Nanophotonics, AMOLF, Science Park 104, 1098 XG Amsterdam, The Netherlands

<sup>‡</sup>Department of Electronic and Electrical Engineering, University College London, London WC1E 7JE, United Kingdom

## Supporting Information



**ABSTRACT:** Nanoscale materials are promising for optoelectronic devices because their physical dimensions are on the order of the wavelength of light. This leads to a variety of complex optical phenomena that, for instance, enhance absorption and emission. However, quantifying the performance of these nanoscale devices frequently requires measuring absolute absorption at the nanoscale, and remarkably, there is no general method capable of doing so directly. Here, we present such a method based on an integrating sphere but modified to achieve submicron spatial resolution. We explore the limits of this technique by using it to measure spatial and spectral absorbance profiles on a wide variety of nanoscale systems, including different combinations of weakly and strongly absorbing and scattering nanomaterials (Si and GaAs nanowires, Au nanoparticles). This measurement technique provides quantitative information about local optical properties that are crucial for improving any optoelectronic device with nanoscale dimensions or nanoscale surface texturing.

**KEYWORDS:** absorption spectroscopy, nanowires, quantitative spectroscopy, Mie resonances, nanoparticles, plasmon resonance

A number of techniques to measure quantitative absorbance on single nanostructures exist,<sup>1–3</sup> such as photothermal spectroscopy,<sup>4–7</sup> extinction (modulation) spectroscopy,<sup>8–10</sup> and scattered field interferometry.<sup>11</sup> Although some of these techniques are extremely sensitive and can even measure single molecules,<sup>5,12</sup> they also rely on at least one of the following assumptions: (i) all absorbed power turns into heat; (ii) the nanoparticle does not scatter light; or (iii) it interacts with light as a dipole. Hence, to date, there is no generally applicable method available for quantitative absorption measurements of nanostructures, even though, for instance, nanostructured semiconductor and plasmonic hot-electron optoelectronic devices<sup>13,14</sup> require such a technique to quantify their performance.

Here, we show that by combining an integrating sphere with a microscope objective with an ultralong working distance, we can achieve submicron spatial resolution inside the integrating

sphere. As a result, quantitative local absorbance measurements can be obtained, even on single nanostructures. We have recently used this method to measure strongly absorbing nanowires either to verify core–shell nanowire antenna properties or for internal quantum efficiency measurements.<sup>15,16</sup> Now, we detail the working mechanism and explore the limits of the technique using weakly absorbing but strongly scattering structures (silicon nanowire and a large gold nanoparticle), a weakly absorbing and weakly scattering structure (small gold nanoparticle), and a strongly absorbing and strongly scattering structure (GaAs nanowire). Additionally, we demonstrate the spatial resolution with absorption

**Received:** September 28, 2016

**Accepted:** January 5, 2017

**Published:** January 5, 2017

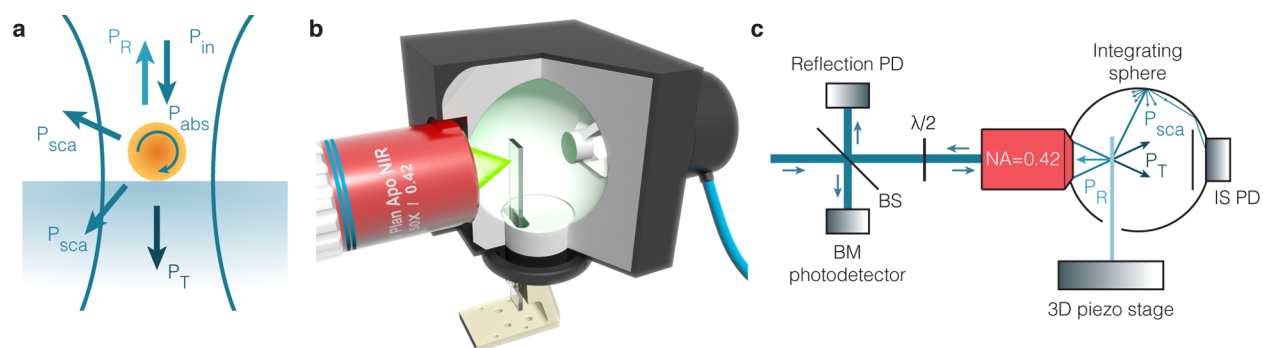


**Figure 1.** Schematic of the integrating sphere setup. (a) When illuminating a nanoparticle with a focused beam, the nanoparticle takes power from the incident beam and absorbs ( $P_{\text{abs}}$ ) or scatters ( $P_{\text{sca}}$ ) it. Most of the power is just reflected ( $P_{\text{R}}$ ) or transmitted ( $P_{\text{T}}$ ). In an integrating sphere, the scattered ( $P_{\text{sca}}$ ) and transmitted light ( $P_{\text{T}}$ ) are both detected, so that by combining that signal with the reflected signal ( $P_{\text{R}}$ ) the absorbance can be determined. (b) Schematic depiction of the combination of microscope objective and integrating sphere. The objective focuses light on the sample holder inside the integrating sphere, and the photodetector is behind a baffle on the backside of the integrating sphere. The sample extends outside of the integrating sphere through a small port, where the sample is mounted on a piezoelectric stage for sample movement. (c) Schematic diagram for the experimental setup, including reflection photodetector (PD) and half-wave plate ( $\lambda/2$ ) to control the polarization. BS stands for beam splitter and BM for beam monitor, which we use to account for fluctuations in laser power. NA stands for the numerical aperture of the objective.

maps on a highly tapered nanowire, where resonances can be seen moving along the length as a function of wavelength.

Single nanoparticle spectroscopy relies on illumination with a focused beam to enhance the interaction with the nanoparticle. When illuminating a nanoparticle, part of the power will be absorbed or scattered by the nanoparticle ( $P_{\text{abs}}$  and  $P_{\text{sca}}$ ; see Figure 1a). Additionally, even for a focused beam, the majority of the incident power will typically not interact with the nanoparticle and be either transmitted or reflected ( $P_{\text{T}}$  and  $P_{\text{R}}$ ). Just as with the standard integrating sphere method,<sup>17,18</sup> integrating sphere microscopy relies on determining the scattered and transmitted light. Due to the diffuse and highly reflective surface of an integrating sphere, this transmitted and scattered light quickly randomizes and covers the inside of the integrating sphere with equal intensity. This homogenized intensity also reaches a photodetector attached to the integrating sphere, which thus detects a power proportional to the total transmitted and scattered power that is independent of the exact scattering pattern. Through a reference measurement (which has no absorbing structure), the absolute transmitted and scattered power can then be determined (see Supporting Information for more details on the setup). Note that no distinction can be made between transmitted and scattered power inside the integrating sphere, and it is therefore not possible to determine the extinction cross section simultaneously.

To combine integrating sphere measurements with sub-micron spatial resolution, we combined an integrating sphere with a microscope objective.<sup>15,16,19</sup> This microscope objective focuses the light on the sample inside the integrating sphere (see Figure 1b). The sample is mounted on a 3D piezoelectric stage, which allows scanning of the sample to obtain quantitative local information on the absorbance. The ability to scan the sample or focused spot position is crucial: without scanning, integrating sphere microscopy can only be used in a wide field configuration, which does not allow for quantitative spatial information.<sup>19</sup>

A detector behind a baffle on the backside of the integrating sphere measures most of the transmitted and scattered power; some light will be reflected or backscattered into the microscope objective. This fraction is imaged on a second

photodetector by the microscope objective and is therefore also collected (see Figure 1c). Hence, by measuring the scattered, reflected, and transmitted light, the absorbed light can be inferred:  $P_{\text{abs}} = 1 - P_{\text{R}} - P_{\text{T}} - P_{\text{sca}}$ . More specifically, for the absorbance, we then obtain

$$A = 1 - \frac{R}{R_{\text{ref}}} - \frac{IS}{IS_{\text{ref}}} - C \quad (1)$$

where  $R$  and  $R_{\text{ref}}$  are the reflection signal and reference measurement and  $IS$  and  $IS_{\text{ref}}$  are the integrating sphere signal and reference measurement. Calibration of the technique is thus extremely simple: it only requires two reference measurements, usually a mirror for  $R_{\text{ref}}$  and a small hole in the substrate for  $IS_{\text{ref}}$  (meaning that the beam misses the sample, but the sample is still in the integrating sphere). The experimental setup is discussed in more detail in the Supporting Information. Note that some samples can be strongly backscattering, and it is therefore important to record the reflected power (see Supporting Information for examples).

In eq 1,  $C$  is an offset that arises from the reflection of the substrate–air interface on the back of the substrate, which the objective collects, but is so far beyond the focal plane that it is not imaged on the photodetector. For glass substrates, it is  $\sim 0.03$  (see Supporting Information), but it depends slightly on how much power is transmitted and scattered forward, and a small error is therefore introduced by assuming that it is constant. The accuracy of the technique additionally depends on the detection efficiency of all nonabsorbed light; for example, if some light is scattered but not detected by either photodetector, it will appear as absorption. Based on measurements on nonabsorbing but strongly scattering silica beads, we estimate that  $95 \pm 1.2\%$  of the total scattered power is collected.<sup>16</sup> Finally, broadband characterization is possible since we use a supercontinuum laser as a light source (400–2000 nm), and the integrating sphere inner surface remains Lambertian from 250 to 2500 nm.

## RESULTS AND DISCUSSION

We will now demonstrate this technique by showing local variation in the absorbance of a tapered silicon nanowire. Semiconductor nanowires are important building blocks for

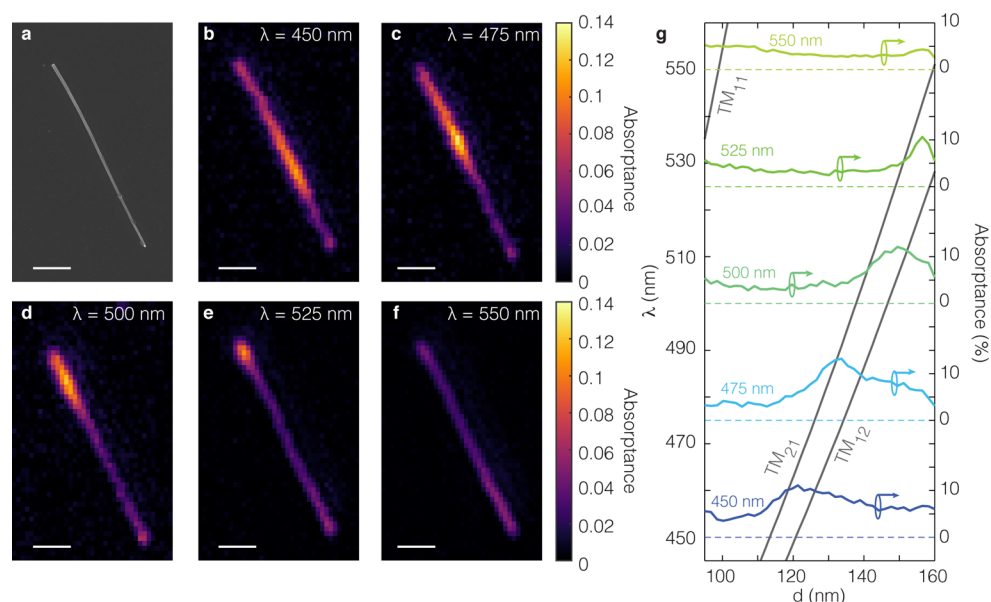


**Figure 2.** Absorbance maps of a silicon nanowire. (a) SEM image of the silicon nanowire under consideration. Its diameter ranges from 95 (bottom) to 160 nm (top). The scale bar is 2  $\mu$ m. (b–f) Absorbance maps over the same spatial range for different wavelengths. For all maps, the laser polarization is aligned with the long axis of the nanowire. The absorption peak shows how the  $TM_{12}$  and  $TM_{21}$  resonances shift position along the wire as the wavelength increases, and the  $TM_{11}$  is seen to appear on the bottom side of the wire. (g) Wavelength dispersion of the resonances of a circular silicon nanowire in vacuum as a function of diameter, with the absorbance spectra at different wavelengths superimposed. The peaks in absorption along the length of the wire clearly correspond to the presence of resonances.

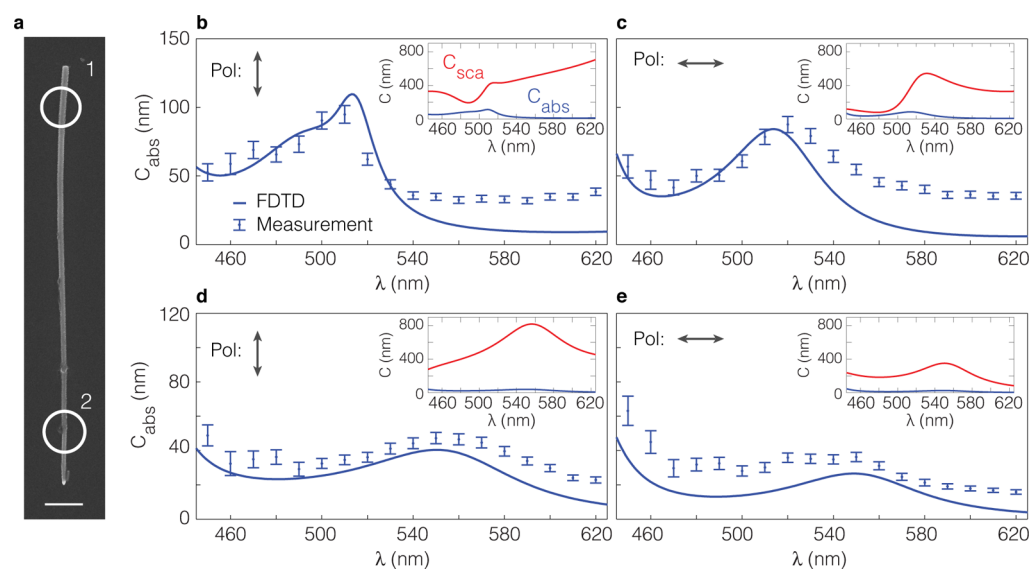


**Figure 3.** Absorption spectra of a silicon nanowire. (a) SEM image of the silicon nanowire indicating the positions at which spectra were measured. The scale bar is 1  $\mu$ m. (b) Measured absorption cross section of the silicon nanowire at position 1 with the electric field polarized along the nanowire axis, compared to simulations of a nanowire on glass with a diameter of 156 nm (blue line; see Methods). The inset shows the simulated absorption cross section (blue) compared to the scattering cross section (red), indicating that the wire scatters much more strongly than it absorbs. (c) Same as in panel (b) but with the electric field polarized perpendicular to the axis. (d,e) Same as panels (b) and (c) but measured at position 2 and with 112 nm diameter nanowire simulation. In (b–e), the error bars are due to variance in the absorbance and uncertainty in the conversion to cross section.

optoelectronics applications,<sup>20</sup> including nanowire solar cells,<sup>21,22</sup> light-emitting diodes,<sup>23–25</sup> lasers,<sup>26</sup> and quantum information technology.<sup>27</sup> Silicon nanowires, in particular, provide a challenging test case for nanoscale absorption measurements because the indirect band gap leads to scattering that can be 2 orders of magnitude stronger than the absorption. Figure 2a shows an scanning electron microscopy (SEM) image of a 10  $\mu$ m long silicon nanowire on a glass substrate. The

nanowire is slightly tapered, with a diameter that varies from 160 nm at the top of the image to 95 nm at the bottom. Figure 2b displays the absorbance  $A$  (absorbed fraction of the incident power,  $P_{abs}/P_{in}$ ) at a wavelength of 450 nm, measured while scanning over the area shown in the SEM image using the 3D piezoelectric stage. In the center of the wire, a peak in absorbance is visible, which corresponds to resonantly enhanced absorption *via* a Mie (geometrical) resonance. Mie

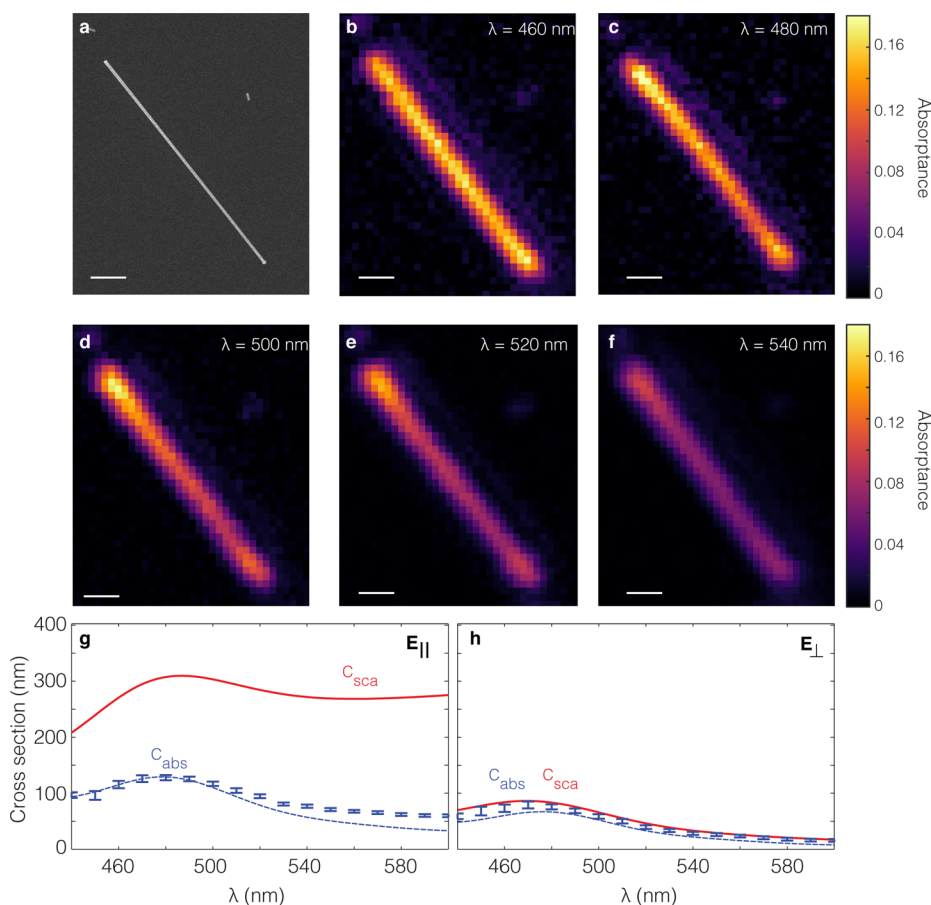


**Figure 4.** Absorption measurements of a GaAs nanowire. (a) SEM image of the GaAs nanowire. The scale bar is 1  $\mu\text{m}$ . (b–f) Absorption maps from 460 to 540 nm. Due to the smaller diameter of the nanowire and the lower tapering angle, the resonances appear to be less confined along the length of the nanowire. (g,h) Absorption spectra with the electric field parallel (g) and perpendicular (h) to the nanowire axis. The solid red and dashed blue lines show full-wave simulations of the scattering and absorption cross sections for a GaAs nanowire with the same diameter (110 nm).

resonances shift to longer wavelengths as the radius of the wire is increased, as they occur for approximately fixed values of the product  $nk_0r$ , where  $n$ ,  $k_0$ , and  $r$  are the refractive index, free space wavenumber, and radius, respectively.<sup>28,29</sup> The absorption maps in Figure 2c–f show the peak moving from smaller to larger diameter along the tapered nanowire as the illumination wavelength increases, providing a direct visualization of these diameter-dependent resonance phenomena.

Figure 2g plots absorption intensity line cuts along the tapered nanowire in Figure 2c–f, together with calculated dispersion relations to identify the relevant Mie resonances.<sup>30</sup> These resonances can be specified with the notation  $\text{TM}_{ml}$ , where TM indicates the magnetic field is transverse to the long axis of the nanowire;  $m$  is the azimuthal mode number, corresponding to the number of field maxima around the nanowire circumference; and  $l$  indicates the number of radial field maxima. From these calculations shown in Figure 2g, it is clear that we observe the  $\text{TM}_{21}$  and  $\text{TM}_{12}$  resonances. These resonances are nearly degenerate and hard to disentangle spatially.

In addition to measuring nanoscale absorption maps at a fixed wavelength, we can also fix the laser position and measure local absorption spectra. Figure 3a shows an SEM image of the same nanowire (but rotated) and indicates two positions where spectra were measured. Figure 3b–e shows the wavelength-dependent absorption cross sections of the nanowire at the two

different positions, with the laser polarized either along or orthogonal to the nanowire axis. A geometric scaling factor is used to convert from absorbance to cross section:

$$C_{\text{abs}} = A\sqrt{\pi w_0^2/2},$$

where  $A$  is absorbance and  $w_0$  is the beam radius. This factor can be derived by assuming that the nanowire is infinitely thin and then integrating the incident intensity along the nanowire.<sup>16</sup> While the nanowire in reality is not infinitely thin, agreement with full-wave simulations is good (see Figure 3b–e). However, because the scattered power significantly exceeds the absorption by up to a factor of 75, the disagreement between the measurement and full-wave simulations is more likely due to the small fraction of scattered light that is not detected.

Due to the indirect band gap of silicon, these nanowires scatter very strongly, therefore providing a particularly challenging test case. Agreement with theory is better for more strongly absorbing materials such as GaAs, as we show in Figure 4. Figure 4a shows an SEM image of a GaAs nanowire with a radius ranging from 110 nm at the top of the image to 84 nm at the bottom. Figure 4b–f shows absorption maps for different wavelengths, just as for the silicon nanowire. However, since this nanowire has a lower tapering angle, the resonances do not appear localized along the nanowire length. Additionally, the nanowire has a smaller diameter, which means that a lower-order resonance is excited (the  $\text{TM}_{11}$  resonance), which

has a broader linewidth and, interestingly, therefore also a larger spatial extent in a tapered nanowire than a resonance with a narrower linewidth would have. Figure 4g,h shows the cross section *versus* wavelength, compared to full-wave simulations of the nanowire absorption and scattering cross section for parallel and perpendicular incident polarizations, measured at the top of the wire. Both spectra show a resonance at 480 nm, which are the  $TM_{11}$  and  $TE_{01}$  resonances in the parallel and perpendicular polarization, respectively. Since GaAs has a direct band gap, the scattering cross section is reduced and the absorption cross section is increased, indeed improving the agreement with numerical predictions.

Due to the linear extent of the nanowire, the intersection with the focused spot is significant and measurements above the noise floor are therefore easily achieved. To probe the detection limits of our setup, we also investigate small spherical gold nanoparticles with a plasmon resonance near 500 nm. While the absorptance of the nanowires reaches >10% easily, the absorptance of a 60 nm diameter gold sphere will lie below 1% due to the small absorption cross section. Since the nanoparticle is localized in three dimensions, we now obtain for the absorptance (assuming that the nanoparticle can be treated as a point)  $A = \sigma_{\text{abs}} I(x,y)$ , where  $I(x,y)$  is the intensity in the Gaussian spot. If the nanoparticle lies exactly in the focus, we obtain  $\sigma_{\text{abs}} = A \times \pi w_0^2 / 2$ , where we used  $I(x=0, y=0) = 2P_{\text{in}} / \pi w_0^2$  and  $A = P_{\text{abs}} / P_{\text{in}}$ . This absorption cross section is shown in Figure 5a for a 60 nm diameter gold sphere and in Figure 5b for a 200 nm diameter gold sphere. Even though the absorptance peaks at 0.5% for the 60 nm diameter nanosphere, the noise floor is low enough for accurate determination of the

absorption cross section. In fact, the error margin shown in Figure 5 arises largely due to the determination of the Gaussian beam radius  $w_0$ .

Even for the gold sphere of 60 nm, the signal-to-noise ratio is  $\sim 30$ , implying that smaller absorption cross sections can be measured. The noise floor depends on the laser characteristics, photodetectors, and detected optical power. While not the case in this experiment, the noise floor could ultimately be determined by photon shot noise. This would enable detection of absorption cross sections only a few square nanometers large, similar to extinction spectroscopy.<sup>12,31</sup>

## CONCLUSIONS

To conclude, we have introduced a technique to perform quantitative and spatially resolved absorption spectroscopy on single scattering nanoparticles. The technique uses an integrating sphere to measure directly the transmitted, reflected, and scattered power, allowing for determination of the absorbed power. Calibration of the absorption measurement is very straightforward, and no assumptions on the nature of the scattering particle are required. We demonstrated integrating sphere microscopy by mapping the absorption cross section of tapered silicon and GaAs nanowires. These are essential characteristics for many optoelectronic devices, in particular, for light-emitting diodes and solar cells, but cannot be measured on the nanoscale with photothermal spectroscopy or any other known method. We therefore believe that this extension of the standard integrating sphere measurement to nanoscale systems can be of great utility in nanoscale optoelectronics, single nanoparticle spectroscopy, and other fields where quantitative and high spatial resolution measurements are desired.

## METHODS

**Experimental Setup.** The light source in the experiment was a supercontinuum laser (Fianium WL-SC-390-3), which was made monochromatic using an acousto-optical tunable filter (AOTF, Crystal Technologies, with roughly 4 nm bandwidth). Power in the focused laser beam is on the order of several microwatts. The long working distance objective is a 17 mm working distance Mitutoyo M Apo Plan NIR 50 $\times$  with NA = 0.42. The integrating sphere is a LabSphere GPS-020-SL, modified so that it can accommodate our objective lens. The photodetectors are Thorlabs amplified Si detectors (PDA100A), read out by Stanford Research Systems SR830 lock-in amplifiers. For the Au nanoparticle measurements the IS photodetector was replaced by a passive Newport 818-UV photodetector, which has a lower noise level than the Thorlabs transimpedance amplifiers. The transmission of the AOTF was digitally modulated at 20 kHz with a 50% duty cycle for the nanowire measurements and at 700 Hz for the Au nanoparticle measurements. The sample holder was mounted on a Piezajena Tritor400 3D piezoelectric stage for high-resolution scanning of the sample, while for rough alignment, the piezoelectric stage was mounted on a Newport mechanical stage.

**Sample Preparation.** The silicon nanowires are grown epitaxially on a silicon substrate by the vapor–liquid–solid growth mechanism using an atmospheric pressure chemical vapor deposition system. The 40 nm gold colloids were used as catalysts. The growth was conducted at 800  $^{\circ}\text{C}$  for 5 min with silicon tetrachloride ( $\text{SiCl}_4$ ) as the precursor. The carrier gas flows during growth were Ar = 200 sccm and  $\text{H}_2$  = 50 sccm, while only 75 sccm Ar gas flows directly through the  $\text{SiCl}_4$  precursor bubbler (held at 0  $^{\circ}\text{C}$  in a temperature-controlled bath). Self-catalyzed GaAs nanowires were grown by solid-source III–V molecular beam epitaxy (MBE) directly on p-type Si(100) substrates by solid-source III–V Veeco MBE GEN-930. The NWs were grown with a Ga beam equivalent pressure, V/III flux ratio, substrate temperature, and growth duration of  $8.7 \times 10^{-8}$  Torr, 50,  $\sim 630$   $^{\circ}\text{C}$ ,

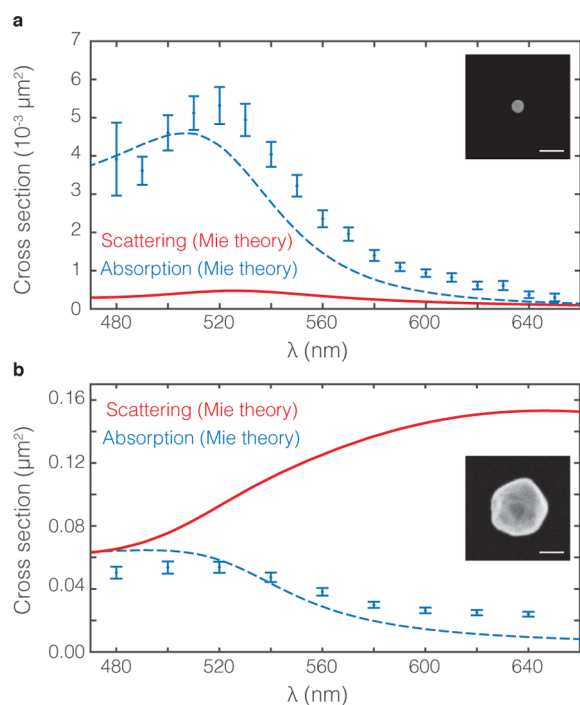


**Figure 5.** Absorption spectra of Au nanoparticles. (a) Absorption spectrum of a 60 nm Au nanoparticle compared to Mie theory predictions for absorption (dashed blue line) and scattering (red line). (b) Absorption spectrum of a 200 nm Au nanoparticle compared to Mie theory calculations for absorption and scattering (dashed blue and red lines, respectively). The insets in both figures show representative gold particles along with a 100 nm scale bar.

and 1 h, respectively. The substrate temperature was measured by a pyrometer. The gold nanoparticles (60 and 200 nm diameter) were acquired from BBI solutions.

**Simulations.** The nanowire cross section simulations were performed with Lumerical FDTD. The nanowire had a hexagonal shape and was assumed to be infinitely long (simulations were 2D). The refractive index of silicon and GaAs was based on tabulated data from Palik.<sup>32</sup> In both the calculations of the dispersion diagrams and simulations, the parallel momentum was assumed to be zero, treating the wire as if illuminated under normal incidence. Considering the low effective NA in the experiment, this is an accurate assumption.

## ASSOCIATED CONTENT

### Supporting Information

The Supporting Information is available free of charge on the ACS Publications website at DOI: 10.1021/acsnano.6b06534.

Technical details on the integrating sphere and sample holder, data analysis procedure details, and all reflection and integrating sphere signals corresponding to the figures in the main text (PDF)

## AUTHOR INFORMATION

### Corresponding Author

\*E-mail: garnett@amolf.nl.

### ORCID

Sander A. Mann: 0000-0002-7742-0615

### Notes

The authors declare no competing financial interest.

## ACKNOWLEDGMENTS

The authors are grateful to Ewold Verhagen and Ruben Maas for critical reading of the manuscript, Henk-Jan Boluijt, Mohamed Tachikirt, Marco Seynen, and the mechanical workshop at AMOLF for help with custom parts of the experimental setup. This work is part of the research programme of The Netherlands Organisation for Scientific Research (NWO). The research leading to these results has received funding from the European Research Council under the European Union's Seventh Framework Programme (FP/2007-2013)/ERC Grant Agreement No. 337328, "Nano-EnabledPV". H.L. and Y.Z. acknowledge the support of Leverhulme Trust. H.L. would like to thank The Royal Society for funding his University Research Fellowship.

## REFERENCES

- (1) Crut, A.; Maioli, P.; Del Fatti, N.; Vallée, F. Optical Absorption and Scattering Spectroscopies of Single Nano-Objects. *Chem. Soc. Rev.* **2014**, *43*, 3921.
- (2) Zijlstra, P.; Orrit, M. Single Metal Nanoparticles: Optical Detection, Spectroscopy and Applications. *Rep. Prog. Phys.* **2011**, *74*, 106401.
- (3) Olson, J.; Dominguez-medina, S.; Hoggard, A.; Wang, L.; Chang, W.; Link, S. Optical Characterization of Single Plasmonic Nanoparticles. *Chem. Soc. Rev.* **2015**, *44*, 40–57.
- (4) Yorulmaz, M.; Nizzero, S.; Hoggard, A.; Wang, L.-Y.; Cai, Y.-Y.; Su, M.-N.; Chang, W.-S.; Link, S. Single-Particle Absorption Spectroscopy by Photothermal Contrast. *Nano Lett.* **2015**, *15*, 3041–3047.
- (5) Gaiduk, A.; Yorulmaz, M.; Ruijgrok, P. V.; Orrit, M. Room-Temperature Detection of a Single Molecule's Absorption by Photothermal Contrast. *Science* **2010**, *330*, 353–356.
- (6) Baffou, G.; Bon, P.; Savatier, J.; Polleux, J.; Zhu, M.; Merlin, M.; Rigneault, H.; Monneret, S. Thermal Imaging of Nanostructures by Quantitative Optical Phase Analysis. *ACS Nano* **2012**, *6*, 2452–2458.
- (7) Berto, P.; Ureña, E. B.; Bon, P.; Quidant, R.; Rigneault, H.; Baffou, G. Quantitative Absorption Spectroscopy of Nano-Objects. *Phys. Rev. B: Condens. Matter Mater. Phys.* **2012**, *86*, 165417.
- (8) Arbouet, A.; Christofilos, D.; Del Fatti, N.; Vallée, F.; Huntzinger, J. R.; Arnaud, L.; Billaud, P.; Broeyer, M. Direct Measurement of the Single-Metal-Cluster Optical Absorption. *Phys. Rev. Lett.* **2004**, *93*, 127401.
- (9) Muskens, O. L.; Bachelier, G.; Del Fatti, N.; Vallée, F.; Brioude, A.; Jiang, X.; Pileni, M. P. Quantitative Absorption Spectroscopy of a Single Gold Nanorod. *J. Phys. Chem. C* **2008**, *112*, 8917–8921.
- (10) Blancon, J.-C.; Paillet, M.; Tran, H. N.; Than, X. T.; Guebrou, S. A.; Ayari, A.; San Miguel, A.; Phan, N.-M.; Zahab, A.-A.; Sauvajol, J.-L.; Del Fatti, N.; Vallée, F. Direct Measurement of the Absolute Absorption Spectrum of Individual Semiconducting Single-Wall Carbon Nanotubes. *Nat. Commun.* **2013**, *4*, 2542.
- (11) Husnik, M.; Linden, S.; Diehl, R.; Niegemann, J.; Busch, K.; Wegener, M. Quantitative Experimental Determination of Scattering and Absorption Cross-Section Spectra of Individual Optical Metallic Nanoantennas. *Phys. Rev. Lett.* **2012**, *109*, 233902.
- (12) Celebrano, M.; Kukura, P.; Renn, A.; Sandoghdar, V. Single-Molecule Imaging by Optical Absorption. *Nat. Photonics* **2011**, *5*, 95–98.
- (13) Brongersma, M. L.; Halas, N. J.; Nordlander, P. Plasmon-Induced Hot Carrier Science and Technology. *Nat. Nanotechnol.* **2015**, *10*, 25–34.
- (14) Clavero, C. Plasmon-Induced Hot-Electron Generation at Nanoparticle/metal-Oxide Interfaces for Photovoltaic and Photocatalytic Devices. *Nat. Photonics* **2014**, *8*, 95–103.
- (15) Sciacca, B.; Mann, S. A.; Tichelaar, F. D.; Zandbergen, H. W.; van Huis, M. A.; Garnett, E. C. Solution-Phase Epitaxial Growth of Quasi-Monocrystalline Cuprous Oxide on Metal Nanowires. *Nano Lett.* **2014**, *14*, 5891–5898.
- (16) Mann, S. A.; Oener, S. Z.; Cavalli, A.; Haverkort, J. E. M.; Bakkers, E. P. A. M.; Garnett, E. C. Quantifying Losses and Thermodynamic Limits in Nanophotonic Solar Cells. *Nat. Nanotechnol.* **2016**, *11*, 1071–1075.
- (17) Burkhard, G. F.; Hoke, E. T.; McGehee, M. D. Accounting for Interference, Scattering, and Electrode Absorption to Make Accurate Internal Quantum Efficiency Measurements in Organic and Other Thin Solar Cells. *Adv. Mater.* **2010**, *22*, 3293–3297.
- (18) Leyre, S.; Coutino-Gonzalez, E.; Joos, J. J.; Ryckaert, J.; Meuret, Y.; Poelman, D.; Smet, P. F.; Durinck, G.; Hofkens, J.; Deconinck, G.; Hanselaer, P. Absolute Determination of Photoluminescence Quantum Efficiency Using an Integrating Sphere Setup. *Rev. Sci. Instrum.* **2014**, *85*, 123115.
- (19) Gargas, D. J.; Gao, H.; Wang, H.; Yang, P. High Quantum Efficiency of Band-Edge Emission from ZnO Nanowires. *Nano Lett.* **2011**, *11*, 3792–3796.
- (20) Duan, X.; Huang, Y.; Cui, Y.; Wang, J.; Lieber, C. M. Indium Phosphide Nanowires as Building Blocks for Nanoscale Electronic and Optoelectronic Devices. *Nature* **2001**, *409*, 66–69.
- (21) Krogstrup, P.; Jørgensen, H. I.; Heiss, M.; Demichel, O.; Holm, J. V.; Aagesen, M.; Nygard, J.; Fontcuberta i Morral, A. Single-Nanowire Solar Cells beyond the Shockley-Queisser Limit. *Nat. Photonics* **2013**, *7*, 306–310.
- (22) Wallentin, J.; Anttu, N.; Asoli, D.; Huffman, M.; Aberg, I.; Magnusson, M. H.; Siefert, G.; Fuss-Kailuweit, P.; Dimroth, F.; Witzigmann, B.; Xu, H. Q.; Samuelson, L.; Deppert, K.; Borgstrom, M. T. InP Nanowire Array Solar Cells Achieving 13.8% Efficiency by Exceeding the Ray Optics Limit. *Science* **2013**, *339*, 1057–1060.
- (23) Svensson, C. P. T.; Mårtensson, T.; Trägårdh, J.; Larsson, C.; Rask, M.; Hessman, D.; Samuelson, L.; Ohlsson, J. Monolithic GaAs/InGaP Nanowire Light Emitting Diodes on Silicon. *Nanotechnology* **2008**, *19*, 305201.
- (24) Minot, E. D.; Kelkensberg, F.; van Kouwen, M.; van Dam, J. A.; Kouwenhoven, L. P.; Zwiller, V.; Borgström, M. T.; Wunnicke, O.; Verheijen, M. A.; Bakkers, E. P. A. M. Single Quantum Dot Nanowire LEDs. *Nano Lett.* **2007**, *7*, 367–371.

(25) van Dam, D.; Abujetas, D. R.; Paniagua-Domínguez, R.; Sánchez-Gil, J. A.; Bakkers, E. P. A. M.; Haverkort, J. E. M.; Gómez Rivas, J. Directional and Polarized Emission from Nanowire Arrays. *Nano Lett.* **2015**, *15*, 4557–4563.

(26) Huang, M. H.; Mao, S.; Feick, H.; Yan, H.; Wu, Y.; Kind, H.; Weber, E.; Russo, R.; Yang, P. Room-Temperature Ultraviolet Nanowire Nanolasers. *Science* **2001**, *292*, 1897–1899.

(27) Heiss, M.; Fontana, Y.; Gustafsson, A.; Wüst, G.; Magen, C.; O'Regan, D. D.; Luo, J. W.; Ketterer, B.; Conesa-Boj, S.; Kuhlmann, A. V.; Houel, J.; Russo-Averchi, E.; Morante, J. R.; Cantoni, M.; Marzari, N.; Arbiol, J.; Zunger, A.; Warburton, R. J.; Fontcuberta i Morral, A. Self-Assembled Quantum Dots in a Nanowire System for Quantum Photonics. *Nat. Mater.* **2013**, *12*, 439–444.

(28) Mann, S. A.; Garnett, E. C. Extreme Light Absorption in Thin Semiconductor Films Wrapped around Metal Nanowires. *Nano Lett.* **2013**, *13*, 3173–3178.

(29) Bohren, C. E.; Huffman, D. R. *Absorption and Scattering of Light by Small Particles*; John Wiley & Sons, Inc.: New York, 1983.

(30) Yu, Y.; Cao, L. Coupled Leaky Mode Theory for Light Absorption in 2D, 1D, and 0D Semiconductor Nanostructures. *Opt. Express* **2012**, *20*, 13847.

(31) McDonald, M. P.; Vietmeyer, F.; Aleksiuik, D.; Kuno, M. Supercontinuum Spatial Modulation Spectroscopy: Detection and Noise Limitations. *Rev. Sci. Instrum.* **2013**, *84*, 113104.

(32) Palik, E. D. *Handbook of Optical Constants of Solids*; Elsevier Academic Press: Waltham, MA, 1985.

## Au-Cu<sub>2</sub>O core-shell nanowire photovoltaics

S. Z. Oener, S. A. Mann, B. Sciacca, C. Sfiligoj, J. Hoang, and E. C. Garnett<sup>a)</sup>

*Center for Nanophotonics, FOM Institute AMOLF, Science Park 104, 1098 XG Amsterdam, The Netherlands*

(Received 22 October 2014; accepted 26 December 2014; published online 12 January 2015)

Semiconductor nanowires are among the most promising candidates for next generation photovoltaics. This is due to their outstanding optical and electrical properties which provide large optical cross sections while simultaneously decoupling the photon absorption and charge carrier extraction length scales. These effects relax the requirements for both the minority carrier diffusion length and the amount of semiconductor needed. Metal-semiconductor core-shell nanowires have previously been predicted to show even better optical absorption than solid semiconductor nanowires and offer the additional advantage of a local metal core contact. Here, we fabricate and analyze such a geometry using a single Au-Cu<sub>2</sub>O core-shell nanowire photovoltaic cell as a model system. Spatially resolved photocurrent maps reveal that although the minority carrier diffusion length in the Cu<sub>2</sub>O shell is less than 1 μm, the radial contact geometry with the incorporated metal electrode still allows for photogenerated carrier collection along an entire nanowire. Current-voltage measurements yield an open-circuit voltage of 600 mV under laser illumination and a dark diode turn-on voltage of 1 V. This study suggests the metal-semiconductor core-shell nanowire concept could be extended to low-cost, large-scale photovoltaic devices, utilizing for example, metal nanowire electrode grids coated with epitaxially grown semiconductor shells. © 2015 Author(s). All article content, except where otherwise noted, is licensed under a Creative Commons Attribution 3.0 Unported License. [<http://dx.doi.org/10.1063/1.4905652>]

Photovoltaics provide electricity in a clean, sustainable, and often decentralized way by utilizing an abundant and virtually unlimited source of primary energy: the sun. Wafer-based silicon solar cells are the main driver of increased installations, which reached a global cumulative installed photovoltaic capacity of 137 GW.<sup>1</sup> Other technologies are being pursued that can either lower the overall fabrication costs or increase the conversion efficiency when compared to silicon solar cells.<sup>2</sup> Cu<sub>2</sub>O thin film solar cells, for example, are made from abundant, non-toxic, and small amounts of material and can potentially reach power conversion efficiencies of up to 20%.<sup>3</sup> With appropriate surface passivation, thin film solar cells can even reach higher open-circuit voltage ( $V_{oc}$ ) values than their bulk counter parts due to shorter charge carrier extraction paths and hence reduced bulk recombination.<sup>4</sup> Furthermore, when combined with silicon as the bottom absorber ( $E_g \sim 1.1$  eV), Cu<sub>2</sub>O is an excellent candidate for the top absorber in a high efficiency multijunction solar cell because its band gap ( $E_g \sim 2$  eV) is close to ideal (1.7–2.0 eV).<sup>5–7</sup>

Recently, several groups have focused on the interface properties of Cu<sub>2</sub>O and were able to increase the  $V_{oc}$  up to 1.2 V by using interfacial layers, such as Ga<sub>2</sub>O<sub>3</sub> and ZnO, combined with transparent conductive oxides (TCOs) as top contacts for Cu<sub>2</sub>O thin-film solar cells.<sup>8–18</sup> Light concentration offers another important way to increase the maximum achievable  $V_{oc}$ , and thereby the conversion efficiency.<sup>19</sup> Conventional triple junction solar cells typically use macroscopic external optics to provide this concentration effect and increase the efficiency, but nanostructures can inherently concentrate light via optical resonances.<sup>20–23</sup> These and other

effects are motivating work on next generation high-efficiency photovoltaics, with semiconductor nanowires being among the most promising candidates.<sup>23–26</sup>

Here, we utilize a metal-semiconductor core-shell geometry to fabricate a single horizontally aligned Au-Cu<sub>2</sub>O nanowire photovoltaic cell. Such a structure has several potential advantages. The thin semiconductor shell in direct vicinity of the metal core electrode allows for facile extraction of photogenerated carriers, even in materials with short minority carrier diffusion lengths. The radial core-shell geometry has already proven useful in semiconductor nanowire photovoltaics, and we expect even better charge carrier extraction in our geometry where photocarriers are injected into a metal immediately.<sup>27–30</sup> Another previously demonstrated advantage of semiconductor nanowires is their high absorption cross section, which can exceed the geometrical one.<sup>22,23,31</sup> The metal-semiconductor core-shell structure can lead to even higher absorption, while further reducing the amount of semiconductor.<sup>32</sup> Several research groups have already utilized metal-semiconductor core-shell nanospheres or rods for plasmon mediated charge carrier dynamics for photovoltaics and photocatalysis. In these examples, however, semiconductor materials were not used for the visible light absorption or materials were suspended completely in solution.<sup>33–39</sup> Here, we fabricate and test a single metal-semiconductor core-shell nanowire photovoltaic cell, utilizing Au for the core and Cu<sub>2</sub>O for the shell.

To fabricate the core-shell nanowires, we followed a procedure developed by Sciacca *et al.* for solution-based synthesis of metal (Ag, Au, or Cu) core Cu<sub>2</sub>O shell nanowires.<sup>40</sup> The metal nanowires were synthesized using the polyol process and subsequently coated with a Cu<sub>2</sub>O shell at room temperature in aqueous solution adapting a protocol

<sup>a)</sup>Electronic mail: garnett@amolf.nl



originally developed for core-shell nanoparticles.<sup>41,42</sup> This specific  $\text{Cu}_2\text{O}$  synthesis route was chosen over other methods to produce  $\text{Cu}_2\text{O}$  nanowires, because it allowed for epitaxial growth on metal nanowires suspended in solution.<sup>43,44</sup> Photoluminescence (PL) measurements showed a peak near 1.9 eV, similar to what has been observed in pure-phase, bulk  $\text{Cu}_2\text{O}$ .<sup>40,45</sup>

Figure 1 shows a schematic of a single nanowire photovoltaic cell illuminated by a laser beam. As can be seen in the drawing, the  $\text{Cu}_2\text{O}$  shell has two contacts: one that collects photogenerated holes and one that is selective for photogenerated electrons. One simple and effective method for inducing this carrier selectivity is to use metal contacts with different work functions such that one metal makes an Ohmic contact to the  $\text{Cu}_2\text{O}$  and the other a Schottky junction.<sup>46</sup> Here, we have chosen Au as the metal nanowire core because it has a large work function ( $\sim 5.4$  eV; similar to that of  $\text{Cu}_2\text{O}$ ) and makes an Ohmic contact to  $\text{Cu}_2\text{O}$ . Furthermore, Au has a high chemical stability, low lattice mismatch with  $\text{Cu}_2\text{O}$  ( $\sim 4\%$ ), and a simple nanowire synthesis route.<sup>40,47–50</sup> As the Schottky contact, we have chosen Ti, which has a low work function ( $\sim 4.3$  eV), excellent adhesion to many materials and a stable surface oxide.<sup>51</sup> As reported in previous literature, it is possible that a redox reaction under the Ti contact converts the  $\text{Cu}_2\text{O}$  to  $\text{TiO}_2$  and Cu at the interface. This modified interface still results in charge carrier separation and extraction, but it does lower the maximum achievable  $V_{oc}$  value.<sup>52</sup> We would expect better performance if the contact geometry was reversed, allowing for a Schottky junction along the whole length of the metal core, but such a low work function metal-semiconductor core-shell structure has not been synthesized so far.<sup>40</sup> A more detailed discussion about the influence of the interfaces and the effect of the Schottky junction can be found in the conclusions.

In the current work, we have examined two different Schottky contact geometries: one where a Ti electrode only contacts one end of the nanowire and the other where a thin

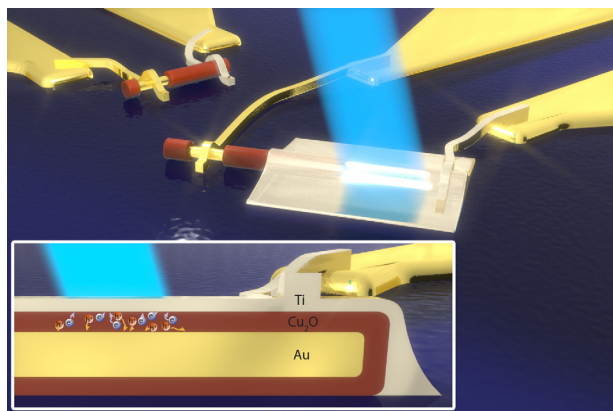


FIG. 1. Schematic drawing of the single metal-semiconductor core-shell nanowire photovoltaic cell geometry. Two devices are electrically connected to electrodes, and a laser beam (bright blue) is incident on one of them. The Au electrode contacts the Au core while a Ti electrode contacts the  $\text{Cu}_2\text{O}$  shell (red) only at the end (top left) or along most of the length via an additional thin Ti pad (center). The inset shows a cross section of the device geometry. The incident light creates electron-hole pairs ( $e^-$ ,  $h^+$ ), which are extracted via the shell and the core, respectively.

( $\sim 10$  nm) layer of Ti is coated along nearly the entire length of the nanowire (Figure 1). By comparing the photocurrent maps in these two geometries, we can directly visualize the effect of local contacts on charge separation and carrier collection efficiency.

To fabricate such samples, we started with  $\text{Si}_3\text{N}_4$  covered Si substrates with evaporated Au electrodes. The core-shell nanowires were contacted using electron beam lithography and metal evaporation. The optical characterization was conducted with a tunable laser source in the range of 410 nm–750 nm. The light was focused through an objective lens to a spot size of  $\sim 1$   $\mu\text{m}$  onto the electrically connected single nanowire photovoltaic cells. The details of the device fabrication and characterization can be found in the supplementary material.<sup>67</sup>

Figure 2(a) shows a scanning electron microscope (SEM) image of a typical single nanowire photovoltaic cell (marked by a red arrow). The reflection map in Figure 2(b) shows the diagonal orientation relative to the parallel contact pads. Figure 2(c) shows photocurrent generation of up to 300 pA under 42  $\mu\text{W}$  laser illumination at  $\lambda = 410$  nm. The overlap with the SEM image in Figure 2(d) reveals that charge carrier collection only occurs near the Ti contact finger, where the Schottky junction induces a built-in electric field, such that the minority charge carriers do not have to travel long distances to get extracted. Due to the optically thick Ti contact, we do not expect any substantial contribution to the photocurrent from the  $\text{Cu}_2\text{O}$  regions under the contact.

This photocurrent collection localized only close to the Ti contact suggests that the minority carrier diffusion length is less than or equal to the beam spot size of  $\sim 1$   $\mu\text{m}$ , consistent with reported values for  $\text{Cu}_2\text{O}$  synthesized by

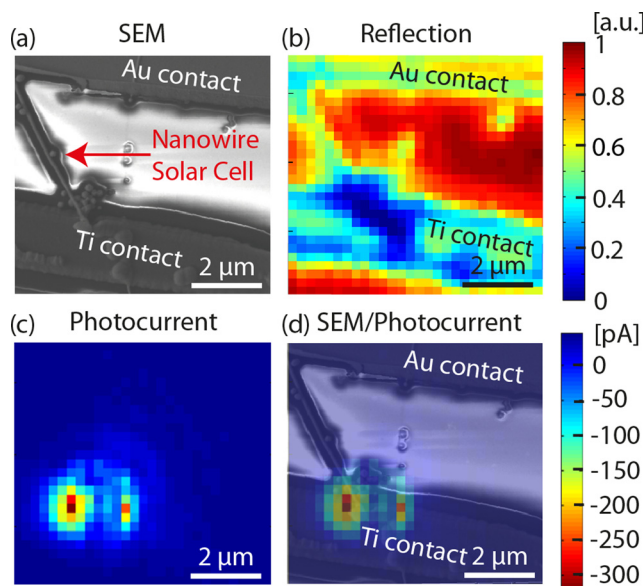


FIG. 2. Metal-semiconductor core-shell nanowire photovoltaic cell with axial charge carrier collection. (a) SEM image of a nanowire (red arrow) connected between Ti and Au contacts. (b) Optical reflection image. (c) Photocurrent map with an incident laser power of 42  $\mu\text{W}$ , polarization perpendicular to the nanowire axis, a spot size of 1  $\mu\text{m}$ , and illumination wavelength of 410 nm. (d) Overlay of the photocurrent map and SEM image, clearly showing the local photocurrent collection at the Ti contact.

different methods.<sup>53,54</sup> Despite the excellent crystallinity and epitaxial shell growth in these core-shell nanowires, the high surface and contact areas could lead to even shorter minority carrier diffusion lengths, as these are known to be sources of increased non-radiative recombination in bulk solar cells.<sup>46</sup> Future studies involving thin interfacial spacing layers and surface passivation are needed to quantify the importance of these effects, and our single core-shell nanowire geometry provides a perfect platform for such studies.

To probe directly the importance of the radial built-in field and carrier collection mechanism, we have compared the above results to the case where a 10 nm thin Ti pad covers approximately 2/3 of the nanowire (Figure 3). This arrangement is closer to a realistic large-scale device, where the whole nanowire would be covered with an additional contact (either a transparent conductive oxide or a continuous thick metal layer with illumination through a transparent substrate). Figure 3(a) shows an SEM image of the device, with a Ti pad on top of the nanowire, which is connected between a Ti contact and an Au contact. Figure 3(b) shows the reflection image and Figure 3(c) the respective photocurrent map under  $7 \mu\text{W}$  laser illumination at  $\lambda = 410 \text{ nm}$ , which reveals photocurrent collection from an extended elongated area. The overlay of the SEM and the photocurrent map in Figure 3(d) clearly demonstrates photocurrent collection from the nanowire along the entire length covered by the Ti pad.

This supports the idea that charge carriers generated by light passing through the 10 nm Ti pad can be separated and collected at the metal core and the Ti top contact. The maximum photocurrent is around 25 times smaller than in the

axial collection case shown in Figure 2, which can be attributed to the reduction in incident power from 42 to  $7 \mu\text{W}$  and the substantially reduced absorption in the wire due to the Ti pad. The responsivity (photocurrent after background subtraction divided by the incident laser power) is only lowered by a factor of four by the Ti pad. These results prove the utility of this concept: photocurrent collection can take place along the whole length of the nanowire, even with materials that have very short minority carrier diffusion lengths.

To investigate the core-shell nanowire spectral response, we map the responsivity under 410 nm, 520 nm, 620 nm, and 700 nm laser illumination (Figures 4(c)–4(f), respectively). The polarization was perpendicular to the nanowire axis for all measurements, which is the polarization that supports plasmon resonances. In the other polarization, we observed weaker currents. Currently, we cannot distinguish between charge carrier generation due to band to band absorption in the  $\text{Cu}_2\text{O}$  and plasmon mediated transfer mechanisms, such as resonance energy transfer, direct energy transfer, and hot electron carrier injection.<sup>33,55–59</sup>

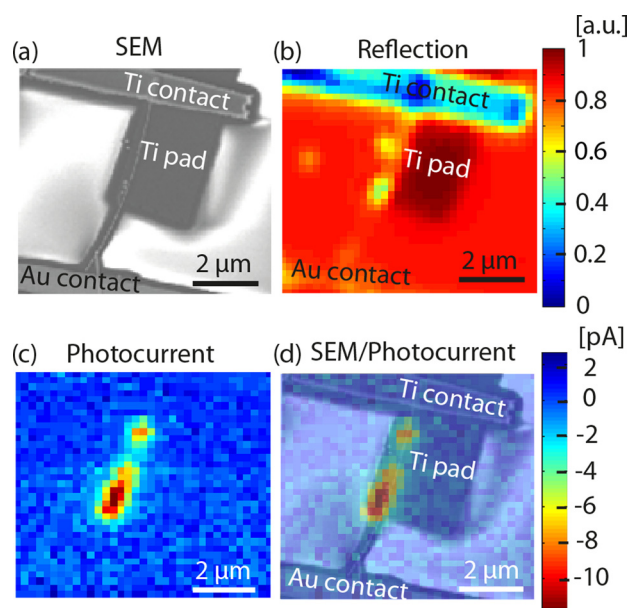


FIG. 3. Metal-semiconductor core-shell nanowire photovoltaic cell with radial charge carrier collection. (a) SEM image of a nanowire connected between Ti and Au contacts and partially covered by a 10 nm thin Ti pad. (b) Reflection map. (c) Photocurrent map with an incident laser power of  $7 \mu\text{W}$ , polarization perpendicular to the nanowire axis, a spot size of  $1 \mu\text{m}$ , and illumination wavelength of 410 nm. (d) Overlay of photocurrent map and SEM image, clearly showing the photocurrent collection from the Ti covered part of the nanowire.

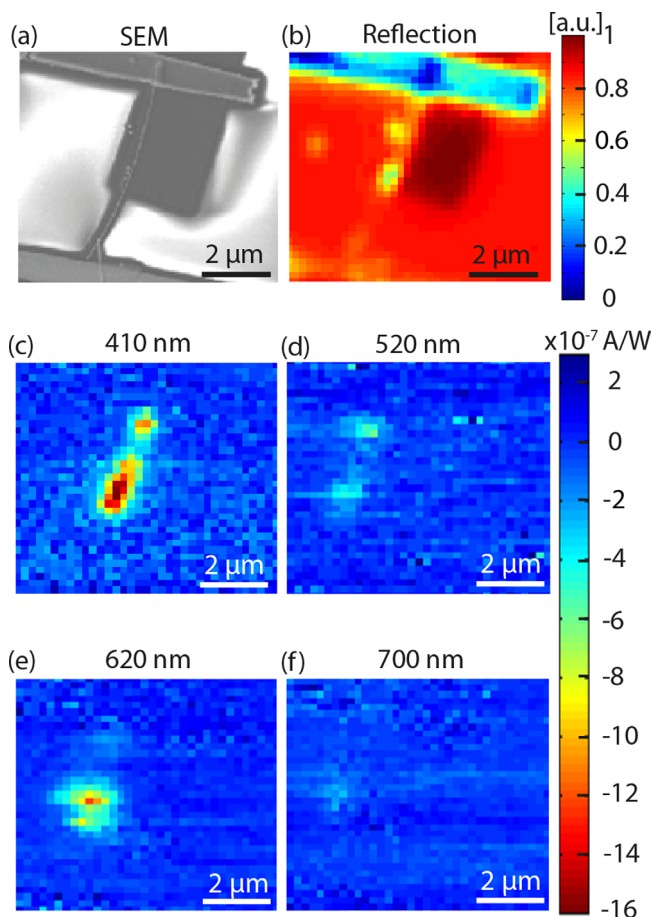


FIG. 4. Spectral response of a metal-semiconductor core-shell nanowire photovoltaic cell. (a) SEM image of the same nanowire solar cell shown in Figure 3. (b) Reflection map at 410 nm showing the contact pad and contact fingers. (c)–(f) Responsivity maps at laser wavelengths of (c) 410 nm, (d) 520 nm, (e) 620 nm, and (f) 700 nm. The responsivity was obtained by first subtracting the background values and subsequently dividing by the incident laser power, to facilitate comparison. In all cases, the laser polarization was perpendicular to the nanowire axis. The spatial shift of the photocurrent with increasing wavelengths is due to chromatic aberration of the objective lens and drift in the mechanical stage.

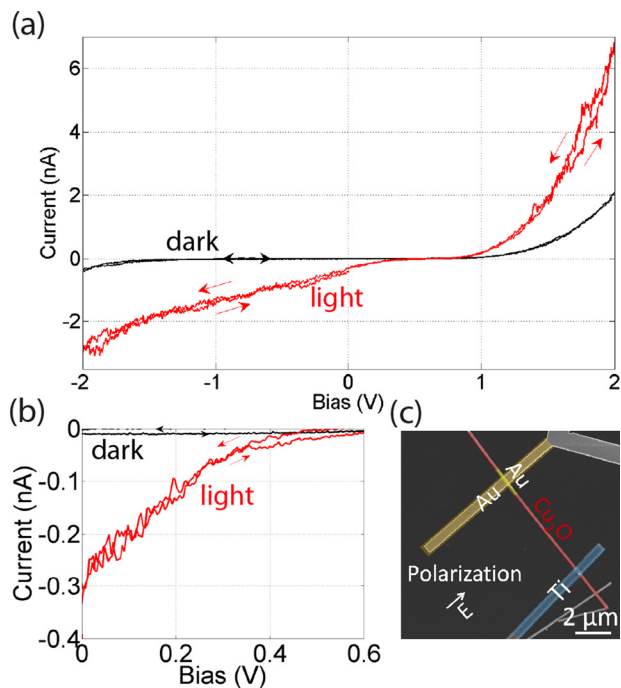


FIG. 5. (a) Current-voltage behavior of a single Au-Cu<sub>2</sub>O core-shell nanowire photovoltaic cell in the dark (black line) and under laser illumination at 410 nm with a power of 42  $\mu$ W and polarization perpendicular to the nanowire axis (red). (b) Magnified view of the region 0 V–0.6 V of the I-V curves. (c) SEM image with color overlay of a connected nanowire.

The strong reduction in photocurrent for  $\lambda = 700$  nm is consistent with the literature value of the optical band gap (1.95 eV or 635 nm) and our own single nanowire PL measurements.<sup>40,60</sup> However, absorption in the Ti pad as well as variations in the optical resonances must be taken into account to quantitatively explain the observed results.

Finally, we show single nanowire current-voltage (I-V) measurements in the dark and under laser illumination (Figure 5). This nanowire device, which did not contain an extended Ti pad (Figure 5(c)), showed clear rectification behavior with a turn on voltage of  $\sim 1$  V in the dark. Under laser illumination with 42  $\mu$ W power at 410 nm, an  $I_{sc}$  of  $-300$  pA and a  $V_{oc}$  of 600 mV were observed. These results clearly demonstrate that single metal-semiconductor core-shell nanowires function as photovoltaic cells. The photocurrent increases at higher reverse voltages and reaches reverse break down before saturating. We attribute this slope to higher photogenerated carrier collection efficiency at larger reverse bias voltages due to an increased depletion region. Furthermore, we observe a substantial charge carrier extraction barrier and hence S-shaped I-V curve, which is a well-known phenomena that can be attributed to accumulated space charges at the material interfaces or a non-ideal Ohmic contact.<sup>61–64</sup> This observation can be explained by the non-optimized metal semiconductor interfaces, which are likely to induce recombination-active trap states and accumulated space charges. We note that the photocurrent under the AM 1.5G spectrum was below the detection limit ( $\sim 1$  pA) of the source measure unit used and therefore did not allow the measurement of our devices under the full solar spectrum. The low photocurrent can partially be explained by the

localized Schottky region close to the optically thick Ti contact, which is mostly inaccessible for the incident light. Only a small fraction at the edge of the contact can contribute to the photocurrent.

In conclusion, we have realized a single metal-semiconductor core-shell nanowire photovoltaic cell. We measured photocurrent maps on individual Au-Cu<sub>2</sub>O core-shell nanowires, showing charge carrier collection via a Schottky contact on the surface, with the metal core being utilized as an Ohmic contact. The spectral response is consistent with a band gap of  $\sim 2$  eV. We show that a  $V_{oc}$  of 0.6 V and  $I_{sc}$  of 300 pA can be achieved without any detailed contact optimization, while much higher values can be expected by incorporating appropriate interfacial layers, as already demonstrated not only with Cu<sub>2</sub>O but also other material systems that use ultrathin absorber layers such as organics and hybrid perovskites.<sup>8,65,66</sup> By depositing a thin (10 nm) Ti layer over the wire, we clearly demonstrate that two conductive radial metal contacts allow for improved photogenerated carrier collection in semiconductors with minority carrier diffusion lengths  $< 1$   $\mu$ m.

While the limitations discussed above explain the overall low photovoltaic performance of our devices, they do not present insurmountable obstacles on the way to high efficiency metal-semiconductor core-shell nanowire solar cells. In fact, the strong dependence of nanostructured solar cells on surface and interface properties presents an opportunity to study these effects in a highly controlled system where changes at the semiconductor surface or metal-semiconductor interface can be directly measured in the photovoltaic response of the device. Any new insights gained here can be applied to existing thin-film technology where the metal-semiconductor contact is also a crucial source of loss but more difficult to isolate and study. Furthermore, we note that the metal-semiconductor core-shell nanowire geometry is not limited to the materials used for this proof-of-concept study. An ideal structure would employ low cost metals with appropriate interfacial layers, replacing Au and Ti. Therefore, we propose metal-semiconductor core-shell nanowire photovoltaics as both an ideal platform for fundamental interfacial studies as well as a promising geometry for high efficiency solar cells made from materials with very short minority carrier diffusion lengths.

We are thankful to Duncan Verheijde, Henk-Jan Boluijt, and Wim Brouwer for help with the design and construction of the electrical measurement components, Marco Seynen for software engineering, Joop Rovekamp for help with wire bonding, Henk-Jan Boluijt for creating the schematic picture in Figure 1, and Jorik van de Groep for a careful reading of the manuscript. Furthermore, we would like to acknowledge support from the Light Management in New Photovoltaic Materials (LMPV) center at AMOLF. This work is part of the research program of the Foundation for Fundamental Research on Matter (FOM), which is part of the Netherlands Organization for Scientific Research (NWO). The research leading to these results has received funding from the European Research Council under the European Union's Seventh Framework Programme (FP/2007-2013)/ERC Grant Agreement No. 337328, "NanoEnabledPV."

- <sup>1</sup>European Photovoltaic Industry Association, Market Report 2013 (2013).
- <sup>2</sup>M. A. Green, *Prog. Photovoltaics: Res. Appl.* **9**, 123 (2001).
- <sup>3</sup>B. K. Meyer, A. Polity, D. Reppin, M. Becker, P. Hering, P. J. Klar, T. Sander, C. Reindl, J. Benz, M. Eickhoff, C. Heiliger, M. Heinemann, J. Bläsing, A. Krost, S. Shokovets, C. Müller, and C. Ronning, *Phys. Status Solidi B* **249**, 1487 (2012).
- <sup>4</sup>M. Green, *IEEE Trans. Electron Devices* **31**, 671 (1984).
- <sup>5</sup>F. Meillaud, A. Shah, C. Droz, E. Vallat-Sauvain, and C. Miazza, *Sol. Energy Mater. Sol. Cells* **90**, 2952 (2006).
- <sup>6</sup>F. Dimroth, M. Grave, P. Beutel, U. Fiedeler, C. Karcher, T. N. D. Tibbits, E. Oliva, G. Siefert, M. Schachtner, A. Wekkeli, A. W. Bett, R. Krause, M. Piccin, N. Blanc, C. Drazek, E. Guiot, B. Ghyselen, T. Salvetat, A. Tauzin, T. Signamarcheix, A. Dobrich, T. Hannappel, and K. Schwarzburg, *Prog. Photovoltaics: Res. Appl.* **22**, 277 (2014).
- <sup>7</sup>Z. M. Beiley and M. D. McGehee, *Energy Environ. Sci.* **5**, 9173 (2012).
- <sup>8</sup>Y. S. Lee, D. Chua, R. E. Brandt, S. C. Siah, J. V. Li, J. P. Mailoa, S. W. Lee, R. G. Gordon, and T. Buonassisi, *Adv. Mater.* **26**, 4704 (2014).
- <sup>9</sup>T. Minami, Y. Nishi, and T. Miyata, *Appl. Phys. Express* **6**, 044101 (2013).
- <sup>10</sup>Y. S. Lee, J. Heo, M. T. Winkler, S. C. Siah, S. B. Kim, R. G. Gordon, and T. Buonassisi, *J. Mater. Chem. A* **1**, 15416 (2013).
- <sup>11</sup>S. W. Lee, Y. S. Lee, J. Heo, S. C. Siah, D. Chua, R. E. Brandt, S. B. Kim, J. P. Mailoa, T. Buonassisi, and R. G. Gordon, *Adv. Energy Mater.* **4**, 1301916 (2014).
- <sup>12</sup>C. Xiang, G. M. Kimball, R. L. Grimm, B. S. Brunschwig, H. A. Atwater, and N. S. Lewis, *Energy Environ. Sci.* **4**, 1311 (2011).
- <sup>13</sup>K. P. Hering, R. E. Brandt, B. Kramm, T. Buonassisi, and B. K. Meyer, *Energy Procedia* **44**, 32 (2014).
- <sup>14</sup>T. Oku, T. Yamada, K. Fujimoto, and T. Akiyama, *Coatings* **4**, 203 (2014).
- <sup>15</sup>C.-C. Chen, L.-C. Chen, and Y.-H. Lee, *Adv. Condens. Matter Phys.* **2012**, 129139.
- <sup>16</sup>A. T. Marin, D. Muñoz-Rojas, D. C. Iza, T. Gershon, K. P. Musselman, and J. L. MacManus-Driscoll, *Adv. Funct. Mater.* **23**, 3413 (2013).
- <sup>17</sup>T. S. Gershon, A. K. Sigdel, A. T. Marin, M. F. A. M. van Hest, D. S. Ginley, R. H. Friend, J. L. MacManus-Driscoll, and J. J. Berry, *Thin Solid Films* **536**, 280 (2013).
- <sup>18</sup>T. Minami, Y. Nishi, T. Miyata, and J. Nomoto, *Appl. Phys. Express* **4**, 062301 (2011).
- <sup>19</sup>W. Shockley and H. J. Queisser, *J. Appl. Phys.* **32**, 510 (1961).
- <sup>20</sup>Z. I. Alferov, V. M. Andreev, and V. D. Rumyantsev, *Concentrator Photovoltaics*, Springer Series in Optical Sciences, edited by A. Luque and V. Andreev (Springer, 2007), pp. 151–174.
- <sup>21</sup>H. A. Atwater and A. Polman, *Nat. Mater.* **9**, 205 (2010).
- <sup>22</sup>P. Krostrup, H. I. Jørgensen, M. Heiss, O. Demichel, J. V. Holm, M. Aagesen, J. Nygard, and A. Fontcuberta i Morral, *Nat. Photonics* **7**, 306 (2013).
- <sup>23</sup>J. Wallentin, N. Anttu, D. Asoli, M. Huffman, I. Aberg, M. H. Magnusson, G. Siefert, P. Fuss-Kailuweit, F. Dimroth, B. Witzigmann, H. Q. Xu, L. Samuelson, K. Deppert, and M. T. Borgström, *Science* **339**, 1057 (2013).
- <sup>24</sup>E. C. Garnett, M. L. Brongersma, Y. Cui, and M. D. McGehee, *Annu. Rev. Mater. Res.* **41**, 269 (2011).
- <sup>25</sup>T. J. Kempa, R. W. Day, S.-K. Kim, H.-G. Park, and C. M. Lieber, *Energy Environ. Sci.* **6**, 719 (2013).
- <sup>26</sup>M. L. Brongersma, Y. Cui, and S. Fan, *Nat. Mater.* **13**, 451 (2014).
- <sup>27</sup>Z. Fan, H. Razavi, J. Do, A. Moriwaki, O. Ergen, Y.-L. Chueh, P. W. Leu, J. C. Ho, T. Takahashi, L. A. Reichertz, S. Neale, K. Yu, M. Wu, J. W. Ager, and A. Javey, *Nat. Mater.* **8**, 648 (2009).
- <sup>28</sup>M. Law, L. E. Greene, J. C. Johnson, R. Saykally, and P. Yang, *Nat. Mater.* **4**, 455 (2005).
- <sup>29</sup>B. Tian, X. Zheng, T. J. Kempa, Y. Fang, N. Yu, G. Yu, J. Huang, and C. M. Lieber, *Nature* **449**, 885 (2007).
- <sup>30</sup>J. M. Spurgeon, H. A. Atwater, and N. S. Lewis, *J. Phys. Chem. C* **112**, 6186 (2008).
- <sup>31</sup>L. Cao, J. S. White, J.-S. Park, J. A. Schuller, B. M. Clemens, and M. L. Brongersma, *Nat. Mater.* **8**, 643 (2009).
- <sup>32</sup>S. A. Mann and E. C. Garnett, *Nano Lett.* **13**, 3173 (2013).
- <sup>33</sup>S. Mubeen, J. Lee, N. Singh, S. Krämer, G. D. Stucky, and M. Moskovits, *Nat. Nanotechnol.* **8**, 247 (2013).
- <sup>34</sup>F. P. Garcia de Arquer, A. Mihi, D. Kufer, and G. Konstantatos, *ACS Nano* **7**, 3581 (2013).
- <sup>35</sup>Y. Nishijima, K. Ueno, Y. Yokota, K. Murakoshi, and H. Misawa, *J. Phys. Chem. Lett.* **1**, 2031 (2010).
- <sup>36</sup>Y. Takahashi and T. Tatsuma, *Appl. Phys. Lett.* **99**, 182110 (2011).
- <sup>37</sup>Y. K. Lee, C. H. Jung, J. Park, H. Seo, G. A. Somorjai, and J. Y. Park, *Nano Lett.* **11**, 4251 (2011).
- <sup>38</sup>P. Reineck, G. P. Lee, D. Brick, M. Karg, P. Mulvaney, and U. Bach, *Adv. Mater.* **24**, 4750 (2012).
- <sup>39</sup>S. Mubeen, J. Lee, W.-R. Lee, N. Singh, G. D. Stucky, and M. Moskovits, *ACS Nano* **8**, 6066 (2014).
- <sup>40</sup>B. Sciacca, S. A. Mann, F. D. Tichelaar, H. W. Zandbergen, M. A. van Huis, and E. C. Garnett, *Nano Lett.* **14**, 5891 (2014).
- <sup>41</sup>B. Wiley, Y. Sun, and Y. Xia, *Acc. Chem. Res.* **40**, 1067 (2007).
- <sup>42</sup>C.-H. Kuo, T.-E. Hua, and M. H. Huang, *J. Am. Chem. Soc.* **131**, 17871 (2009).
- <sup>43</sup>S. Hacialioglu, F. Meng, and S. Jin, *Chem. Commun.* **48**, 1174 (2012).
- <sup>44</sup>S. Brittman, Y. Yoo, N. P. Dasgupta, S. Kim, B. Kim, and P. Yang, *Nano Lett.* **14**, 4665 (2014).
- <sup>45</sup>J. I. Jang, *Cuprous Oxide (Cu<sub>2</sub>O): A Unique System Hosting Various Excitonic Matter and Exhibiting Large Third-Order Nonlinear Optical Responses* (InTech, Rijeka, 2011), pp. 137–164.
- <sup>46</sup>P. Wuerfel, *Physics of Solar Cells*, 2nd ed. (Wiley-VCH, Weinheim, 2009), p. 150.
- <sup>47</sup>E. E. Huber, *Appl. Phys. Lett.* **8**, 169 (1966).
- <sup>48</sup>*Cuprous Oxide (Cu<sub>2</sub>O) Crystal Structure, Lattice Parameters*, edited by O. Madelung, U. Roessler, and M. Schulz (Springer, Berlin, Heidelberg, 1998), pp. 1–3.
- <sup>49</sup>M. B. Brodsky, *J. Phys., Colloq.* **45**, C5 (1984).
- <sup>50</sup>J.-D. Kwon, S.-H. Kwon, T.-H. Jung, K.-S. Nam, K.-B. Chung, D.-H. Kim, and J.-S. Park, *Appl. Surf. Sci.* **285**, 373 (2013).
- <sup>51</sup>*CRC Handbook of Chemistry and Physics*, 85th ed., edited by D. R. Lide (CRC Press, New York, 2005).
- <sup>52</sup>L. C. Olsen, R. C. Bohara, and M. W. Urie, *Appl. Phys. Lett.* **34**, 47 (1979).
- <sup>53</sup>K. P. Musselman, Y. Ievskaya, and J. L. MacManus-Driscoll, *Appl. Phys. Lett.* **101**, 253503 (2012).
- <sup>54</sup>Y. Liu, H. K. Turley, J. R. Tumbleston, E. T. Samulski, and R. Lopez, *Appl. Phys. Lett.* **98**, 162105 (2011).
- <sup>55</sup>S. K. Cushing, J. Li, F. Meng, T. R. Senty, S. Suri, M. Zhi, M. Li, A. D. Bristow, and N. Wu, *J. Am. Chem. Soc.* **134**, 15033 (2012).
- <sup>56</sup>P. Fan, Z. Yu, S. Fan, and M. L. Brongersma, *Nat. Mater.* **13**, 471 (2014).
- <sup>57</sup>P. Fan, K. C. Y. Huang, L. Cao, and M. L. Brongersma, *Nano Lett.* **13**, 392 (2013).
- <sup>58</sup>P. Fan, U. K. Chettiar, L. Cao, F. Afshinmanesh, N. Engheta, and M. L. Brongersma, *Nat. Photonics* **6**, 380 (2012).
- <sup>59</sup>S. Brittman, H. Gao, E. C. Garnett, and P. Yang, *Nano Lett.* **11**, 5189 (2011).
- <sup>60</sup>F. C. Akkari and M. Kanzari, *Phys. Status Solidi A* **207**, 1647 (2010).
- <sup>61</sup>A. Wagenpfahl, D. Rauh, M. Binder, C. Deibel, and V. Dyakonov, *Phys. Rev. B* **82**, 115306 (2010).
- <sup>62</sup>M. Zhang, H. Wang, and C. W. Tang, *Appl. Phys. Lett.* **99**, 213506 (2011).
- <sup>63</sup>R. Saive, C. Mueller, J. Schinke, R. Lovrincic, and W. Kowalsky, *Appl. Phys. Lett.* **103**, 243303 (2013).
- <sup>64</sup>A. Kumar, S. Sista, and Y. Yang, *J. Appl. Phys.* **105**, 094512 (2009).
- <sup>65</sup>S. Ryu, J. H. Noh, N. J. Jeon, Y. Chan Kim, W. S. Yang, J. Seo, and S. II Seok, *Energy Environ. Sci.* **7**, 2614 (2014).
- <sup>66</sup>A. W. Hains, J. Liu, A. B. F. Martinson, M. D. Irwin, and T. J. Marks, *Adv. Funct. Mater.* **20**, 595 (2010).
- <sup>67</sup>See supplementary material at <http://dx.doi.org/10.1063/1.4905652> for experimental details.

## CHAPTER 2: FROM SINGLE NW TOWARDS ARRAY: TRANSPARENT ELECTRODES

To facilitate device integration of core-shell nanowires one could imagine the situation where the nanowire metallic cores are all interconnected before the shell growth. In this scenario they would indeed be a truly macroscopic nanowire transparent electrode (Figure 10), that could be coated with a semiconducting shell via solution or vapour deposition processes. This requires the realisation of nanowire transparent electrodes, that is another scientific domain that can have a strong impact on technology, especially in optoelectronics. This aspect will be discussed in this section.

Transparent conductors are crucial components in optoelectronic devices, such as touch screens, organic light emitting diodes and solar cells. The efficiency of these devices strongly depends on the performances of the transparent electrodes, which must present the best conductivity to the transport of electrons and, at the same time, the best transparency to photons (low absorption and reflection). These are antithetical properties, being an improvement in conductivity generally linked to a reduction in transparency. Transparent

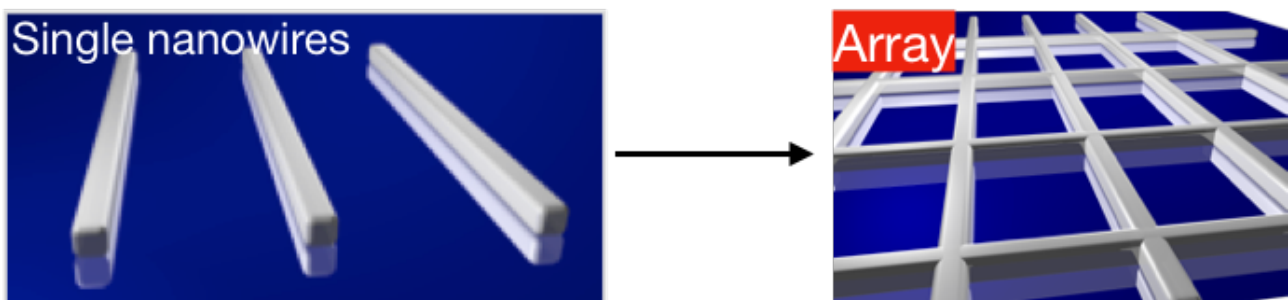


**Figure 10:** Schematic illustrating the transition between individual nanowires, that are suitable as a platform for fundamental studies, to a nanowire transparent electrode that could be an architecture compatible with macroscopic devices.

conductive oxides are most commonly used in these applications, with indium tin oxide (ITO) leading the market. However, the deposition process of ITO is expensive and its brittleness makes it incompatible with flexible electronics. Thus, it is crucial to study and develop valid alternatives that provide with high electrical conductivity and high optical transmission, but that can be fabricated at low-cost on rigid or flexible substrates. The materials recently studied include carbon nanotubes, conductive polymers, graphene, and networks of metallic nanowires<sup>76</sup>. The latter, generally composed of Ag, Cu or Al, have proven to be excellent transparent conductors, displaying better properties than competing technologies. The conductivity of these metals is high and the nanostructured wires effectively couple light into an underlying substrate through the excitation and scattering of plasmon modes.

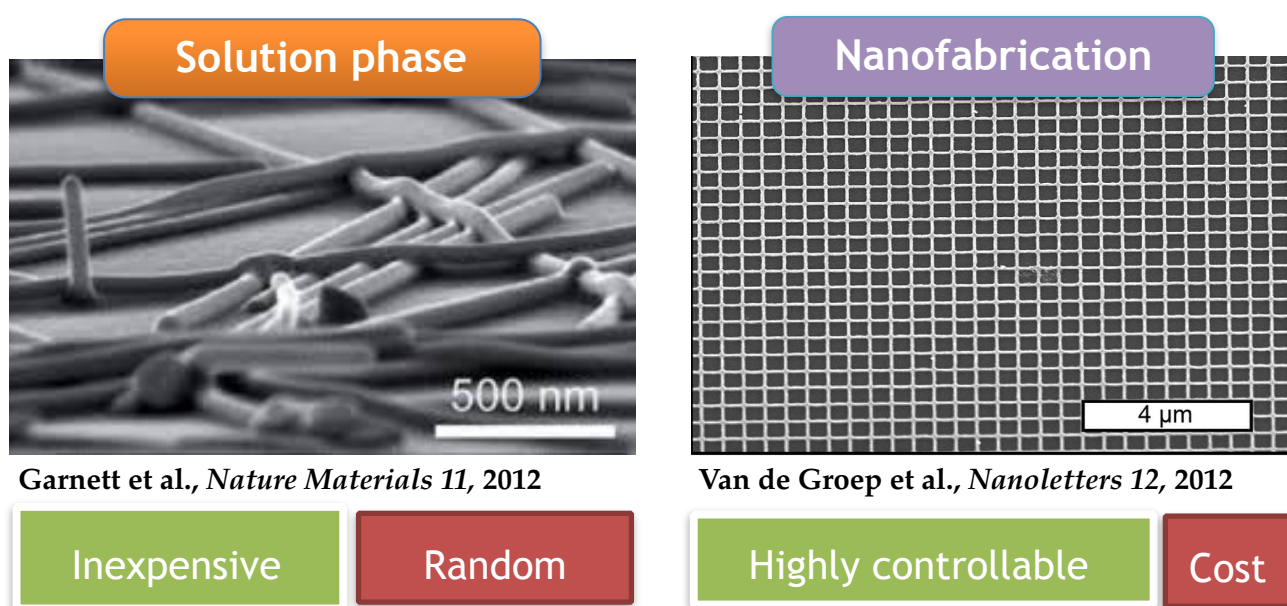


**Figure 11:** Nanowire transparent electrodes obtained by solution processes(left) or nanofabrication (right).

Several approaches to fabricating metallic nanowire arrays combining high transmittance and low resistivity have been explored so far (Figure 11). One approach consists on the deposition and welding of colloidal metallic nanowires, that has proven effective in obtaining transparent electrodes with remarkable performance. This shows that solution-based processes can produce materials of similar quality to those made by vacuum methods. Although this method provides a relatively simple fabrication scheme, the random geometry limits control over the optical transmission characteristics, which are determined by the subtle interaction between the substrate and surface plasmons supported on the nanowires. To obtain such control, ordered arrays of nanowires have been produced by lithographic techniques, that allows precise tuning of the array geometry (width, height and periodicity). The precise design of nanoscale patterns can produce electrodes with superior optoelectronic performance. In fact, it achieves (i) minimum resistance (for a certain transmission) via geometry tuning, (ii) coupling to specific optical modes and (iii) light trapping or emission directional. Such optimal characteristics are only achievable with an engineered pattern, that however requires the use of nanofabrication approaches, that typically require thermal evaporation to deposit the metal<sup>77</sup>. Although vacuum processes can deposit high quality materials, they are energy intensive and time consuming.

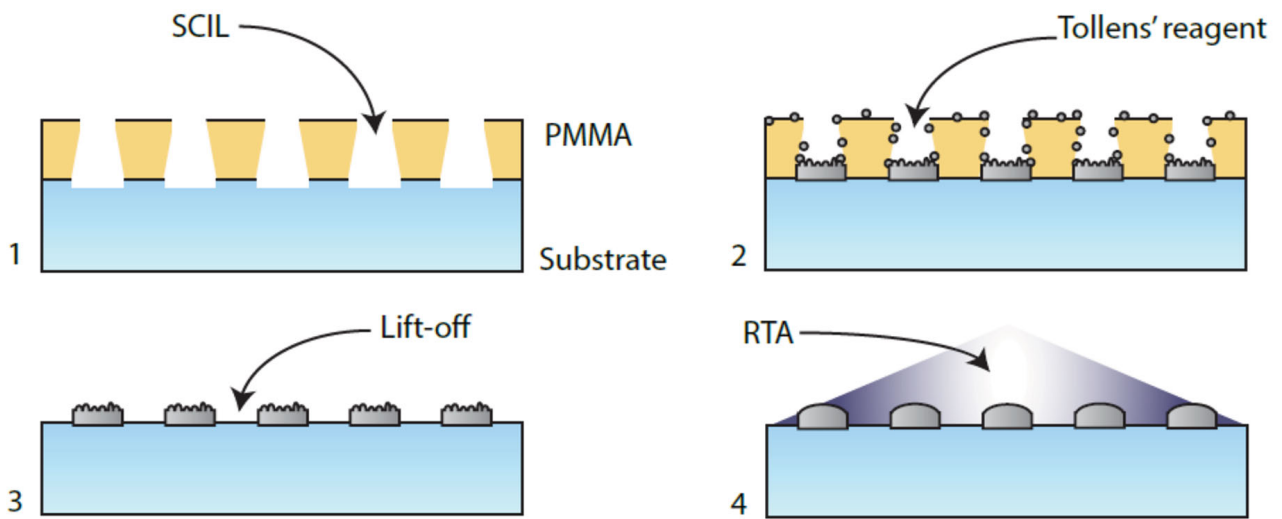


**Figure 12:** Cartoon illustrating the nanowire transparent electrode fabrication process.

Integrating the nanopattern with solution processing techniques would be a key step towards replacing expensive metal oxide films as transparent electrodes.

To succeed in this challenge, an hybrid approach was taken (Figure 12), in which the nanoscale pattern was first defined via substrate conformal nanoimprint lithography (SCIL) and then a solution process (the Tollens' reaction) was used to grow metal nanowires (as opposed to the expensive metal evaporation)<sup>31</sup>.

The Tollens' reaction consists in the reduction of a diaminesilver(I) complex by glucose, that causes the nucleation and growth of silver nanocrystals that nucleate on the substrate surface. The polymer layer used to confine the growth is dissolved in the lift-off process, to yield continuous nanopatterned Ag nanowire arrays, that are subsequently exposed to a rapid thermal annealing (RTA) for few seconds to provide with a smoother surface. Samples with different width, periodicity and thickness of the array were prepared on a 4 mm<sup>2</sup> scale, and

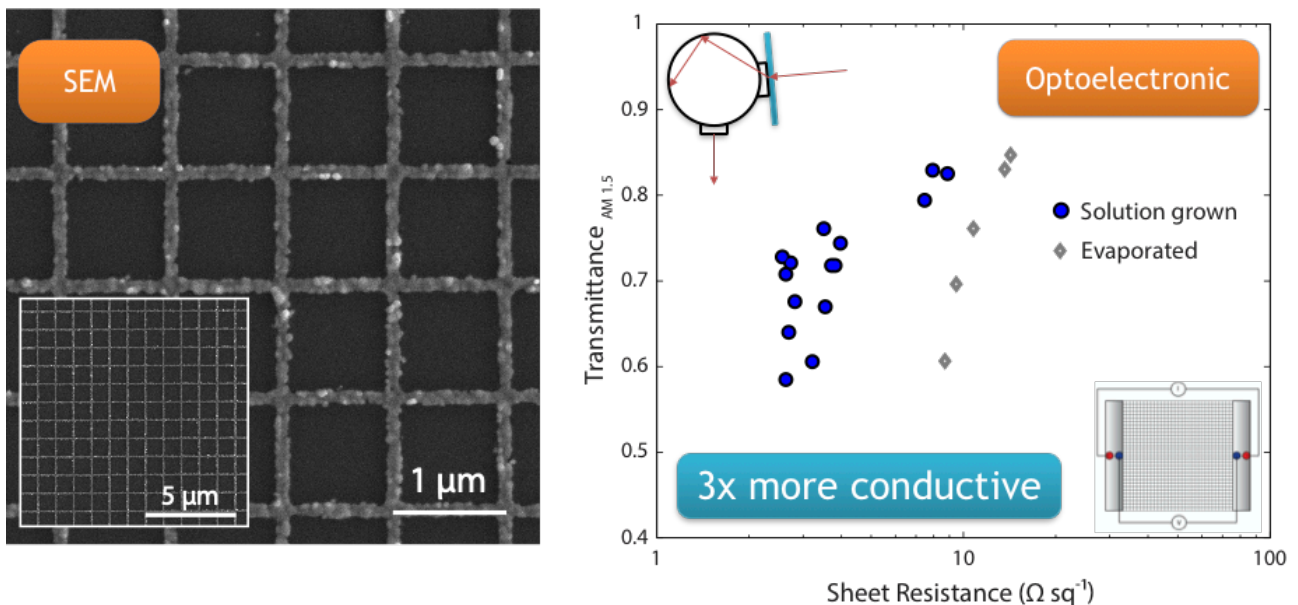


**Figure 13:** SEM image of ordered Ag nanowire array obtain via a hybrid solution process (left) and optoelectronic performance (right).

the optoelectronic performance were assessed by measuring the sheet resistance and the diffused transmittance (Figure 13). These arrays were compared to those prepared with the standard approach, in which Ag is deposited by thermal evaporation. The transmittance, weighted over the AM1.5 spectrum, was similar regardless of the preparation method. This is more or less expected as the transmittance mostly depend on the array geometry, and in particular on the filling fraction (area occupied by the metal). In contrast, the conductivity of solution processed transparent electrodes was on average three times higher than those prepared by metal evaporation. X-ray diffraction and analysis via the Scherrer's equation showed that the average crystal size was four times larger (~15 nm vs ~60 nm) in the samples prepared via the solution approach. Theoretical models for conductivity that account for electron scattering at grain boundaries confirmed quantitatively the difference observed (Figure 14).

This hybrid approach allowed to improve the performance of transparent electrodes in

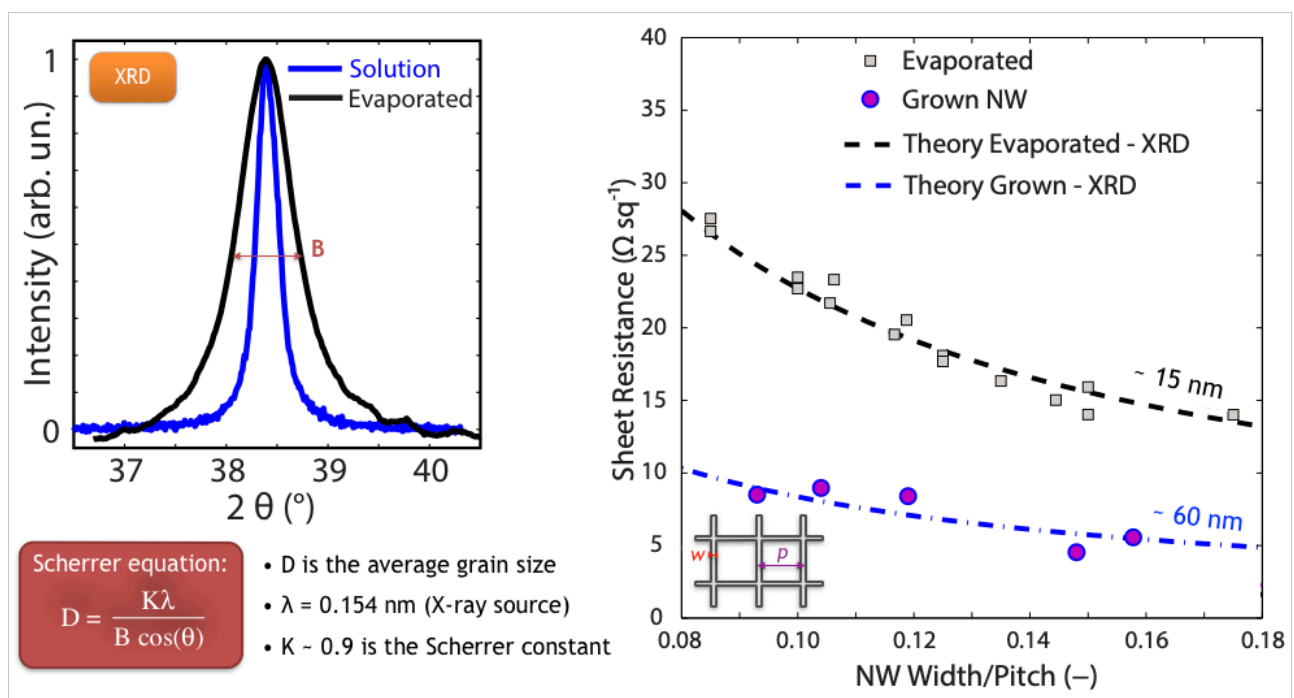


**Figure 14:** XRD (left) and sheet resistance (right) of solution processed ordered Ag nanowire arrays.

terms of conductivity and to reduce fabrication costs. A literature survey, presented in Figure 15, show the conductivity of state of the art nanowire arrays as a function of the estimated average grain size (computed from XRD analysis). The solid curve takes into account also surface scattering, that at the nanoscale has a non negligible impact on the conductivity. This shows that, in comparison with other metal nanowire -based technologies, the intrinsic conductivity obtained with this hybrid approach is outstanding, still allowing for nanopattern engineering. However, the theoretical limit (monocrystalline silver) is still a factor two better. As an example this limit can be achieved in individual monocrystalline silver nanowires. Unfortunately, when deposited in a macroscopic random array and welded together the conductivity drops by a factor larger than two<sup>76,78</sup>.

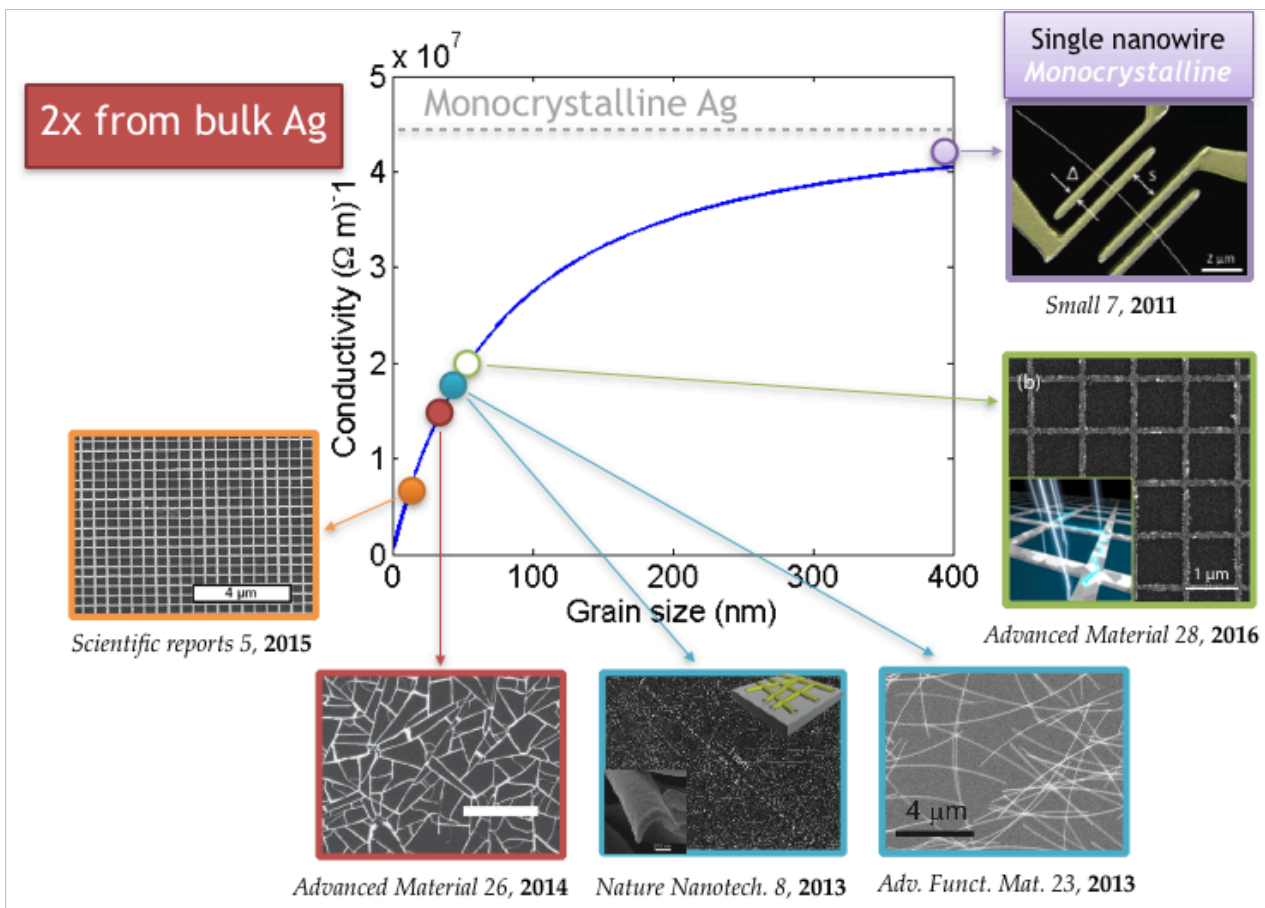


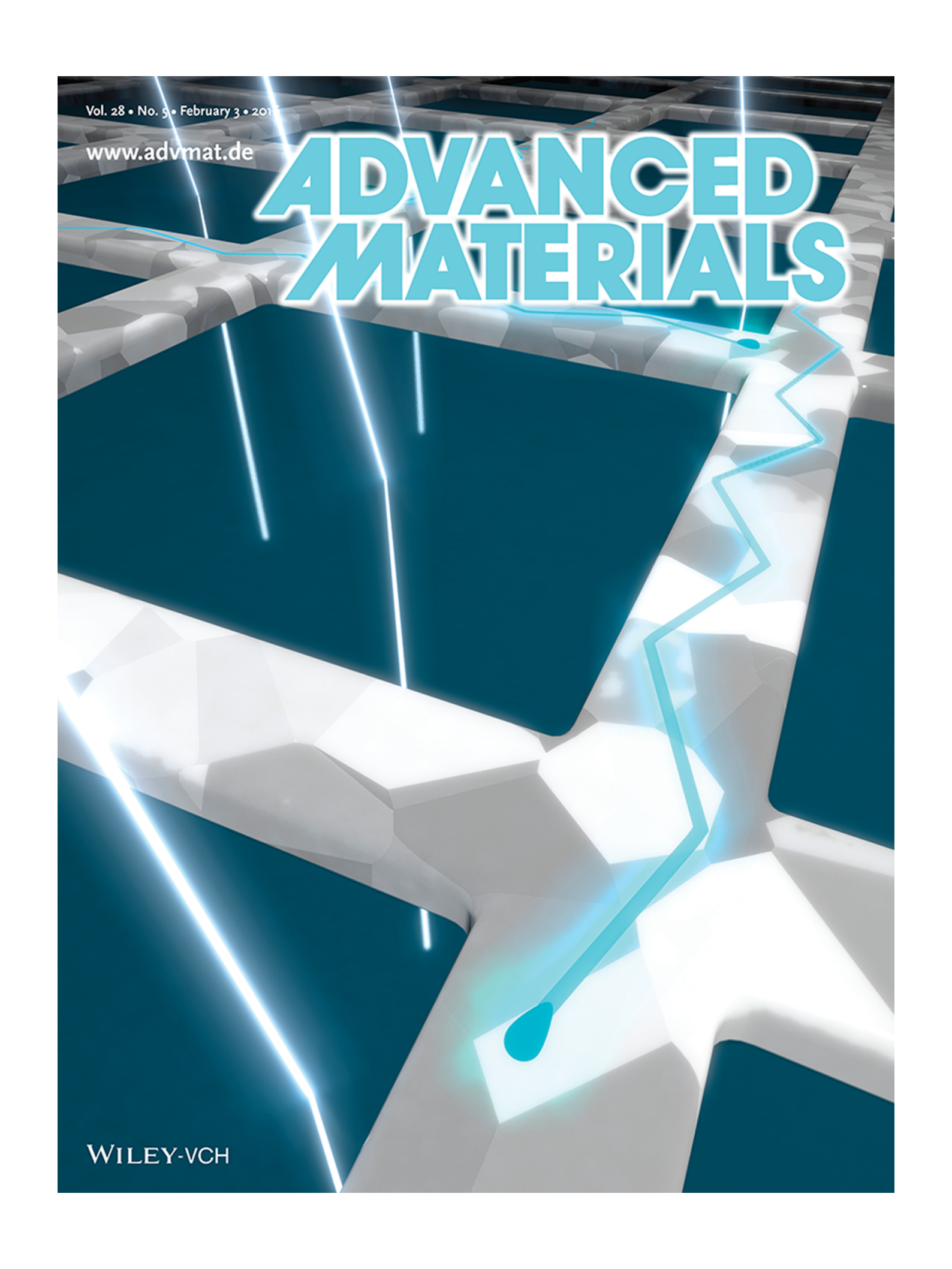
**Figure 15:** Literature survey on Ag nanowire transparent electrodes, showing the conductivity as a function of grain size estimated from available data.

This led to the scientific question on how one can realise monocrystalline materials with an arbitrary nanoscale pattern entirely with bottom up approaches. This will be discussed in Chapter 3.

Vol. 28 • No. 5 • February 3 • 2016

[www.advmat.de](http://www.advmat.de)

# ADVANCED MATERIALS

The background of the cover is an abstract, 3D-rendered landscape composed of white, faceted geometric shapes. Several bright blue, glowing lines of varying thicknesses and colors (some cyan, some white) traverse the scene, creating a sense of depth and movement. One prominent line curves across the middle ground, ending in a small, glowing teardrop-shaped droplet. The overall aesthetic is clean, modern, and futuristic, typical of a scientific journal cover.

WILEY-VCH

# Solution-Grown Silver Nanowire Ordered Arrays as Transparent Electrodes

Beniamino Sciacca, Jorik van de Groep, Albert Polman, and Erik C. Garnett\*

Transparent conductors are crucial components in optoelectronic devices, such as touch screen displays, organic light emitting diodes, and solar cells.<sup>[1,2]</sup> Transparent conducting oxides are the most commonly used in these applications, with indium-tin-oxide (ITO) leading the market.<sup>[3]</sup> However, the costly deposition process of ITO and the incompatibility with flexible electronics, due to the brittleness of thick films,<sup>[4,5]</sup> have triggered intensive research toward alternative schemes that can simultaneously provide high electrical conductivity, high optical transmittance, and flexibility. Materials that have recently been investigated include carbon nanotubes,<sup>[4,6–8]</sup> conducting polymers,<sup>[4,9,10]</sup> percolated metal films,<sup>[11–13]</sup> graphene,<sup>[4,14,15]</sup> and metal nanowire networks.<sup>[4,16–24]</sup>

Metal nanowire networks composed of, e.g., Ag, Cu, and Al have proven to be excellent transparent conductors.<sup>[16–18,22,23,25]</sup> The bulk conductivity of these metals is high, and nanostructured wires effectively couple light into an underlying substrate through the excitation and scattering of plasmons.<sup>[16,17,23,24]</sup> Several approaches to realize metal nanowire networks with high transmittance and low sheet resistance that can be made at low costs have been explored so far. These include nanowire meshes prepared by metal evaporation on various templates, such as electrospun fibers,<sup>[22,26,27]</sup> self-cracking templates,<sup>[19]</sup> or lithography-defined nanopatterns.<sup>[16,17]</sup> Such approaches typically require thermal evaporation in order to deposit metal. Although vacuum processes allow to deposit high quality materials, they are energy intensive, time consuming, and make inefficient use of metal. Cost-effective alternatives based on deposition and welding of metal nanowires prepared in solution have proven effective to achieve transparent electrodes with remarkable performance.<sup>[5,21,24,28,29]</sup> This shows that solution processes can yield material of similar quality compared to vacuum-based methods. Although this method provides a relatively simple fabrication scheme, the random geometry limits control over the optical transmission characteristics, which are determined by the subtle interplay between plasmons on the interacting nanowires. To achieve such control, ordered arrays of nanowires have been made by lithographic techniques.<sup>[16,17,30]</sup> Using these arrays, accurate control over the excited plasmon modes and their interaction, via tuning of the nanowire width, height, and pitch of the array, has led to performance beyond that of ITO.<sup>[17]</sup> Furthermore,

it has been shown that the accurate design of patterns at the nanoscale (such as fractal geometries), can yield electrodes with superior optoelectronic performance.<sup>[31]</sup> In fact, this enables (i) minimum sheet resistance (for a certain transmittance) via tuning of the geometry, (ii) coupling to specific optical modes, and (iii) light trapping or directional emission. As such optimal features are only achievable with an engineered pattern, the successful integration of nanopatterning with solution processing techniques would be an important step toward replacing expensive metal oxide films as transparent electrodes.

Here, we demonstrate a strategy that bridges the gap between the efficiency of solution phase processes, and the control of light-matter interaction at the nanoscale using nanopatterning. We combine substrate-conformal imprint-lithography (SCIL) with a soft solution process to fabricate highly controlled 2D networks of silver nanowires without metal evaporation steps. First, SCIL is used to make a square array of trenches in a poly(methyl methacrylate) (PMMA) film that is spin-coated on glass (trench width 50–130 nm, pitch 300–1000 nm). Second, the reduction of a silver salt ( $\text{AgNO}_3$ ) by a sugar (glucose) in an aqueous solution is used to locally infill the trenches with silver, following a chemical route commonly employed as a simple test for the presence of aldehydes (Tollens' test). Using this method, we obtain a solution-grown nanowire network on glass with a well-controlled geometry. We find that the electrical performance outperforms that of evaporated networks with an almost three-fold decrease in resistivity ( $3.5 \Omega \text{ sq}^{-1}$  vs  $10.7 \Omega \text{ sq}^{-1}$  at a transmission of 76%, weighted for AM1.5 photon density). The controlled 2D network allows us to confidently compare different metal deposition pathways and derive conclusions about their performance. Based on detailed characterization and a simple conductivity model, we show that the high conductance of the solution-grown networks can be explained by a large increase in the grain size of silver nanocrystallites within the nanowires, compared to the evaporated wires. This shows that the material quality achievable with solution deposition methods can match or even exceed that obtained with vacuum-based techniques.

The fabrication of solution-grown nanowire networks is summarized in **Figure 1a**. It involves four steps (see the Supporting Information for more details): (i) use of SCIL to imprint nanosized trenches in a PMMA template, organized in a grid fashion; (ii) use of the Tollens' reaction to nucleate and grow crystalline silver on the substrate surface; (iii) lift-off of the PMMA template to obtain a transparent and conductive nanowire network; (iv) use of rapid thermal annealing (RTA) to reduce surface roughness.

Silver was chosen as the material for the solution grown nanowire networks because of its exceptional conductivity and better chemical stability compared to copper. The Tollens'

Dr. B. Sciacca, J. van de Groep,  
Prof. A. Polman, Dr. E. C. Garnett  
Center for Nanophotonics  
FOM Institute AMOLF  
Science Park 104, 1098 XG Amsterdam, The Netherlands  
E-mail: e.garnett@amolf.nl



DOI: 10.1002/adma.201504045

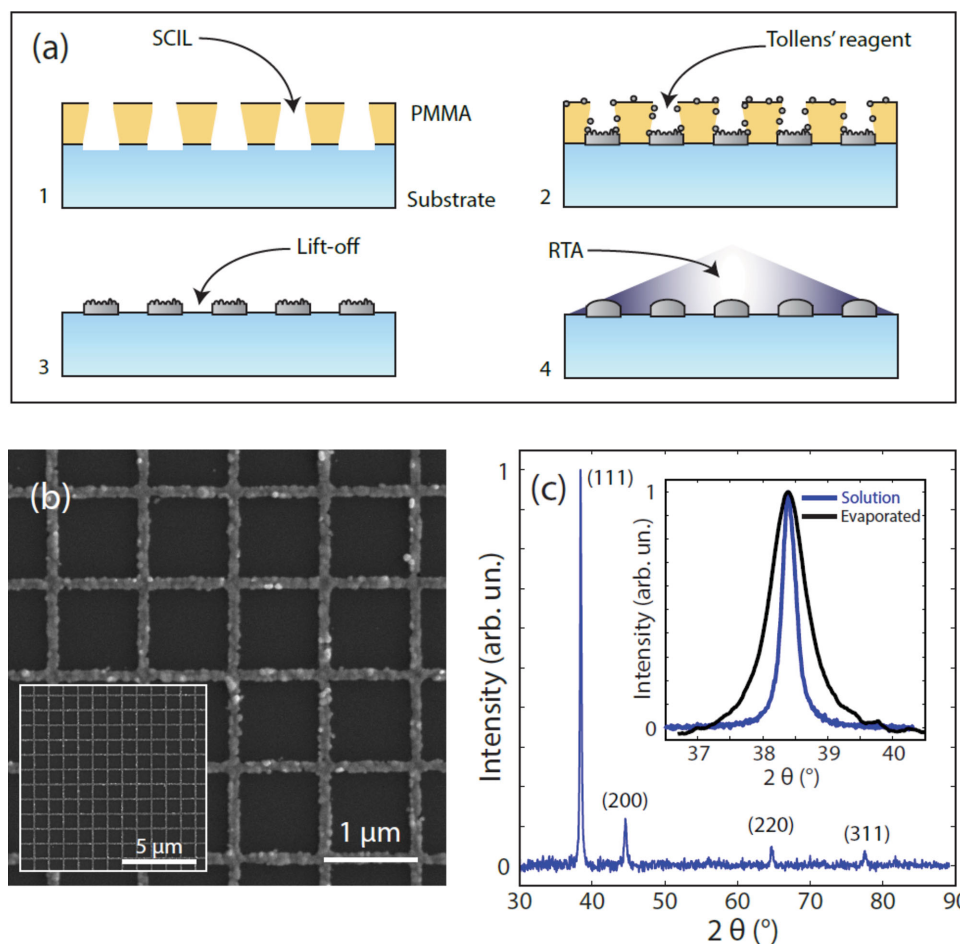
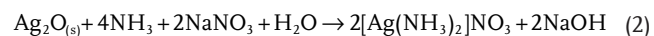
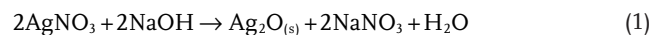


**Figure 1.** a) Schematic of the solution grown nanowire network fabrication process: (1) SCIL to produce a grid nanopattern in PMMA, (2) solution phase growth of Ag nanowires in the trenches defined by the template via the Tollens' reaction, (3) lift-off, and (4) RTA to smooth the nanowire surface. b) SEM images of a freshly grown nanowire network before RTA treatment, showing the confinement of the growth over a large area. c) XRD before RTA treatment of solution grown nanowire network measured in the range  $30^{\circ}$ – $90^{\circ}$  with the  $\theta$ – $2\theta$  configuration, showing the crystalline nature of the nanowire; inset: comparison of the (111) Ag reflection peak for solution grown and evaporated silver, indicating the larger average grain size in the former.

reaction,<sup>[32]</sup> causes the formation of silver nanocrystals when a sugar with an aldehyde group, such as glucose, is present in a solution containing diamminesilver(I) complexes (see Equation (1)–(3))



Nanocrystals preferentially form at the substrate surface due to the lower nucleation barrier. Some partial nucleation occurs also on the PMMA template surface, at a much lower rate compared to that at the glass substrate. This allows for successful lift-off on the entire sample because the nanowires growing in the trenches and nanoparticles nucleating on the template are physically separated. The SCIL stamp contained several fields with different nanowire width and pitch, each field having a total size of  $2 \times 2 \text{ mm}^2$ .

Figure 1b shows scanning electron microscope (SEM) images of a solution grown nanowire network after lift-off. The images show the confined growth of silver only on the exposed glass surface, and indicate the continuity of the network over a large area. A dark-field optical image of the network is displayed in Figure S1 (Supporting Information). High-magnification SEM images are shown in Figure S2 (Supporting Information). The surface texture of the silver nanogrid suggests that nucleation takes place at many different positions in the trench on the substrate surface, followed by growth of individual nanocrystals until merging with neighbors. As a result, a continuous network of crystalline silver is formed. The X-ray diffraction (XRD) pattern presented in Figure 1c shows the characteristic reflection peaks of crystalline silver with no secondary phases.

The average Ag grain size for the solution-grown nanowires, estimated from the X-ray diffraction peak width using the Scherrer equation (see the Supporting Information), is  $\approx 60 \text{ nm}$  (inset in Figure 1c). X-ray diffraction peak width measurements were also performed on silver evaporated using the method described in ref. [16], and show a silver grain size of  $\approx 15 \text{ nm}$ .

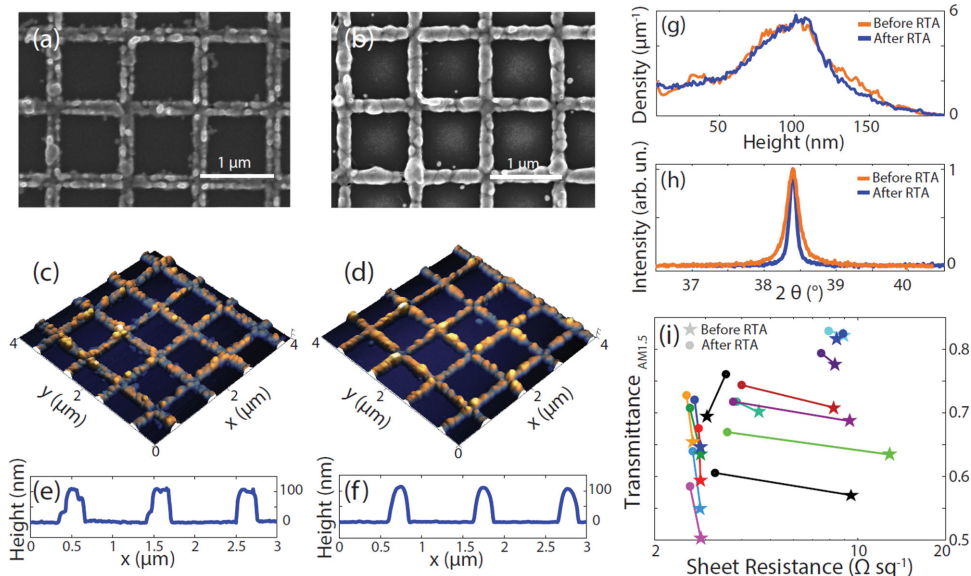


**Figure 2.** a–d) SEM and AFM images of solution grown nanowire networks samples a,c) before and b,d) after RTA; the aspect ratio of AFM images is 1. e,f) Cross-cuts of the AFM map of (c) and (d), respectively. g) Probability density function of the height distribution computed from (c) and (d), showing a slightly narrower peak after RTA annealing, as a result of smoothing and homogenization of the nanowires. h) XRD of solution grown nanowire networks before and after RTA, showing a narrower (111) silver reflection peak as a result of the larger average grain size due to RTA. i) Evolution of the optical /electrical performance of solution grown nanowire networks of various height, as a result of RTA; star and circle markers indicate the sample before and after RTA, respectively.

Clearly, the solution-growth method leads to larger Ag grains and thus a smaller density of grain boundaries.

The surface topography of the solution-grown silver nanowire networks was characterized by atomic force microscopy (AFM) on a  $100 \mu\text{m}^2$  area (Figure S3a, Supporting Information). The average height across a Ag nanowire network is shown in Figure S3b (Supporting Information), indicating for this particular sample a typical nanowire height of 30–40 nm. The nanowire height can be controlled by adjusting the growth time.

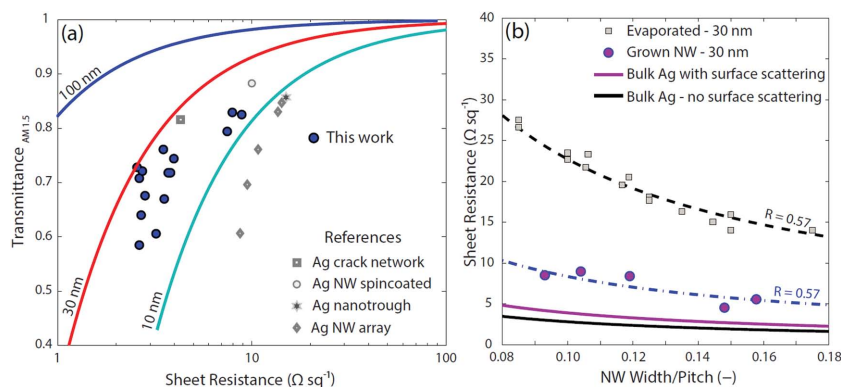
Because of the formation process, i.e., random nucleation and growth, the surface of as grown nanowire networks is rough. This causes strong scattering and absorption of light, which limits optical transmittance and therefore reduces performance. It has been shown that solution synthesized silver nanowires can be plasmonically welded by RTA,<sup>[18]</sup> at temperatures below the melting point of silver, preserving the nanowire shape. High intensity broad-band light is absorbed by the metal nanowires, causing heating; silver atoms become highly mobile well below the melting point,<sup>[18]</sup> and diffuse to minimize the surface to volume ratio. Furthermore, the electromagnetic field can be locally enhanced due to roughness, resulting in hot spots that create additional heating where the surface is rougher. This effectively contributes to the reduction of the surface to volume ratio, therefore leading to a smoother surface. Following this paradigm we performed RTA on solution grown nanowire.

Figure 2a–d compares SEM and AFM images of solution grown nanowire networks before and after 7 s of RTA. The difference in surface texture observed in the figure, indicates a smoothing of the nanowires as a result of RTA. Cross-cuts of AFM data show that indeed after RTA, the nanowires display a rounded cross-section compared to as grown nanowires

(Figure 2e,f), and become smoother. Statistical analysis of the entire AFM scan was performed, by computing the probability density function of the nanowire height distribution. This allows us to investigate trends representative of a larger area. Figure 2g compares the height distribution of the nanowires before (orange) and after (blue) RTA. It shows that after RTA the distribution is slightly narrower, indicating that the nanowires become more uniform in height. Figure 2h compares XRD data of the (111) silver peak before (orange) and after RTA (blue). It shows that a narrower peak is obtained after RTA, corresponding to an average grain size of  $\approx 200$  nm, calculated using the Scherrer equation. Considering the relatively low temperature achieved during the process,<sup>[18]</sup> which is expected to be well below the melting point ( $T_{\text{mp}}$ ) of silver, we exclude melting of the nanowires followed by solidification to achieve recrystallization with larger grains. This increase in average grain size can however be explained in terms of gain of interfacial free energy as a result of grain boundary migration, which has been reported to occur at temperatures as small as  $0.2 T_{\text{mp}}$  in metals.<sup>[33]</sup>

We next characterized electrical and optical response of RTA-processed solution-grown nanowire networks. This is presented in Figure 2i, which compares performance before RTA (star) and after RTA (circle), for networks of various height, pitch and width. The performance of the networks improves upon RTA processing, independent of the array geometry. The transmittance ( $T$ ) of the network improves significantly, up to 10% absolute. Furthermore, an improvement of sheet resistance ( $R_{\text{sh}}$ ) is observed as well in almost every sample, due to the enlargement of the average grain size and the concurrent homogenizations of the nanowire height distribution.

Having demonstrated the efficacy of RTA to improve the performance of solution grown nanowire networks, we summarize



**Figure 3.** a) Optical versus electrical performance of solution grown nanowire networks, represented by blue solid markers, for different nanowire width, height, and pitch of the array. The performance of Ag nanowire array,<sup>[14]</sup> Ag nanotrough,<sup>[20]</sup> Ag crack network,<sup>[17]</sup> Ag nanowire spincoated,<sup>[19]</sup> is reported for comparison after weighting for the AM 1.5 spectrum; solid lines represent the performance of ideal nanowire grids of different thicknesses. b) Sheet resistance of 30 nm thin nanowire grids as a function of nanowire width/pitch, according to the Mayadas–Shatzkes model described in Equation (S2f) (Supporting Information), that accounts for electron scattering at the surface and by grain boundaries, with a  $p = 0.5$  specularly parameter and  $R = 0.57$  reflection coefficient; the average grain size employed in the model was calculated from XRD measurements and corresponds to 15 nm for evaporated (black dashed line) and 60 nm for solution grown nanowire networks (blue dashed line); the solid curve represent the sheet resistance of a defect-free nanowire grid, accounting for surface scattering ( $p = 0.5$ , magenta curve) and assuming values for bulk materials ( $p = 1$ , black curve); data points represent measured sheet resistance of solution-grown (magenta dots) and of evaporated nanowire networks (gray squares) with a thickness of 30 nm; the smaller sheet resistance measured for solution-grown networks compared to evaporated networks is due to the larger average grain size in the former (60 nm vs 15 nm); this is accurately described by the Mayadas–Shatzkes model.

in **Figure 3a** optical transmission and sheet resistance measurements of best performing samples. The solid blue points represent solution-grown nanowire networks with different nanowire widths in the range 90–180 nm, periodicities of 800, 900, and 1000 nm and heights in the range 30–100 nm. The transmittance data were calculated by weighting the transmission spectra over the photon density in the AM1.5 spectrum (see Figure S4, Supporting Information, for transmission spectra), and normalized to the transmission of a bare, flat substrate (see Figure S5, Supporting Information, for an example of a haze measurement). We note that the transmittance derived this way is underestimated, as this analysis does not take into account light coupled into guided modes in the substrate (see ref. [16]); such scattered and trapped light does contribute to power generation in a photovoltaic device. The sheet resistance was obtained from four-point-probe measurements.

As reference, the lines drawn in **Figure 3a** represent the calculated performance for defect-free metal nanowire grids of three different thicknesses based on a simple geometrical transmission model. The curves are obtained by varying the nanowire width to pitch ratio. The calculated transmittance accounts for both transmission through the voids and transmission through the metal (this is important for thin films). The transmittance is weighted for the AM1.5 spectrum. While no plasmonic effects are included in the calculation, this simple model accurately represents experimental transmittance data (see Figure S6 in the Supporting Information), which we attribute to the fact that the relatively narrow resonances only have a small effect on the average broadband response. The

sheet resistance accounts for electron scattering at the surface but assumes no grain boundaries, and was calculated by employing the Mayadas and Shatzkes model<sup>[34]</sup> (see the Supporting Information). The curves show the typical trade-off between  $T$  and  $R_{sh}$ , which can be accurately controlled by varying pitch, width, and thickness of the nanowire networks.

Next, the performance of our solution-grown nanowire networks is compared to that of nanowire-based transparent electrodes fabricated in other ways reported in the literature; the data are shown for reference in **Figure 3a**. We find superior performance for the solution-grown networks compared to the same nanowire networks obtained by metal evaporation (gray diamonds).<sup>[16]</sup> Ag crack networks are obtained by metal evaporation on a cracked gel film template;<sup>[19]</sup> Ag nanotroughs are obtained by metal evaporation on suspended electrospun fibers;<sup>[22]</sup> spincoated Ag nanowires are obtained by spincoating Ag nanowires prepared in solution with the polyol process.<sup>[21]</sup> This shows that our solution grown nanowire networks have outstanding performance. Note that the values reported for the reference networks were calculated by applying the AM1.5 weighting function to the wavelength dependent trans-

mittance data available in the references. Also, all data in **Figure 3a** are referenced to the transmission of a glass substrate; this results in absolute 8% overestimation of the transmittance.

We chose not to overlay in **Figure 3a** the widely used figure of merit (defined as the ratio between DC conductivity to optical conductivity)<sup>[8,17,19,20,28]</sup> because it is not applicable in the optical frequency regime studied here, and it is only true for the limiting case where optical and DC conductivity are equal (see the Supporting Information for a more detailed explanation). Furthermore, the relative performance of transparent electrodes having different geometry,  $T$  and  $R_{sh}$  strongly depends on the technological application.<sup>[35]</sup> Using a single number (or figure of merit) to compare unconditionally transparent electrodes can be highly deceiving, as this number can be made arbitrarily large (see the Supporting Information for a practical example).

In order to understand the superior performance of solution deposited Ag nanowire compared to those made by evaporation, we employed the model developed by Mayadas and Shatzkes,<sup>[34]</sup> which describes the relation between conductivity of nanoscale metallic films and electron scattering at grain boundaries and at the surface (see Equation (S2), Supporting Information). The sheet resistance of solution-grown nanowire networks and evaporated networks (both with a thickness of 30 nm) is reported in **Figure 3b** as a function of the ratio between the nanowire width and the pitch of the array, showing the trend that larger filling fractions correspond to smaller sheet resistances. It also shows that for a fixed nanowire width/pitch ratio, the conductivity of solution grown nanowire networks is on average 2.5 times better than that of evaporated networks.

Figure 3b shows the modeled sheet resistance of the grid calculated from Equation (S2f) (Supporting Information), for 60 nm grain size (dashed blue line) and 15 nm grain size (dashed black line), in accordance with the average grain size obtained from XRD data (Figure 1c). The excellent match between the model and experimental data for solution processed and evaporated films, indicates that the larger conductivity of the solution processed wires originates from the larger grain size. Note that the data reported in Figure 3b for solution-grown nanowire networks were measured before RTA processing. Using the same grain boundary and surface scattering model parameters (see the Supporting Information for full description), we could achieve good fits to the experimental data for both solution-grown and evaporated nanowire networks simply by inputting the grain size calculated from XRD. The calculated sheet resistance of the same silver nanowire grid without grain boundary scattering (i.e., monocrystalline Ag) is also given in Figure 3b for comparison, both with and without surface scattering contributions (magenta and black solid lines, respectively). This shows that our solution grown nanowire networks are less than a factor of 2 from the sheet resistance expected from a defect-free grid. Detailed characterization of the nanowire networks thus indicates that solution deposition methods can match or even exceed the material quality of vacuum-based deposition, in stark contrast to the conventional wisdom in the field.

We demonstrate high-quality silver nanowire networks fabricated by a combination of soft-imprint lithography and soft-solution processing (Tollens' reaction). This relatively simple method yields ordered metal nanowire grids as transparent electrodes, without the need for energy intensive vacuum metal evaporation processes. We show that the solution process, combined with a short RTA treatment, yields superior performance compared to the thermally evaporated networks. This important result shows that solution-based methods can lead to material quality comparable or even superior to vacuum-based deposition methods, in contrast with common assumptions. We demonstrate that the lower material resistance is due to the larger average grain size, which decreases electron scattering from grain boundaries. The simplicity of this solution approach can be extended to other types of template-assisted metal nanowire network transparent electrodes, thus providing a general pathway for further improvement of transparent conductor performance at low cost.

## Supporting Information

Supporting Information is available from the Wiley Online Library or from the author.

## Acknowledgements

The authors gratefully acknowledge Dr. Wim Noorduyn for careful reading of the manuscript, Sander Mann for his help with haze measurements, and Henk-Jan Boluijt for the ToC schematic. The work at AMOLF is part of the research program of the "Stichting voor Fundamenteel Onderzoek der Materie (FOM)," which is financially supported by the "Nederlandse Organisatie voor Wetenschappelijk Onderzoek (NWO)." The research leading to these results received funding from the European Research Council under the European Union's Seventh Framework Programme

(FP/2007–2013)/ERC Grant Agreement no. 337328, "NanoEnabledPV" and no. 267634, "Plasmeta".

Received: August 19, 2015

Revised: September 28, 2015

Published online: December 3, 2015

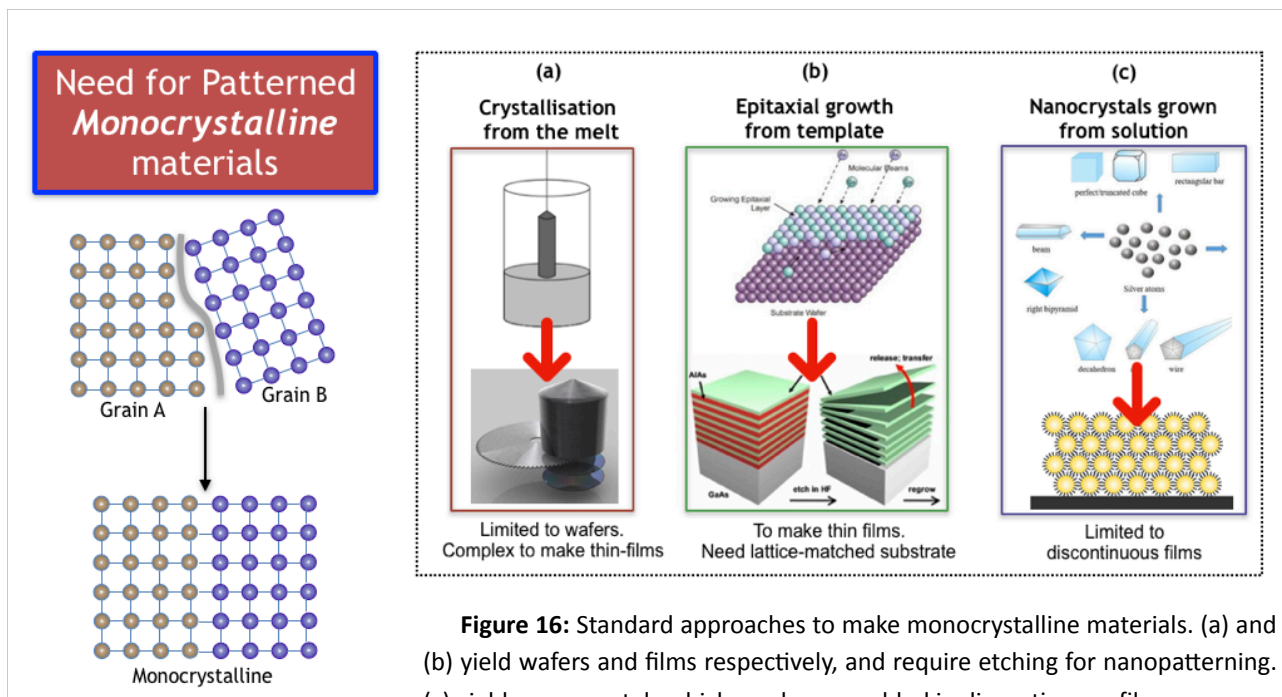
- [1] K. Ellmer, *Nat. Photonics* **2012**, *6*, 808.
- [2] E. Fortunato, P. Barquinha, R. Martins, *Adv. Mater.* **2012**, *24*, 2945.
- [3] K. Ghaffarzadeh, R. Das, *Transparent Conductive Films (TCF) 2015–2025: Forecasts, Markets, Technologies (IDTechEx)* June, **2015**.
- [4] D. S. Hecht, L. B. Hu, G. Irvin, *Adv. Mater.* **2011**, *23*, 1482.
- [5] S. R. Ye, A. R. Rathmell, Z. F. Chen, I. E. Stewart, B. J. Wiley, *Adv. Mater.* **2014**, *26*, 6670.
- [6] Q. Cao, S. H. Hur, Z. T. Zhu, Y. G. Sun, C. J. Wang, M. A. Meitl, M. Shim, J. A. Rogers, *Adv. Mater.* **2006**, *18*, 304.
- [7] Z. C. Wu, Z. H. Chen, X. Du, J. M. Logan, J. Sippel, M. Nikolou, K. Kamaras, J. R. Reynolds, D. B. Tanner, A. F. Hebard, A. G. Rinzler, *Science* **2004**, *305*, 1273.
- [8] L. Hu, D. S. Hecht, G. Gruner, *Nano Lett.* **2004**, *4*, 2513.
- [9] S. I. Na, S. S. Kim, J. Jo, D. Y. Kim, *Adv. Mater.* **2008**, *20*, 4061.
- [10] A. A. Argun, A. Cirpan, J. R. Reynolds, *Adv. Mater.* **2003**, *15*, 1338.
- [11] K. Tvingstedt, O. Inganas, *Adv. Mater.* **2007**, *19*, 2893.
- [12] T. C. Gao, B. M. Wang, B. Ding, J. K. Lee, P. W. Leu, *Nano Lett.* **2014**, *14*, 3694.
- [13] P. C. Hsu, S. Wang, H. Wu, V. K. Narasimhan, D. Kong, H. R. Lee, Y. Cui, *Nat. Commun.* **2013**, *4*, 2522.
- [14] G. Eda, G. Fanchini, M. Chhowalla, *Nat. Nanotechnol.* **2008**, *3*, 270.
- [15] K. S. Kim, Y. Zhao, H. Jang, S. Y. Lee, J. M. Kim, K. S. Kim, J. H. Ahn, P. Kim, J. Y. Choi, B. H. Hong, *Nature* **2009**, *457*, 706.
- [16] J. van de Groep, D. Gupta, M. A. Verschuuren, M. M. Wienk, R. A. Janssen, A. Polman, *Sci. Rep.* **2015**, *5*, 11414.
- [17] J. V. van de Groep, P. Spinelli, A. Polman, *Nano Lett.* **2012**, *12*, 3138.
- [18] E. C. Garnett, W. S. Cai, J. J. Cha, F. Mahmood, S. T. Connor, M. G. Christoforo, Y. Cui, M. D. McGehee, M. L. Brongersma, *Nat. Mater.* **2012**, *11*, 241.
- [19] B. Han, K. Pei, Y. L. Huang, X. J. Zhang, Q. K. Rong, Q. G. Lin, Y. F. Guo, T. Y. Sun, C. F. Guo, D. Carnahan, M. Giersig, Y. Wang, J. W. Gao, Z. F. Ren, K. Kempa, *Adv. Mater.* **2014**, *26*, 873.
- [20] L. B. Hu, H. Wu, Y. Cui, *MRS Bull.* **2011**, *36*, 760.
- [21] D. S. Leem, A. Edwards, M. Faist, J. Nelson, D. D. C. Bradley, J. C. de Mello, *Adv. Mater.* **2011**, *23*, 4371.
- [22] H. Wu, D. S. Kong, Z. C. Ruan, P. C. Hsu, S. Wang, Z. F. Yu, T. J. Carney, L. B. Hu, S. H. Fan, Y. Cui, *Nat. Nanotechnol.* **2013**, *8*, 421.
- [23] P. B. Catrysse, S. H. Fan, *Nano Lett.* **2010**, *10*, 2944.
- [24] J. Y. Lee, S. T. Connor, Y. Cui, P. Peumans, *Nano Lett.* **2008**, *8*, 689.
- [25] K. Critchley, B. P. Khanal, M. L. Gorzny, L. Vigderman, S. D. Evans, E. R. Zubarev, N. A. Kotov, *Adv. Mater.* **2010**, *22*, 2338.
- [26] P. C. Hsu, D. S. Kong, S. Wang, H. T. Wang, A. J. Welch, H. Wu, Y. Cui, *J. Am. Chem. Soc.* **2014**, *136*, 10593.
- [27] H. Wu, L. B. Hu, M. W. Rowell, D. S. Kong, J. J. Cha, J. R. McDonough, J. Zhu, Y. A. Yang, M. D. McGehee, Y. Cui, *Nano Lett.* **2010**, *10*, 4242.
- [28] S. De, T. M. Higgins, P. E. Lyons, E. M. Doherty, P. N. Nirmalraj, W. J. Blau, J. J. Boland, J. N. Coleman, *ACS Nano* **2009**, *3*, 1767.
- [29] L. B. Hu, H. S. Kim, J. Y. Lee, P. Peumans, Y. Cui, *ACS Nano* **2010**, *4*, 2955.
- [30] M. G. Kang, L. J. Guo, *Adv. Mater.* **2007**, *19*, 1391.
- [31] F. Afshinmanesh, A. G. Curto, K. M. Milaninia, N. F. van Hulst, M. L. Brongersma, *Nano Lett.* **2014**, *14*, 5068.
- [32] B. Z. Shakhshiri, *Chemical Demonstrations: A Handbook for Teachers of Chemistry*, Vol. 4, The University of Wisconsin Press, Madison, WI, USA, **1992**.
- [33] C. V. Thompson, *Annu. Rev. Mater. Sci.* **1990**, *20*, 245.
- [34] A. F. Mayadas, M. Shatzkes, *Phys. Rev. B* **1970**, *1*, 1382.
- [35] M. W. Rowell, M. D. McGehee, *Energy Environ. Sci.* **2011**, *4*, 131.

# CHAPTER 3: NANOCUBE EPITAXY FOR MONOCRYSTALLINE NANOSTRUCTURED MATERIALS

## 3.1 Ag Nanocube epitaxy

The realisation of nanostructured monocrystalline materials is a complex and energy intensive process that faces some constraints (Figure 16). The general methodology to obtain them is a (top-down) two-steps process in which a monocrystalline thin film is grown and then is nanopatterned. High quality monocrystalline thin films with precise thickness control are typically obtained via epitaxial growth on a monocrystalline carrier substrate with the same crystal lattice parameter<sup>79</sup>; nanopatterning is obtained via optical/nanoimprint lithography and etching, enabling for the realisation of nanoscale features with unprecedented resolution, thanks to cutting edge innovation in the semiconductor industry.

Although this seems an approach to achieve monocrystalline nanopatterns that is general in terms of materials and nanoscale geometry, in practice there are fundamental constraints that hamper its viability in the fabrication of devices, which are composed by many metal and semiconducting layers. Some of these constraints are related to lattice matching requirements, that strongly limit the materials that can be grown as monocrystalline in a monolithic device stack<sup>80</sup> and eventually nanopatterned. Techniques are available to obtain free-standing monocrystalline thin films by etching bulk single crystal wafers<sup>81</sup>, or by epitaxial lift-off via a sacrificial layer<sup>82</sup>, but are complex, time consuming or not cost-effective and mostly limited to  $\mu\text{m}$ -thick films. Van der Waals epitaxy can allow crystalline growth of 2D or even 3D materials on a 2D material host<sup>83</sup>, without need to satisfy lattice matching requirements, and with the potential to transfer the grown material to a new substrate; however growth is typically performed in vacuum conditions and/or at high temperature, and control over the geometry is limited. In addition, nanopatterning introduces surface damage, removes most of the expensively grown material and can also damage other layers of the



device. Techniques such as template stripping are successful in obtaining ultrasmooth nanopatterned metal films, which are however polycrystalline.

In synthetic chemistry, enormous advances enabled remarkable control over size, shape and chemical composition of high-quality nanoscale materials that readily self-assemble in 1D, 2D or 3D structures and superlattices<sup>84,85</sup>. This can yield mesocrystals upon oriented attachment<sup>86</sup> and epitaxy, resulting in the formation of monocrystalline 1D/2D architectures, films and even multilayers<sup>87</sup>. Unfortunately, these methods lack control over the final macroscopic geometry and of the nanoscale pattern, in some case require calcination at high temperature to desorb capping ligands prior to epitaxy, are limited to ultrathin (<10nm) films<sup>88</sup>, or yield discontinuous nanoparticle assembly. This strongly limits the potential for integration in efficient functional devices, and may not be compatible with soft substrates.

I therefore studied and developed a fundamentally new paradigm to make monocrystalline nanopatterns, which removes the dependence on substrate epitaxy and instead relies on epitaxy between monocrystalline nanocube building blocks<sup>89</sup>. Nanocubes have the advantages of being the perfect building blocks, since (i) they are single-crystalline, (ii) they readily self-assemble in closely packed lattices due to the geometry via the strong van der Waals interaction between nanocubes facets, and (iii) when closely packed they all share the same crystallographic orientation since they are capped by six (100) facets, resembling to a discontinuous monocrystalline material. The nanocubes are assembled in a predefined pattern and then epitaxially connected at the atomic level by chemical growth in solution, to form monocrystalline nanopatterns on arbitrary substrates. The entire process is presented in Figure 17. The nanowire shape was chosen because it provides a simple platform for measuring conductivity and optical properties, but this new approach to make monocrystalline materials is not limited to nanowire shapes. Instead it is compatible with arbitrary nanoscale patterns that can be assembled in polydimethylsiloxane (PDMS), as has been previously demonstrated in the literature. After assembly in straight lines via capillary assembly, the nanocubes were printed to a receiving substrate (Si for SEM inspection, a Si<sub>3</sub>N<sub>4</sub> membrane for TEM characterisation, and SiO<sub>2</sub> for electrical characterisation). After printing

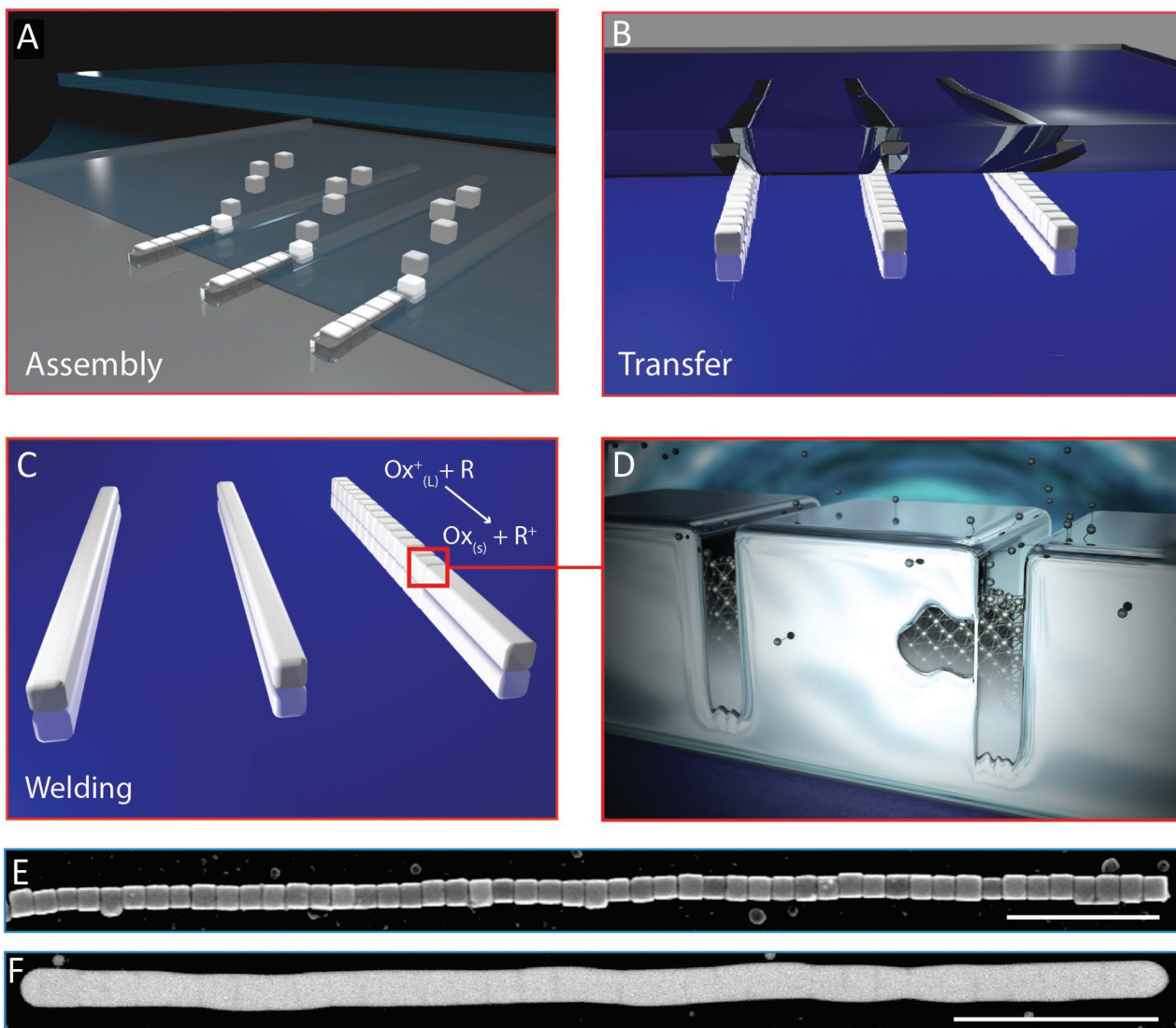


**Figure 17:** Cartoon of Ag nanocube assembly and epitaxy process (A-D). SEM images of Ag nanocubes before welding (E) and after welding (F).

the ligands (mainly PVP) present at the nanocube surface were stripped by washing in  $NaBH_4$ <sup>90</sup>. Chemical welding was then obtained by exposing the pristine nanocubes to a solution consisting of an aqueous diamminesilver(I) complex with glucose as the reducing reagent. This led to nucleation and epitaxial growth of silver on the nanocube surface. As a result of the identical crystallographic orientation, filling of the sub-1 nm gap between adjacent nanocubes resulted in the formation of a continuous monocrystalline material. This was assessed by high resolution TEM characterisation and electron diffraction (Figure 18). The electrical properties were analysed by applying four electrical contacts on monocrystalline nanowires 8-10  $\mu m$  long obtained from epitaxy of  $\sim 100-150$  Ag nanocubes. This measurements showed an ohmic behaviour with an intrinsic resistivity of  $2 \times 10^{-8} \Omega m$  that is only 10% higher than that of bulk silver ( $1.8 \times 10^{-8} \Omega m$  if surface scattering is taken into account).

It worth emphasising that this process has the potential to work on any substrate since it does not interfere in the homoepitaxial growth between the cubes. This is a general pathway to achieve nanocube epitaxy at low temperature, as opposed to thermal welding, or plasmonic welding<sup>78</sup> which is specific for materials supporting plasmon resonances.

These results opened a new pathway towards the realisation of monocrystalline nanopatterns. Nevertheless, open questions remained on the possibility to generalise this approach for other materials, and on the feasibility to integrate such monocrystalline nanopatterns on any substrate. Further work in these directions is presented in the next section.

## 3.2 Au Nanocube epitaxy

Epitaxy of gold nanocubes was studied to test the hypothesis that the approach proposed can be generalised to other materials. In addition, it appeared important to demonstrate the possibility to print monocrystalline nanoantenna arrays by-design to any substrate, and to improve control of the nanostructure geometry, that for colloidal synthesis is mostly limited to that of Platonic solids. This is in stark contrast to nanostructures obtained by top-down methods, that offer unlimited capability for plasmon resonance engineering, but present poor material quality and have doubtful perspectives for scalability. Gold was chosen as a candidate because of its relevance in plasmonics applications and because the absence of oxide layers enable a detailed study on the mechanism leading to epitaxy.

Monodisperse gold nanocubes were synthesised following a procedure earlier reported in literature<sup>91</sup>. The solutions are highly monodisperse, and when dropcasted on a substrate nanocubes self-assemble face-to-face in a 2D closed-packed configuration, separated by a layer of adsorbed ligands ( $0.4 \pm 0.1$  nm) residual from the synthesis.

After deposition, nanocubes are extensively washed with solvents and sodium borohydride ( $\text{NaBH}_4$ ) to remove the ligands (see experimental section) and obtain pristine surfaces separated by sub-nanometer gaps. This constitutes an ideal platform to study nanocube epitaxy, as the product can swiftly be characterized with scanning electron microscopy (SEM). If exposed to a solution containing a gold precursor ( $\text{HAuCl}_4$ ) and a weak reductant (ascorbic acid), adjacent nanocubes grow and merge, producing continuous gold nanostructures. Unfortunately, reduction of  $\text{AuCl}_4^-$  in the bulk of the solution leads to homogeneous nucleation, causing contamination of the sample with small nanocrystals and inefficient use of reactants. We therefore explored the opportunity to achieve nanocube epitaxy in the absence of a reducing agent. This requires that the chemical reactions involved takes place at the nanocube surface only (Figure 19). It was found that by accurately designing the epitaxy chemistry, competitive redox processes of oxidative etching at the nanocube corners and simultaneous heterogeneous nucleation at their surface can be

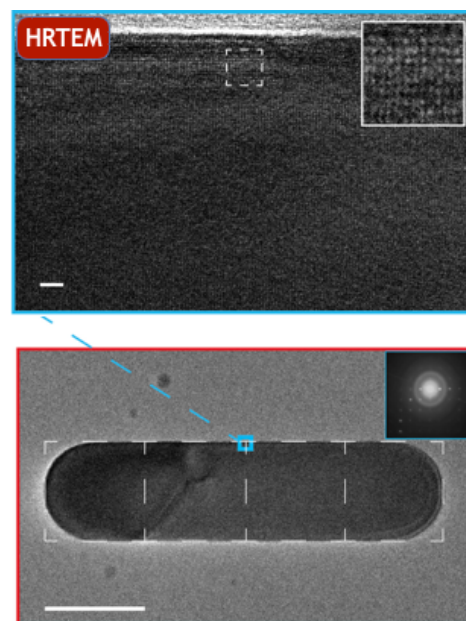


**Figure 18:** TEM image of a Ag nanowire obtained via nanocube epitaxy.

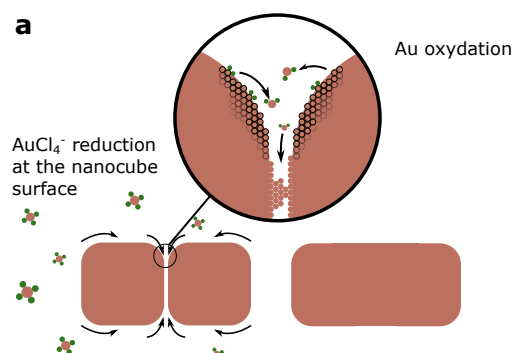


**Figure 19:** Au nanocube epitaxy redox-approach.

used to fill the sub-nanometer gap in a self-limited manner. Tuning the concentration of the gold precursor ( $\text{HAuCl}_4$ ) and the temperature was sufficient to achieve epitaxy. The radius of curvature increases after epitaxy, which is attributed to oxidative etching of the nanocube corners, and it is amplified as the  $\text{HAuCl}_4$  concentration increases or when  $\text{Cl}^-$  ions are added to the solution. Besides preventing homogeneous nucleation and avoiding sample contamination with small nanocrystals, we found that this strategy is robust, as it leads to successful welding over a wide range of  $\text{HAuCl}_4$  concentration (1  $\mu\text{M}$  - 10 mM), reaction temperature (room temperature (RT) - 80°C) and pH, with a time scale from less than a second to a few minutes, despite the fact that no reductant is introduced in the solution (Figure 20).

The mechanism was studied with *operando* spectroscopy. Dimer nanoreactors were taken as the simplest model for studying epitaxy *operando*, because the change in the spectral signature as welding takes place can be swiftly be modelled with numerical simulations. In fact, the strong light confinement in plasmonic nanoparticle systems allows extraordinary sensitivity to their geometry and their environment. Compared to other *operando* techniques, such as liquid-phase TEM, optical approaches ensure minimal perturbation, that is especially important to study redox chemical reactions.

Nanocube dimer arrays were assembled in a nanostructured PDMS mold with capillary assembly techniques. The sample was inspected with an inverted microscope equipped with a spectrometer. Figure 20e presents the kinetics of nanocube epitaxy, corresponding to the collective reflection of  $\sim 40$  dimers nanoreactors supported on PDMS, starting from the exposure to the welding solution to complete epitaxy. The main features that can be evidenced in the kinetic response are illustrated in Figure 20f. At time  $t = 0$ , electron tunneling through the  $< 0.5$  nm gap enables a dipolar response of the entire dimer via a charge transfer plasmon mode. As welding takes place ( $t > 0$ ) new adatoms from the nanocube corners and from the solution slowly fill the nanogap, eventually establishing a bridge between the isolated nanocubes. As the bridge widens, electron tunneling is superseded by electron conduction through the lattice. As a consequence of the larger electron current in the gap, the scattering cross-section of the dipolar mode increases. This leads to an increase of the array reflectance in the far-field, as observed in Figure 20e,f. The blue-shift ( $\sim 25$  nm) of the dipolar mode is associated with the rounding of the nanocube corners (from  $r \sim 5$  nm to  $r \sim 9$  nm) and the increase in width (from  $w \sim 38$  nm to  $w \sim 43$  nm) during welding. These data are the signature of changes of the atomic arrangement inside a sub-nanometer gap with unprecedented resolution, and confirm that the processes of oxidation, growth and welding take place simultaneously.

Such monocrystalline nanophotonic surface can be transferred from PDMS to other substrates for integration in optoelectronic devices, or for further characterisation. Figure 20b, shows nanoantennas of different lengths deposited from PDMS to silicon. During this process, the PDMS stamp is pressed against a receiving substrate, and the nanostructures are released due to the larger adhesion forces. It is worth noticing that the bottom surface of the nanoantennas, initially in contact with PDMS, also exhibit a continuous, gap-free surface. The nanoantenna arrays were printed from PDMS to a  $\text{Si}_3\text{N}_4$  membrane for high-resolution TEM (HRTEM) characterization (see Appendix). This provided evidence (i) for a perfect crystallographic alignment of the two nanocubes at the time of assembly, (ii) for epitaxy between individual building blocks, and (iii) that the junction is filled in its entirety yielding gap-free monocrystalline nanostructures.

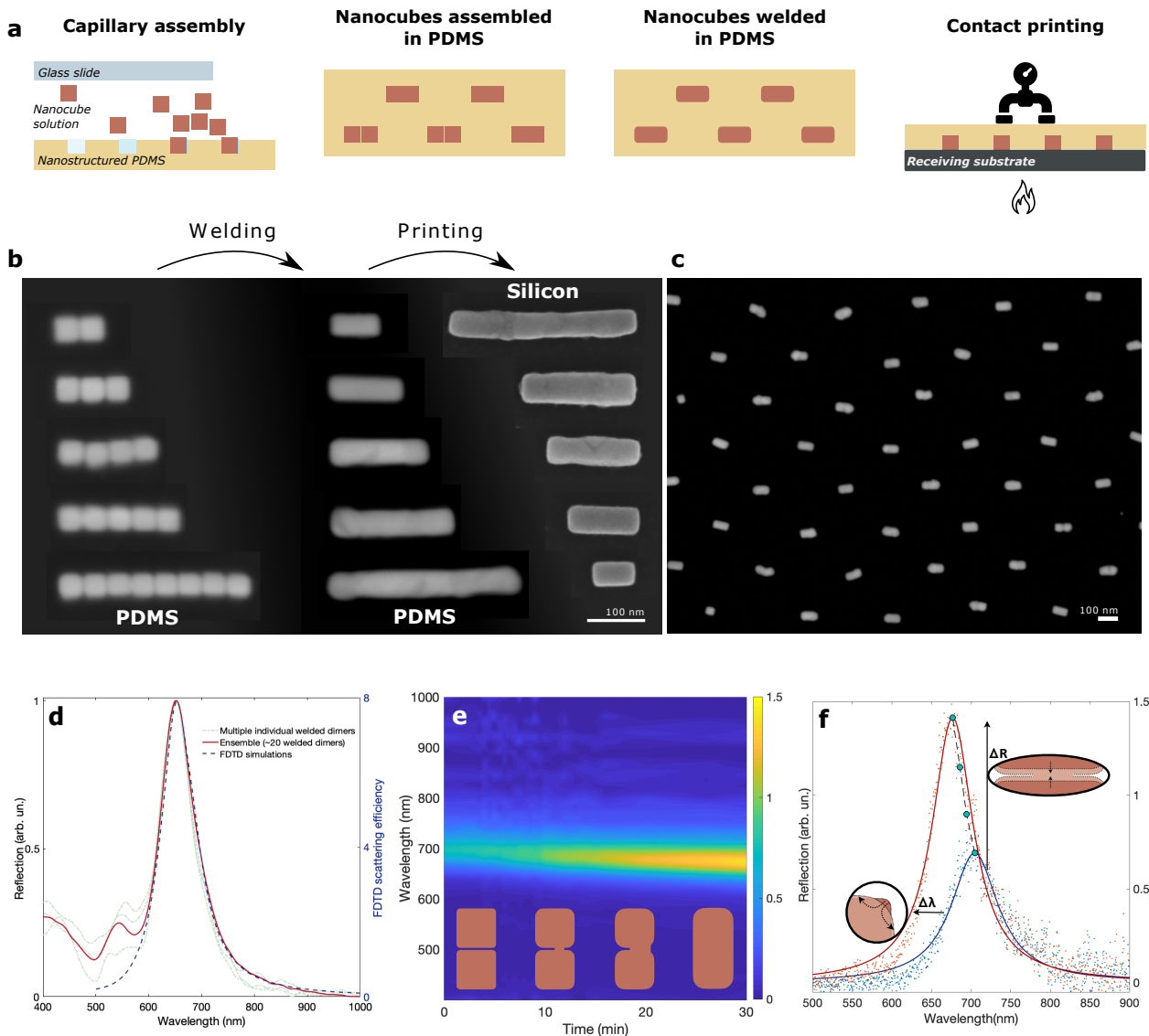


**Figure 20:** Realisation of monocrystalline printable nanophotonic surfaces via Au nanocube epitaxy. (a) Capillary assembly in nanopatterned PDMS, nanocube epitaxy in solution and printing of monocrystalline nanostructures to any substrate. (b) Collage of SEM images showing 38 nm gold nanocubes assembled into 1D nanostructures of arbitrary length in PDMS before nanocube epitaxy (left image), after nanocube epitaxy in PDMS (middle image) and after printing to a silicon substrate (right image). (c) SEM image of nanoantenna arrays on PDMS after nanocube epitaxy. (d) Optical response of multiple individual nanoantennas (dotted line) and nanoantenna array (solid line) supported on PDMS and FDTD simulations. (e) Nanocube epitaxy on a model system *operando*. (f) Data in panel (d) at the beginning ( $t = 0$  s) and at the end ( $t = 30$  min) of nanocube epitaxy, and the corresponding Lorentzian fits (solid lines). The scale bar in SEM images is 100 nm.

A series of control experiments allowed to identify the role of pH, temperature and Cl<sup>-</sup> concentration, suggesting that gold atoms effectively migrate from (111) and (110) facets to (100) facets (including the gap) via dissolution in the presence of Cl<sup>-</sup> ions and redeposition, as illustrated in Figure 21. This is in agreement with the interpretation of the optical characterization results. In addition it was found that water acts as mild reducing agent for AuCl<sub>4</sub> and enable nucleation of new Au adatoms at the nanocube surface.

The profound understanding of the mechanism allowed to gain control on the nanostructure morphology after epitaxy, and build a phase diagram of the process, as evidenced in Figure 21.

Unlike conventional nanofabrication techniques where the (polycrystalline) nanostructures are fabricated directly on the substrate, this work show that nanocube epitaxy can be

performed directly on PDMS and that (monocrystalline) plasmonic surfaces by-design can be printed to any substrate, unleashing from lattice matching requirements. This is highly promising for the integration of monocrystalline gold nanostructures, such as transparent electrodes or plasmonic scatterers, in devices that are sensitive to temperature, water or other nanofabrication processes, as for example perovskite solar cells.

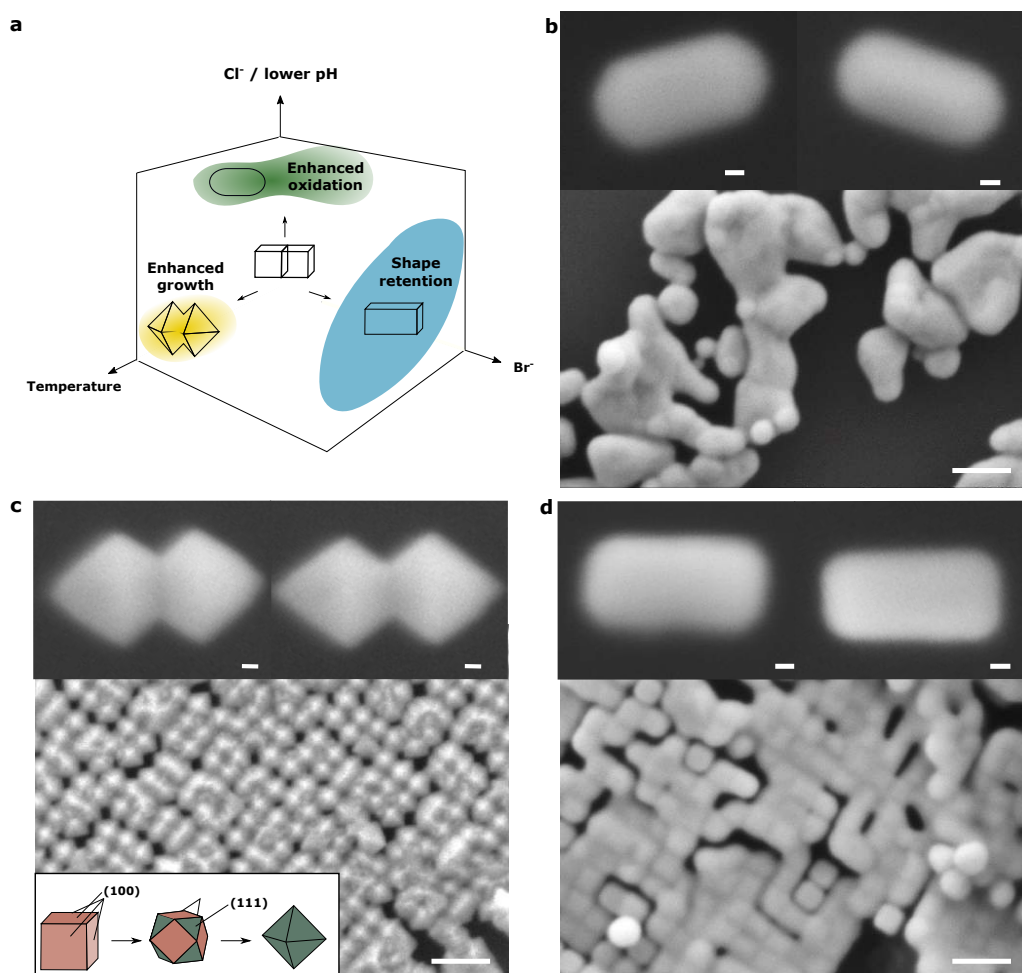


**Figure 21:** Control over the morphology during epitaxy via  $\text{Cl}^-/\text{pH}$  (b), reaction temperature (c) or  $\text{Br}^-$  (d). The scale bar is 100 nm in the main images and 10 nm in the insets.

# Monocrystalline Nanopatterns Made by Nanocube Assembly and Epitaxy

*Beniamino Sciacca, Annemarie Berkhout, Benjamin J. M. Brenny, Sebastian Z. Oener, Marijn A. van Huis, Albert Polman, and Erik C. Garnett\**

Monocrystalline materials are essential for optoelectronic devices such as solar cells, LEDs, lasers, and transistors to reach the highest performance. Advances in synthetic chemistry now allow for high quality monocrystalline nanomaterials to be grown at low temperature in solution for many materials; however, the realization of extended structures with control over the final 3D geometry still remains elusive. Here, a new paradigm is presented, which relies on epitaxy between monocrystalline nanocube building blocks. The nanocubes are assembled in a predefined pattern and then epitaxially connected at the atomic level by chemical growth in solution, to form monocrystalline nanopatterns on arbitrary substrates. As a first demonstration, it is shown that monocrystalline silver structures obtained with such a process have optical properties and conductivity comparable to single-crystalline silver. This flexible multiscale process may ultimately enable the implementation of monocrystalline materials in optoelectronic devices, raising performance to the ultimate limit.

The performance of optoelectronic, plasmonic, and nanophotonic devices depends ultimately on the quality of the materials employed; monocrystalline materials represent the best option to bring the capabilities of such devices to the limit.<sup>[1–5]</sup> Epitaxy from a lattice-matched substrate or seeded growth from the melt are the main strategies that are routinely employed to make continuous monocrystalline materials with an arbitrary geometry. These approaches require high vacuum, high temperature, or both, constraining the range of materials and device geometries that can be practically achieved.<sup>[6]</sup> This calls for a more general approach to widen substantially the toolbox

of monocrystalline materials available to be employed in devices.

Advances in synthetic chemistry now allow for high-quality monocrystalline nanomaterials at low temperature via solution processing techniques such as colloidal synthesis and oriented attachment, for a multitude of metals, semiconductors, and insulators.<sup>[7–13]</sup> However, such bottom-up techniques offer limited possibilities to achieve extended structures with control over the final 3D geometry, restricting the use of high quality nanomaterials to niche applications. Here, we present a fundamentally new paradigm to make monocrystalline nanopatterns, which removes the dependence on substrate epitaxy and instead relies on epitaxy between monocrystalline nanocube building blocks. The nanocubes are assembled in a predefined pattern and then epitaxially

connected at the atomic level by chemical growth in solution, to form monocrystalline nanopatterns on arbitrary substrates. As a first demonstration, we show that monocrystalline silver structures obtained with such a process have optical properties and conductivity comparable to single-crystalline silver.

The nanowire shape was chosen because it provides a simple platform for measuring conductivity and optical properties, but our new approach to make monocrystalline materials is not limited to nanowire shapes. Instead it is compatible with arbitrary nanoscale patterns that can be assembled in polydimethylsiloxane (PDMS), as has been previously demonstrated in the literature.<sup>[14]</sup> We chose to use silver for this proof of concept study because it is one of the most studied materials for making monodispersed nanocubes and also has direct implications in the fields of plasmonics, nanophotonics, and optoelectronics. Furthermore, it has many chemical similarities to other metals such as copper, which is extremely important in the microelectronics industry. Semiconductors and dielectrics will certainly be more challenging to realize, but in principle can also be made with this process for materials that can be synthesized colloiddally as nanocubes. In that case, this flexible multiscale process could be implemented for monocrystalline materials in optoelectronic devices, raising performance to the ultimate limit.

Figure 1 gives an overview of the process we have developed to make monocrystalline nanopatterns. First, monocrystalline nanocubes are synthesized in solution, purified, and

Dr. B. Sciacca, A. Berkhout, Dr. B. J. M. Brenny, Dr. S. Z. Oener,  
Prof. A. Polman, Dr. E. C. Garnett  
Center for Nanophotonics  
AMOLF Science Park 104, 1098 XG, Amsterdam, The Netherlands  
E-mail: garnett@amolf.nl

Prof. M. A. van Huis  
Debye Institute for Nanomaterials Science  
Utrecht University  
Princetonplein 5, 3584 CC, Utrecht, The Netherlands

Prof. M. A. van Huis  
NCHREM  
Kavli Institute of Nanoscience  
Delft University of Technology  
Lorentzweg 1, 2628 CJ, Delft, The Netherlands

DOI: 10.1002/adma.201701064

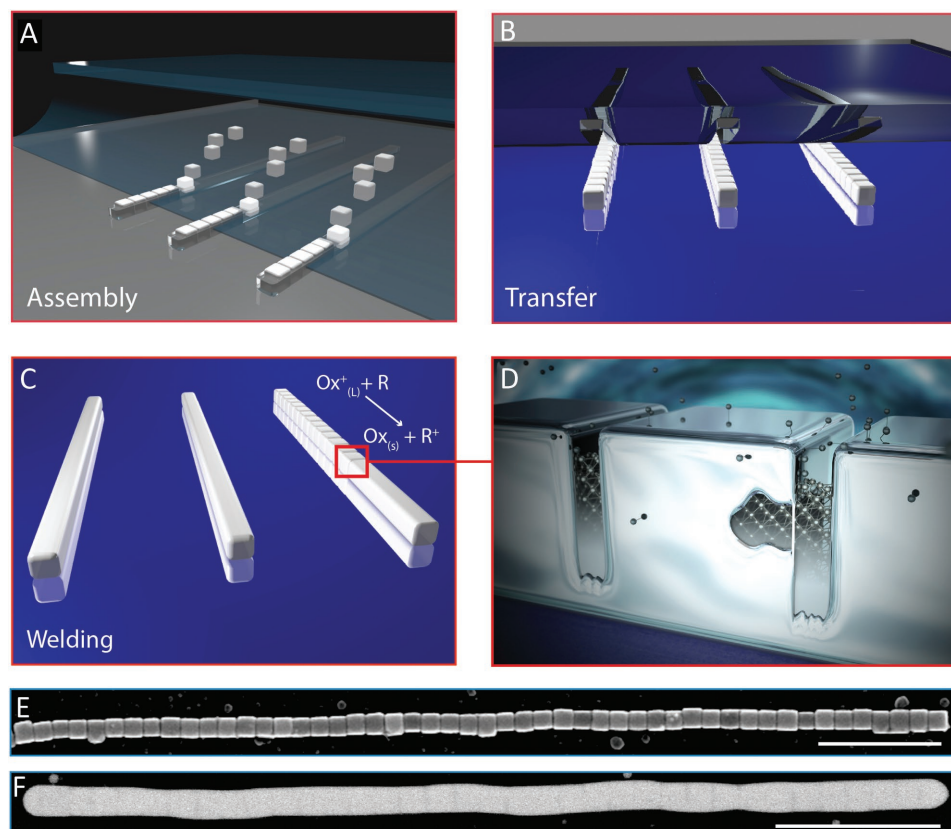


**Figure 1.** Diagram of the process presented. A) Direct assembly from solution of nanocubes into trenches patterned in a PDMS mold. B) Transfer of the assembled nanocubes to a new substrate. C) Epitaxial welding of the nanocubes into a patterned monocrystalline material via solution processing. D) Artistic representation of the epitaxial nanowelding process. E) SEM image of silver nanocubes on a silicon substrate before and F) after chemical welding. The scale bars are 500 nm.

resuspended to make a colloidal ink. Colloidal synthesis of a wide range of metal, semiconductor, and dielectric nanocubes has been reported previously;<sup>[9,15–21]</sup> here we use 70 nm {100}-faceted silver nanocubes to demonstrate the concept. These nanocubes are assembled into nanoscale trenches patterned in a flexible PDMS template (Figure 1A). The evaporation of the liquid in a receding meniscus drives a flow of nanoparticles toward the contact line, where the nanoparticles accumulate and are trapped by geometrical confinement in the trenches as the solvent evaporates.<sup>[22,23]</sup> Although we use patterned PDMS, nanoparticle assembly has also been carried out on unpatterned substrates to make close-packed films either by dipcoating or using a Langmuir–Blodgett trough.<sup>[24,25]</sup> Second, the assembled nanocubes are transferred by contact printing from the PDMS to a new substrate such as silicon, glass, or a transmission electron microscope (TEM) membrane (Figure 1B), with excellent pattern fidelity. This is consistent with previous literature showing that highly complex patterns can be transferred with >95% yield and better than 100 nm positional accuracy.<sup>[14]</sup> Third, adjacent nanocubes are bridged at the atomic level by the growth of epilayers from a liquid solution at room temperature, with a process that we call “chemical welding.” This leads to extended monocrystalline thin wires (Figure 1C,D), in a similar fashion to the Volmer–Weber growth and coalescence of 2D islands on a surface.

Figure 1E shows a scanning electron microscopy (SEM) image of a line of 50 silver nanocubes packed closely together after transfer printing onto a silicon substrate. The excellent assembly occurs due to (i) the intrinsic geometrical symmetry of the nanocubes, (ii) the strong van der Waals attraction between their flat {100} facets, and (iii) the tight confinement provided by an accurate design of the master—the width of the trenches can fit only one nanocube, and in a single orientation, the (100) direction. As a result, the nanocubes are all aligned in the same crystallographic orientation, which is necessary to achieve monocrystallinity after welding. Chemical welding leads to a continuous silver nanowire (Figure 1F). This occurs by epitaxial growth in the sub-1 nm gap between adjacent nanocubes. The contrast visible in the SEM image is due to slight variations in the surface topography. The chemical welding procedure consists of a chemical reaction similar to that employed to synthesize the nanocubes, but under conditions (temperature and concentration) that preclude homogeneous nucleation. In the case of metals, this typically involves the reduction of metal ions, where the nanocube surface acts as a seed for heterogeneous nucleation. Here, we have used a chemical welding solution consisting of an aqueous diamminesilver(I) complex with glucose as the reducing reagent.<sup>[26]</sup> The process takes 90 s at room temperature. A pretreatment with sodium borohydride was found to be helpful in improving reproducibility,

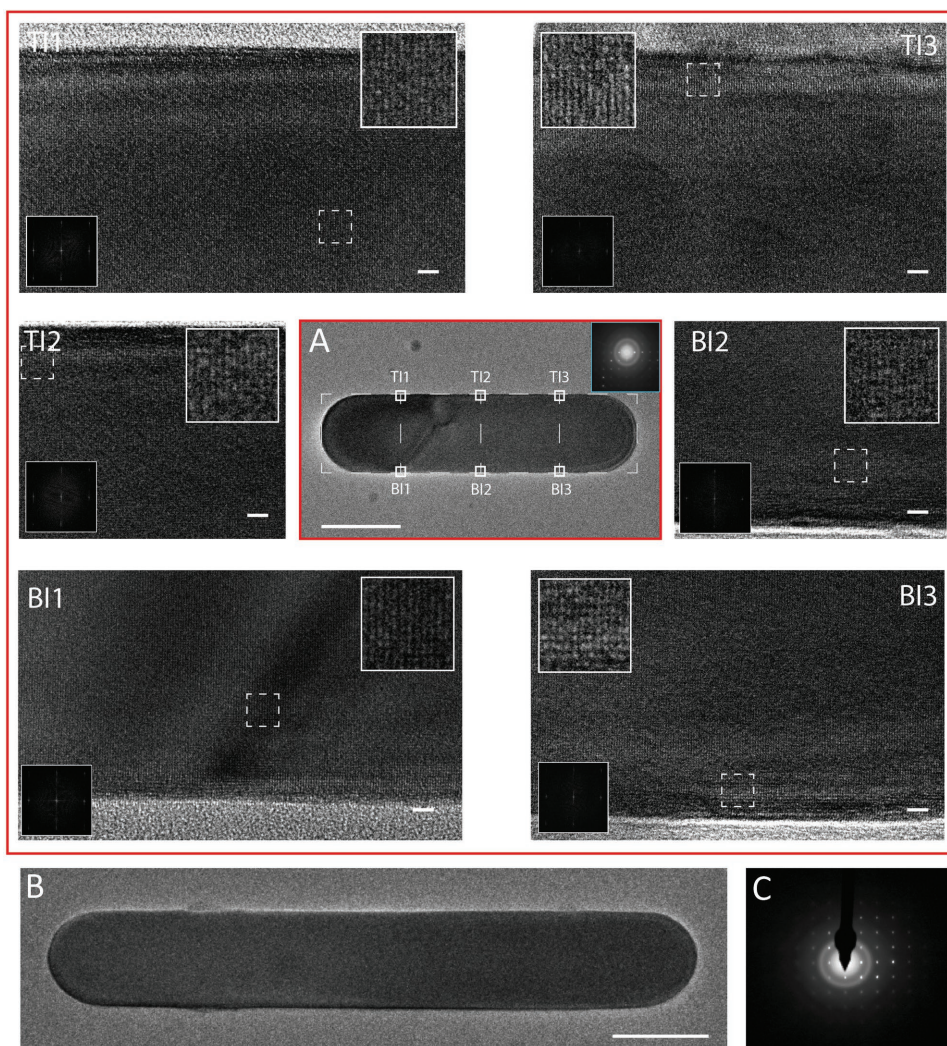


**Figure 2.** TEM images of welded silver nanocube lines. A) Overview image (center) surrounded by six high-resolution magnifications T11–3 (top interfaces) and B11–3 (bottom interfaces) of a bar originally composed of four silver nanocubes; the dashed lines in (A) indicate the location of the nanocubes before welding; the solid squares in (A) indicate the locations where the HRTEM images were taken, at the expected locations of the interfaces; the inset in (A) represents the SAED pattern of the entire welded line. The insets presented in the HRTEM images show magnified areas corresponding to the dashed squares (top inset) and the respective Fourier Transforms of the entire images (bottom inset). B) TEM image of seven welded nanocubes and C) its SAED pattern showing monocrystallinity on the full scale. The scale bars are 75 nm for TEM images (A, B) and 2 nm for HRTEM images.

presumably by removing excess polyvinylpyrrolidone that remained on the nanocube surface after the synthesis. To release the stress formed at the interfaces due to slight nanocube misalignment, a very short rapid thermal annealing (RTA) treatment (5 s) was used. Note that rounding of the nanowire ends occurs as a consequence of the RTA treatment. Full details of the process are given in the Supporting Information and results of different welding conditions with and without RTA are reported in Figure S1 (Supporting Information).

The assembled nanocubes act as seeds for epitaxial growth of silver adatoms from solution; since the nanocubes share the same crystallographic orientation, this homoepitaxial growth then leads to extended monocrystalline structures. Note that this approach is substantially different from previous reports, which obtained epitaxial attachment of stochastically assembled nanocrystals via simple removal of the surface ligands.<sup>[27,28]</sup>

Here, nanocubes are first assembled in a desired geometry and then exposed to a chemical reaction that provides the material to fill the subnanometer gaps. This key difference makes our approach more broadly applicable, for example, to materials with low atomic mobility and to imperfect assemblies where adjacent nanocubes are separated by larger distances.

**Figure 2A** (center image) shows a TEM overview of an assembly of four adjacent nanocubes after welding, lying on a thin  $\text{Si}_3\text{N}_4$  membrane. The segment looks very homogeneous, and the original position of the nanocubes (before welding) can only be inferred from the geometry; the dashed lines superimposed on the image indicate the expected original location of the nanocubes. High resolution TEM (HRTEM) images were taken for the three interfaces—top (TI) and bottom (BI)—at locations corresponding to original interfaces between nanocubes, as indicated by the white squares in Figure 2A. The

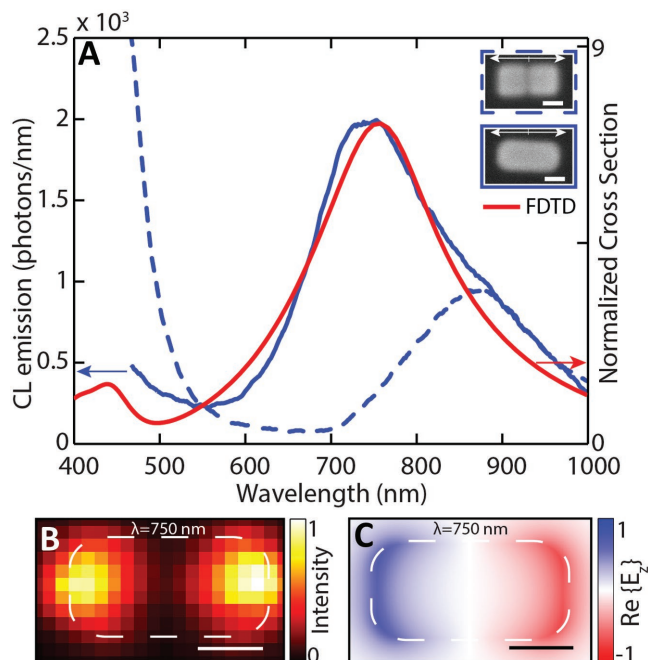
lattice-resolved images display no sign of interfaces, but a continuous crystal lattice in all directions, for every location analyzed. The bottom insets in the HRTEM images are the Fourier transforms of the entire image and indicate the presence of only one lattice period (2.04 Å), corresponding to the {200} lattice spacing for silver. The top insets are taken at higher magnification and clearly resolve the atomic columns.

The inset in Figure 2A (center) shows the selected area electron diffraction (SAED) pattern for the entire line, corresponding to a single [100]-oriented face-centered cubic (fcc) lattice. These analyses imply that a monocrystalline line can be obtained by chemically welding distinct nanocubes with the above-mentioned procedure. Figure 2B shows an overview TEM image of a bar composed of seven nanocubes after welding (see Figure S2, Supporting Information, for HRTEM), along with its SAED pattern (Figure 2C), which again indicates absence of grain boundaries and a [100]-oriented fcc lattice. Clearly, the epitaxial welding procedure is independent of the number of nanocubes that are welded and yields monocrystalline materials regardless of the scale. Additional TEM analysis of samples processed under the same conditions is reported in Figure S3 (Supporting Information). Our multiscale approach operates at the atomic scale during the chemical welding step but enables monocrystallinity at the full scale of the assembly.

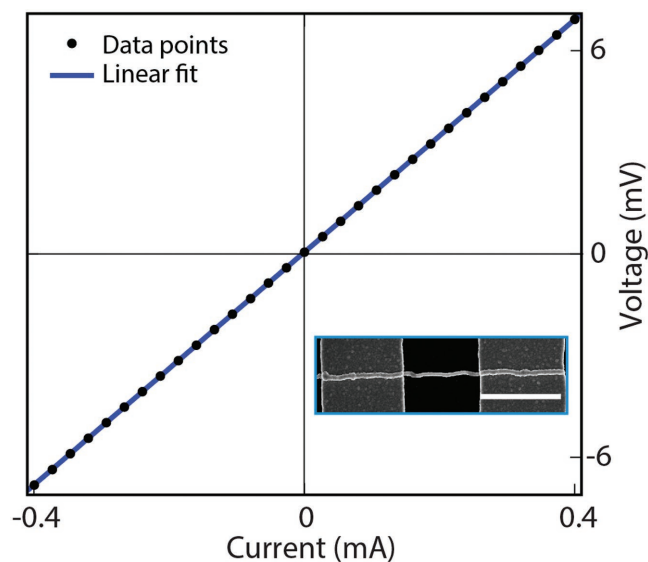
Cathodoluminescence (CL) imaging spectroscopy<sup>[29]</sup> was employed to characterize the optical properties of assembled nanocubes before and after welding. Figure 3A shows the CL spectrum of a silver nanocube dimer before and after welding as well as the scattering spectrum for a welded dimer computed by finite difference time domain (FDTD) simulations, all for polarization parallel to the longitudinal axis. The experimental and calculated spectra for the welded structure are very similar, with one main peak at  $\approx 750$  nm due to the longitudinal dipolar plasmon mode of the dimer. Note that the difference in the line width of the CL data and FDTD simulations is less than 2%, suggesting that the welded structures exhibit optical constants equivalent to monocrystalline silver. The unwelded sample shows a completely different spectrum featuring a weak peak at 870 nm and a more intense feature at higher energy (peaking outside the spectral sensitivity range of our detector).

Figure 3B shows the 2D CL map of the welded dimer measured at 750 nm, using a  $10 \times 10$  nm<sup>2</sup> grid. Figure 3C displays a time snapshot of the simulated amplitude of the  $z$ -component of the electric field calculated at 750 nm (in CL the electron beam couples to this  $z$ -component<sup>[30]</sup>). In both experiment and simulation, the signature of the dipolar mode can be clearly observed. This provides further evidence for our hypothesis that after welding the nanocube subunits become electrically connected and behave as a true continuous material. This suggests that optical materials with properties close to theoretical ones can be realized from a simple solution process.

The DC conductivity of monocrystalline lines obtained from assembly and welding of silver nanocubes was characterized using a specially designed four-point probe geometry (see Figure S4, Supporting Information). Figure 4 shows the current–voltage ( $I$ – $V$ ) characteristic of a 6  $\mu\text{m}$  long line with a cross section of  $85 \times 85$  nm<sup>2</sup>. The electric response is ohmic, with a resistance of 17  $\Omega$ , which corresponds to an intrinsic resistivity of  $2.0 \times 10^{-8}$   $\Omega\text{m}$ . For this calculation, the full length



**Figure 3.** Optical characterization via CL. A) Measured CL spectra of a dimer before (dashed line) and after (solid blue line) welding; the insets show the SEM images. The red line represents the scattering spectrum normalized by the geometrical cross section of a welded dimer, computed by FDTD. For all curves the polarization is parallel to the long axis of the dimer. B) Normalized 2D CL map for the welded dimer measured at  $\lambda = 750$  nm, integrated over a 30 nm bandwidth. C) Simulated 2D field profile of the real part of the  $E_z$  electric field at  $\lambda = 750$  nm for a welded dimer of comparable size, indicating a dipolar mode; the distribution was taken at half-height of the dimer. All scale bars are 50 nm.



**Figure 4.** Electrical characterization of a 6  $\mu\text{m}$  long welded line. A resistance of  $R = 17$   $\Omega$  is measured, which corresponds to a resistivity of  $2 \times 10^{-8}$   $\Omega\text{m}$ . The inset shows an SEM image of the two internal contacts at which the voltage is measured. The scale bar is 2  $\mu\text{m}$ .

of the bar was used (6  $\mu\text{m}$ ), which includes the metal contact width (2  $\mu\text{m}$  each). According to previous literature on electrical characterization of Ag nanowires, the full contact width has to be taken into account to get accurate resistivity measurements.<sup>[31]</sup> The intrinsic resistivity of silver is  $1.63 \times 10^{-8} \Omega\text{m}$  at 300 K; if surface scattering is taken into account, an ideal silver line with the dimensions of our sample would have an intrinsic resistivity of  $1.8 \times 10^{-8} \Omega\text{m}$  (see Figure S5, Supporting Information), only 10% lower than the measured value. This indicates that grain boundary scattering does not play an important role and that the resistivity is determined by electron–phonon scattering, as in an ideal metal,<sup>[32]</sup> further supporting the epitaxial welding model. These findings are in accordance with other literature reports that studied the conductivity of quasi-monocrystalline (pentatwinned) Ag nanowires grown in solution with a one-step polyol process.<sup>[31]</sup>

We have presented a new versatile bottom-up method to obtain ultrahigh quality nanopatterned truly monocrystalline (no twinning) silver lines that uses epitaxy between aligned nanocubes instead of substrate epitaxy. The new method removes the substrate requirements of conventional epitaxial growth methods and opens up the possibility to create 1D, 2D, and 3D single-crystalline silver architectures. Following this first demonstration for silver, the same strategy should in principle be applicable to other metals or even semiconductors and dielectrics, further expanding the application range of the new method presented here. A key requirement for transferability to other materials is the ability to synthesize monodispersed nanocubes in solution, which has been demonstrated for many metals, semiconductors, and dielectrics including Cu, Au, Pd, Cu<sub>2</sub>O, FeS<sub>2</sub>, halide perovskites, oxide perovskites, piezoelectrics, and CeO<sub>2</sub> but so far not for III–V or group IV materials such as GaAs and Si. The major technical challenge will be to develop suitable chemical welding procedures for each new material. This may ultimately leverage the knowledge in nanocrystal synthesis and epitaxial core–shell growth to make monocrystalline materials at the macroscale.

## Supporting Information

Supporting Information is available from the Wiley Online Library or from the author.

## Acknowledgements

The work at AMOLF is part of the research program of the “Nederlandse Organisatie voor Wetenschappelijk Onderzoek” (NWO). This work was supported by the NWO VIDI grant (project number 14846) and by the European Research Council (Grant Agreements Nos. 337328, 683076, and 695343). B.S. and E.C.G. conceived the idea of the project. A.B. helped in developing the process and performed preliminary experiments. B.S. performed the nanocube synthesis, assembly and welding, the electrical measurements and the FDTD simulations. B.J.M.B. performed CL measurements, under the supervision of A.P. and S.Z.O. fabricated the Si<sub>3</sub>N<sub>4</sub> membrane used for TEM measurements. M.A.H. performed the TEM characterization. B.S. wrote the paper. E.C.G. supervised the project. All authors contributed to the paper. The authors thank Dr. Wim Noorduyn and Dr. Sarah Brittman for carefully reading the paper, Ricardo Struik for the artwork of Figure 1d, and Bob Drent for the realization of the silicon master used for PDMS patterning.

## Conflict of Interest

A.P. is cofounder and coowner of Delmic BV, a startup company marketing a commercial product based on the cathodoluminescence system that was used in this work.

## Keywords

chemical welding, monocrystalline nanopatterns, nanocube assemblies, silver nanostructures, solution phase homoepitaxy

Received: February 22, 2017

Revised: March 16, 2017

Published online: May 3, 2017

- [1] Y. J. Lu, J. Kim, H. Y. Chen, C. H. Wu, N. Dabidian, C. E. Sanders, C. Y. Wang, M. Y. Lu, B. H. Li, X. G. Qiu, W. H. Chang, L. J. Chen, G. Shvets, C. K. Shih, S. Gwo, *Science* **2012**, *337*, 450.
- [2] Y. W. Wu, C. D. Zhang, N. M. Estakhri, Y. Zhao, J. Kim, M. Zhang, X. X. Liu, G. K. Pribil, A. Alu, C. K. Shih, X. Q. Li, *Adv. Mater.* **2014**, *26*, 6106.
- [3] A. A. High, R. C. Devlin, A. Dibos, M. Polking, D. S. Wild, J. Perczel, N. P. de Leon, M. D. Lukin, H. Park, *Nature* **2015**, *522*, 192.
- [4] D. Shi, V. Adinolfi, R. Comin, M. J. Yuan, E. Alarousu, A. Buin, Y. Chen, S. Hoogland, A. Rothenberger, K. Katsiev, Y. Losovyj, X. Zhang, P. A. Dowben, O. F. Mohammed, E. H. Sargent, O. M. Bakr, *Science* **2015**, *347*, 519.
- [5] A. Polman, M. Knight, E. C. Garnett, B. Ehrler, W. C. Sinke, *Science* **2016**, *352*, aad4424.
- [6] X. Sheng, C. A. Bower, S. Bonafede, J. W. Wilson, B. Fisher, M. Meitl, H. Yuen, S. D. Wang, L. Shen, A. R. Banks, C. J. Corcoran, R. G. Nuzzo, S. Burroughs, J. A. Rogers, *Nat. Mater.* **2014**, *13*, 593.
- [7] B. O. Dabbousi, J. RodriguezViejo, F. V. Mikulec, J. R. Heine, H. Mattoussi, R. Ober, K. F. Jensen, M. G. Bawendi, *J. Phys. Chem. B* **1997**, *101*, 9463.
- [8] X. G. Peng, M. C. Schlamp, A. V. Kadavanich, A. P. Alivisatos, *J. Am. Chem. Soc.* **1997**, *119*, 7019.
- [9] S. E. Habas, H. Lee, V. Radmilovic, G. A. Somorjai, P. Yang, *Nat. Mater.* **2007**, *6*, 692.
- [10] M. P. Boneschanscher, W. H. Evers, J. J. Geuchies, T. Altantzis, B. Goris, F. T. Rabouw, S. A. P. van Rossum, H. S. J. van der Zant, L. D. A. Siebbeles, G. Van Tendeloo, I. Swart, J. Hilhorst, A. V. Petukhov, S. Bals, D. Vanmaekelbergh, *Science* **2014**, *344*, 1377.
- [11] B. Sciacca, S. A. Mann, F. D. Tichelaar, H. W. Zandbergen, M. A. van Huis, E. C. Garnett, *Nano Lett.* **2014**, *14*, 5891.
- [12] J. J. De Yoreo, P. U. P. A. Gilbert, N. A. J. M. Sommerdijk, R. L. Penn, S. Whitelam, D. Joester, H. Z. Zhang, J. D. Rimer, A. Navrotsky, J. F. Banfield, A. F. Wallace, F. M. Michel, F. C. Meldrum, H. Colfen, P. M. Dove, *Science* **2015**, *349*, aaa6760.
- [13] Z. J. Ning, X. W. Gong, R. Comin, G. Walters, F. J. Fan, O. Voznyy, E. Yassitepe, A. Buin, S. Hoogland, E. H. Sargent, *Nature* **2015**, *523*, 324.
- [14] T. Kraus, L. Malaquin, H. Schmid, W. Riess, N. D. Spencer, H. Wolf, *Nat. Nanotechnol.* **2007**, *2*, 570.
- [15] Y. G. Sun, Y. N. Xia, *Science* **2002**, *298*, 2176.
- [16] A. Tao, P. Sinsermsuksakul, P. D. Yang, *Angew. Chem., Int. Ed.* **2006**, *45*, 4597.
- [17] F. Dang, K. Mimura, K. Kato, H. Imai, S. Wada, H. Haneda, M. Kuwabara, *CrystEngComm* **2011**, *13*, 3878.
- [18] H. A. Macpherson, C. R. Stoldt, *ACS Nano* **2012**, *6*, 8940.

- [19] H. J. Yang, S. Y. He, H. L. Chen, H. Y. Tuan, *Chem. Mater.* **2014**, *26*, 1785.
- [20] H. S. Chen, S. C. Wu, M. H. Huang, *Dalton Trans.* **2015**, *44*, 15088.
- [21] L. Protesescu, S. Yakunin, M. I. Bodnarchuk, F. Krieg, R. Caputo, C. H. Hendon, R. X. Yang, A. Walsh, M. V. Kovalenko, *Nano Lett.* **2015**, *15*, 3692.
- [22] Y. Cui, M. T. Bjork, J. A. Liddle, C. Sonnichsen, B. Boussert, A. P. Alivisatos, *Nano Lett.* **2004**, *4*, 1093.
- [23] L. Malaquin, T. Kraus, H. Schmid, E. Delamarche, H. Wolf, *Langmuir* **2007**, *23*, 11513.
- [24] A. Tao, P. Sinsermsuksakul, P. Yang, *Nat. Nanotechnol.* **2007**, *2*, 435.
- [25] A. R. Tao, J. X. Huang, P. D. Yang, *Acc. Chem. Res.* **2008**, *41*, 1662.
- [26] B. Sciacca, J. van de Groep, A. Polman, E. C. Garnett, *Adv. Mater.* **2016**, *28*, 905.
- [27] Y. Nakagawa, H. Kageyama, Y. Oaki, H. Imai, *Langmuir* **2015**, *31*, 6197.
- [28] K. Nakamura, Y. Nakagawa, H. Kageyama, Y. Oaki, H. Imai, *Langmuir* **2016**, *32*, 4066.
- [29] T. Coenen, F. B. Arango, A. F. Koenderink, A. Polman, *Nat. Commun.* **2014**, *5*, 3250.
- [30] F. J. G. de Abajo, *Rev. Mod. Phys.* **2010**, *82*, 209.
- [31] M. M. Kolesnik, S. Hansel, T. Lutz, N. Kinahan, M. Boese, V. Krstic, *Small* **2011**, *7*, 2873.
- [32] R. A. Matula, *J. Phys. Chem. Ref. Data* **1979**, *8*, 1147.

# Nanocube Epitaxy for the Realization of Printable Monocrystalline Nanophotonic Surfaces

Anna Capitaine and Beniamino Sciacca\*

Plasmonic nanoparticles of the highest quality can be obtained via colloidal synthesis at low-cost. Despite the strong potential for integration in nanophotonic devices, the geometry of colloidal plasmonic nanoparticles is mostly limited to that of platonic solids. This is in stark contrast to nanostructures obtained by top-down methods that offer unlimited capability for plasmon resonance engineering, but present poor material quality and have doubtful perspectives for scalability. Here, an approach that combines the best of the two worlds by transforming assemblies of single-crystal gold nanocube building blocks into continuous monocrystalline plasmonic nanostructures with an arbitrary shape, via epitaxy in solution at near ambient temperature, is introduced. Nanocube dimers are used as a nanoreactor model system to investigate the mechanism in operando, revealing competitive redox processes of oxidative etching at the nanocube corners and simultaneous heterogeneous nucleation at their surface, that ensure filling of the sub-nanometer gap in a self-limited manner. Applying this procedure to nanocube arrays assembled in a patterned poly(dimethylsiloxane) (PDMS) substrate, it is able to obtain printable monocrystalline nanoantenna arrays that can be swiftly integrated in devices. This may lead to the implementation of low-cost nanophotonic surfaces of the highest quality in industrial products.

## 1. Introduction

Controlling the geometry of individual nanostructures and their assembly into organized arrays, on a large area at low cost, is key to take nanophotonic and plasmonic devices from a laboratory scale to industrial products.<sup>[1–3]</sup> In particular, metal nanoparticles support surface plasmon resonances that are responsible for confining light to a dimension much smaller than the corresponding free-space wavelength and enable for large optical cross-sections.<sup>[4–10]</sup> As a result of this intense light confinement, the optical and electrical properties strongly depend on size, shape, material properties, and dielectric environment. The unique features of plasmonic nanostructures have led to countless applications in various fields. As an example, supported on a substrate they have been proposed for surface-enhanced spectroscopy,<sup>[11–14]</sup> catalysis,<sup>[15–17]</sup> sensing,<sup>[14,18,19]</sup> and diverse photonic

applications<sup>[20]</sup> that take advantage of the properties of individual nanoparticles<sup>[21]</sup> or of the collective resonances of phased arrays<sup>[6,8,22]</sup> to name a few.

Control on the nanoscale geometry is commonly achieved by patterning thin films via lithography techniques followed by evaporation and lift-off processes or etching.<sup>[23]</sup> Such top-down nanofabrication steps not only are expensive, time consuming, and hardly scalable, but produce materials that are polycrystalline, have substantial surface roughness or present damages as a result of etching. On the contrary, material quality is of paramount importance to building high-efficiency optoelectronic and nanophotonic devices.<sup>[6,24–26]</sup> Therefore, monocrystalline materials are ideal constituents to reach ultimate performance. However, this requirement adds further fabrication complexity owing to an epitaxial growth step to form a thin film prior to nanostructuring. This substantially restricts the integration to layers that are lattice-matched and that can

withstand high temperature, vacuum,<sup>[24]</sup> and possibly wet lift-off steps.<sup>[27]</sup>

Chemical syntheses on the other hand allow one to obtain high-quality colloidal nanoparticles, free of grain boundaries or stress that hamper electron conduction and weaken plasmon resonances.<sup>[24,28]</sup> A variety of shapes (nanowires, nanocubes, nanoplates, nanoflowers, nanoprisms, etc.) can be achieved by tuning the synthesis parameters or by particle attachment,<sup>[29]</sup> with extensive control of size and material composition. Nevertheless, gaining further control on the shape of nanocrystals beyond that of conventional Platonic solids, is crucial to introduce morphological anisotropy by design and tune the physicochemical properties to specific applications.<sup>[30]</sup> This hinders the realization of nanophotonic surfaces having individual units with an arbitrarily complex geometry that is often needed in plasmonics, and therefore limits substantially their potential.

Here, we lift this barrier and take advantage of solution-processed nanomaterials (nanocubes) to fabricate extended 1D and 2D monocrystalline nanostructure arrays of arbitrary shape (at near ambient temperature) and print them to any substrate. Single-crystal nanocubes are ideal building blocks because they have the highest intrinsic material quality and they have a fourfold rotational invariance. This ensures identical crystallographic orientation of adjacent units that is crucial to transform

A. Capitaine, B. Sciacca  
Aix Marseille Univ, CNRS, CINaM, AMUtech  
Marseille, France  
E-mail: beniamino.sciacca@cnrs.fr

 The ORCID identification number(s) for the author(s) of this article can be found under <https://doi.org/10.1002/adma.202200364>.

DOI: 10.1002/adma.202200364

a discontinuous assembly into a continuous monocrystalline nanostructure via nanocube epitaxy.<sup>[31]</sup> This makes solution synthesis a promising route toward the fabrication of low cost nanophotonic surfaces of highest quality.

A variety of materials used for optoelectronic applications can be synthesized as single-crystal nanocubes in solution, as for example Ag, Au, Cu, Al<sup>[32–34]</sup> (metals), Cu<sub>2</sub>O, PbS, CsPbX<sub>3</sub><sup>[35–37]</sup> (semiconductors), and BiFeO<sub>3</sub>, SrTiO<sub>3</sub> and CeO<sub>2</sub><sup>[38–40]</sup> (dielectric), to name a few. Among them, gold stands as an excellent candidate because it exhibits very good electrical and optical properties, and it is a prime choice in many plasmonic and nanophotonic devices.<sup>[6,41]</sup> In addition, the excellent thermal and chemical stability enable to study nanocube epitaxy without interference from the environment, oxide layers, or adsorbed species.

First, we demonstrate that the strategy described above can be used as a general method to transform arbitrary assemblies of gold nanocubes (supported on a silicon substrate) into 1D and 2D monocrystalline nanostructures. This is enabled by the introduction of a novel approach of simultaneous oxidative dissolution and growth that can also be used to control the faceting of the resulting continuous monocrystalline nanostructures by tuning few key parameters. Then, we show for the first time that by applying this procedure to nanocubes organized in poly(dimethylsiloxane) (PDMS) via directed assembly, monocrystalline Au nanopatterns by design can then be transferred to virtually any kind of substrate. This paves the way for swift integration of nanophotonic surfaces of the highest quality in optical and optoelectronic devices and architectures that are incompatible with classic nanopatterning strategies such as perovskite layers. Finally, we extensively study the chemical framework for nanocube epitaxy with a set of controlled experiments *ex situ* and *in operando* on a nanocube dimer model system. This provides with invaluable insights on the mechanism with atomic scale resolution.

## 2. Results and Discussions

### 2.1. Welding of Adjacent Nanocubes on Silicon

Gold nanocubes (30–40 nm) are synthesized following the procedure earlier reported by Park et al.<sup>[28]</sup> The solutions are highly monodisperse, and when drop-cast on a substrate nanocubes self-assemble face-to-face in a 2D closed-packed configuration, separated by a layer of adsorbed ligands (0.4 ± 0.1 nm) residual from the synthesis (Figures S1 and S14, Supporting Information).

After deposition, nanocubes are extensively washed with solvents and sodium borohydride (NaBH<sub>4</sub>) to remove the ligands (see Section 4) and obtain pristine surfaces separated by subnanometer gaps.<sup>[31,42]</sup> This constitutes an ideal platform to study nanocube epitaxy, as the product can swiftly be characterized with scanning electron microscopy (SEM). If exposed to a solution containing a gold precursor (HAuCl<sub>4</sub>) and a weak reductant (ascorbic acid), adjacent nanocubes grow and merge, producing continuous gold nanostructures (Figure S2, Supporting Information). Unfortunately, reduction of AuCl<sub>4</sub><sup>-</sup> in the bulk of the solution leads to homogeneous nucleation, causing

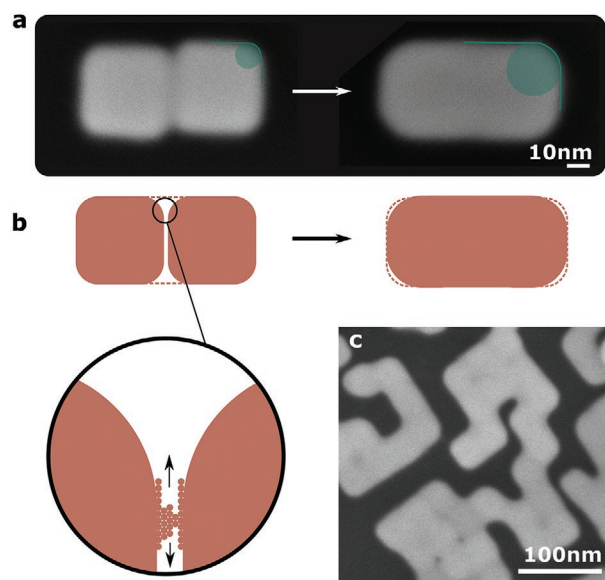


**Figure 1.** Epitaxial welding of gold nanocubes on silicon using a solution of HAuCl<sub>4</sub> only. a) SEM image of two 38 nm ligand-free nanocubes on silicon before (left) and after exposure to a  $80 \times 10^{-6}$  M HAuCl<sub>4</sub> solution at 40 °C for 5 min (right); the green circles represent the radius of curvature. b) Schematic representation of the welding. c) SEM image of self-assembled 35 nm nanocubes after ligand removal and welding with a  $80 \times 10^{-6}$  M HAuCl<sub>4</sub> solution at 40 °C for 1 s.

contamination of the sample with small nanocrystals and inefficient use of reactants. We therefore explored the opportunity to achieve nanocube epitaxy in the absence of a reducing agent, so that AuCl<sub>4</sub><sup>-</sup> ions can reach the nanocubes surface without being consumed in the bulk of the solution.

Figure 1 presents evidence of nanocube epitaxy at near ambient temperature, for 35 and 38 nm nanocubes (Figure 1c and Figure 1a, respectively) achieved using a solution of HAuCl<sub>4</sub>  $80 \times 10^{-6}$  M only. The sub-nanometer gaps are successfully filled, yielding to continuous 1D and 2D nanostructures whose geometry is directed by the position of the nanocubes prior to welding, with good shape and angle retention. The resulting 1D nanostructures (Figure 1a) are on average ≈10% wider compared to the nanocubes before welding (from  $35.5 \pm 2.2$  to  $39.6 \pm 3.4$  nm and from  $37.8 \pm 1.2$  nm to  $42.7 \pm 1.8$  nm), whereas the length is unchanged ( $70 \pm 0.7$  nm for 35 nm nanocubes and  $78.3 \pm 3$  nm for 38 nm nanocubes) (Figure S14, Supporting Information). This is key to the realization of nanostructures that have an arbitrary geometry with control down to the nanometer scale. The radius of curvature increases after welding (see statistics in Figure S14, Supporting Information), which is attributed to oxidative etching of the nanocube corners, and it is amplified as the HAuCl<sub>4</sub> concentration increases or when Cl<sup>-</sup> ions are added to the solution (see Section 2.3). Besides preventing homogeneous nucleation and avoiding sample contamination with small nanocrystals, we found that this strategy is robust, as it leads to successful welding over a wide range of HAuCl<sub>4</sub> concentration ( $1 \times 10^{-6}$  M to  $10 \times 10^{-3}$  M), reaction temperature (room temperature (RT) to 80 °C) and pH, with a time-scale from less than a second (Figure 1c) to a few minutes, despite the fact that no reductant is introduced in the solution. A good compromise between fast kinetic and nanocube shape retention was found using  $80 \times 10^{-6}$  M HAuCl<sub>4</sub> at a temperature of 40 °C.

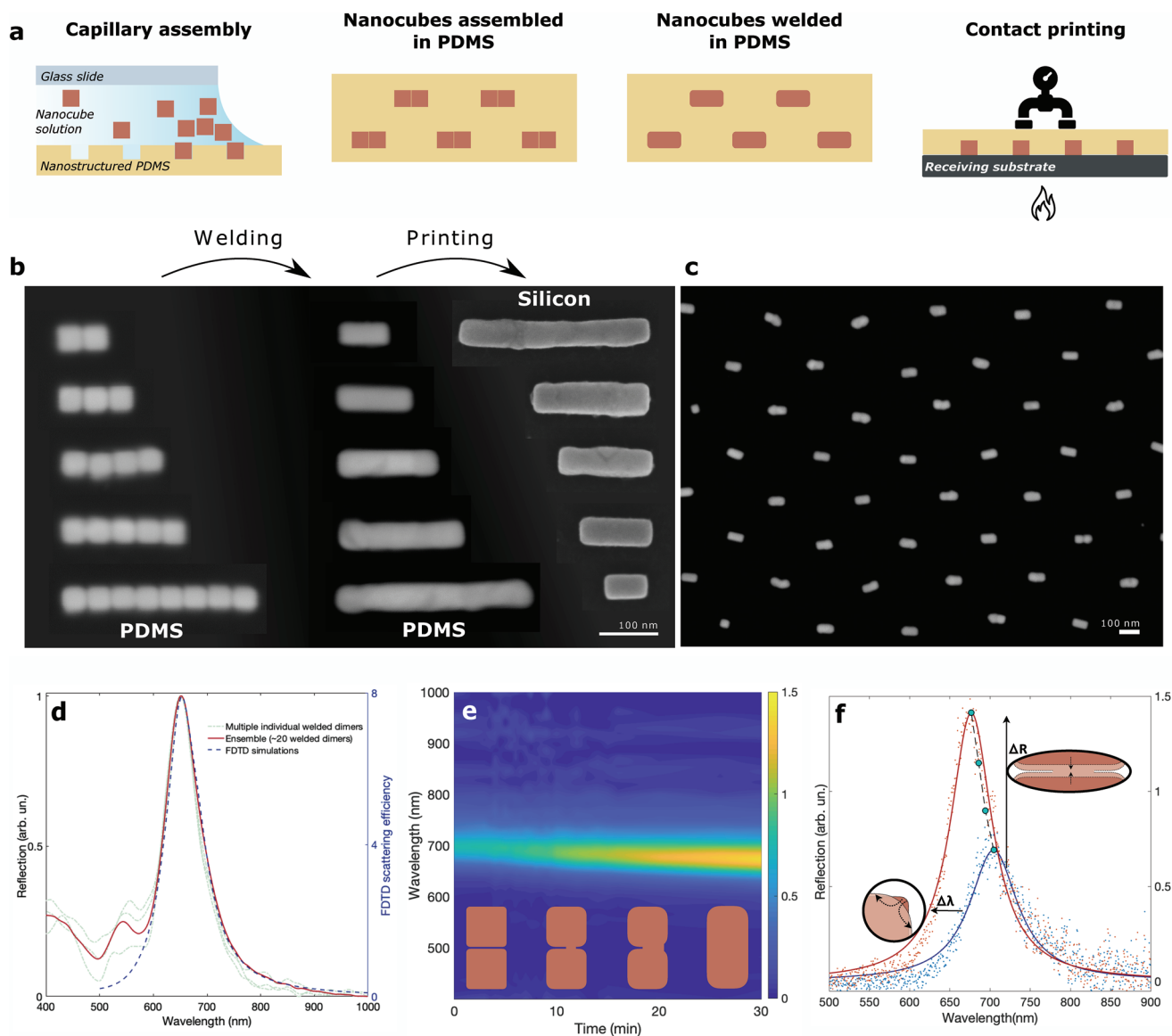


**Figure 2.** Realization of monocrystalline nanostructures by design on PDMS. a) Illustration of the process: capillary assembly in nanopatterned PDMS, nanocube epitaxy in solution and printing of monocrystalline nanostructures to any substrate. b) Collage of SEM images taken from large arrays made of 2, 3, 4, 5 and 8 nanocubes, showing 38 nm gold nanocubes assembled into 1D nanostructures of arbitrary length in PDMS before nanocube epitaxy (left image), after nanocube epitaxy in PDMS (middle image), and after printing to a silicon substrates (right image). c) SEM image of nanoantenna arrays on PDMS after nanocube epitaxy. d) Optical response (unpolarized light) of multiple individual nanoantennas (dotted line) and nanoantenna array (solid line) supported on PDMS, showing the intense dipolar longitudinal mode at 680 nm and the transverse mode at 550 nm. Realistic FDTD simulations of the nanoantenna array in PDMS (blue dashed line, polarization parallel to the dimer long axis); the agreement with experimental data in terms of resonance position and full-width-half-max (FWHM) confirms the realization of a material of the highest quality. e) Nanocube epitaxy on a model system in operando. An ensemble of  $\approx 40$  dimers in an array configuration on PDMS (c) is probed during epitaxy performed at RT; inset: diagram illustrating the evolution of nanocube dimers into a continuous welded bar. f) Data in (d) at the beginning ( $t = 0$  s) and at the end ( $t = 30$  min) of nanocube epitaxy, and the corresponding Lorentzian fits (solid lines). The green dots represent the resonance position at intermediate times. The blueshift, the increase in intensity of the dipolar mode, and the narrowing of the linewidth testify changes of the system morphology at the atomic scale. The scale bar in SEM images is 100 nm.

These conditions will be used as reference in this article when performing the welding on silicon, unless stated otherwise.

## 2.2. Printable Monocrystalline Nanoantenna Arrays

Applying the welding procedure on gold nanocubes organized in arrays enables us to realize monocrystalline nanopatterned

surfaces with extensive morphology control, that is especially important for plasmonics and nanophotonics. The low surface energy of PDMS makes it a convenient support for nanostructures self-assembly and growth, and ensures that those can be later released to virtually any substrate by contact printing (Figure 2a). Micro- and nanoparticles can be assembled in nanostructured PDMS using capillary assembly.<sup>[43–47]</sup> Silicon masters were patterned using e-beam lithography and used to

fabricate PDMS molds with traps designed to accommodate a certain number of nanocubes in a given geometry. Using this technique we realized periodic arrays of 2, 3, 4, 5, and 8 nanocubes as a proof of concept (Figure 2b; Figure S12, Supporting Information), but there is no limit to the geometry that can be obtained.

The welding procedure using  $\text{HAuCl}_4$  only optimized for nanocubes supported on a silicon substrate did not yield consistent results on different substrates, such as glass,  $\text{Si}_3\text{N}_4$ , or PDMS, most likely due to differences in surface chemistry and surface energy that impact the local reaction environment (more detail in Supporting Information). Results on silicon revealed that two mechanisms were at play: oxidation of the nanocube corners and gold reduction at the surface. Slight modification of the welding procedure, by performing the reaction at pH 1 (to promote oxidation) and introducing micromolar concentrations of NaBr (to enhance (100) facets reactivity<sup>[48]</sup>) enabled gold nanocube epitaxy on all substrates, including PDMS, transforming the welding procedure developed on silicon into a general solution route toward continuous monocrystalline nanostructures of arbitrary shape (Figure 2b). Figure 2c illustrates a periodic array of gold nanoantennas (with an aspect ratio of 2) obtained via nanocube epitaxy on a PDMS substrate. The sample exhibits homogeneous welding and very good shape retention throughout the entire substrate ( $200\ \mu\text{m} \times 200\ \mu\text{m}$ ). The optical response of individual nanoantennas and of an ensemble is compared in Figure 2d. The reflection peak at 650 nm corresponds to the longitudinal dipolar mode. It is worth noting that: i) different individual dimers show approximately the same behavior; ii) the collective response of an ensemble of  $\approx 20$  dimers is almost identical to that of individual dimers; and iii) the resonance linewidth and position are in extraordinary agreement with finite difference time domain (FDTD) simulations, indicating a material of the highest quality. This provides evidence that nanocube epitaxy enables the realization of bottom-up nanophotonic surfaces, with an exquisite control of position and geometry of individual resonators (comparable to e-beam lithography), and a material quality superior to what can be achieved with metal evaporation, that is the standard approach in nanofabrication.

The regular geometry of the nanoantenna array constitutes an ideal platform to examine nanocube epitaxy in operando, permitting to probe simultaneously the optical response of a number of nanoreactors. The strong light confinement in plasmonic nanoparticle systems allows extraordinary sensitivity to their geometry and their environment.<sup>[21]</sup> Compared to other in operando techniques, such as liquid-phase TEM, optical approaches ensure minimal perturbation that is especially important to study redox chemical reactions. We will show that this can be used to access information on nanocube epitaxy, with atomic resolution.

Figure 2e presents the kinetics of nanocube epitaxy, corresponding to the collective reflection of  $\approx 40$  dimers nanoreactors supported on PDMS, starting from the exposure to the welding solution to complete epitaxy. The main features that can be evidenced in the kinetic response are illustrated in Figure 2f. At time  $t = 0$ , electron tunneling through the  $< 0.5$  nm gap (see Figure S14, Supporting Information) enables a dipolar response of the entire dimer via a charge transfer plasmon mode, as evi-

denced by the  $E_z$  field profile shown in Figure S16a, Supporting Information. As welding takes place ( $t > 0$ ) new adatoms from the nanocube corners and from the solution slowly fill the nanogap, eventually establishing a bridge between the isolated nanocubes. As the bridge widens, electron tunneling is superseded by electron conduction through the lattice (see Figure S16b, Supporting Information). As a consequence of the larger electron current in the gap, the scattering cross-section of the dipolar mode increases. This leads to an increase of the array reflectance in the far-field, as observed in Figure 2e,f. The blueshift ( $\approx 25$  nm) of the dipolar mode is associated with the rounding of the nanocube corners (from  $r \approx 5$  nm to  $r \approx 9$  nm) and the increase in width (from  $w \approx 38$  nm to  $w \approx 43$  nm) during welding. The impact of the morphology of the welded dimer on the mode resonance is simulated in Figure S17a,b, Supporting Information ( $w$  or  $r$  only) and Figure S17c, Supporting Information ( $w$  and  $r$  combined). Figure S18, Supporting Information compares the FDTD response of a dimer array before welding with the corresponding array after welding, taking into consideration the change in morphology. The main features observed experimentally can be reproduced almost quantitatively. Note that the morphology of the interfaces has a strong impact on the optical response of dimers as they merge into a continuous nanoscale object.<sup>[49,50]</sup> These data are the signature of changes of the atomic arrangement inside a sub-nanometer gap with unprecedented resolution, and suggest that the processes of oxidation, growth, and welding take place simultaneously.

Finally, such monocrystalline nanophotonic surface can be transferred from PDMS to other substrates for integration in optoelectronic devices, or for further characterization. Figure 2b, shows nanoantennas of different lengths deposited from PDMS to silicon. During this process, the PDMS stamp is pressed against a receiving substrate, and the nanostructures are released due to the larger adhesion forces. It is worth noticing that the bottom surface of the nanoantennas, initially in contact with PDMS, also exhibit a continuous, gap-free surface. The nanoantenna arrays were printed from PDMS to a  $\text{Si}_3\text{N}_4$  membrane for high-resolution TEM (HRTEM) characterization. HRTEM images on different locations and electron diffraction on the whole nanostructure are presented in Figure 3. These provide evidence: i) for a perfect crystallographic alignment of the two nanocubes at the time of assembly; ii) for epitaxy between individual building blocks; and iii) that the junction is filled in its entirety yielding gap-free monocrystalline nanostructures. In addition, we noticed that epitaxy can be achieved also in the presence of non-cubic nanoparticles (defects) with a different crystallographic orientation, and result in the formation of a grain boundary (Figure S13, Supporting Information). This could promote grain boundaries engineering and trigger new material-by-design approaches.<sup>[51,52]</sup>

### 2.3. Unveiling the Mechanism of Nanocube Epitaxy

A number of control experiments were carried out to establish the framework of nanocube epitaxy and shine light on the mechanism. Thermodynamics drives a system to lower its total free energy, which ultimately controls the equilibrium shape of nanostructures, although kinetic barriers have to be overcome

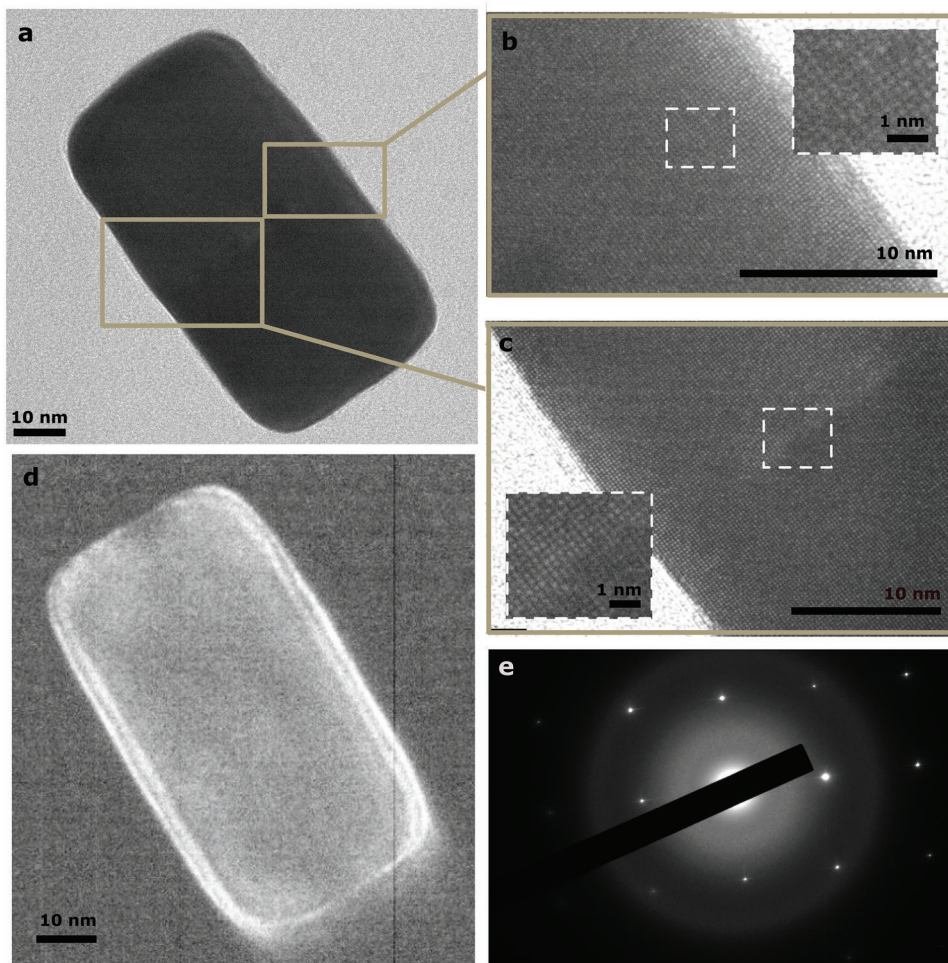


**Figure 3.** TEM characterization of the dimer arrays after epitaxy. a) Bright-field image. b,c) HRTEM showing a continuous gap-free material at the approximate location of where the junction between two nanocubes was before welding. d) Dark-field image showing no contrast at the junction. e) Electron diffraction over the dimer showing the typical pattern of a single-crystal.

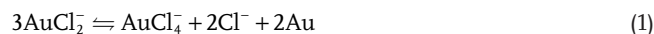
in most circumstances. In the case of two almost touching, ligand-free nanocubes, the total free energy is reduced if the dimer welds in a continuous bar, as a result of the disappearance of two surfaces. However, from TEM analysis we observed that, on average, adjacent nanocubes were separated by a gap corresponding to  $\approx 1 \times$  the lattice constant (corresponding to two atomic planes) that is sufficient to prevent spontaneous welding in water at RT, even after a few days (Figures S7, Supporting Information).

In the previous section we hypothesized that two mechanisms were at play: heterogeneous nucleation on the nanocubes (growth) and oxidative etching.

In **Figure 4c** we present the Pourbaix diagram to illustrate the thermodynamic equilibrium of the the  $\text{AuCl}_4^-/\text{Au}(0)$  redox couple as a function of pH in the absence of ligands (removed before welding). While there should be no stability domain for Au(III) species ( $\text{AuCl}_4^-$ ) in our experimental conditions (black solid line), increasing  $\text{Cl}^-$  concentration and reducing pH can drive the system to a chemical equilibrium in which  $\text{AuCl}_4^-$  species are stable in solution, and therefore oxidative dissolution (corrosion) can take place. The strong binding affinity

of chloride ions toward (111) and (110) facets<sup>[30]</sup> implies an enhanced reactivity of nanocube corners and edges toward oxidative dissolution. This is qualitatively validated with a set of experiments summarized in Figures S3–S5, Supporting Information showing that rounding of nanocube corners is more pronounced at larger  $\text{Cl}^-$  concentration and lower pH. The apparent quantitative disagreement with the Pourbaix diagram can be explained by considering that, as a result of adsorption, the  $\text{Cl}^-$  concentration on the nanocube surface is substantially larger than in the bulk.

Studies on oxidative etching of gold nanoparticles in chlorinated solutions revealed that  $\text{AuCl}_2^-$  (Au(I)) was the main dissolution product.<sup>[53–55]</sup> It is however unstable at low temperature<sup>[56,57]</sup> and can disproportionate to  $\text{AuCl}_4^-$  and Au(0) at the nanocube surface (Equation (1)).



From the macroscopic point of view this would result in the displacement of Au atoms via chlorinated species intermediates. To test this hypothesis and identify the role of  $\text{Cl}^-$ , we

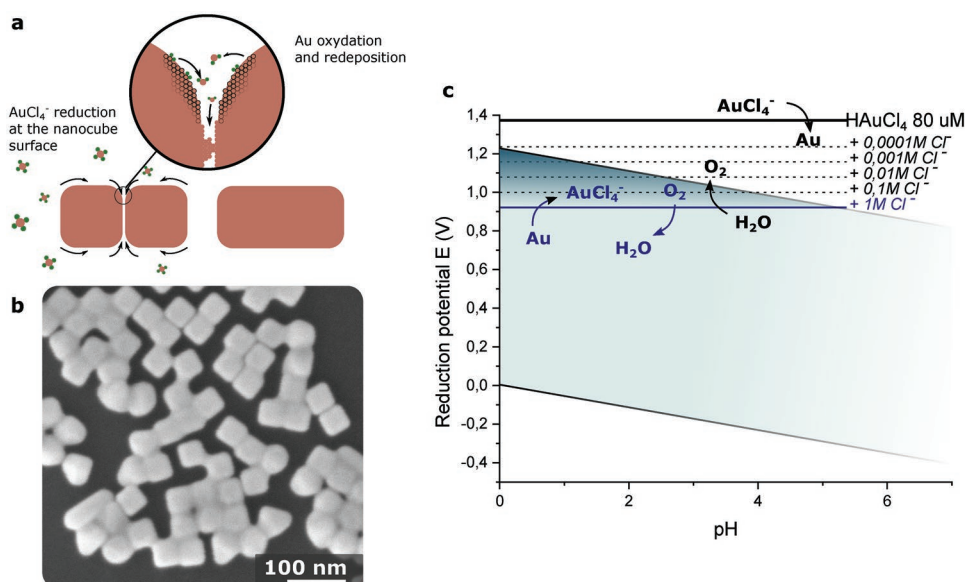
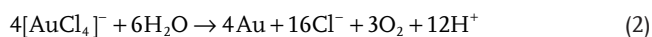


**Figure 4.** Insight into the welding mechanism. a) Illustration of the welding mechanism exhibiting simultaneous oxidation and growth. b) 38 nm gold nanocubes on silicon, partially welded using micromolar NaCl concentration only at 40 °C. c) Pourbaix diagram of  $\text{AuCl}_4^-/\text{Au}(0)$  redox couple for  $\text{AuCl}_4^-$  concentration of  $80 \times 10^{-6}$  M at RT (black line). The green area shows the stability domain of water, while the dashed and blue line correspond to  $\text{AuCl}_4^-/\text{Au}(0)$  reduction potential in the presence of chloride.

replaced the  $80 \times 10^{-6}$  M  $\text{HAuCl}_4$  solution with a NaCl solution containing an equivalent concentration of free chloride ( $2.5 \times 10^{-6}$  M—calculations are detailed in the Supporting Information) and observed partial welding (Figure 4b). This suggests that gold atoms effectively migrate from (111) and (110) facets to (100) facets (including the gap) via dissolution in the presence of  $\text{Cl}^-$  ions and redeposition, as illustrated in Figure 4a. It is worth noticing that this mechanism is in agreement with the interpretation of the optical characterization results presented in Figure 2f. Nevertheless, we were not able to achieve complete welding while securing the shape of the nanocubes using NaCl only. Therefore, when performing nanocube epitaxy in the  $\text{HAuCl}_4$  solution, part of the welding material is coming from the nanocubes but a fraction must come from the gold precursor. UVvis spectra performed on the welding solution after 1 h at 40 °C revealed  $\approx 2\times$  larger Au(III) consumption in the presence of the nanocube substrate, corroborating our hypothesis (Figure S10, Supporting Information).

According to the Pourbaix diagram, in our experimental conditions it is thermodynamically possible for water to reduce Au (III) directly to Au (0) (Equation (2)), or to Au (I), that can be further reduced to Au (0) or can disproportionate following Equation (1) (Figure S20, Supporting Information).



Although this seems in stark contrast with the fact that gold chloride aqueous solutions are typically stable in ambient conditions, the Pourbaix diagram does not take into account the kinetics of the system. Previous research has shown that in certain experimental conditions (aerosol microdroplets or microwave reactors), water oxidation could even lead to the formation of gold nanoparticles from  $\text{HAuCl}_4$  solutions without reducing agents.<sup>[4,58]</sup>

In addition, we observed that in most experimental conditions the morphology of the nanostructures does not evolve

after welding is complete, even if the substrate is left to react for longer time (Figure S11, Supporting Information). This is the trademark of a self-limited reaction, and indicates that the equilibrium between oxidative etching and growth is reached once the gap has been filled.

#### 2.4. Controlling the Morphology

The accurate choice of experimental parameters allows to shift this equilibrium and to favor dissolution or growth, providing a useful knob to finely control the morphology of the nanostructures resulting from nanocube epitaxy. Figure 5a summarizes some key parameters that can be tuned to design a specific surface and examples are given in Figure 5b–d for 42 nm nanocubes drop-cast onto silicon and exposed to the welding solution for 1 h.

As discussed previously, chloride ions enhance oxidative dissolution and can be used to fabricate smooth nanostructures with important bending radius. However, as shown in Figure 5b, shape retention is very limited for large 2D nanocube assemblies.

Retention of sharp corners can be achieved by performing epitaxy at RT. However, in addition to the slow kinetics, many face-to-face nanocubes remained unwelded at the end of the reaction (Figure S6, Supporting Information). This induced us to investigate the opportunity to control the evolution equilibrium between (100) and (111) facets by the introduction of  $\text{Br}^-$  ions at micromolar concentration to achieve flat surfaces even at higher temperature (Figure 5d). Bromine ions are commonly used in nanocube synthesis to direct crystal growth because they bind to (100) facets, reducing their surface energy and growth rate.<sup>[28,48]</sup>

Increasing the temperature leads to rough morphologies, due to stronger heterogeneous nucleation as shown in Figure 5c. As the reaction temperature increases from RT to 40 °C,

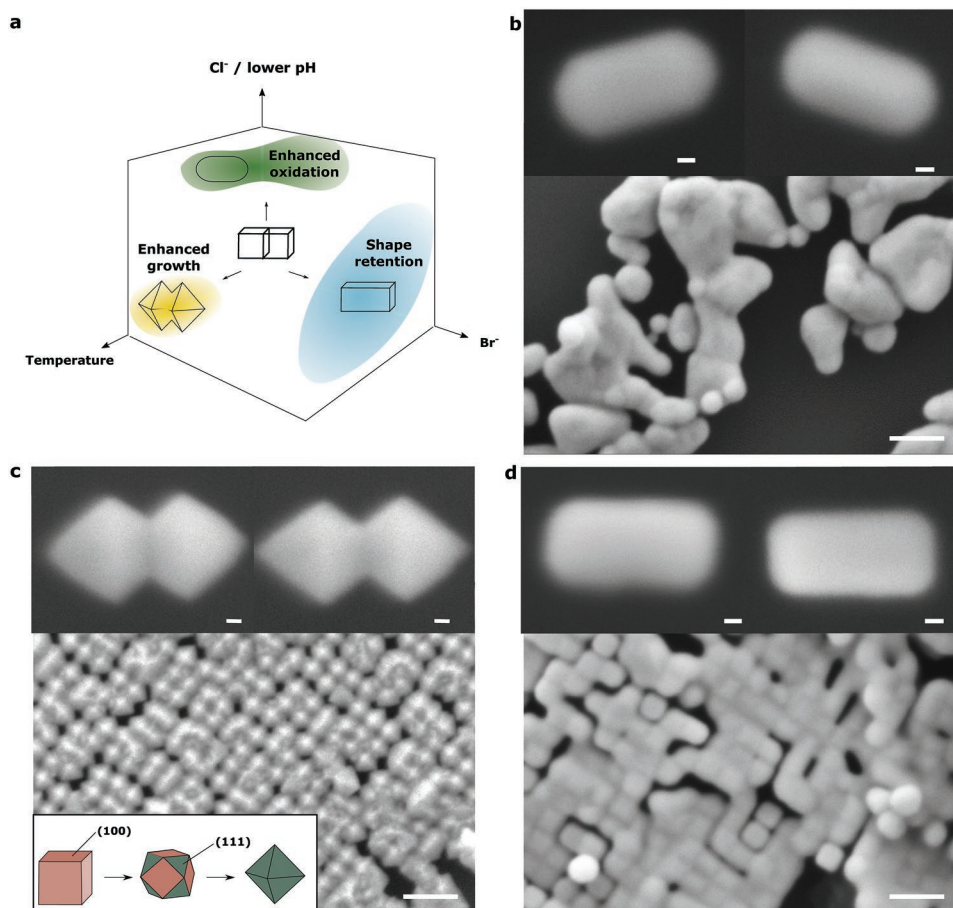


**Figure 5.** Control over the morphology. a) Schematic summary of the effect of experimental conditions on the nanostructure morphology. b) SEM images of gold nanocubes after welding for one hour in the presence of extra chloride ( $80 \times 10^{-6}$  M  $\text{HAuCl}_4$ ,  $100 \times 10^{-6}$  M  $\text{NaCl}$ ,  $40^\circ\text{C}$ ) to enhance oxidation dissolution. c) SEM images of gold nanocubes after welding for 1 h at higher temperature ( $80 \times 10^{-6}$  M  $\text{HAuCl}_4$ ,  $60^\circ\text{C}$ ) to promote overgrowth and the advent of egg-boxes structures made of (111) facets. The inset is a schematic representation of (100) capped nanocube reshaping into (111) capped octahedron. d) SEM images of gold nanocubes after welding for one hour in the presence of small quantities of  $\text{NaBr}$  ( $80 \times 10^{-6}$  M  $\text{HAuCl}_4$ ,  $50 \times 10^{-6}$  M  $\text{NaBr}$ ,  $40^\circ\text{C}$ ) to promote shape retention. The scale bar is 100 nm in the main images and 10 nm in the insets.

nanostructures with irregular surfaces and egg-box shape start to appear after welding, exhibiting (111) facets. This effect is strengthening if the temperature is further increased to 60 and  $80^\circ\text{C}$  (Figure S6, Supporting Information). In the absence of surfactants or additives, the surface free energy of (111) facets is lower than that of (100) facets. This drives the reorganization of (100) capped nanostructures into (111) and their intermediates, as illustrated in the inset of Figure 5c. In addition, Figure 5c shows that only the surfaces that are not blocked by the substrate or the surrounding nanocubes are able to evolve toward (111) facets, and in the case of isolated dimers this results in the formation of bowties nanostructures. The larger volume after the reaction confirms that growth takes place on (100) facets exposed to the welding solution despite the absence of a reductant.

### 3. Conclusion

We have shown for the first time that gold monocrystalline nanostructure arrays of arbitrary shape could be fabricated via a bottom-up approach, using nanocubes as building blocks.

This report challenges conventional approaches in the fields of plasmonics and crystal growths. In the former, focus is either put on the fabrication of plasmonic structures of average material quality with accurate control of the nanoscale geometry via top-down techniques, or on Platonic colloidal nanoparticles of high material quality enabled by low cost bottom-up chemical synthesis. In the latter, single crystal ingots are obtained from the melt using one single-crystal seed, whereas monocrystalline thin films are obtained via epitaxy in vacuum on substrates with the same lattice parameter. The results presented here represent a considerable step forward compared to the state of the art of these fields, and they have the potential to foster different research avenues. They show that monocrystalline gold nanostructures can be simply obtained via nanocube epitaxy at near ambient temperature from many single-crystal seeds (nanocubes) that could be assembled deterministically. This is especially important because the organization of nanocubes before epitaxy determines the final shape of the monocrystalline nanostructure, allowing spatial resolution comparable to e-beam lithography, but with a process that has a strong potential from the technological perspective. The absence of a reducing agent

during the nanocube epitaxy step simplifies the process substantially and avoids homogeneous nucleation of nanoparticles that would otherwise deteriorate the optical properties of the plasmonic surface. Optical measurements confirmed the excellent material quality and showed a strong reproducibility of process. In addition, unlike conventional nanofabrication techniques where the (polycrystalline) nanostructures are fabricated directly on the substrate, we have shown that nanocube epitaxy can be performed directly on PDMS and that (monocrystalline) plasmonic surfaces by-design can be printed to any substrate, unleashing from lattice matching requirements. This is highly promising for the integration of monocrystalline gold nanostructures, such as transparent electrodes or plasmonic scatterers, in devices that are sensitive to temperature, water, or other nanofabrication processes, as for example perovskite solar cells. Detailed analysis of the chemical landscape and optical spectroscopy in operando shone light on the nanocube epitaxy mechanism, revealing that gold atoms are displaced from the nanocube corners to the sub-nanometer gap via a self-limited redox reaction mediated by  $\text{Cl}^-$  ions. Tuning this redox equilibrium allows to change the morphology of the nanostructures after epitaxy, transforming a nanocube dimer either into a continuous rectangular bar or into a bowtie element. The opportunity to configure the crystal facets during epitaxy widens the toolbox of geometries that can be achieved.

#### 4. Experimental Section

PDMS was purchased from Wacker (RT601),  $\text{HAuCl}_4$ ,  $\text{HNO}_3$ ,  $\text{NaBr}$ ,  $\text{NaCl}$ ,  $\text{NaBH}_4$  were purchased from Merck at the highest purity available.

**Gold Nanocube Synthesis:** Nanocubes were synthesized following Park et al. procedure.<sup>[28]</sup> Briefly, 10 nm CTAC-capped seeds were overgrown in a 50 mL round bottom flask using 6 mL of  $100 \times 10^{-3}$  M CTAC, 30  $\mu\text{L}$  of sodium bromide at  $40 \times 10^{-3}$  M, 100  $\mu\text{L}$  of the 10 nm seed solution at 2 OD in  $20 \times 10^{-3}$  M CTAC, 390  $\mu\text{L}$   $10 \times 10^{-3}$  M ascorbic acid and 6 mL of  $0.5 \times 10^{-3}$  M  $\text{HAuCl}_4$  solution. The solution was left to react for 25 min at RT with gentle stirring prior to centrifugation. The nanocube solution was washed twice and redispersed in 10 mL of ultrapure water.

**Ligands Removal:** Ligands were removed after nanocubes were supported on a substrate (drop-cast on a flat substrate such as silicon or assembled into patterned PDMS). The substrate was first dipped (sequentially) in ultrapure water, acetone, isopropanol, and ultrapure water again (1 min each) to have the substrate as clean as possible before ligand desorption. The ligands adsorbed on the nanocube surface (CTAC, SDS, Triton-X45 residual from the synthesis or the assembly solution) were removed by exposing the substrate to a  $100 \times 10^{-3}$  M  $\text{NaBH}_4$  solution for 30 min. Hydrides having a higher binding affinity to gold effectively displaced the ligands, as reported in ref. [42]. Finally, the samples were rinsed thoroughly with ultrapure water and stored in ultrapure water until welding.

**Nanocube Epitaxy on Silicon:** Typically 2  $\mu\text{L}$  of an aqueous nanocube solution ( $10^{12}$  nanocubes  $\text{mL}^{-1}$ ) was drop-cast on a silicon substrate. Ligands were always removed after complete evaporation of the solution with the procedure described above. Welding was performed by introducing the silicon substrate into a 20 mL vial containing 10 mL of a  $\text{HAuCl}_4$  aqueous solution with concentrations ranging from  $1 \times 10^{-6}$  M to  $10 \times 10^{-3}$  M, at a temperature between RT and  $80^\circ\text{C}$  between 1 s and 1 h using a water bath, with no agitation. The standard welding reaction on silicon was performed at  $40^\circ\text{C}$  with  $80 \times 10^{-6}$  M  $\text{HAuCl}_4$  unless mentioned otherwise. When  $\text{NaCl}$ ,  $\text{NaBr}$ ,  $\text{NaOH}$ ,  $\text{HCl}$ , and  $\text{HNO}_3$  were added to control the shape of the nanostructures, the concentrations and/or measured pH were systematically indicated in the main text or figure captions. After welding the substrates were rinsed with ultrapure water and  $\text{N}_2$  dried.

**PDMS Molds Fabrication:** The silicon master was fabricated with e-beam lithography using poly(methyl methacrylate) (PMMA) resist on

silicon. Upon exposition and development, a thin layer of chrome was evaporated on the substrate to be used as a hardmask. PMMA was then lifted-off in acetone. Silicon was then etched by 40 nm using reactive ion etching. Chrome was finally removed using a commercial chrome etchant. After oxygen plasma, the silicon master was silanized with perfluorodecyltrichlorosilane at room temperature in a desiccator for 20 min to ease PDMS demolding. PDMS molds were fabricated on a glass slide by depositing liquid degassed PDMS (commercial monomer and polymerizing agent mixed to a 9:1 ratio) on the silicon master and covering it by a glass slide. Upon reticulation of PDMS at  $100^\circ\text{C}$  for 10 min on a hot plate, the PDMS template was demolded from the silicon master. The PDMS molds were then stored in ethanol for at least a few days prior to assembly to remove un-reacted species in PDMS.

**Capillary Assembly:** The nanocube solution was centrifuged at 9000 RPM for 10 min and redispersed in 10 mL of  $0.75 \times 10^{-3}$  M SDS and 0.0075 wt% Triton X45 at a concentration of  $10^{12}$  nanocubes  $\text{mL}^{-1}$ . Assembly was performed by dragging the nanocube solution (50  $\mu\text{L}$ ) with a glass slide fixed 1 mm above the PDMS substrate, in a homemade system. The speed was set at  $1 \mu\text{m s}^{-1}$ , the temperature at  $55^\circ\text{C}$  and the humidity at 40%.<sup>[45]</sup>

**Nanocube Epitaxy on PDMS:** Assemblies were left to fully dry in air for at least 1 h before removing the ligands with the strategy described above (when dipping the samples in  $\text{NaBH}_4$  right after assembly, part of the assembly would come off the substrate). Welding was performed by introducing the PDMS substrate into a solution containing  $80 \times 10^{-6}$  M  $\text{HAuCl}_4$ ,  $50 \times 10^{-6}$  M  $\text{NaBr}$ , and 100  $\mu\text{L}$  of  $\text{HNO}_3$  to lower the pH to 1. Reaction was performed at  $40^\circ\text{C}$  for 1 h, with no agitation. Upon welding substrates were rinsed with ultrapure water and dried with a stream of nitrogen.

**Printing:** Printing was performed on silicon substrates and  $\text{Si}_3\text{N}_4$  TEM grids, used as the receiving substrates. For silicon substrate, an oxygen plasma (10 min, 200 W,  $150^\circ\text{C}$ ) was first performed, then 5  $\mu\text{L}$  of ethanol was drop-cast on the substrate at  $20^\circ\text{C}$  and the PDMS sample was slowly put in contact and pressed on the silicon substrate before evaporation of the ethanol. The whole process was monitored using optical microscope by looking through the transparent PDMS, to ensure for good contact between the two substrates and to position assembled areas on silicon. When the two substrates were fully in contact, the temperature was then raised and maintained at  $50^\circ\text{C}$  for 10 min for the ethanol to dry. Upon releasing the pressure nanocubes remained in the silicon for which they have more affinity. The  $\text{Si}_3\text{N}_4$  TEM grids were used as purchased without plasma treatment. Because they cannot handle much pressure without breaking, 1  $\mu\text{L}$  of PMMA was deposited on the TEM grids to increase their adhesion, which allowed to print the nanocube assemblies with good resolution. Upon contact with PDMS, PMMA was pushed out of the sample which allowed imaging.

**Characterization and Simulations:** Assemblies of nanocubes on PDMS were imaged using a scanning electron microscope (JEOL 7900F) in low-vacuum mode with a pressure of 60 Pa. TEM and electron diffraction was performed with a JEOL 2100F. Optical characterization was performed with an inverted microscope (Zeiss Axiovert 200M) with an air objective (100x, NA = 0.9) in reflection. The PDMS without nanoantennas was used as the reference to take into account of the spectral response of the system. Light was coupled into a 25  $\mu\text{m}$  optical fiber, yielding a collection spot diameter of 1.3  $\mu\text{m}$ . To minimize perturbation of the nanostructures during operando measurements, spectra were taken at discreet intervals: the first 15 spectra were collected each 30 s, the following 5 spectra each 60 s, and the last 4 spectra each 4 min.

The commercial software Lumerical was used to simulate the response of individual gold nanoantennas. The nanostructure was placed on PDMS to simulate the experimental environment as accurately as possible, as depicted in Figure S17d, Supporting Information. A total field scattered field source (electric field polarized along the nanoantenna long axis) was used in all simulations, except in Figure S18, Supporting Information, where a periodic array with lattice parameters equivalent to experiments is simulated. In Figure 2d the following nanostructure dimensions are used:  $w = 44$  nm,  $L = 84$  nm,  $r = 8$  nm. The dielectric constant from Johnson and Christy was used for gold.

To fully understand how the far-field optical response changes, one has to consider that the dimers before welding were separated by a gap <0.5 nm (measured by TEM and presented in Figure S14, Supporting Information—middle panel). In this regime, electron tunneling dominated the optical response. The gap can thus be considered as an element with a given (small) impedance. The establishment of a bridge between the two nanocubes and its widening effectively reduced the gap impedance further and increased the plasmonic current in the gap. The increased current improves the cross-section of the resonator. This had, however, a negligible effect on the resonance position, given that the optical mode before welding corresponded already to that of a continuous dimer (due to electron tunneling) and the effective length of the resonator is virtually unchanged as the gap was filled. This was consistent with theoretical predictions for flat interfaces reported in refs. [49,50]. It is worth mentioning that this particular behavior was strongly dependent on the morphology of the gap, as shown in theoretical and numerical studies of plasmonic dimers of different shapes. In particular, in ref. [49] it was shown that gaps constituted by flat interfaces display strikingly different behavior than those constituted by spherical interfaces.

**Statistical Analysis:** The information given on width, length, radius of curvature of nanocubes and nanostructures, as well as the size of the gap between two nanocubes (before welding) were extracted from manual measurements performed on TEM images. Mean values were indicated with standard deviation (SD) calculated for: i) 6 values for the bending radius of dimers and individual nanocubes; ii) 11 values for the size of the gap between two nanocubes; and iii) 8 values for the width and length of the dimers before and after welding. All the measures are presented in Figure S14, Supporting Information.

## Supporting Information

Supporting Information is available from the Wiley Online Library or from the author.

## Acknowledgements

The authors thank M. Abbarchi and L. Santinacci for fruitful discussions and for carefully reading the paper, D. Chaudanson and A. Altié for support with TEM characterization, and F. Bedu for support with e-beam lithography. The project leading to this publication has received funding from MITI CNRS (project COMPACT), ANR (project MeMeNtO) and Excellence Initiative of Aix-Marseille A\*MIDEX, a French “Investissements d’Avenir” programme through the AMUtech Institute.

## Conflict of Interest

The authors declare no conflict of interest.

## Data Availability Statement

The data that support the findings of this study are available from the corresponding author upon reasonable request.

## Keywords

chemistry in operando, monocrystalline gold nanoantennas, nanocube epitaxy, plasmonics

Received: January 12, 2022

Revised: April 4, 2022

Published online:

- [1] E. C. Garnett, B. Ehrler, A. Polman, E. Alarcon-Llado, *ACS Photonics* **2021**, *8*, 61.
- [2] A. F. Koenderink, A. Alú, A. Polman, *Science* **2015**, *348*, 516.
- [3] J. H. Choi, H. Wang, S. J. Oh, T. Paik, P. S. Jo, J. Sung, X. Ye, T. Zhao, B. T. Diroll, C. B. Murray, C. R. Kagan, *Science* **2016**, *352*, 205.
- [4] J. K. Lee, D. Samanta, H. G. Nam, R. N. Zare, *Nat. Commun.* **2018**, *9*, 1562.
- [5] S. A. Maier, *Fundamentals and Applications Plasmonics: Fundamentals and Applications*, Springer, New York **2007**.
- [6] M. S. Bin-Alam, O. Reshef, Y. Mamchur, M. Z. Alam, G. Carlow, J. Upham, B. T. Sullivan, J. M. Ménard, M. J. Huttunen, R. W. Boyd, K. Dolgaleva, *Nat. Commun.* **2021**, *12*, 974.
- [7] K. L. Kelly, E. Coronado, L. L. Zhao, G. C. Shatz, *J. Phys. Chem. B* **2003**, *107*, 668.
- [8] R. Keunen, D. MacOretta, N. Cathcart, V. Kitaev, *Nanoscale* **2016**, *8*, 2575.
- [9] S. Eustis, M. A. El-Sayed, *Chem. Soc. Rev.* **2006**, *35*, 209.
- [10] G. Baffou, R. Quidant, *Chem. Soc. Rev.* **2014**, *43*, 3898.
- [11] Q. Shi, T. U. Connell, Q. Xiao, A. S. Chesman, W. Cheng, A. Roberts, T. J. Davis, D. E. Gómez, *ACS Photonics* **2019**, *6*, 314.
- [12] S. Nie, S. R. Emory, *Science* **1997**, *275*, 1102.
- [13] K. A. Willets, R. P. Van Duyne, *Annu. Rev. Phys. Chem.* **2007**, *58*, 267.
- [14] J. Nuñez, A. Boersma, J. Grand, S. Mintova, B. Sciacca, *Adv. Funct. Mater.* **2021**, *31*, 2101623.
- [15] E. Cortés, W. Xie, J. Cambiasso, A. S. Jermyn, R. Sundararaman, P. Narang, S. Schlücker, S. A. Maier, *Nat. Commun.* **2017**, *8*, 14880.
- [16] M. Navlani-García, D. Salinas-Torres, K. Mori, Y. Kuwahara, H. Yamashita, *Catal. Surv. Asia* **2019**, *23*, 127.
- [17] S. Linic, U. Aslam, C. Boerigter, M. Morabito, *Nat. Mater.* **2015**, *14*, 567.
- [18] J. N. Anker, W. P. Hall, O. Lyandres, N. C. Shah, J. Zhao, R. P. V. Duyne, *Nat. Mater.* **2008**, *7*, 442.
- [19] X. Yang, M. Yang, B. Pang, M. Vara, Y. Xia, *Chem. Rev.* **2015**, *115*, 10410.
- [20] H. A. Atwater, A. Polman, *Nat. Mater.* **2010**, *9*, 205.
- [21] E. Oksenberg, I. Shlesinger, A. Xomalis, A. Baldi, J. J. Baumberg, A. F. Koenderink, E. C. Garnett, *Nat. Nanotechnol.* **2021**, *16*, 1378.
- [22] R. Won, *Nat. Photonics* **2017**, *11*, 462.
- [23] A. Biswas, I. S. Bayer, A. S. Biris, T. Wang, E. Dervishi, F. Faupel, *Adv. Colloid Interface Sci.* **2012**, *170*, 2.
- [24] Y. Wu, C. Zhang, N. M. Estakhri, Y. Zhao, J. Kim, M. Zhang, X.-X. Liu, G. K. Pribil, A. Alú, C.-K. Shih, X. Li, *Adv. Mater.* **2014**, *26*, 6106.
- [25] A. Capitaine, B. Sciacca, *Adv. Mater.* **2021**, *33*, 2102588.
- [26] P. Nagpal, N. C. Lindquist, S.-H. Oh, D. J. Norris, *Science* **2009**, *325*, 594.
- [27] H. Zhang, C. Kinnear, P. Mulvaney, *Adv. Mater.* **2020**, *32*, 1904551.
- [28] J. E. Park, Y. Lee, J. M. Nam, *Nano Lett.* **2018**, *18*, 6475.
- [29] J. J. D. Yoreo, P. U. P. A. Gilbert, N. A. J. M. Sommerdijk, R. L. Penn, S. Whitelam, D. Joester, H. Zhang, J. D. Rimer, A. Navrotsky, J. F. Banfield, A. F. Wallace, F. M. Michel, F. C. Meldrum, H. Cölfen, P. M. Dove, *Science* **2015**, *349*, aaa6760.
- [30] J. E. Millstone, W. Wei, M. R. Jones, H. Yoo, C. A. Mirkin, *Nano Lett.* **2008**, *8*, 2526.
- [31] B. Sciacca, A. Berkhout, B. J. Brenny, S. Z. Oener, M. A. van Huis, A. Polman, E. C. Garnett, *Adv. Mater.* **2017**, *29*, 1701064.
- [32] H. J. Yang, S. Y. He, H. L. Chen, H. Y. Tuan, *Chem. Mater.* **2014**, *26*, 1785.
- [33] B. D. Clark, C. R. Jacobson, M. Lou, D. Renard, G. Wu, L. Bursi, A. S. Ali, D. F. Swearer, A. L. Tsai, P. Nordlander, N. J. Halas, *ACS Nano* **2019**, *13*, 9682.
- [34] Y. Wang, Y. Zheng, C. Z. Huang, Y. Xia, *J. Am. Chem. Soc.* **2013**, *135*, 1941.
- [35] C. H. Kuo, C. H. Chen, M. H. Huang, *Adv. Funct. Mater.* **2007**, *17*, 3773.

- [36] H. S. Chen, S. C. Wu, M. H. Huang, *Dalton Trans.* **2014**, 44, 15088.
- [37] M. Imran, P. Ijaz, D. Baranov, L. Goldoni, U. Petralanda, Q. Akkerman, A. L. Abdelhady, M. Prato, P. Bianchini, I. Infante, L. Manna, *Nano Lett.* **2018**, 18, 7822.
- [38] F. Dang, K. I. Mimura, K. Kato, H. Imai, S. Wada, H. Haneda, M. Kuwabara, *CrystEngComm* **2011**, 13, 3878.
- [39] U. A. Joshi, J. S. Jang, P. H. Borse, J. S. Lee, *Appl. Phys. Lett.* **2008**, 92, 2006.
- [40] S. Yang, L. Gao, *J. Am. Chem. Soc.* **2006**, 128, 9330.
- [41] M. Haggui, M. Dridi, J. Plain, S. Marguet, H. Perez, G. C. Schatz, G. P. Wiederrecht, S. K. Gray, R. Bachelot, *ACS Nano* **2012**, 6, 1299.
- [42] S. M. Ansar, F. S. Ameer, W. Hu, S. Zou, C. U. Pittman, D. Zhang, *Nano Lett.* **2013**, 13, 1226.
- [43] S. Ni, J. Leemann, I. Buttinoni, L. Isa, H. Wolf, *Sci. Adv.* **2016**, 2, e1501779.
- [44] V. Flauraud, M. Mastrangeli, G. D. Bernasconi, J. Butet, D. T. Alexander, E. Shahrabi, O. J. Martin, J. Brugger, *Nat. Nanotechnol.* **2017**, 12, 73.
- [45] T. Kraus, L. Malaquin, H. Schmid, W. Riess, N. D. Spencer, H. Wolf, *Nat. Nanotechnol.* **2007**, 2, 570.
- [46] L. Malaquin, T. Kraus, H. Schmid, E. Delamarche, H. Wolf, *Langmuir* **2007**, 23, 11513.
- [47] S. Ni, L. Isa, H. Wolf, *Soft Matter* **2018**, 14, 2978.
- [48] M. E. King, I. A. Kent, M. L. Personick, *Nanoscale* **2019**, 11, 15612.
- [49] R. Esteban, G. Aguirregabiria, A. G. Borisov, Y. M. Wang, P. Nordlander, G. W. Bryant, J. Aizpurua, *ACS Photonics* **2015**, 2, 295.
- [50] D. Knebl, A. Hörl, A. Trügler, J. Kern, J. R. Krenn, P. Puschnig, U. Hohenester, *Phys. Rev. B* **2016**, 93, 081405.
- [51] M. H. Oh, M. G. Cho, D. Y. Chung, I. Park, Y. P. Kwon, C. Ophus, D. Kim, M. G. Kim, B. Jeong, X. W. Gu, J. Jo, J. M. Yoo, J. Hong, S. McMains, K. Kang, Y.-E. Sung, A. P. Alivisatos, T. Hyeon, *Nature* **2020**, 577, 359.
- [52] R. G. Mariano, K. McKelvey, H. S. White, M. W. Kanan, *Science* **2017**, 358, 1187.
- [53] S. Yoon, C. Kim, B. Lee, J. H. Lee, *Nanoscale Adv.* **2019**, 1, 2157.
- [54] S. Seisko, M. Lampinen, J. Aromaa, A. Laari, T. Koiranen, M. Lundström, *Miner. Eng.* **2018**, 115, 131.
- [55] M. J. Nicol, *Gold Bull.* **1980**, 13, 105.
- [56] J. A. Peck, C. D. Tait, B. I. Swanson, G. E. Brown, *Geochim. Cosmochim. Acta* **1991**, 55, 671.
- [57] C. H. Gammons, Y. Yu, *Geochim. Cosmochim. Acta* **1997**, 61, 1971.
- [58] C. Vargas-Hernandez, M. M. Mariscal, R. Esparza, M. J. Yacamán, *Appl. Phys. Lett.* **2010**, 96, 2013115.

## CHAPTER 4: PERSPECTIVES

The quest for new technologies to fabricate monocrystalline materials with an arbitrary (nanoscale) geometry at low cost, is destined to involve bottom-up approaches. This is especially true in applications with a small economic margin that can benefit or rely entirely on nanostructuring. One example is the field of metasurfaces, that relies on plasmonics. Plasmonics is one of the most prolific research fields in the last decades, that rapidly grew after the discovery of extreme light confinement in metallic nanostructures. Quickly, two entirely different approaches emerged: (1) design of nanostructures with increasingly exotic properties followed by top-down fabrication; (2) development of new synthetic methods to obtain colloidal nanoparticles from the bottom-up. In the first approach the geometry can be truly arbitrary, and therefore it enables to fabricate complex nanostructures of any material composition that is extremely important to validate theoretical models. However, the quality of the plasmonic material is often rather poor because of grain boundaries in the polycrystalline evaporated metal; in addition, the cost and complexity of nanofabrication raise profound questions on the realistic industrial potential. In the second approach nanoparticles of the highest quality (single-crystals) are synthesised in arbitrarily large number with frugal use of reagents and strong potential for scalability. Despite the exquisite control of material composition, shape and size down to the nanometer, the overall geometry cannot be chosen *à la carte* but typically belongs to Platonic solids. This hinders the realisation of plasmonic surfaces with an arbitrarily complex geometry of the individual units, that is often needed in metasurfaces.

This argument can be extended to optoelectronic devices, that are made of stacked metal and semiconductor layers, that fulfil the basic requirements of light absorption, carrier separation and carrier transport. The overall performance of the device can thus be related to the efficiency of these fundamental processes. Grain boundaries dramatically affect performance: in metals they increase resistivity, while in semiconductors cause degradation in mobility and life-time of minority carriers, and are responsible for non-radiative recombinations. Therefore, all grain boundaries must be removed in order to achieve efficient carrier dynamics and reach the highest possible performance, both for the metal and the semiconductor part of the device.

The work presented in the previous chapters takes place in this context. I plan to further develop my research activity around the disruptive approach of nanocube epitaxy to make monocrystalline nanopatterned materials and integrate them in optical and optoelectronic devices, at a macroscopic scale. This will combine the advantages of bottom-up processes (scalability, low cost, efficient use of materials) with those of nanostructuring (functionality, enhanced light matter interaction, tuneable properties) and pave the way for new technologies.

Meeting this ambitious objective requires advances and innovations at the interface between physics, chemistry and nanotechnology. In particular, (i) new chemical processes have to be developed to build a wide toolbox of materials that can be obtained with this strategy, and encompass the constituents of optoelectronic devices (metals, semiconductors and insulators); (ii) improvement of the quality of nanocube assembly to reduce or eliminate defects that can be deleterious to the properties of the material; (iii) generation of knowledge on how to effectively integrate monocrystalline layers made of different materials to properly function, addressing questions regarding the interfaces between layers. Overcoming these challenges will enable for the realisation of monolithic devices made of monocrystalline stacks without restrictions on the lattice constants and with complex nanostructuring.

To meet this challenge, my future research will revolve around three focus areas, each devoted to develop fundamental understanding to strengthen the potential of this approach.

1. **Epitaxial Nanowelding - epitaxial welding of nanocube building blocks**

The first objective is to develop experimental procedures as **general** as possible for different classes of materials: metals, semiconductors and insulators. The hypothesis is that the assembled nanocubes are closely packed with a **face to face** arrangement (due to van der Waals interaction), and are oriented in the same crystallographic direction, because of geometrical and lattice symmetry. Different welding strategies will be investigated, to identify the ones that yields the best material quality and minimise defects (if any) at the welding interface.

2. **Nanocube assembly - assembling nanocube patterns on a large scale**

The goal of this Focus Area is to extend the concept described in Figure 22 to a macroscopic area (mm-cm size), to make this approach relevant for real world devices. The assumption is that the mechanism of the nanocube epitaxy procedures developed does not depend on the scale, but only on the **quality** of the assembly (i.e. the nanocubes have to be reasonably close - gap <5nm). Langmuir-Blodgett assembly of colloidal crystals has been demonstrated on a wafer scale already<sup>92</sup>, but with the presence of defects<sup>84</sup>. The objective is to explore new avenues to improve the quality of the nanocube assembly in the PDMS nanopatterned template, to allow for a defect free assembly on a macroscopic scale, and ensure that the advantages of the high-quality monocrystalline nanopatterns are preserved.

3. **3D building - stacking of monocrystalline nanopatterns**

The ambition of this Focus Area is to generate knowledge on how to integrate different nanopatterns vertically. This will result in a better use of the substrate real estate and will make this technology viable for the fabrication of opto/nanoelectronic devices. The idea is to finely align and print layers subsequently on top of each other. To achieve this goal the epitaxial welding procedure will be applied to the nanopatterns in the PDMS mould before printing to a new substrate. The welded nanopattern/film layer will be transferred to the substrate. Then, a second welded (monocrystalline) nanopattern layer will be printed on top of the first welded nanopattern. This will be repeated for many layers, to obtain a fully bottom-up monocrystalline device.

To summarise, **Focus Area 1** will allow to gain fundamental understanding of *nanocube epitaxy*, and developing experimental procedures as general as possible for different classes of materials (metals, metal oxides and nitrides, inorganic halide perovskites) that crystallise in the cubic system. Simple motifs of nanocubes will be assembled in PDMS substrates, as a

starting point to enable for correlative characterisation and studying epitaxial welding in a controlled fashion. I will also explore new fundamental mechanisms to use light to control nanocube epitaxy via optical resonances in Ag nanocube assemblies, at low temperature; this will pave the way for new research avenues. In **Focus Area 2** I will study in details nanocube assembly techniques to improve the quality of the assembly and to allow for large area. Applying the procedures developed in **Focus Area 1** will allow to fabricate monocrystalline layers (thin films and nanopatterns) on a cm lateral scale. Finally, **Focus Area 3** will allow to generate knowledge on how to sequentially stack (from PDMS) multiple monocrystalline layers to achieve functional optoelectronic devices. Major focus will be given to characterising and engineering the interfaces between the monocrystalline layers, to minimise surface recombination and to ensure a flawless charge transfer throughout the entire device.

### MATERIALS FOCUS

Nanowelding procedures will be developed for metals (Al, Cu), metal oxides ( $\text{Cu}_2\text{O}$ ,  $\text{CeO}_2$ ), metal sulphides (PbS), metal nitrides ( $\text{Cu}_3\text{N}$ ) and lead halide perovskites ( $\text{CsPbX}_3$ ). Most of these are relevant for optoelectronics applications and will serve the purpose of model materials to demonstrate the potential of the approach proposed and enlarge the toolbox of monocrystalline materials that can be obtained via nanocube epitaxy. Here some further details on selected materials:

-**Al**: highly abundant, good conductivity, good reflectivity, it passivates spontaneously with a  $\text{Al}_2\text{O}_3$  layer, it can be used as electrical contact and back reflector, emerging use as plasmonic material in the UV, procedures to make colloidal nanostructures of various geometry are in their infancy compared to Ag, Au, Cu, but the potential for applications in optoelectronics is high.

-**Cu**: highly abundant, good conductivity, it can be used as an electrical contact.

- **$\text{Cu}_2\text{O}$** : it is a semiconductor with a direct bandgap, it is earth abundant, I have already experience on<sup>74</sup>, it is relevant for photocatalysis, emerging use as a moderate refractive index material ( $n \sim 2.7$ ) supporting strong optical resonances, very recent (unpublished) preliminary results for nanowelding are promising, although further work is needed.

- **$\text{CsPbX}_3$** : all-inorganic perovskites, high quantum yield, tuneable bandgap, outstanding optoelectronics performance, defect tolerant<sup>93</sup>, very difficult to make ultra-thin monocrystalline structures with precisely controlled geometry, high potential for LED, lasers and solar cells.

This would arguably contribute to show the generality of the nanowelding approach for metal oxides and perovskites.

### LAYERS MORPHOLOGY

The main focus will be on the following layer morphologies:

-**1D lines/2D motifs**: 1D Line arrays with various aspect ratios and 2D cross-like motifs (1 nanocube thick) will be realised for all materials to study nanowelding and results will be compared. In addition to having four interfaces that could be studied simultaneously, 2D cross-like motifs will show the potential for complex nanopatterns and tune nanowelding conditions.

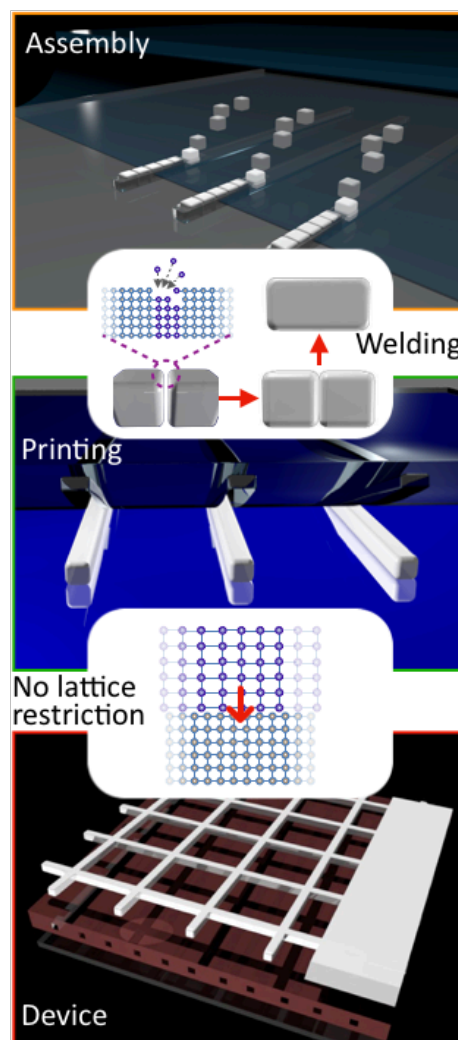


**Figure 22: Diagram of the strategy.** From the top: Direct assembly from solution of nanocubes into trenches patterned in a PDMS mold; epitaxial welding of the nanocubes into a patterned monocrystalline material; transfer of the assembled nanocubes to a new substrate; stack layers to make a functional device.

**-Nanophotonic layers:** Array of oriented 1D/2D motifs (1 nanocube thick) will be realised to achieve optimal light trapping in the devices. The design is defined via Finite Difference Time Domain (FDTD) simulations. We will develop monocrystalline dielectric and plasmonic layers.

**-Compact 2D films:** Continuous monocrystalline films (1 nanocube thick) will be made for all materials, to be used as reflector/electrode or absorber.

## METHODOLOGY

The **heart** of my research program is the ability to transform a closely packed assembly of nanocubes into a **continuous monocrystalline** material.

This approach is relevant since high-quality monocrystalline nanocubes can already be obtained for the classes of materials suitable to optoelectronic devices (metals, semiconductors and insulator). As already mentioned, nanocubes have the advantages of being the perfect building blocks, since (i) they are single-crystalline, (ii) they readily self-assemble in closely packed lattices due to the geometry via the strong van der Waals interaction between nanocubes facets, and (iii) when closely packed they all share the same crystallographic orientation since they are capped by six (100) facets, resembling to a discontinuous monocrystalline material. Nanocube epitaxy aims at **connecting these building blocks, via homoepitaxial growth from a solution precursor**. This process can work on any substrate since it does not interfere in the homoepitaxial growth between the cubes. This is a **general pathway to achieve nanocube epitaxy at low temperature**, as opposed to thermal welding, or plasmonic welding<sup>78</sup> which is specific for materials supporting plasmon resonances.

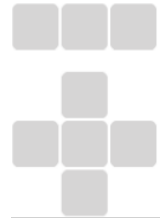
## **Focus Area 1: Epitaxial Nanowelding - epitaxial welding of nanocube building blocks.**

This Focus Area aims at gaining fundamental understanding of nanocube epitaxy, and developing experimental procedures as general as possible for different classes of materials (metals, semiconductors and insulators) for the first time. We will develop nanowelding procedures to promote epitaxial welding at low temperature, in solution, of adjacent nanocubes that were beforehand assembled in a PDMS mold. We will develop such procedures on *1D motifs* to enable a detailed **correlative characterisation** approach with electron microscopy and crystallography techniques. We will then apply them on *2D cross-like motifs* to test the hypothesis that such procedures are independent from the geometry of the pattern. The resulting nanowelded material must have the same (or better) optoelectronic properties of the colloidal nanocubes. The scientific advances enabled by this WP have the potential to be applied to assemblies at a large scale.

### 1.1 Materials preparation

**Nanocube synthesis.** It is essential that the constituent building blocks are (i) monocrystalline, (ii) monodisperse in size and (iii) have the same shape, to ensure optimal assembly and epitaxy. Synthesis procedures yielding high quality nanocubes are available in literature for the materials mentioned earlier. Starting from these procedures we will adjust the synthesis parameters to tune nanocube size.

**Nanocube assembly.** Capillary assembly techniques will be used to assemble nanocubes from a colloidal solution into nanopatterns realised in PDMS templates. Realisation of 1D lines (aspect ratio from 1:1 to 1:10) and 2D cross-like motifs (5 nanocubes) will support the development of nanowelding procedures, enabling for correlative characterisation. The PDMS template will be realised by moulding from silicon masters fabricated via e-beam lithography and etching.



## 1.2 Development of nanowelding procedures

Figure 23 illustrates a simplified mechanism that helps to understand the stages of nanocrystal synthesis and the idea behind nanocube epitaxy. During the first stage of nanocrystal synthesis, as a precursor is decomposed, the concentration of atoms steadily increases, but there is a **kinetic barrier** to forming nuclei in a homogeneous solution. Once a point of supersaturation is reached the atoms start to aggregate into small clusters (nuclei) larger than the critical size, via homogenous nucleation; this depletes the solution in growth material, causing concentration to drop below the critical level, thereby stopping the formation of new nuclei. The deposition of atoms on the stable nuclei is energetically favourable and nuclei will grow into seeds and eventually into larger nanocrystals. If seeds have a single-crystal structure, they will maintain it during the growth stage.

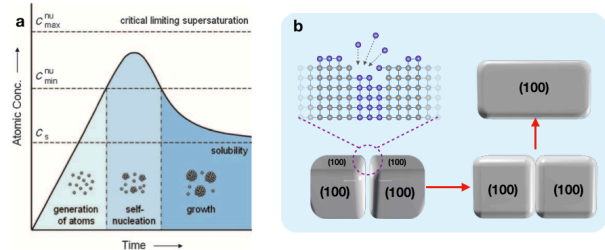


**Figure 23:** (a) Schematic diagram illustrating La Mer's condition for nucleation and growth. (b) Diagram showing epitaxial nanowelding of a nanocube dimer.

This approach takes advantage of the kinetic barrier to have growth without making new seeds, and will be applied to nanocubes already closely assembled in PDMS.

For a successful epitaxial welding, the small gap between adjacent nanocubes (typically 0.5-2 nm) has to be filled entirely to produce a continuous single-crystal. For a given material we will start to study epitaxial nanowelding in the same chemical environment used to synthesise the nanocubes; by carefully tuning the synthesis parameters (such as precursors concentration and temperature) we will ensure the solution is oversaturated ( $C > C_s$ ) but the minimum supersaturation (nucleation threshold to make new nuclei) is not reached ( $C < C_{min}$ ), avoiding nucleation in solution, which may deteriorate the quality of the nanopattern. In these conditions atoms will be added only to the surface of the nanocubes already assembled in PDMS. According to chemical deposition studies, such adatoms will diffuse around on the surface until they end up in a location where they can be incorporated. The choice to have the same chemical environment (solvent, surfactants, precursors, reducing agent) used in the nanocube synthesis as the starting point for developing nanowelding is strategic: it enables to avoid issues related to instability of nanocubes, as for example oxidation for non noble metals, etc...

If one considers the simplest case of a nanocube dimer (see Figure 23b), after epitaxial nanowelding (given that the facets stay unchanged) the total free energy of a single-crystalline bar (capped by six (100) facets) is lower than that of the initial dimer, since two interfaces are removed in the ideal process. This is analog to Ostwald ripening. Therefore, from thermodynamics considerations the 'perfect' welding is the most likely outcome, but a variety of experimental contingencies can drive the system into a kinetic control. Despite the formation of a grain boundary is highly unlikely (given the nanocube arrangement in assemblies), other type of defects such as point, line or bulk defects can be generated, including vacancies, dislocations or even voids, which can be detrimental to materials properties, especially for semiconductors where they can be source of non-radiative recombination. The likelihood of these defects will depend on intrinsic material properties such as surface diffusion, but also on the nanowelding experimental conditions.

A systematic approach will be put in place to optimise the procedure to avoid properties degradation after nanowelding, and in particular to avoid the formation of defects. First, ligands that maybe present on the nanocube surface will be stripped to yield a pristine

surface<sup>89</sup>. Then, starting from the specific nanocube synthesis chemistry, we will tune reaction conditions with this priority: precursor and reducing agent concentration, temperature, precursor and reducing agent type, surfactants, chemical environment etc. Then we will assess the quality of the welded interface with various complementary techniques, that will be used in a close-feedback loop to understand and improve the procedure. This will then be applied to nanocubes of different size to test the hypothesis that the optimal procedure is general and independent on the size of the building blocks.

This comprehensive study will allow us to identify the most critical aspects of the procedure and improve either the nanowelding chemistry or the sample preparation, or both, to achieve a perfect continuous monocrystalline material.

### 1.3 Characterisation of nanowelded layers and optimisation

The welded materials will be characterised *ex-situ* and *operando* with various state of the art techniques to assess the welding strategies developed and improve them. To gain insight from different perspectives, a correlative characterisation approach will be employed. After nanowelding, the monocrystalline object (1D/2D) will be transferred to a home-made TEM grid equipped with electrodes to enable structural (SEM, HRTEM, HAADF-STEM, SAED, EBSD), electrical (conductivity, EBIC), chemical (EELS, EDX, micro-Raman) and optical (resonance line-width, Photoluminescence lifetime, absorption) characterisation on the **very same object**. For the electrical measurements we will fabricate simple devices via e-beam lithography on the TEM grid to assess optoelectronics properties of individual 1D nanowelded materials<sup>61</sup>. At CINaM most of the equipment to perform such measurements is already available. Photoluminescence life-time measurements on  $\text{Cu}_2\text{O}$  and  $\text{CsPbI}_3$ , will be performed in collaboration with Dr. J. Wenger (Institute Fresnel, Marseille), and absorption measurements on individual nanostructures will be realised in collaboration with Dr. G. Baffou (Institute Fresnel).

The precious information gathered with this correlative characterisation approach will be used to better understand the nanowelding process for a given material and improve it, and will enable to characterise defects in the weld (if any) and assess their impact on optoelectronic properties.

**Characterisation:** We will perform in-depth characterisation of the nanopatterns and films by microscopy and spectroscopy techniques, with the aims at identifying (and quantifying) the presence of defects. Optical microscopy will be used to identify the presence of defects on a large scale. X-Ray diffraction will enable to identify the presence of islands with different orientation in films and dense nanopatterns. Optical spectroscopy will allow to assess the ensemble response of metasurfaces. Electron microscopy will be used to support other characterisation techniques to allow for high resolution investigation of the assembly.

### 1.4 Light-controlled nanocube epitaxy

The goal is to explore the opportunity to use **light** to promote and control epitaxial nanowelding of Ag nanocubes. This aims at discovering and understanding new fundamental processes. Nanostructures can support a variety of **optical resonances** that are associated with an enhancement of the electromagnetic field in the near vicinity of the particle (hotspot)<sup>94</sup>. In the case of nanoparticles separated by a very small distance, the field of certain optical modes is localised in the gap (dipolar mode), and that is true both for metal and semiconducting nanoparticles. The field enhancement increases with the mode confinement and therefore increases with the decrease of the gap size (this is true until quantum mechanics effects start to have a substantial contribution). After assembly, nanocubes are separated by a tuneable

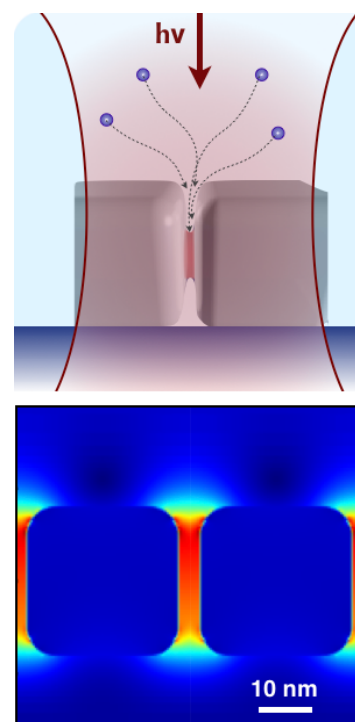


**Figure 24. Light-assisted nanowelding concept** Hotspots due to optical resonances are used to drive the nanowelding chemical reaction.

nanogap of 0.5-5nm, and therefore are the ideal platform to generate a strong local field enhancement and investigate the effect of light on chemical welding, in a similar way to light induced photomorphic reactions or syntheses<sup>95</sup>.

We will study and exploit the effect of this enhanced field to (i) act as a driving force to drag reactants from the solution into the nanogap<sup>96,97</sup> and (ii) alter the kinetics of the chemical welding reaction<sup>98,99</sup>; this will allow to draw a new light-assisted nucleation and growth curve for a given material, possibly different than that of Figure 23. As a result, we expect to have a different concentration of atoms or a different reactivity (or both) inside and outside the nanogap, and therefore to confine the epitaxial growth.

Dipolar modes are strongly dependent on the polarisation, therefore 2D cross-like motifs are ideal to assess the contribution of optical resonances.

The methodology employed in this task consist of the following steps:

- i. FDTD simulations and optical characterisation of Ag nanocube assemblies to select the laser wavelength. Preliminary simulations (Figure 24) indicate that in an infinite array of Ag nanocubes separated by a  $\sim 1$  nm, a strong field enhancement in the gap is obtained for a wide range of wavelength, suggesting that a single laser can be used for light-induced nanocube epitaxy.
- ii. Laser-assisted epitaxial nanowelding as a function of wavelength, polarisation and light intensity.
- iii. Characterisation of the optical response in real-time, to follow the evolution during welding as a function of time and of the illumination parameters. FDTD will support data interpretation.
- iv. Structural characterisation of the sample with an electron microscope to link the optical response to the nanostructure morphology after or at different stages of the welding process.

This will enable to assess important parameters such as the nanowelding kinetics as a function of incidence power, that is essential to be able to separate the contribution of photothermal effects (Arrhenius dependence) from photochemical effects (linear dependence)<sup>100</sup>. The correlative approach followed in this task (simulation, optical characterisation in-situ, structural characterisation in a SEM/TEM) will be crucial to succeed. The ultimate purpose of this idea is to fabricate monocrystalline 2D nanopatterns without the need for a pre-patterned PDMS template, by promoting nanocube epitaxy in a nanocube film with a rastered or spatially structured light beam. This is similar to direct laser writing techniques, but much better resolution, better material quality and less complexity.

## **Focus Area 2: Nanocube assembly - assembling nanocube patterns on a large scale.**

Nanotechnologists are able to print non-continuous 2D nanopatterns of colloidal nanocrystals onto soft or hard substrates with high yield, by transferring them from a patterned PDMS mold where they self-assemble via capillary forces<sup>101</sup>. During assembly, nanocubes accumulate on the contact line and are trapped by the presence of geometrical recessions in the PDMS mold (the nanopattern)<sup>102</sup>. By placing the mold in contact with a substrate with higher surface energy, the nanocubes can be released from the PDMS to a new substrate. The resulting non-continuous nanopattern has a resolution comparable to that of e-beam lithography, so substantially superior to that of UV lithography, and much higher throughput. Compared to nanoimprint lithography<sup>103</sup>, this approach allows to avoid etching

steps, deposition and lift off. Finally, the quality of the printed material is superior, since nanopatterns of monocrystalline nanocrystals (such as nanocubes) can be obtained.

I previously showed that compact lines (without defects) of about 8-10 microns can be made out of 70 nm silver nanocubes (>100 nanocubes), on substrates such as silicon, silica or silicon nitride<sup>89</sup>. The nanocubes are closely packed on their [100] facets, and therefore are all oriented in the same

crystallographic direction, which is critical to obtain epitaxial welding (see *Focus Area 1*). However this is still limited to a relatively small scale.

Although researchers have shown the ability to self-assemble colloids into films on a large scale<sup>92,104</sup>, the presence of defects (line, point...) hampers the penetration of such techniques into the industry.

**This focus area will explore the realisation of defect-free 2D nanopatterns and films of colloidal nanocubes on a mm-cm scale, with control over the orientation of individual nanocubes.**

Different avenues will be explored.

### 2.1 Template design and fabrication

To achieve a defect free reproduction of 2D nanopatterns, we will put efforts in designing better PDMS templates. In fact, a perfect assembly in the flexible PDMS stamp is essential to have a perfect nanopattern transferred to a substrate. A recent study has shone light onto some nanoscale phenomena that occur during capillary assembly of gold nanorods in silicon hard templates, and demonstrated how crucial the design of template is to achieve excellent yield<sup>102</sup>. It is shown that control over the width, depth and geometry of the recessions enables to trap the nanorods and ensure their 'resilience' against the receding suspension front. Although these findings are not directly applicable to obtain a defect-free assembly of nanocubes in a flexible stamp, and ensure their transfer to a new substrate, they demonstrate the importance of the topographical control of the template. In fact, to allow for printing the pattern from the template to a new substrate, the template should be flexible and the depth of the recessions should be smaller than the nanocube size, so that van der Waals forces can transfer the nanocubes from the low surface energy stamp to the high surface energy substrate. We will use heuristic and numerical methods to improve the design of the three dimensional contour of the nanoscale features in the flexible PDMS template, to ensure that nanocubes are assembled in a closely packed fashion, separated at most by few nanometers. We will also systematically investigate the effect of the mechanical properties, such as stiffness, of the PDMS stamp on the assembly quality<sup>105</sup>, by numerical simulations and experimentally by changing the degree of cross-linking of the stamp. The simulations will be performed with COMSOL Multiphysics.

An optimal design for example will avoid early pinning of nanocubes to the template during the assembly phase, which would cause a defect with a large gap between adjacent nanocubes. An optimal design will also avoid the removal of nanocubes already pinned to the substrate (low resilience), which will cause a missing nanocube. For example, we will study the effect of the trenches depth profile to improve resilience.

A careful design of the template geometry will also enable control over the orientation of individual nanocubes. This can be based on the consideration that the size of the nanocubes

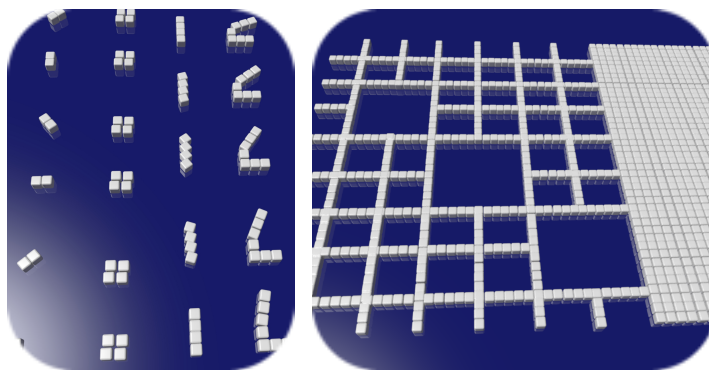


**Figure 25. Nanopatterns concept:** Films and 2D nanopatterns of nanocubes with control over the orientation of individual nanocubes are assembled and printed on any substrate over a large area.

along the diagonal is 1.4 times larger than the edge, and that a size dispersion better than 5-10% percent is achievable already for many nanocube materials.

The flexible PDMS template will be moulded from a hard silicon master fabricated with standard nanofabrication techniques available at CINaM (platform *Planete*). E-beam lithography is used to define the nanopattern, and etching to control the depth profile, to obtain a negative mould for PDMS. This will ensure the definition of nanopatterns with an arbitrary geometry and a resolution <10 nm; the master can be reused many times to mould new PDMS templates. Changing the ratio between the curing agent and the monomer, or the structure of the monomer allows to tune the mechanical properties of the final cured template. After moulding and curing, the flexible PDMS template will be removed from the mould and washed extensively in solvents such as ethanol to remove any unreacted monomer or any low molecular weight compounds dissolved in the PDMS matrix.

## 2.2 Nanocube assembly

Three different strategies are explored for nanocube assembly.

1) **Langmuir-Blodgett techniques**<sup>84,104</sup> will be studied for the realisation of compact 2D films on unstructured PDMS substrates. Nanocubes are dispersed at the air-liquid interface and slowly compressed to obtain a compact monolayer on a cm<sup>2</sup> lateral scale. The surface tension is monitored in real time via a Wilhelmy plate and can be related to the film compactness. The monolayer will be then transferred to a PDMS substrate (via dipping or decanting) for nanowelding. Although long range (mm scale) order is not perfect, on a lateral scale of several microns defect-free assembly of closely-packed nanocubes is achievable<sup>106</sup>. An ongoing project financed by CNRS-MITI aims at achieving defect-free assembly of nanocube monolayers on a cm scale via the use of optical forces (see next) to control the interaction between adjacent floating nanocubes.



**Figure 26:** Langmuir-Blodgett trough used to prepare nanocube compact films.

2) Nanophotonic layers with low density are realised with a **capillary assembly** setup. This setup enables control over temperature, relative humidity and speed at which the colloidal solution of nanocube moves with respect to the template. Monodisperse nanocubes are assembled in the nanostructured PDMS template, and the assembly monitored in real-time with an optical microscope. The contact angle of the nanocube dispersion is adjusted by selecting an adequate solvent (such as water) and adding a surfactant to achieve the optimal target value identified in 2.1. The optimal nanocube concentration, assembly temperature and speed will be determined experimentally and will be supported by COMSOL simulations. If needed we will tailor the interaction between adjacent nanocubes and the PDMS substrate by employing ligands to modify the surface chemistry of the nanocubes, to further optimise the quality of the assembly.

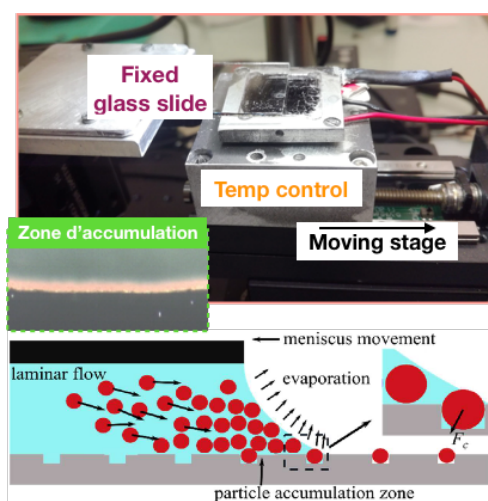


**Figure 27:** Capillary assembly setup and mechanism

3) **Nanoimprint** will be studied to realise nanophotonic layers with high density, such as metasurfaces, and to fabricate nanowire transparent electrodes. The achievement of a nanocube assembly which is compact and continuous on a macroscopic area, has so far never been demonstrated with techniques of capillary assembly, that are extremely sensitive to the morphology of the nanostructured template. Therefore, a different

approach will be employed to realise nanopatterns that require an electrical conductivity on a large scale, such as nanowire transparent electrodes. Recently, an approach similar to nanoimprint lithography has been successfully employed by our collaborators<sup>107</sup>. In this approach nanocubes are deposited on a substrate that is pressed against a nanostructured PDMS template. As a result of the experimental conditions, solid state nanocubes are pushed inside the template nanopattern. Dealing with nanocubes in the solid phase allows to avoid issues related to colloidal stability and to the complex (often uncontrolled) interaction between the solution and the nanostructured template.

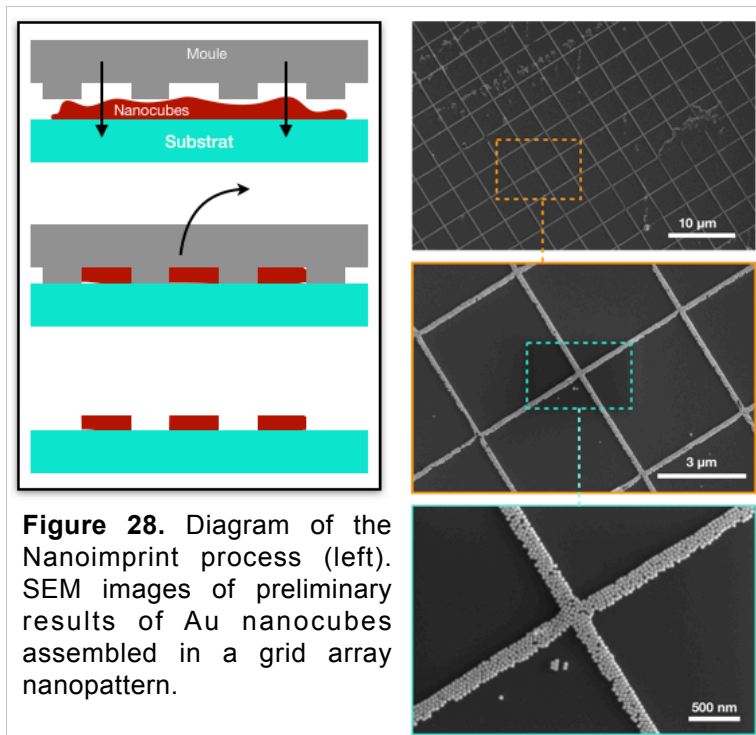


**Figure 28.** Diagram of the Nanoimprint process (left). SEM images of preliminary results of Au nanocubes assembled in a grid array nanopattern.

Although the nanoimprint approach is promising, it is still in its infancy and the mechanism is not yet fully understood. Further work in this direction has to be done to:

- Deeply understand the mechanism and develop a consistent framework that relates physical and chemical properties of the ink and its mechanical interaction with the nanostructured template.
- Develop a formulation of a nanocube ink that enables sufficient lateral mobility, to obtain a continuous, defect-free pattern on a  $\text{cm}^2$  area.
- Weld and integrate these layers in optoelectronic devices. Preliminary results on Ag and Au nanocubes are promising, but further work is required for the successful realisation of monocrystalline nanowire transparent electrodes.

### 2.3 Optical forces mediated assembly

I will also explore the opportunities to improve the compactness of the nanopattern/film by using light to introduce optical trapping forces<sup>96</sup>. It has been shown that optical resonances supported by coupled dimer antennas can be used to trap colloids as small as 10 nm under low laser intensity<sup>108</sup>. Compared to van der Waals interactions, optical forces can act at a longer range ( $<10\text{-}20$  nm), basically depending on the electromagnetic field distribution. By carefully selecting the excitation wavelength, plasmonic resonances and Mie resonances will be excited in metal and dielectric nanocubes, respectively<sup>109</sup>. The resonant excitation of nanocubes already pinned to the substrate can be used to trap nanocubes traveling in the near field<sup>108</sup>. Although the diffraction limited excitation beam is larger than the nanocube size, its intensity is relatively low compared to the field enhancement that optical resonances cause in the near vicinity of the nanocubes. As an example, this field enhancement can be as large as several orders of magnitude in the case of nanogaps between metal nanoparticles<sup>110</sup>. Therefore the experimental conditions will be tuned in such a way that only nanocubes within few tens of nanometers from the last assembled nanocube are attracted. This will improve compactness and order of the nanopattern/film. Numerical simulations will be employed to support experiment design.

A dedicated spectroscopic tool is being developed to study in real-time the assembly process on simple motifs such as lines, identify the emergence of defects, correlate them with experimental parameters, and quantify the effect of optical forces. This can also serve as a feedback system to act on the assembly parameters, such as substrate temperature, speed,

humidity, light fluency, wavelength and polarization. This dedicated system will be built on a optical microscope with the opportunity to (i) spectroscopically monitor the assembly process, and (ii) introduce optical forces to improve the assembly. Light from a tuneable laser will be coupled in the microscope and scattered light collected. This unique platform has the advantage that the effect of the optical forces can be monitored and adjusted in real-time if needed.

A similar equipment will be built to study the impact of optical forces on floating nanocubes in a Langmuir-Blodgett trough. Dark-field spectroscopy will enable to assess the distance between nanocubes as a function of the light intensity. This will be correlated with macroscopic surface tension measurements.

#### 2.4 Nanopatterns examples and realisation of macroscopic monocrystalline layers

The versatility of the approach introduced will enable to realise complex nanopatterns supporting multiple optical resonances to tune light-matter interaction. FDTD simulations will be used to design the nanopatterns that will be realised and integrated in **Focus Area 3** in the short term:

(i) a monocrystalline moderate-index  $\text{Cu}_2\text{O}$  nanopattern for light-trapping into the  $\text{Cu}_2\text{O}$  film (3.3). Dielectric resonators have recently gained much interest by the nanophotonics and optoelectronics community due to the reduced ohmic losses and the possibility to engineer optical resonances with scattering properties comparable to plasmonic antennas<sup>14</sup>.  $\text{Cu}_2\text{O}$  has the advantage to have a moderate-refractive index, to be earth abundant and easy to synthesise as nanocubes.

(ii) a monocrystalline Al nanopattern in a patch antennas (MIM) configuration (3.4). The patch antenna appears ideal to maximise light absorption in the ultra-thin (~10-20 nm)  $\text{CsPbI}_3$  monocrystalline layer, while being compatible with the vertical device architecture.

The optimal recipes for nanocube epitaxy developed in Focus Area 1 are applied here to realise monocrystalline layers on a larger lateral scale, ready for Focus Area 3.

## **Focus Area 3: 3D building - Nanocube printing and stacking of monocrystalline nanopatterns**

Optoelectronic devices are made of a stack of metal and semiconductor layers. As an example, in a solar cell the number of layers go from a minimum of three (for a prototypical single-junction) to more than ten for the record-efficiency multi-junction solar cell<sup>3</sup>. Fabrication is however complicated, since each layer has to be lattice matched and current matched (produce the same current), which puts constraints on the band gap and, as a result, on the viable materials.

**The objective of this Focus Area is to generate knowledge on how to stack monocrystalline layers (nanopatterns and films) obtained in WP2 to achieve functional monocrystalline devices.**

Here, we will combine the knowledge and expertise gathered in the entire project to validate the approach by fabricating **monocrystalline photodetectors and solar cells**. We will tackle this ambitious task gradually and systematically, by first fabricating a photodetector where nanowelding is used to prepare only one material (e.g.  $\text{Cu}_2\text{O}$  film,  $\text{Cu}_2\text{O}$  nanopattern), and then all the device layers (e.g. Al film,  $\text{CsPbI}_3$  absorber, Al nanopattern), except charge transport layers and transparent electrode. Finally, in a further development a

monocrystalline nanowire transparent electrode will be integrated as well as the front electrode.

### 3.1 Layer transfer

We will develop a technique to transfer monocrystalline nanopatterns and films from PDMS to a receiving substrate, with control over the printing position. This requires the implementation of methodologies of (i) alignment and (ii) printing.

**Alignment.** The PDMS template will be designed with four fiducial marks (one on each corner), where nanocubes will be assembled and nanowelded as in the rest of the nanopattern. The marks will be printed in the printing phase as well. The absolute position (x,y) of the four marks will be measured optically in the reference frame of the motorised stage of the assembly setup. While printing a new layer, the marks of this layer will also be measured, and their position referenced to the same reference frame, thus enabling alignment with the previous layer. A precision in the order of the  $\mu\text{m}$  is easily achievable, and will be largely enough for the demonstrators that we envisaged.

**Printing.** Transferring nanocrystals from a nanopatterned PDMS template to a new substrate is possible if the adhesion forces to the new substrate are higher than those that keep the nanocrystals in contact with the PDMS. These adhesion forces depend on the interfacial area and on the difference in surface energy between the receiving and the giving substrate. Since PDMS has a low surface energy, it has been shown that assembly of nanocrystals of different morphology, size and material assembled in a PDMS nanostructured template can be dry-transferred to a new flat substrate by conformal contact<sup>101</sup>. I was able to obtain a nearly 100% transfer yield of Ag nanocubes to Si, SiO<sub>2</sub> and Si<sub>3</sub>N<sub>4</sub> flat substrates<sup>89</sup>, by developing a wet-transfer approach. The printing of a continuous monocrystalline nanostructured layer from PDMS is expected to be facilitated by the presence of a continuous material opposed to isolated nanocrystals. The receiving substrate (e.g. glass) is fixed on a temperature controlled stage, while the PDMS substrate containing the monocrystalline layer is placed on a vertical motorised stage; the two substrates are approached. Inspection with an optical microscope allows to perform layer alignment, and assess when conformal contact is achieved. Temperature of the substrate, printing environment (dry/wet), exerted pressure and approaching/retracting velocity is tuned to optimise the transfer. The PDMS substrate is then retracted while the monocrystalline layer remains on the receiving substrate. These procedures (alignment/printing) are repeated for every layer until the entire device is completed.

### 3.2 Characterisation and interface engineering

The interfaces between different layers are a critical part of optoelectronic devices, and can strongly affect performance. Individual monocrystalline motifs are studied in T1.3 to assess the intrinsic quality of the nanowelded material, whereas in this task we will characterise the quality of the interfaces that are formed between the different layers, and assess the impact of the printing procedure.

For printed Al films we will test the conductivity with four-point-probe measurements first, and then the current-voltage (I-V) characteristics of **two** monocrystalline Al films printed on top of each other, to evaluate the conductivity of the interface and compare it to the ideal ohmic behaviour. These simple measurements enable to assess any detrimental bottleneck in electron flow through the interface, such as surface contamination or poor contact/adhesion between the printed layers that could cause inadequate electric performance.

For printed semiconductors layers, one further unique advantage of the approach introduced by MeMeNtO is that **surface passivation AND interface engineering** procedures can be easily applied on both surfaces, since one surface is exposed before printing and the other one is exposed after printing. To test this hypothesis, we will employ **passivation** schemes on both

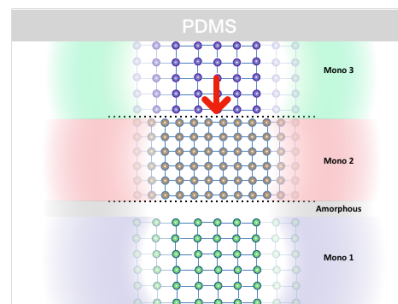


**Figure 29.** Diagram showing the stacking of monocrystalline layers. It highlights the possibility to print layers on amorphous or crystalline materials

surfaces to reduce surface recombination and improve carriers transport through the interface. These include the deposition of layers via ALD or spin-coating, or the modification of the surface chemistry with ligands chosen on the basis of their dipole moment<sup>111</sup>. The selection and choice of specific compounds will depend on the outcome of the characterisation and on the material. Photoluminescence (PL) life-time and quantum yield will be compared before printing, after printing and after passivation. We will print the layers on a conductive film and evaporate electrodes to measure I-V characteristics and perform impedance spectroscopy measurements under a variety of experimental conditions to characterise charge transfer processes. This will allow us to identify the presence of interface states, Fermi level pinning, surface contamination or poor electrical contact, and improve the printing procedure accordingly. XPS, XPS profiling characterisation will be performed in a synchrotron environment. Finally, this task will allow to study simple combinations of layers that will be used in a full device developed.

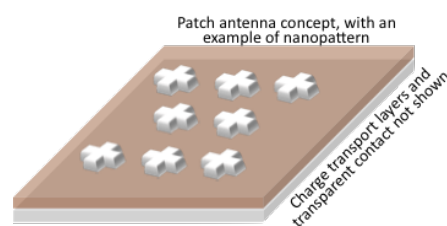
### 3.3 Cu<sub>2</sub>O monocrystalline photoconductive detector (2 nanowelded layers)

We will combine the knowledge and expertise gathered in the entire project to validate the approach. We will fabricate a simple monocrystalline **Cu<sub>2</sub>O photoconductive detector** on a 10-100 μm scale, by printing the materials developed in **Focus Area 1-2**. First, interdigitated back metal contacts will be deposited by thermal evaporation on a dielectric substrate. Next, a monocrystalline Cu<sub>2</sub>O film will be printed on the contacts with the technique optimised in 3.1/3.2. Finally, a monocrystalline Cu<sub>2</sub>O moderate-index nanopattern will be designed and deposited on the Cu<sub>2</sub>O film for light management. We will measure the optical response and compare to simulations. I-V characteristics under dark and illumination will be performed to assess the device responsivity as a function of incident power, and as a function of incident wavelength. The opportunity to improve performance via interface engineering/surface passivation described in 3.2 will be assessed. In this task we have a relatively simple scenario, with limited risks (2 nanowelded layers of the same material on which preliminary data are available, simple architecture). Nonetheless it will establish the methodology, it will help gaining valuable information on the critical aspects of the procedure (that will be useful for 3.4), and will show for the first time the use of a monocrystalline dielectric nanophotonic layer for light management, that could be integrated on any host substrate.

### 3.4 CsPbI<sub>3</sub> monocrystalline photovoltaic detector (3 nanowelded layers)

We will raise the bar by applying the **nanocube epitaxy & printing** to fabricate a stack composed of 3 monocrystalline layers, to function as a photovoltaic detector on a 1-100 μm scale, based on a MIM patch antenna configuration, where the absorber is a 10-30nm CsPbI<sub>3</sub> layer.

Non-radiative bulk recombinations are dramatically reduced in ultra-thin semiconducting layers, and as a result the photovoltaic efficiency increases<sup>2</sup>. It is however, challenging to (i) obtain monocrystalline CsPbI<sub>3</sub> films in this thickness range and (ii) efficiently absorb incoming light. This task will show that the strategy studied and developed in MeMeNtO paves the way to overcome these challenges. By using a patch antenna configuration<sup>112</sup>, we aim at designing a system that is critically coupled to maximise light absorption in a minute material volume. A patch antenna is composed of a dielectric photonic cavity sandwiched between two metallic planes, and allows coupling plasmonic cavity modes at frequencies which depends on the size and shape of the metal planes. Patch antenna are of special interest since they can lead to broad-band and polarization-independent light in-coupling. In addition, the large PL quantum yield of CsPbI<sub>3</sub>, combined with its ultra-small thickness enables us to realise a system that operates near the radiative limit; it is therefore the ideal platform for testing concepts of nanophotonic engineering to study ultimate material performance<sup>72</sup>. Finally, all-inorganic perovskites are defect-tolerant and are a promising solution to the instability issues observed in their hybrid counterpart<sup>113</sup>.



The technique developed will be used iteratively to build the following n-i-p architecture on

a glass/soft substrate, with the materials prepared in the Focus Area 1/2 :

FTO (transparent electrode), Al monocrystalline nanopattern (antenna), TiO<sub>2</sub> (electron transport layer, spincoated/ALD), CsPbI<sub>3</sub> (monocrystalline layer 10-30 nm thick), spiro-OMeTAD (hole transport layer- spincoated), Al monocrystalline film (back reflector and back contact).

We will employ the best available carrier selective charge transport layers, that were used in record efficiency solar cells reported earlier<sup>113</sup>. We will measure the external/internal quantum efficiency (EQE, IQE) as a function of wavelength, I-V characteristics under a solar simulator, and scanning photocurrent measurements to correlate with PL quantum yield, PL life-time and SEM images. This highly ambitious task will allow to assess the properties and the performance of the monocrystalline perovskite layer (obtained with the approach developed in this project) when implemented in a photovoltaic device, and compare it to literature. Thorough characterisation will enable to identify aspects that need improvement (band alignment, surface passivation, contacts, etc...). Depending on the outcomes of 3.2 regarding surface passivation/interface engineering schemes, different transport layers could be used to improve the alignment of energy levels, supported by UPS characterisation, if needed.

# ACKNOWLEDGMENTS

There are a lot of people that made my research work possible, from previous group members at different stages of my career, to present group members. In particular I would like to acknowledge Dr. Lionel Santinacci to welcome me in his team and for his considerable help in setting up my research activities at CINaM.

I would like also to thank my whole family for the support, and Stéphanie in particular.

## REFERENCES

- 1 Pugno, N. M. Space elevator: out of order? *Nano Today* **2**, 44-47, (2007).
- 2 Polman, A., Knight, M., Garnett, E. C., Ehrler, B. & Sinke, W. C. Photovoltaic materials: Present efficiencies and future challenges. *Science* **352**, aad4424, (2016).
- 3 Green, M. A., Emery, K., Hishikawa, Y., Warta, W. & Dunlop, E. D. Solar cell efficiency tables (version 46). *Prog Photovoltaics* **23**, 805-812, (2015).
- 4 Luque, A. & Hegedus, S. Handbook of Photovoltaic Science and Engineering. (Wiley, 2003).
- 5 Green, M. A. Limits on the open-circuit voltage and efficiency of silicon solar cells imposed by intrinsic Auger processes. *IEEE Transactions on* **31**, 671-678, (1984).
- 6 Lauhon, L. J., Gudixsen, M. S., Wang, C. L. & Lieber, C. M. Epitaxial core-shell and core-multishell nanowire heterostructures. *Nature* **420**, 57-61, (2002).
- 7 Lu, W. & Lieber, C. M. Nanoelectronics from the bottom up. *Nature Materials* **6**, 841-850, (2007).
- 8 Gong, S. H., Alpegiani, F., Sciacca, B., Garnett, E. C. & Kuipers, L. Nanoscale chiral valley-photon interface through optical spin-orbit coupling. *Science* **359**, 443-+, (2018).
- 9 Cao, L. Y. *et al.* Engineering light absorption in semiconductor nanowire devices. *Nat Mater* **8**, 643-647, (2009).
- 10 Fan, Z. Y. *et al.* Three-dimensional nanopillar-array photovoltaics on low-cost and flexible substrates. *Nat. Mater.* **8**, 648-653, (2009).
- 11 Konstantatos, G. & Sargent, E. H. Nanostructured materials for photon detection. *Nat Nanotechnol* **5**, 391-400, (2010).
- 12 Polman, A. & Atwater, H. A. Photonic design principles for ultrahigh-efficiency photovoltaics. *Nat. Mater.* **11**, 174-177, (2012).

- 13 Krogstrup, P. *et al.* Single-nanowire solar cells beyond the Shockley-Queisser limit. *Nat Photonics* **7**, 306-310, (2013).
- 14 Brongersma, M. L., Cui, Y. & Fan, S. H. Light management for photovoltaics using high-index nanostructures. *Nat. Mater.* **13**, 451-460, (2014).
- 15 Esfandyarpour, M., Garnett, E. C., Cui, Y., McGehee, M. D. & Brongersma, M. L. Metamaterial mirrors in optoelectronic devices. *Nat Nanotechnol* **9**, 542-547, (2014).
- 16 Priolo, F., Gregorkiewicz, T., Galli, M. & Krauss, T. F. Silicon nanostructures for photonics and photovoltaics. *Nature Nanotechnology* **9**, 19-32, (2014).
- 17 Aieta, F., Kats, M. A., Genevet, P. & Capasso, F. Multiwavelength achromatic metasurfaces by dispersive phase compensation. *Science* **347**, 1342-1345, (2015).
- 18 Koenderink, A. F., Alu, A. & Polman, A. Nanophotonics: Shrinking light-based technology. *Science* **348**, 516-521, (2015).
- 19 Alivisatos, P. Colloidal quantum dots. From scaling laws to biological applications. *Pure Appl Chem* **72**, 3-9, (2000).
- 20 Tang, J. Y., Huo, Z. Y., Brittman, S., Gao, H. W. & Yang, P. D. Solution-processed core-shell nanowires for efficient photovoltaic cells. *Nat Nanotechnol* **6**, 568-572, (2011).
- 21 Wallentin, J. *et al.* InP Nanowire Array Solar Cells Achieving 13.8% Efficiency by Exceeding the Ray Optics Limit. *Science* **339**, 1057-1060, (2013).
- 22 Aberg, I. *et al.* A GaAs Nanowire Array Solar Cell With 15.3% Efficiency at 1 Sun. *Ieee J Photovolt* **6**, 185-190, (2016).
- 23 Mann, S. A. *et al.* Quantifying losses and thermodynamic limits in nanophotonic solar cells. *Nat Nanotechnol* **11**, 1071-1075, (2016).
- 24 Wu, Y., Xiang, J., Yang, C., Lu, W. & Lieber, C. M. Single-crystal metallic nanowires and metal/semiconductor nanowire heterostructures. *Nature* **430**, 61-65, (2004).
- 25 Polman, A., Knight, M., Garnett, E. C., Ehrler, B. & Sinke, W. C. Photovoltaic materials: Present efficiencies and future challenges. *Science* **352**, (2016).
- 26 Nagpal, P., Lindquist, N. C., Oh, S. H. & Norris, D. J. Ultrasoft Patterned Metals for Plasmonics and Metamaterials. *Science* **325**, 594-597, (2009).
- 27 Zhang, J. T., Tang, Y., Lee, K. & Min, O. Y. Nonepitaxial Growth of Hybrid Core-Shell Nanostructures with Large Lattice Mismatches. *Science* **327**, 1634-1638, (2010).
- 28 Wu, Y. W. *et al.* Intrinsic Optical Properties and Enhanced Plasmonic Response of Epitaxial Silver. *Adv. Mater.* **26**, 6106-+, (2014).
- 29 Shi, D. *et al.* Low trap-state density and long carrier diffusion in organolead trihalide perovskite single crystals. *Science* **347**, 519-522, (2015).
- 30 Yang, Y. *et al.* Low surface recombination velocity in solution-grown CH<sub>3</sub>NH<sub>3</sub>PbBr<sub>3</sub> perovskite single crystal. *Nature Communications* **6**, (2015).
- 31 Sciacca, B., van de Groep, J., Polman, A. & Garnett, E. C. Solution-Grown Silver Nanowire Ordered Arrays as Transparent Electrodes. *Adv. Mater.* **28**, 905-909, (2016).
- 32 Li, Y., Qian, F., Xiang, J. & Lieber, C. M. Nanowire electronic and optoelectronic devices. *Mater Today* **9**, 18-27, (2006).
- 33 Yan, H. *et al.* Programmable nanowire circuits for nanoprocessors. *Nature* **470**, 240-244, (2011).

- 34 Thelander, C. *et al.* Nanowire-based one-dimensional electronics. *Mater Today* **9**, 28-35, (2006).
- 35 Brittman, S., Gao, H. W., Garnett, E. C. & Yang, P. D. Absorption of Light in a Single-Nanowire Silicon Solar Cell Decorated with an Octahedral Silver Nanocrystal. *Nano Lett* **11**, 5189-5195, (2011).
- 36 Garnett, E. C., Brongersma, M. L., Cui, Y. & McGehee, M. D. Nanowire Solar Cells. *Annu Rev Mater Res* **41**, 269-295, (2011).
- 37 Tian, B. Z. & Lieber, C. M. Design, synthesis, and characterization of novel nanowire structures for photovoltaics and intracellular probes. *Pure Appl Chem* **83**, 2153-2169, (2011).
- 38 Garnett, E. C., Peters, C., Brongersma, M., Cui, Y. & McGehee, M. Improving light absorption in thin silicon nanowire photovoltaics. *Abstr Pap Am Chem S* **239**, (2010).
- 39 Dong, Y. J., Tian, B. Z., Kempa, T. J. & Lieber, C. M. Coaxial Group III-Nitride Nanowire Photovoltaics. *Nano Lett* **9**, 2183-2187, (2009).
- 40 Tian, B., Kempa, T. J. & Lieber, C. M. Single nanowire photovoltaics. *Chem Soc Rev* **38**, 16-24, (2009).
- 41 Kempa, T. J. *et al.* Single and Tandem Axial p-i-n Nanowire Photovoltaic Devices. *Nano Lett* **8**, 3456-3460, (2008).
- 42 Lieber, C. Nanowire-based photovoltaics build small powerful solar cells. *Adv Mater Process* **166**, 24-24, (2008).
- 43 Tian, B. Z. *et al.* Coaxial silicon nanowires as solar cells and nanoelectronic power sources. *Nature* **449**, 885-U888, (2007).
- 44 Jiang, Z., Qing, Q., Xie, P., Gao, R. X. & Lieber, C. M. Kinked p-n Junction Nanowire Probes for High Spatial Resolution Sensing and Intracellular Recording. *Nano Lett* **12**, 1711-1716, (2012).
- 45 Estephan, E. *et al.* Peptides for the Biofunctionalization of Silicon for Use in Optical Sensing with Porous Silicon Microcavities. *Adv Funct Mater* **21**, 2003-2011, (2011).
- 46 Jiang, X. C. *et al.* Rational growth of branched nanowire heterostructures with synthetically encoded properties and function. *P Natl Acad Sci USA* **108**, 12212-12216, (2011).
- 47 Gao, X. P. A., Zheng, G. F. & Lieber, C. M. Subthreshold Regime has the Optimal Sensitivity for Nanowire FET Biosensors. *Nano Lett* **10**, 547-552, (2010).
- 48 Zheng, G. F., Gao, X. P. A. & Lieber, C. M. Frequency Domain Detection of Biomolecules Using Silicon Nanowire Biosensors. *Nano Lett* **10**, 3179-3183, (2010).
- 49 Patolsky, F., Zheng, G. F. & Lieber, C. M. Nanowire-based biosensors. *Anal Chem* **78**, 4260-4269, (2006).
- 50 Patolsky, F., Zheng, G. & Lieber, C. M. Nanowire sensors for medicine and the life sciences. *Nanomedicine-Uk* **1**, 51-65, (2006).
- 51 Wang, W. U., Chen, C., Lin, K. H., Fang, Y. & Lieber, C. M. Label-free detection of small-molecule-protein interactions by using nanowire nanosensors. *P Natl Acad Sci USA* **102**, 3208-3212, (2005).
- 52 Zhong, Z. H., Wang, D. L., Cui, Y., Bockrath, M. W. & Lieber, C. M. Nanowire crossbar arrays as address decoders for integrated nanosystems. *Science* **302**, 1377-1379, (2003).
- 53 Huang, Y. *et al.* Logic gates and computation from assembled nanowire building blocks. *Science* **294**, 1313-1317, (2001).

- 54 Qing, Q. *et al.* Nanowire transistor arrays for mapping neural circuits in acute brain slices. *P Natl Acad Sci USA* **107**, 1882-1887, (2010).
- 55 Cohen-Karni, T., Timko, B. P., Weiss, L. E. & Lieber, C. M. Flexible electrical recording from cells using nanowire transistor arrays. *P Natl Acad Sci USA* **106**, 7309-7313, (2009).
- 56 Lu, W., Xie, P. & Lieber, C. M. Nanowire Transistor Performance Limits and Applications. *Ieee T Electron Dev* **55**, 2859-2876, (2008).
- 57 Lieber, C. M. Design, synthesis and properties of programmable nanowire transistors for nanoscale circuits and processors. *Abstr Pap Am Chem S* **243**, (2012).
- 58 Tian, B. Z. & Lieber, C. M. Single nanowire photovoltaics. *Abstr Pap Am Chem S* **238**, (2009).
- 59 Schmidt, V., Senz, S. & Gosele, U. Influence of the Si/SiO<sub>2</sub> interface on the charge carrier density of Si nanowires. *Appl Phys a-Mater* **86**, 187-191, (2007).
- 60 Kempa, T. J. *et al.* Facet-selective growth on nanowires yields multi-component nanostructures and photonic devices. *J Am Chem Soc* **135**, 18354-18357, (2013).
- 61 Korte, K. E., Skrabalak, S. E. & Xia, Y. N. Rapid synthesis of silver nanowires through a CuCl- or CuCl<sub>2</sub>-mediated polyol process. *J Mater Chem* **18**, 437-441, (2008).
- 62 Sun, Y. G., Mayers, B., Herricks, T. & Xia, Y. N. Polyol synthesis of uniform silver nanowires: A plausible growth mechanism and the supporting evidence. *Nano Lett* **3**, 955-960, (2003).
- 63 Sun, Y. G., Gates, B., Mayers, B. & Xia, Y. N. Crystalline silver nanowires by soft solution processing. *Nano Lett* **2**, 165-168, (2002).
- 64 Sun, Y. G. & Xia, Y. N. Large-scale synthesis of uniform silver nanowires through a soft, self-seeding, polyol process. *Adv Mater* **14**, 833-837, (2002).
- 65 Kempa, T. J., Day, R. W., Kim, S. K., Park, H. G. & Lieber, C. M. Semiconductor nanowires: a platform for exploring limits and concepts for nano-enabled solar cells. *Energ Environ Sci* **6**, 719-733, (2013).
- 66 Yuhas, B. D. & Yang, P. D. Nanowire-Based All-Oxide Solar Cells. *J Am Chem Soc* **131**, 3756-3761, (2009).
- 67 Zhang, Q. F., Uchaker, E., Candelaria, S. L. & Cao, G. Z. Nanomaterials for energy conversion and storage. *Chem Soc Rev* **42**, 3127-3171, (2013).
- 68 Cao, L. Y. *et al.* Semiconductor Nanowire Optical Antenna Solar Absorbers. *Nano Lett* **10**, 439-445, (2010).
- 69 Mann, S. A. & Garnett, E. C. Extreme Light Absorption in Thin Semiconductor Films Wrapped around Metal Nanowires. *Nano Lett* **13**, 3173-3178, (2013).
- 70 Cohen-Karni, T. *et al.* Synthetically Encoded Ultrashort-Channel Nanowire Transistors for Fast, Pointlike Cellular Signal Detection. *Nano Lett* **12**, 2639-2644, (2012).
- 71 Nam, S., Jiang, X. C., Xiong, Q. H., Ham, D. & Lieber, C. M. Vertically integrated, three-dimensional nanowire complementary metal-oxide-semiconductor circuits. *P Natl Acad Sci USA* **106**, 21035-21038, (2009).
- 72 van der Burgt, J. S. & Garnett, E. C. Nanophotonic Emission Control for Improved Photovoltaic Efficiency. *ACS Photonics* **7**, 1589-1602, (2020).

- 73 Xia, Y. N., Xiong, Y. J., Lim, B. & Skrabalak, S. E. Shape-Controlled Synthesis of Metal Nanocrystals: Simple Chemistry Meets Complex Physics? *Angew Chem Int Edit* **48**, 60-103, (2009).
- 74 Sciacca, B. *et al.* Solution-Phase Epitaxial Growth of Quasi-Monocrystalline Cuprous Oxide on Metal Nanowires. *Nano Lett* **14**, 5891-5898, (2014).
- 75 Mann, S. A. *et al.* Integrating Sphere Microscopy for Direct Absorption Measurements of Single Nanostructures. *Acs Nano* **11**, 1412-1418, (2017).
- 76 Ye, S. R., Rathmell, A. R., Chen, Z. F., Stewart, I. E. & Wiley, B. J. Metal Nanowire Networks: The Next Generation of Transparent Conductors. *Adv Mater* **26**, 6670-6687, (2014).
- 77 van de Groep, J. V., Spinelli, P. & Polman, A. Transparent Conducting Silver Nanowire Networks. *Nano Lett* **12**, 3138-3144, (2012).
- 78 Garnett, E. C. *et al.* Self-limited plasmonic welding of silver nanowire junctions. *Nat Mater* **11**, 241-249, (2012).
- 79 Scheel, H. J. Historical aspects of crystal growth technology. *Journal of Crystal Growth* **211**, 1-12, (2000).
- 80 Cotal, H. *et al.* III-V multijunction solar cells for concentrating photovoltaics. *Energy & Environmental Science* **2**, 174-192, (2009).
- 81 Wang, S. *et al.* Large-Area Free-Standing Ultrathin Single-Crystal Silicon as Processable Materials. *Nano Lett* **13**, 4393-4398, (2013).
- 82 Cheng, C. W. *et al.* Epitaxial lift-off process for gallium arsenide substrate reuse and flexible electronics. *Nat Commun* **4**, 1577, (2013).
- 83 Kim, J. *et al.* Principle of direct van der Waals epitaxy of single-crystalline films on epitaxial graphene. *Nat Commun* **5**, (2014).
- 84 Tao, A., Sinsermsuksakul, P. & Yang, P. Tunable plasmonic lattices of silver nanocrystals. *Nat Nanotechnol* **2**, 435-440, (2007).
- 85 Fang, J., Ding, B. & Gleiter, H. Mesocrystals: syntheses in metals and applications. *Chem Soc Rev* **40**, 5347-5360, (2011).
- 86 De Yoreo, J. J. *et al.* Crystallization by particle attachment in synthetic, biogenic, and geologic environments. *Science* **349**, aaa6760, (2015).
- 87 Nakagawa, Y., Matsumoto, R., Kageyama, H., Oaki, Y. & Imai, H. Layer-by-layer manipulation of anisotropic nanoblocks: orientation- switched superlattices through orthogonal stacking of a and c directions. *Nanoscale* **10**, 12957-12962, (2018).
- 88 Schliehe, C. *et al.* Ultrathin PbS sheets by two-dimensional oriented attachment. *Science* **329**, 550-553, (2010).
- 89 Sciacca, B. *et al.* Monocrystalline Nanopatterns Made by Nanocube Assembly and Epitaxy. *Adv Mater* **29**, (2017).
- 90 Ansar, S. M. *et al.* Removal of Molecular Adsorbates on Gold Nanoparticles Using Sodium Borohydride in Water. *Nano Lett* **13**, 1226-1229, (2013).
- 91 Park, J. E., Lee, Y. & Nam, J. M. Precisely Shaped, Uniformly Formed Gold Nanocubes with Ultrahigh Reproducibility in Single-Particle Scattering and Surface-Enhanced Raman Scattering. *Nano Lett* **18**, 6475-6482, (2018).
- 92 Hsu, C. M., Connor, S. T., Tang, M. X. & Cui, Y. Wafer-scale silicon nanopillars and nanocones by Langmuir-Blodgett assembly and etching. *Appl. Phys. Lett.* **93**, (2008).

- 93 Kang, J. & Wang, L. W. High Defect Tolerance in Lead Halide Perovskite CsPbBr<sub>3</sub>. *J Phys Chem Lett* **8**, 489-493, (2017).
- 94 Kuznetsov, A. I., Miroshnichenko, A. E., Brongersma, M. L., Kivshar, Y. S. & Luk'yanchuk, B. Optically resonant dielectric nanostructures. *Science* **354**, (2016).
- 95 Jin, R. *et al.* Photoinduced conversion of silver nanospheres to nanoprisms. *Science* **294**, 1901-1903, (2001).
- 96 Juan, M. L., Righini, M. & Quidant, R. Plasmon nano-optical tweezers. *Nat Photonics* **5**, 349-356, (2011).
- 97 Shoji, T. & Tsuboi, Y. Plasmonic Optical Tweezers toward Molecular Manipulation: Tailoring Plasmonic Nanostructure, Light Source, and Resonant Trapping. *J Phys Chem Lett* **5**, 2957-2967, (2014).
- 98 Cortes, E. *et al.* Plasmonic hot electron transport drives nano-localized chemistry. *Nat Commun* **8**, (2017).
- 99 de Nijs, B. *et al.* Plasmonic tunnel junctions for single-molecule redox chemistry. *Nat Commun* **8**, (2017).
- 100 Baffou, G., Bordacchini, I., Baldi, A. & Quidant, R. Simple experimental procedures to distinguish photothermal from hot-carrier processes in plasmonics. *Light-Sci Appl In press*, (2020).
- 101 Kraus, T. *et al.* Nanoparticle printing with single-particle resolution. *Nat. Nanotechnol.* **2**, 570-576, (2007).
- 102 Flauraud, V. *et al.* Nanoscale topographical control of capillary assembly of nanoparticles. *Nat. Nanotechnol.* **12**, 73-80, (2017).
- 103 van de Groep, J. *et al.* Large-area soft-imprinted nanowire networks as light trapping transparent conductors. *Sci Rep* **5**, 11414, (2015).
- 104 Tao, A. R., Huang, J. X. & Yang, P. D. Langmuir-Blodgett of Nanocrystals and Nanowires. *Accounts of Chemical Research* **41**, 1662-1673, (2008).
- 105 Ni, S. B., Leemann, J., Wolf, H. & Isa, L. Insights into mechanisms of capillary assembly. *Faraday Discuss* **181**, 225-242, (2015).
- 106 Patra, B. K. *et al.* Close-Packed Ultrasoft Self-assembled Monolayer of CsPbBr<sub>3</sub> Perovskite Nanocubes. *Acs Appl Mater Inter* **12**, 31764-31769, (2020).
- 107 Agrawal, H. & Garnett, E. C. Nanocube Imprint Lithography. *Acs Nano* **14**, 11009-11016, (2020).
- 108 Zhang, W. H., Huang, L. N., Santschi, C. & Martin, O. J. F. Trapping and Sensing 10 nm Metal Nanoparticles Using Plasmonic Dipole Antennas. *Nano Lett* **10**, 1006-1011, (2010).
- 109 Jahani, S. & Jacob, Z. All-dielectric metamaterials. *Nat Nanotechnol* **11**, 23-36, (2016).
- 110 Aizpurua, J. *et al.* Optical properties of coupled metallic nanorods for field-enhanced spectroscopy. *Phys Rev B* **71**, (2005).
- 111 Lin, X. *et al.* Dipole-field-assisted charge extraction in metal-perovskite-metal back-contact solar cells. *Nat Commun* **8**, 613, (2017).
- 112 Reynaud, C. A. *et al.* Enhancing Reproducibility and Nonlocal Effects in Film-Coupled Nanoantennas. *Adv Opt Mater* **6**, (2018).
- 113 Wang, Y. *et al.* Thermodynamically stabilized beta-CsPbI<sub>3</sub>-based perovskite solar cells with efficiencies >18. *Science* **365**, 591-595, (2019).



# **APPENDIX A: SELECTED CONTRIBUTIONS TO THE FIELD OF OPTICAL SENSING**

In this appendix I wish to briefly summarise some contribution I made to the field of optical (bio)sensing. During my career I've worked on the detection of different analyte targets: organic vapours, fluorescent dyes, pollutants in water, protein biomarkers, gas traces. Although light is used to transduce the detection of the target, these applications are based on three entirely different systems. In one case, a porous silicon photonic crystal substrate transduces changes in refractive index to a modification of its optical spectrum, that can be analysed in real time; or is used to amplify emission from fluorescent dyes. In the second system, plasmonic nanoparticles supported on the tip of an optical fiber transduce the presence of a biomarker (captured by antibody linked to the nanoparticle surface) whose presence alter the optical spectrum due to changes in the local refractive index. In the last example, traces of benzene are detected via its molecular fingerprint in a hybrid system composed of a thin sorbent film of zeolites supported on infrared nanoantennas.

## **A.1 Porous silicon optical sensors**

During my PhD, my research was focused on the emerging properties of nanostructured materials such as porous silicon, that plays an important role in the field of biosensing, as a large surface area, tunable optical features, visible luminescence emission and relatively easy derivatization are favorable properties for the development of biosensors. Porous silicon as platform material for sensing and biosensing has arisen many high- impact proof of principle studies. Although in some cases a sensitive detection of low concentrated biomolecules can be demonstrated, conventional systems as ELISA assay display an higher sensitivity. In the other hand porous silicon based biosensors outperform ELISA assays in terms of response time, amount of volume required, label- free operation. However, a lot of efforts must be

spent to give birth to a stable and reliable commercial sensor, but the potentiality are quite promising.

Within this complex and intriguing context my research activities interests have been turned to the realization of porous silicon nanostructures displaying novel interaction features towards some species, detectable through the special photonic features of the synthesized material, such as the dramatical fluorescence enhancement achieved in a double resonant microcavity for the detection of labeled proteins, or the excitation of Bloch surface waves in a multilayered nanostructure.

Below are briefly summarized the topics managed in my research activity I carried on during my PhD and postdoc at Politecnico di Torino, with the respective journal publications.

### **Realization of high quality porous silicon photonic nanostructure:**

I carried out a noticeable improvement of porous silicon synthesis for the fabrication of high optical quality porous silicon nanostructures, achieved by:

- a better preprocessing of the silicon wafer prior to the etch to remove the parasitic layer;
- the employment of low temperature synthesis (-45 °C and -25 °C) to reduce the roughness, to strongly limit the chemical etch, and to avoid fluctuation of the etch rate due to variation of the temperature during the synthesis;
- the use of etch breaks properly defined for any etching current to yield depth homogeneity and a better control of the quality of calibration curves to design the photonic structures.

All these tasks allowed an high control of the synthesis condition and enabled to yield nanostructures that display reduced light scattering.

As an example, the synthesis at -45 °C enabled the fabrication of high quality resonant microcavities, that were proven to be successful for enhancing the fluorescence emitted by a labeled protein embedded inside the porous silicon structure. In particular, great levels of sensitivity were achieved employing a doubly resonant microcavity, with one resonance tuned at the source excitation and one at the dye silicon membranes emission. A molar concentration of Cy-3-H dye as low as  $10^{-12}$  was measured and of  $10^{-9}$  in the case of labeled protein A. The doubly-enhancement of fluorescence could be exploited for labeled biomolecules such as proteins that, despite the large steric hindrance, have been demonstrated to diffuse within the mesoporous stratified structure allowing high sensitivity, which foresee promising applications in bio and life science (Sensor and actuators B: Chemical, 137, 2009). With a similar approach a EU (III) fluorescent complex was detected (ACS App Mat Int, 6, 2016).

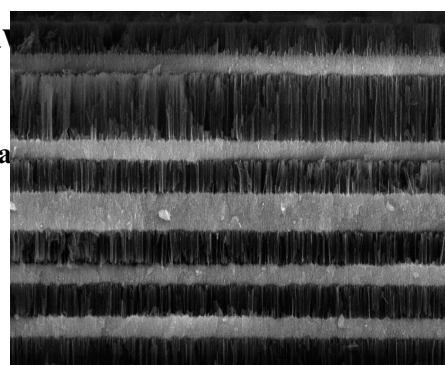


**Figure A1.** SEM cross-section of doubly resonant porous silicon microcavity

Employing high quality microcavities I designed and developed a porous silicon based analog integrated device for the detection of ethanol vapors, that despite has some limit as the selectivity towards some particular species, it can be improved employing surface functionalization with proper molecules. The example presented showed the capabilities of sensing based on porous silicon and reveals a lot of applications involving such material.

## Surface waves in porous silicon photonic nanostructures:

The coupling of surface electromagnetic waves (SEW) on porous silicon multilayers was experimentally demonstrated both in Otto and in Kretschmann configuration, showing a great agreement with the theory. The modeling of the electromagnetic interaction between the source and the multilayer is necessary prior to the design of an optimised structure and its experimental realisation. Such modeling has been realised through the implementation of the transfer matrix method in Matlab. SEW-based detection can be fruitfully employed in real-time monitoring of physical/chemical processes that takes place at the multilayer surface (Applied Physics Letters 91, 241109, 2007).

Employing free-standing porous silicon membranes allows excitation of the surface waves and sensing of the associated perturbation upon the exposure to organic vapours, reaching an unprecedented response time, smaller than the experimental resolution of our setup. Three vapours have been tested in the experiments, displaying different long term time constants, and diffusion coefficients which are well described by a model in which the diffusion constant is proportional to the molecular volume (Phys Chem Chem Phys, 12, 2010).

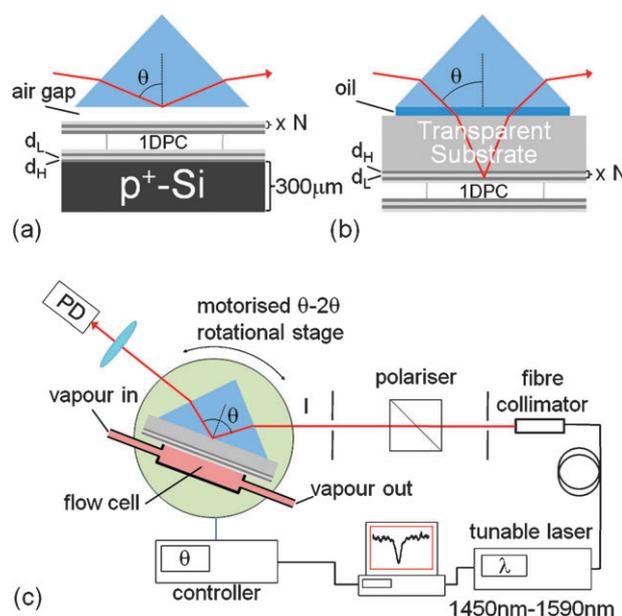


**Figure A2.** Experimental setup to excite surface wave in porous silicon multilayers. Otto (a) and Kretschmann (b) configuration respectively.

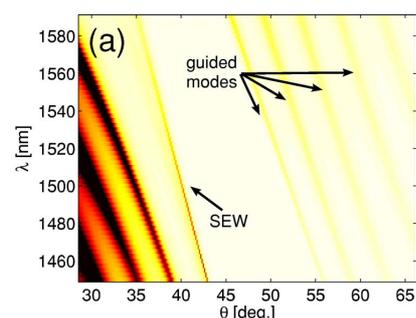


**Figure A3.** Band diagram of a porous silicon Bragg reflector in Otto configuration.

## Functionalisation and bioconjugation of porous silicon sensors:

The stability of sensors is extremely important and can be improved by means of surface functionalisation. I reported a novel method to functionalize thermally carbonized porous silicon film with carboxylic groups, employing a proper initiator that form radicals both on the carbonized porous silicon surface and on the dicarboxylic acid, thus covalently binding the acid to the surface (Dalton transactions, 39 (2010)). The excellent stability of such a surface in physiological media was demonstrated.

I successfully functionalized porous silicon with chitosan oligomers, obtaining a novel chitosan/porous silicon hybrid material, that enabled to improve the sensitivity towards

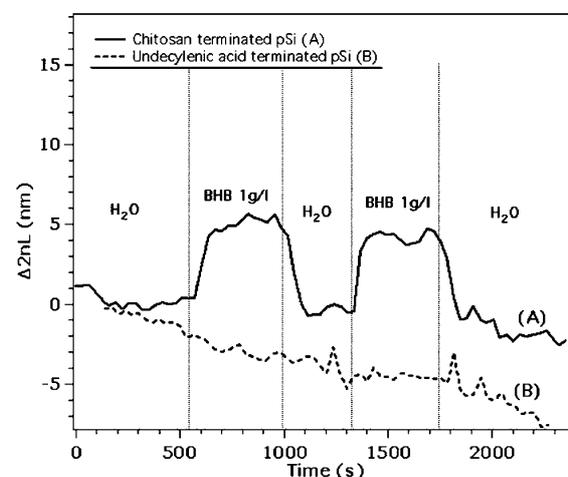


**Figure A4.** Optical thickness variation of a porous silicon film during the exposure to a positively-charged drug.

molecules with a certain pKa, taking advantages of the polycationic properties of chitosan. In particular, I demonstrated the functioning with some carboxyl-containing drugs as ibuprofen, which could be detected at concentration a hundred times smaller in the system where chitosan was present; I showed that an uncharged drug as caffeine is not affected by the presence of chitosan and displays the same response than that of porous silicon without chitosan. Moreover, I demonstrated a potential application of such hybrid system for the detection of an illicit drug such as gamma-hydroxybutyric acid (GHB), whose detection is important in several forensic cases. The combination of porous silicon with chitosan resulted to be a material more performant than porous silicon alone (Journal of Material Chemistry, 21 (2011)).

A nanoreactor was developed for the real time detection of Reactive Oxygen Species such as peroxyxynitrite, and to assess antioxidant materials (such as glutathione) towards ROS generated during metabolic reaction in the organism. The immobilization of a leucofluorescent dye (dichlorofluorescein, that is fluorescent in its oxidized form) was used as a transducer of the redox environment. The measurement of fluorescence intensity enables to real time detect redox reactions occurring within the porous substrate, which was demonstrated observing the switching of fluorescence mediated by a peroxyxynitrite-glutathione redox reaction inside the porous silicon substrate (Phys. Chem. Chem. Phys., 14 (15), (2012)).

I was also involved in the development of a new surface modification route for porous silicon microparticles (RSC Advances, 3 (2013)).

In the light of the results obtained during my research activity, porous silicon revealed to be a material with a strong potential for label free and fluorescence sensing, and also as a tool to study biological interactions.

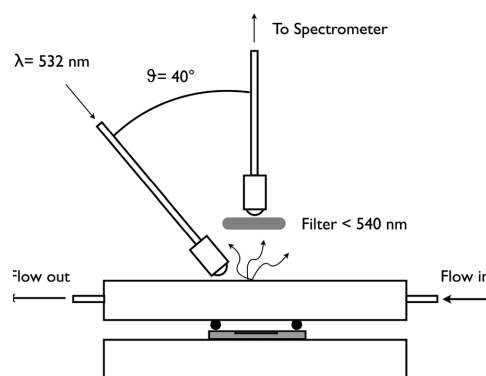


**Figure A5.** Experimental setup for the detection of ROS species.

## A.2 Surface plasmon resonance biosensors

During my postdoc at IPAS, my research activities were centered around an optical fiber based surface plasmon resonance (SPR) platform (patented and developed at IPAS) for the label free early diagnosis of gastric cancer. The aim of the project is to develop a multiplexed sensor able to detect and quantify a set of gastric cancer biomarkers, identified by collaborators working in the field of proteomics. The regulation (concentration) of such biomarkers in gastric cancer individuals needs to be properly quantified to discern if the subject is healthy or not. Such informations are obtained in the typical immunosensor approach, covalently binding specific antibody to the sensor surface, to capture the bait protein (biomarker). **The challenge here is the application of a label free platform to detect specifically and simultaneously several small proteins (< 60 kDa) quantifying their concentration.** I demonstrated that properly bioconjugating the surface of the sensor to have a correct orientation of the antibodies, it is possible to detect apolipoprotein E, a small

molecular weight protein reported to be up-regulated in gastric cancer individuals, and to quantify its regulation from the analysis of the binding kinetics results (Nanomedicine:NBM, 9 (2013)). I also proved that the multiplexed sensing is possible with this platform, using one optical fiber with two different sensing regions, a first step to the simultaneous detection of several biomarkers (Sensors and Actuators B 183 (2013)).

Improvements in the platform and in the biological interface were necessary to achieve this important target. In particular:

- I introduced substantial improvement in the setup, as the employment of a different light source for reduced background, improved signal to noise ratio and reduced costs;
- I employed a different glass substrate for the optical fiber that allowed to improve the sensitivity of five times, as predicted from theoretical modeling results;
- I designed an appropriate flow cell to reduce costs, improve flow and reproducibility of the experiments, necessary for kinetics analysis;
- I developed a new surface functionalization strategy to properly orient the antibodies to capture bait proteins with small molecular weight, reducing the detection limit;
- I developed an automated data analysis routine to follow the binding kinetics in real time.

I also started other research projects in localized surface plasmons for the realization of **dip-biosensors** (Langmuir, 30 (2014)), and fluorescence enhancement by plasmonic waves (Optical Material Express, 2128, 2016). In particular, localized surface plasmons are a good asset for multiplexed detection of biomolecules and for studying biological interactions thanks to their tunability in terms of photonics features, and their high sensitivity to interaction with analytes.

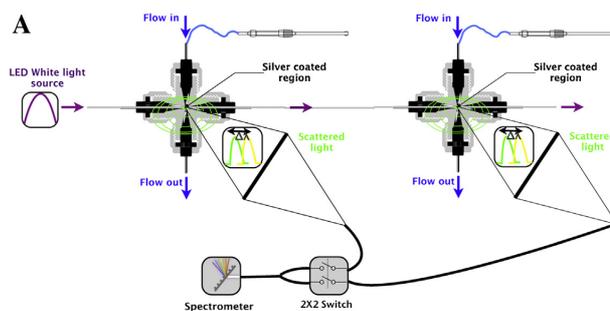


**Figure A6.** Multiplexed emission-SPR biosensor for the detection of gastric cancer biomarkers.

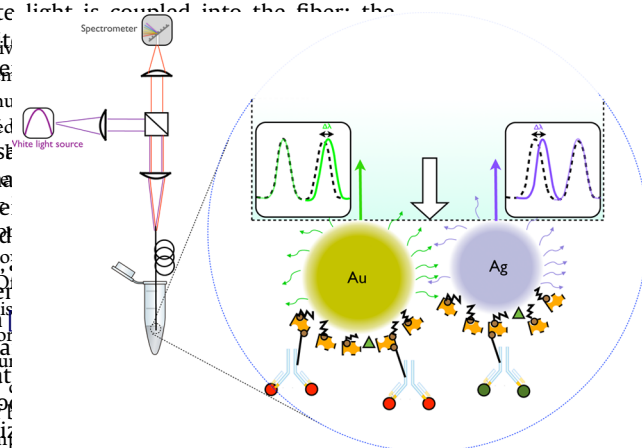


**Figure A7.** Dip biosensor based on plasmonic nanoparticle for the simultaneous detection and quantification of gastric cancer biomarkers.

### A.3 Infrared gas sensors

Infrared spectroscopy is a powerful analytical tool that allows the identification of molecular species. The sensitivity of this technique, strongly limited by the low absorption cross section of molecular vibrations, can be greatly improved by a resonant interaction with nano-antennas via the mechanism of enhanced infrared absorption (Surface-enhanced Infrared Absorption - **SEIRA**). However, most examples of SEIRA involve solid-state molecular layers adsorbed onto the nano-antennas, while trace gas detection still remains elusive due to the spatial extent of the near field that is used to amplify molecular vibrations in resonance.

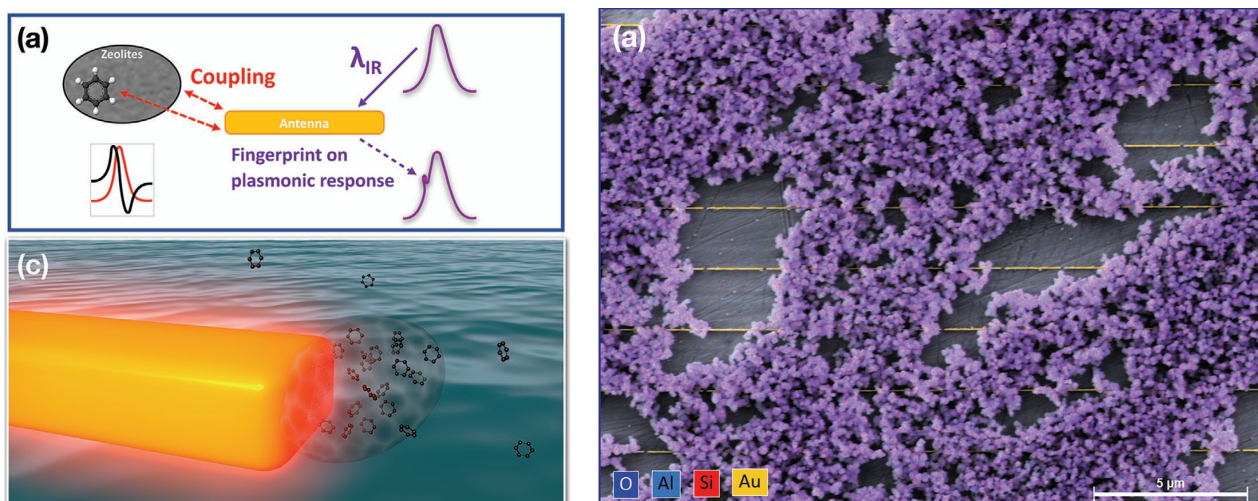


**Figure A8.** Cartoon (a), (b) and coloured SEM images of hybrid zeolite-gold infrared nanoantennas for the detection of benzene traces, via SEIRA.

We have developed a hybrid system composed of an array of plasmonic nano-antennas coupled to a nanometric zeolite coating which allows molecules, such as volatile organic compounds, to be trapped in the near field of the resonators and to amplify their response. The concerted action of the coating and the nano-antennas allowed us to detect record traces of **benzene (25 ppb)** in 10 min. This approach may ultimately enable the fabrication of a compact system for the rapid detection of pharmaceuticals and biocompounds with high sensitivity and selectivity. In the future, the electronic lithography step used for the fabrication of this surface could be substituted with a process of assembly and epitaxy of nanocubes presented earlier.

# APPENDIX B: CURRICULUM VITAE

## BENIAMINO SCIACCA, PhD

---

Email: [beniamino.sciacca@cnr.fr](mailto:beniamino.sciacca@cnr.fr);

Website: [http://www.cinam.univ-mrs.fr/sciacca/pro\\_perso/](http://www.cinam.univ-mrs.fr/sciacca/pro_perso/)

Tel: +33 (0)660362822

### CURRENT POSITION

**CNRS Research Scientist working at the  
Institute CINaM (Marseille)  
Team SuNE (direction Dr. L. Santinacci)**

Dr. Beniamino Sciacca is a scientist whose research activities lie in the edge between physics, chemistry and nanotechnology. He is involved in the synthesis, characterization and elaboration of nanomaterials for nano-enabled optoelectronics, in light-matter interaction at the nanoscale and in the realization of devices (single nanowire and large scale) for solar energy conversion. He has expertise in the domain of photovoltaics, synthesis and characterization of nanomaterials, thin films, optics, plasmonics, surface plasmon resonance, surface functionalization, biosensing.

### EDUCATION

---

#### **High Qualified Research Doctor – Politecnico di Torino, 2010**

“Nanotechnologies and nanostructured innovative materials” (Materials Science), under the supervision of Prof. Francesco Geobaldo Thesis: “Porous silicon nanostructures for biosensing devices”, with the mention: “The Board unanimously assessed as excellent his research work”. Recognition as “European Doctorate”, fulfilling all the criteria required by the European University Association.

#### **Alta Scuola Politecnica Diploma – 2007**

(<http://www.asp-poli.it>); mention: “with merit”

#### **M.S. in Biomedical engineering, Politecnico di Milano – 2006**

#### **M.S. in Biomedical engineering, Politecnico di Torino – 2006**

## RESEARCH EXPERIENCES

with the mention “cum laude”. Thesis: “A molecular mechanics study of the interaction between microcantilever and DNA fragments”, under the supervision of Prof. Franco Montevercchi.

### **B.S. in Biomedical engineering, Politecnico di Torino — 2004**

with the mention “cum laude”. Thesis: “Electrical characterization of micro-electrode matrices: noise measurement”, under the supervision of Prof. Marco Knäflitz.

---

### **Research Scientist, TNO; Eindhoven, Netherlands - 2017-2018**

Developed a new concept for mid-infrared based gas sensing, based on the combination of resonant antennas with concentrating coatings. Also worked on the investigation and characterization of new dyes for fast STED lithography.

### **Research Scientist, ASML; Veldhoven, Netherlands - 2017**

Introduced a new concept mark for wafer alignment, based on the modulation of the amplitude of diffracted light by a resonant grating.

### **Senior postdoc, FOM Institute AMOLF; Amsterdam — 2013-2016**

Advisor: Dr. Erik Garnett

Worked on nanoscale solar cells. Involved in the *synthesis* (solution phase) and *characterization* (structural, compositional, optical, electrical) of metal-semiconductor core-shell nanowires as building blocks for efficient and inexpensive solar cells. Light management in photovoltaics (*nanophotonics*): involved in the development of optical microscopy techniques to characterize quantitatively individual nanostructures. Also worked on the realization of monocrystalline transparent electrodes based on ordered array of metal nanowires from nanocube building blocks. Involved on design (*simulations*) and *devices* fabrication of core-shell nanowires arrays for large scale photovoltaics.

### **Research Associate, Institute for Photonics & Advanced Sensing; Adelaide (Australia) — 2011-2012**

Advisor: Prof. Tanya Monro

Worked on the development of optical fiber-based surface plasmon resonance biosensors for early stages diagnosis of gastric cancer. Developed the radiative-SPR platform to allow for the multiplexed detection of multiple biomarkers simultaneously real-time to be applied both as a diagnostic tool and in Proteomics research. Work involved improvements in the platform architecture and in the surface functionalization. Developed also a dip sensing architecture based on localized surface plasmons for multiplexed detection of biomarkers.

### **PhD student, Politecnico di Torino; — 2006-2010**

Advisor: Prof. Francesco Geobaldo

Worked on the development of 1D porous silicon photonics nanostructures for sensing. Explored several approaches for label free (e.g. porous silicon multilayer supporting surface waves) and fluorescence based sensing (e.g. doubly resonant porous silicon microcavity for fluorescence enhancement of labeled protein). Developed a porous silicon based nanoreactor for the real time detection of ROS species by means of hybrid resonant microcavity.

### **Visiting student, University of Montpellier; — May-August 2009**

Advisor: Dr. Frederique Cunin

Developed a hybrid material porous silicon/chitosan to detect low concentrated pollutants in water.

**Visiting student, UCSD; San Diego (USA); – May-November 2008**

Advisor: Prof. Michael Sailor

Developed a novel functionalization route to modify the surface chemistry of thermally carbonized porous silicon chips for further bioconjugation chemistry for the development of biosensors with an improved stability in buffer solutions.

## SKILLS

- 
- Synthesis of porous silicon thin film optical structures (resonant microcavities, bragg mirrors, rugate filters)
  - Synthesis of nanomaterials: nanowires, nanoparticles, metal-semiconductor core-shell heterostructures; primarily via solution phase
  - Functionalization via surface chemistry for bioconjugation;
  - Characterization of nanomaterials:
    - **Chemical:** FT-IR, Raman spectroscopy, EDS, XRD
    - **Structural:** SEM, TEM (analysis), SAED (analysis)
    - **Optical:** Photoluminescence lifetime, Interferometry, UV-Vis, Ellipsometry, Single nanowire quantitative absorption measurement, scanning photocurrent measurements, SNOM, Confocal microscopy.
    - **Topological:** AFM, low voltage SEM (20V-100 V) highly sensitive to surface texturing and elemental composition
    - **Electrical:** I-V characteristics of nanowire devices
  - Self-assembly of nanomaterials in arbitrary pattern.
  - Nanofabrication/Cleanroom: optical lithography, e-beam lithography, metallization (thermal, sputtering, e-beam) etching, Focused Ion Beam.
  - Realization of Immunoassays for biosensing: SPR on planar substrate, SPR on optical fibers, LSPR on metal nanoparticles.
  - Experimental optics for building characterization setups
  - Modeling of 1D photonic structures (Transfer matrix method) and rigorous coupled wave analysis for grating-like structured multilayers
  - FDTD (Lumerical)
  - Programming: Matlab, C, Simulink, IgorPro
  - FEM: COMSOL

- 
- Supervision of 5 PhD, 5 Master and 3 Bachelor students
  - Peer reviewer for Advanced Materials, Advanced Electronic Materials, JACS, Sensors and Actuators B, Langmuir, Optics Express, Nature Electronics, Advanced Science, Journal of Crystal Growth
  - Project Coordination (1 ANR, 1 Region Sud, 1 CNRS-MITI)

## AWARDS

- 
- Best talk in the conference NANOSMAT 2007, symposium “porous semiconductors”, title: “Controlled light emission and propagation in porous silicon resonant multilayers”, (2007).

- Winner of a national scholarship granted by MIUR-INAIL - 2003-2004

---

## PATENTS

- (1) "Method for manufacturing a patterned monocrystalline film and such a patterned monocrystalline film", #2016849
- (2) "Resonant Amplitude Marks: a novel alignment mark family that is insensitive to process-induced asymmetries", #17197914.9EP
- (3) "Gas sensing via concentrated coatings supported on infrared resonant nanoantennas", #18182298.2EP

---

## LANGUAGES

Italian, English, French.

## APPENDIX C: PUBLICATION LIST

1. A. Capitaine, B. Sciacca\*  
*Nanocube epitaxy for the realisation of printable monocrystalline nanophotonic surfaces*  
**Advanced Materials** (2022)  
<https://doi.org/10.1002/adma.202200364> ➔ pdf
2. A. Capitaine, B. Sciacca\*  
*Monocrystalline methylammonium lead halide perovskite materials for photovoltaics*  
**Advanced Materials** (2021)  
<https://onlinelibrary.wiley.com/doi/abs/10.1002/adma.202102588> ➔ pdf
3. J. Nunez, A. Boersma, J. Grand, S. Mintova, B. Sciacca\*  
*Thin functional zeolite layer supported on infrared resonant nano-antennas for the detection of benzene traces*  
**Advanced Functional Materials** (2021) <https://doi.org/10.1002/adfm.202101623> ➔ pdf
4. S. H. Gong, F. Alpeggiani, B. Sciacca, E. C. Garnett, L. Kuipers  
*Nanoscale chiral valley-photon interface through optical spin-orbit coupling*  
**Science** 359, 51 (2018) ➔ pdf
5. B. Sciacca, A. Berkhout, B. J. M. Brenny, S. Z. Oener, M. A. van Huis, A. Polman, E. C. Garnett  
*Monocrystalline Nanopatterns Made by Nanocube Assembly and Epitaxy*  
**Advanced Materials** 29, 1701064 (2017) ➔ pdf
6. S. A. Mann, B. Sciacca, Y. Y. Zhang, J. Wang, E. Kontoleta, H. Y. Liu, E. C. Garnett  
*Integrating Sphere Microscopy for Direct Absorption Measurements of Single Nanostructures*  
**Acs Nano** 11, 1412 (2017) ➔ pdf

7. M. de Goede, E. Johlin, B. Sciacca, F. Boughorbel, E. C. Garnett  
*3D multi-energy deconvolution electron microscopy*  
**Nanoscale** 9, 684 (2017) → [pdf](#)
8. E. Klantsataya, A. Francois, H. Ebendorff-Heidepriem, B. Sciacca, A. Zuber, T. M. Monro  
*Effect of surface roughness on metal enhanced fluorescence in planar substrates and optical fibers*  
**Optical Material Express** 6, 2128 (2016) → [pdf](#)
9. X. Z. Zheng, B. Sciacca, E. C. Garnett, L. W. Zhang  
*AgFeS<sub>2</sub>-Nanowire-Modified BiVO<sub>4</sub> Photoanodes for Photoelectrochemical Water Splitting*  
**ChemPlusChem** 81, 1075 (2016) → [pdf](#)
10. B. Sciacca, J. van de Groep, A. Polman, E. C. Garnett  
*Solution-Grown Silver Nanowire Ordered Arrays as Transparent Electrodes*  
**Advanced Materials** 28, 905 (2016) → [pdf](#)
11. B. Sciacca, A. O. Yalcin, E. C. Garnett  
*Transformation of Ag Nanowires into Semiconducting AgFeS<sub>2</sub> Nanowires*  
**Journal of the American Chemical Society** 137, 4340 (2015) → [pdf](#)
12. S. Z. Oener, S. A. Mann, B. Sciacca, C. Sfiligoj, J. Hoang, E. C. Garnett  
*Au-Cu<sub>2</sub>O core-shell nanowire photovoltaics*  
**Applied Physics Letters** 106, 023501 (2015) → [pdf](#)
13. B. Sciacca, S. A. Mann, F. D. Tichelaar, H. W. Zandbergen, M. A. van Huis, E. C. Garnett  
*Solution-Phase Epitaxial Growth of Quasi-Monocrystalline Cuprous Oxide on Metal Nanowires*  
**Nano Letters** 14, 5891 (2014) → [pdf](#)
14. S. N. A. Jenie, S. Pace, B. Sciacca, R. D. Brooks, S. E. Plush, N. H. Voelcker  
*Lanthanide Luminescence Enhancements in Porous Silicon Resonant Microcavities*  
**Acs Applied Materials & Interfaces** 6, 12012 (2014) → [pdf](#)
15. B. Sciacca\* and T. M. Monro  
*Dip Biosensor Based on Localized Surface Plasmon Resonance at the Tip of an Optical Fiber*  
**Langmuir** 30, 946 (2014) → [pdf](#)
16. S. Pace, B. Sciacca, F. Geobaldo  
*Surface modification of porous silicon microparticles by sonochemistry*  
**Rsc Advances** 3, 18799 (2013) → [pdf](#)
17. B. Sciacca\*, A. Francois, P. Hoffmann, T. M. Monro  
*Multiplexing of radiative-surface plasmon resonance for the detection of gastric cancer biomarkers in a single optical fiber*  
**Sensors & Actuators B:Chemical** 183, 454 (2013) → [pdf](#)

18. B. Sciacca\*, A. Francois, M. Klingler-Hoffmann, J. Brazzatti, M. Penno, P. Hoffmann, T. M. Monro  
*Radiative-surface plasmon resonance for the detection of apolipoprotein E in medical diagnostics applications*  
**Nanomedicine: Nanotechnology Biology and medicine** 9, 550 (2013) → [pdf](#)
19. B. Sciacca, S. Pace, P. Rivolo, F. Geobaldo  
*Switching of fluorescence mediated by a peroxyxynitrite-glutathione redox reaction in a porous silicon nanoreactor*  
**Physical Chemistry Chemical Physics** 14, 5251 (2012) → [pdf](#)
20. B. Sciacca, E. Secret, S. Pace, P. Gonzalez, F. Geobaldo, F. Quignard, F. Cunin  
*Chitosan-functionalized porous silicon optical transducer for the detection of carboxylic acid-containing drugs in water*  
**Journal of Materials Chemistry** 21, 2294 (2011) → [pdf](#)
21. B. Sciacca, S. D. Alvarez, F. Geobaldo, M. J. Sailor  
*Bioconjugate functionalization of thermally carbonized porous silicon using a radical coupling reaction*  
**Dalton Transactions** 39, 10847 (2010) → [pdf](#)
22. F. Michelotti, B. Sciacca, L. Dominici, M. Quaglio, E. Descrovi, F. Giorgis, F. Geobaldo  
*Fast optical vapour sensing by Bloch surface waves on porous silicon membranes*  
**Physical Chemistry Chemical Physics** 12, 502 (2010) → [pdf](#)
23. B. Sciacca, F. Frascella, A. Venturello, P. Rivolo, E. Descrovi, F. Giorgis, F. Geobaldo  
*Doubly resonant porous silicon microcavities for enhanced detection of fluorescent organic molecules*  
**Sensors & Actuators B:Chemical** 137, 467 (2009) → [pdf](#)
24. E. Descrovi, F. Frascella, B. Sciacca, F. Geobaldo, L. Dominici, F. Michelotti  
*Coupling of surface waves in highly defined one-dimensional porous silicon photonic crystals for gas sensing applications*  
**Applied Physics Letters** 91, 241109 (2007) → [pdf](#)
25. W. Navarrini, E. Canesi, M. Cantini, G. Resnati, P. Metrangolo, F. Ugger, V. Arcella, A. Casati, M. Masella, C. Guala, A. Ranzoni, L. Sallemi, B. Sciacca, F. Scotti  
*ASP studies on fluorine in biomedicine: two innovative applications*  
**Chimica Oggi-Chemistry Today** 25, 48 (2007) → [pdf](#)